



MAX-PLANCK-INSTITUT
FÜR CHEMISCHE PHYSIK FESTER STOFFE



TECHNISCHE
UNIVERSITÄT
DRESDEN

Superstructures in Heusler compounds and investigation of their physical properties

Dissertation

zur Erlangung des akademischen Grades

Doctor of Philosophy

(Ph. D.)

vorgelegt von

Praveen Vir

geboren am 28.12.1994 in Bhagalpur, India

Eingereicht am 20.05.2020

Verteidigt am 24.08.2020

dem Bereich Mathematik und Naturwissenschaften

der Technischen Universität Dresden

Die Dissertation wurde in der Zeit von August 2016 bis Juli 2020 am Max-Planck-Institut für Chemische Physik fester Stoffe in Dresden angefertigt.

Gutachter

1. Prof. Dr. Claudia Felser
2. Prof. Dr. Dmytro S. Inosov

To my family and friends

Contributions

Praveen Vir and Claudia Felser conceived the idea of the work discussed in Chapter 4. **Praveen Vir** prepared the polycrystalline and single crystal sample of $\text{Mn}_{1.4}\text{PtSn}$ and performed its structural characterization, magnetic and electrical transport properties measurements. Horst Borrmann performed the X-ray diffraction measurements. **Praveen Vir** performed the Reitveld refinement of powder XRD data. Horst Borrmann performed the refinement of single-crystal XRD data. **Praveen Vir** performed the microstructural and compositional analysis with scanning electron microscopy- Energy-dispersive X-ray spectroscopy (SEM-EDX). Gudrun Auffermann performed the chemical analysis to measure the composition of the single crystals. Ulrich Burkhardt (Metallography group at the MPI-CPfS, Dresden) performed the microstructural investigation (polishing and polarized-light optical microscopy). Marcus Schmidt and his co-workers performed the differential scanning calorimetry (DSC) experiments. **Praveen Vir** did the orientation of single crystals for magnetic and electrical transport properties. Françoise Damay (LLB, CEA Saclay, France) performed the powder neutron diffraction experiments. Alexandr S. Sukhanov did the refinement of powder neutron diffraction data. Jacob Gayles, Yan Sun, and Jürgen Kübler performed the theoretical calculations. This work is published in *Chem. Mater.* **31**, 5876 (2019) and *Phys. Rev. B* **99**, 140406(R) (2019).

Praveen Vir, Chandra Shekhar, and Claudia Felser conceived the idea of the work discussed in Chapters 5 and 6. **Praveen Vir** prepared the samples and performed their structural characterization, magnetic and electrical transport properties measurements. Horst Borrmann performed the X-ray diffraction measurements. **Praveen Vir** did the Reitveld refinement of powder XRD data. **Praveen Vir** performed the microstructural and compositional analysis with SEM-EDX. Ulrich Burkhardt (Metallography group at the MPI-CPfS, Dresden) performed the microstructural investigation (polishing and polarized-light optical microscope). Rana Saha at MPI-Halle prepared the thin lamella and did transmission electron microscopy experiment. Marcus Schmidt and his co-workers performed the DSC experiments. **Praveen Vir** performed magnetic and electrical transport properties. Françoise Damay (LLB, CEA Saclay, France) performed the powder neutron diffraction experiments. Alexandr S. Sukhanov did the refinement of powder neutron diffraction data. The manuscript based on this work is under preparation.

Praveen Vir and Claudia Felser conceived the idea of the work discussed in Chapter 7. **Praveen Vir** prepared the single crystal and performed its structural characterization, magnetic and electrical transport properties measurements. **Praveen Vir**, Joyce Pham, and Horst Borrmann performed single-crystal XRD measurements and did the structural analysis. **Praveen Vir** did the Reitveld refinement of powder XRD data. **Praveen Vir** performed the microstructural and compositional analysis with SEM-EDX. **Praveen Vir** performed magnetic and electrical transport properties with the help of Chandra Shekhar and Nitesh Kumar. The manuscript based on this work is under preparation.

List of publications

The work presented in publications 1 to 4 are part of the thesis.

1. **P. Vir**, N. Kumar, H. Borrmann, B. Jamijansuren, G. Kreiner, C. Shekhar, and C. Felser, Tetragonal superstructure of the antiskyrmion hosting Heusler compound $\text{Mn}_{1.4}\text{PtSn}$. *Chem. Mater.* **31**, 5876 (2019).
2. **P. Vir**, J. Gayles, A. S. Sukhanov, N. Kumar, F. Damay, Y. Sun, J. Kübler, C. Shekhar, and C. Felser., Anisotropic topological Hall effect with real and momentum space Berry curvature in the antiskyrmion hosting Heusler compound $\text{Mn}_{1.4}\text{PtSn}$. *Phys. Rev. B* **99**, 140406(R) (2019).
3. **P. Vir**, A. S. Sukhanov, V. Kumar, C. Shekhar, and C. Felser, Towards possibility of tuning the size of antiskyrmions by elemental substitution in $\text{Mn}_{1.4}\text{PtSn}$, *to be submitted*.
4. **P. Vir**, J. Pham, H. Borrmann, C. Shekhar, and C. Felser, $\text{Mn}_{1.7}\text{Pt}_{0.8}\text{In}$: A $3 \times 3 \times 3$ superstructure of Heusler compound with possible compensated ferrimagnetic structure, *to be submitted*.

-
5. A. S. Sukhanov, **P. Vir (equal contribution)**, A. Heinemann, D. Kriegner, H. Borrmann, C. Shekhar, C. Felser, and D. S. Inosov, Giant enhancement of the skyrmion stability in a chemically strained helimagnet, *Phys. Rev. B* **100**, 180403(R) (2019).
 6. A. S. Sukhanov, **P. Vir**, A. S. Cameron, H.-Ch. Wu, N. Martin, S. Mühlbauer, A. Heinemann, H.-D. Yang, C. Felser, and D. S. Inosov, Increasing the skyrmion stability in Cu_2OSeO_3 by chemical substitution, *Phys. Rev. B* **100**, 184408 (2019).
 7. S. N. Guin, **P. Vir**, Y. Zhang, N. Kumar, S. J. Watzman, C. Fu, E. Liu, K. Manna, W. Schnelle, J. Gooth, C. Shekhar, Y. Sun, and C. Felser, Zero-Field Nernst Effect in a Ferromagnetic Kagome-Lattice Weyl-Semimetal $\text{Co}_3\text{Sn}_2\text{S}_2$. *Adv. Mater.* **31**, 180622 (2019).
 8. K. Geishendorf, **P. Vir**, C. Shekhar, C. Felser, Jorge I. Facio, J. van den Brink, K. Nielsch, A. Thomas, and S. T. B. Goennenwein, Signatures for the entropy change in the anomalous Hall and Nernst signals in microstructures of the magnetic Weyl semimetal $\text{Co}_3\text{Sn}_2\text{S}_2$, *Nano Lett.* **20**, 300-305 (2020).
 9. G. S. Thakur, **P. Vir**, S. N. Guin, C. Shekhar, R. Wehrich, Y. Sun, N. Kumar, and C. Felser, Intrinsic anomalous Hall effect in Ni-substituted magnetic Weyl semimetal $\text{Co}_3\text{Sn}_2\text{S}_2$, *Chem. Mater.* **32**, 1612–1617 (2020).

10. K. Geishendorf, R. Schlitz, **P. Vir**, C. Shekhar, C. Felser, K. Nielsch, S. T. B. Goennenwein, and A. Thomas, Magnetoresistance and anomalous Hall effect in micro-ribbons of the magnetic Weyl semimetal $\text{Co}_3\text{Sn}_2\text{S}_2$. *Appl. Phys. Lett.* **114**, 092403 (2019).
11. T. Ma, A. K. Sharma, R. Saha, A. K. Srivastava, P. Werner, **P. Vir**, V. Kumar, C. Felser, and S. S. P. Parkin, Tunable antiskyrmion size and helix period from nanometers to microns, *Adv. Mater.* (accepted).
12. N. Kumar, J. Gayles, N. Rani, **P. Vir**, S. S. Guin, Y. Sun, C. Felser, and C. Shekhar, Giant anomalous Hall conductivity in the flatband magnetic metal LaCrSb_3 , *submitted*.
13. S. N. Guin, Q. Xu, N. Kumar, **P. Vir**, K. Manna, G. Auffermann, W. Schnelle, J. Gooth, C. Shekhar, Y. Sun, C. Felser, Room temperature 2D topological magnet, *submitted*.
14. S. Howard, L. Jiao, Z. Wang, N. Morali, R. Batabyal, P. K. Nag, N. Avraham, H. Beidenkopf, **P. Vir**, C. Shekhar, C. Felser, T. Hughes, and V. Madhavan, Observation of linearly dispersive edge modes in a magnetic Weyl semimetal $\text{Co}_3\text{Sn}_2\text{S}_2$, *submitted*.
15. A. S. Sukhanov, **P. Vir**, B. E. Z. Cespedes, A. S. Cameron, A. Heinemann, N. Martin, G. Chaboussant, L. M. Eng, C. Felser, and D. S. Inosov, Anisotropic magnetic texture in bulk $\text{Mn}_{1.4}\text{PtSn}$ revealed by small-angle neutron scattering, *to be submitted*.
16. B. E. Z. Cespedes, P. Milde, **P. Vir**, V. Kumar, M. König, C. Felser, and L. M. Eng, Magnetic structure dependence on plate thickness in $\text{Mn}_{1.4}\text{PtSn}$ single crystals, *to be submitted*.

Acknowledgements

Doing Ph.D. at Max Planck Institute for Chemical Physics of Solids (MPI-CPfS), Dresden is an excellent opportunity to learn new instrumental techniques and outstanding science. The research environment is impressive, where everyone is supportive and helpful. I sincerely thank Prof. Dr. Claudia Felser for providing me an opportunity to join her research group and work on an exciting topic as well as the support and advice throughout my Ph.D. career.

I especially would like to thank my advisor Dr. Chandra Shekhar at MPI-CPfS and Prof. Dr. Dmytro Inosov at TU Dresden, for their constant guidance, helpful discussions, which led to great ideas and new discoveries.

I would like to thank Alexandr Sukhanov with whom I shared the projects. I had a great experience working with you in the institute and during the neutron beamtimes. Also, I thank you for introducing me to powder neutron refinement.

I thank Dr. Nitesh Kumar for introducing me to basic of sample preparations and the help concerning manuscript preparation, Dr. Kaustuv Manna for Bridgman technique and Laue diffraction method, Dr. Jacob Gayles and Dr. Yan Sun for assisting my experimental results with theoretical calculations, Dr. Horst Borrmann for single crystal and powder X-ray diffraction, Dr. Gohil Thakur for introducing to Rietveld refinement by Topas, Dr. Joyce Pham for introducing single-crystal refinement by SHELX, Dr. Walter Schnelle and Ralf Koban for introducing to PPMS and MPMS instruments and all the help related to special measurements, Dr. Ulrich Burkhard and Sylvia Kostmann for polarized light microscopy and all the help related to metallography, Dr. Gudrun Auffermann for chemical analysis, Dr. Markus Schmidt and Susann Scharsach for DSC measurements, and Iryna Zelenina for focused ion beam (FIB).

Many thanks to Dr. Vivek Kumar, Dr. Satya Narayan Guin, Sukriti Singh, Johannes Kroder, and other colleagues at MPI-CPfS.

Last but not least, I would like to thank my family and friends for constant support and motivation.

Contents

1. Introduction	1
2. Theoretical background	5
2.1. Heusler compounds	5
2.2. Superstructure.....	8
2.3. Magnetic skyrmions and antiskyrmions.....	12
3. Techniques	17
3.1. Arc melting.....	17
3.2. Induction melting	17
3.3. Flux method.....	18
3.4. Bridgman method.....	19
3.5. X-ray diffraction.....	20
3.5.1. Powder X-ray diffraction.....	20
3.5.2. Single-crystal X-ray diffraction.....	21
3.5.3. Laue diffraction	21
3.6. Powder neutron diffraction.....	21
3.7. Physical properties measurements	21
3.7.1. Magnetic measurements	21
3.7.2. Electric transport measurements.....	21
4. Mn_{1.4}PtSn	23
4.1. Single crystal growth.....	23
4.1.1. Bridgman method	23
4.1.2. Flux method.....	26
4.2. Tetragonal superstructure	31
4.3. Magnetic properties.....	40
4.4. Electrical transport properties	43
4.5. Powder neutron diffraction.....	50
4.6. Theory	53

5. Mn_{1.4}Pt_{1-x}Ir_xSn (x = 0.1–1)	55
5.1. Sample preparation.....	55
5.2. Tetragonal superstructure.....	56
5.3. Magnetic properties.....	60
5.4. Powder neutron diffraction.....	68
5.5. Electrical transport properties	75
5.6. Single crystal growth.....	89
6. Mn_{1.4}Y_xPtSn (Y = Co, Ni, Cu; x = 0.1–0.6)	95
6.1. Sample preparation.....	95
6.2. Tetragonal superstructure.....	95
6.2.1. Cobalt addition	95
6.2.2. Nickel addition	100
6.2.3. Copper addition	104
6.3. Magnetic properties.....	108
6.3.1. Cobalt addition	108
6.3.2. Nickel addition	109
6.3.3. Copper addition	110
7. Mn_{1.7}Pt_{0.8}In	111
7.1. Single crystal growth.....	111
7.2. Superstructure.....	113
7.3. Magnetic properties.....	120
7.4. Electrical transport properties	122
Summary and future prospects	125
References	127

1. Introduction

Information technology has become part of our daily life and is involved everywhere, even in common items such as vehicles and phones. In this rapidly expanding sector of the world, to store an enormous amount of newly generated data, there is an immense demand to increase the memory density of electronic devices. Moore's law, which states that the transistor density of integrated circuits would be doubled every two years¹, is coming to a saturation point. To tackle this problem, spintronics is becoming a rapidly growing area of research. The term 'spintronics' is coined from the abbreviation of spin-based electronics, where the spin property of electrons is exploited instead of electric charge^{2,3}. The main advantages of spintronics based devices are nonvolatility and faster processing rate. The first breakthrough in this field was Giant Magnetoresistance (GMR)^{4,5} in 1988–89 for which Albert Fert and Peter Grünberg were awarded Nobel prize. Since then, the field has evolved and several high-performance devices such as magnetic tunnel junctions⁶, magnetic random-access memory (MRAM)⁶, racetrack memory^{7,8} have emerged.

Recently, magnetic skyrmions^{9–16} have received a gaint attention in the spintronics community. They are topologically stable vortex-like spin structures^{10,17} and are smaller in size compared to the magnetic domain walls (one of the main constituents in hard disk drive). Additionally, they can be moved with almost 3–5 orders of smaller current density required to move domain walls^{18,19}. Therefore, they were proposed to replace magnetic domain walls in novel racetrack memory devices²⁰. Skyrmions were first experimentally discovered in 2009 in a chiral magnetic compound MnSi at quite a low temperature of 30 K¹⁶. Since then, many skyrmions hosting compounds such as FeGe²¹, Cu₂OSeO₃¹³, GaV₄S₈²², and VOSe₂O₅¹² have been discovered. The previously mentioned compounds only display magnetic ordering below room-temperature. Another class of chiral compounds is Co-Zn-Mn^{14,23} that has skyrmions stability above room-temperature. However, the existence of these skyrmions is limited to a narrow region of the magnetic field and temperatures in the bulk limit, hindering its possibility towards application. Another limitation of skyrmions is their deviation from transversing in a straight-line path²⁴. A different type of vortex-like spin structure is antiskyrmions^{25,26} that were discovered for the first time in polycrystalline samples of tetragonal inverse Heusler compounds Mn_{1.4}PtSn and Mn_{1.4}Pt_{0.9}Pd_{0.1}Sn²⁷. Antiskyrmions are also topologically protected and asymmetric in their tangential direction²⁵. The advantage of antiskyrmions is the wide range of magnetic field and temperature range of stability²⁸. Additionally, the compound Mn_{1.4}PtSn is interesting as it has magnetic ordering temperature of 400 K, which means it can stabilize antiskyrmions even at elevated temperatures.

Since the discovery of antiskyrmions, the tetragonal Heusler compounds^{29–32} have gained attention in the skyrmion community as the magnetic ordering temperatures in the Heusler compounds could be much above the room temperature. Additionally, Heusler compounds are known for their tunable properties^{33,34}, which are advantageous over other skyrmions hosting materials as the properties of antiskyrmions can also be tuned. Thus, a

Heusler family of materials provides a rich playground to search for new antiskyrmions hosting materials and fine tuning of the properties.

Heusler family of compounds is known to show a diverse variety of physical properties. In addition, some interesting structure variants such as structural distortions^{33,34} and superstructures³⁵⁻³⁷ have been discovered in this family. In the former category, tetragonal and hexagonal crystal structure can be obtained, depending upon distortion directions. Whereas in the latter category, a $2 \times 2 \times 2$ superstructure of the half-Heusler structure has been found in CoMnSb³⁵.

The motivation of the works presented in this thesis is to unearth the new superstructure forms, which could lead to the stabilization of vortex-like spin structures such as antiskyrmions and the investigation of their interesting physical properties.

In chapter 2, a theoretical background of Heusler compounds, superstructure, skyrmions, antiskyrmions, and the anomalous and topological Hall effects are presented. In chapter 3, a brief overview of the involved techniques in the synthesis, characterization, and physical properties measurements are presented.

In chapter 4, the detailed single crystal growth and physical properties of Mn_{1.4}PtSn are presented. The X-ray refinements on single crystals reveal the presence of superstructure form in Mn_{1.4}PtSn. This is the first discovered tetragonal superstructure in the Heusler compounds, and forms due to the ordered vacancies at Mn sites. From the magnetic measurements, two magnetic transitions are found at 392 K (Curie temperature) and 170 K (spin-reorientation transition temperature). A large magnetic moment of 4.7 μ_B /f.u. is obtained at 2 K. The refinement of the powder neutron diffraction pattern reveals that the low-temperature phase has a non-coplanar spin structure while the high-temperature phase has a collinear spin structure. The existence of a ground state non-coplanar spin structure is supported by theoretical calculations. A large value of topological Hall effect is discovered that shows an anisotropic behavior for applied magnetic field along [100] and [001]. The observed topological Hall effect arises from the non-coplanar spin structure of the compound.

In chapter 5, a comprehensive study of iridium (Ir) substitution at the platinum (Pt) site in Mn_{1.4}PtSn is presented. Interestingly, all the compounds in this series possess the tetragonal superstructure form and are isostructural to Mn_{1.4}PtSn. The magnetization measurements with the support of powder neutron diffraction reveal that the magnetic structure changes from out-of-plane ferromagnet to in-plane ferrimagnet upon Ir-substitution. The Curie temperature is found to be decreasing linearly. The magnetic moment is almost constant up to $x = 0.3$ and follows a linear trend for higher Ir-substituted compounds. A large anomalous Hall conductivity is observed for $x = 0.3$, which reduces with increasing Ir-substitution.

In chapter 6, the study related to the addition of transition-metal elements cobalt, nickel, and copper at vacancies in the unit cell of $\text{Mn}_{1.4}\text{PtSn}$ is presented. It is found that the compounds retain tetragonal superstructure up to a certain concentration of cobalt ($x = 0.2$) and nickel ($x = 0.4$), after which they transform into a cubic structure. However, for the addition of copper, the compounds retain the tetragonal superstructure in the whole concentration range. The magnetization measurements reveal that only compounds with tetragonal superstructure show the presence of magnetic transition at low-temperature (spin-reorientation transition), whereas it is absent for compounds with cubic structure.

In chapter 7, the complete structural and physical properties of a newly discovered Heusler compound $\text{Mn}_{1.7}\text{Pt}_{0.8}\text{In}$ are presented. The single-crystal refinement reveals that the crystal structure of $\text{Mn}_{1.7}\text{Pt}_{0.8}\text{In}$ is the $3 \times 3 \times 3$ superstructure form of the Heusler structure. This is the largest supercell discovered so far in the Heusler family of compounds. Magnetic measurements reveal the presence of two magnetic transitions: one is at 330 K (Curie temperature) and the other is at 220 K (spin-reorientation transition temperature). The saturation magnetization is very small for this compound, indicating the possible compensated ferrimagnetic spin structure.

2. Theoretical background

2.1. Heusler compounds

Heusler compounds are a class of intermetallic compounds and are known to exhibit a diverse range of physical properties. The first Heusler compound Cu_2MnAl was discovered in 1903 by Friedrich Heusler³⁸, where he discovered that Cu_2MnAl shows ferromagnetism despite none of the constituent elements displaying a ferromagnetic order.

The empirical formula of Heusler compounds is either XYZ or X_2YZ , where X and Y are usually the transition-metal elements, while Z is the main-group element. With the formula XYZ , the compound is called as half-Heusler compound and when the empirical formula is X_2YZ , the compound is known as full-Heusler compound. The full-Heusler compound can further be classified in two sub-classes, a) the compound possessing centrosymmetric crystal structure is called as regular Heusler compound which has the space group $Fm\bar{3}m$, and b) the compound with non-centrosymmetric crystal structure is known as inverse Heusler compound which has the space group $F\bar{4}3m$.

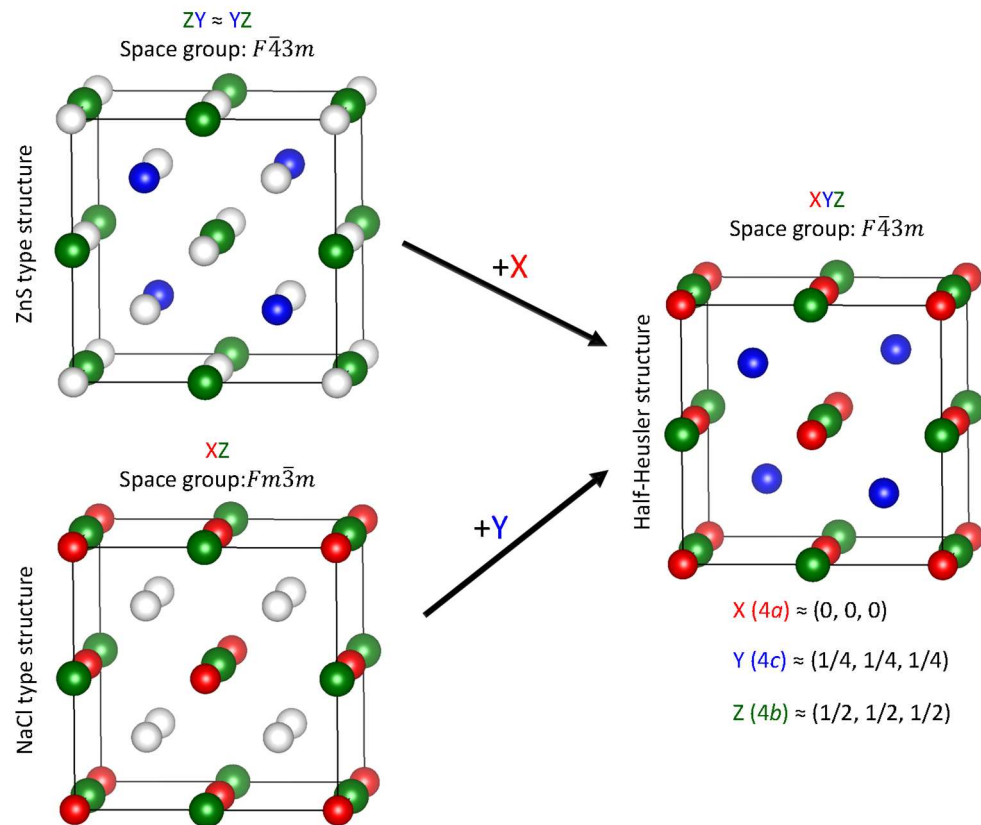


Figure 2.1. Evolution of half-Heusler structure from either ZnS- or NaCl-type structure.

The crystal structure of a half-Heusler compound is simply described by three interpenetrating FCC sublattices while full-Heusler compounds can be understood as four inter-

penetrating FCC sublattices of XY and XZ elements. Generally, the structure of the half-Heusler compounds can be understood in two ways. First, as ZnS-type sublattice in which the octahedral sites are filled and second, as NaCl-type sublattice where half of the tetrahedral sites are filled. In the former model, Y and Z atoms are bonded together with covalent bonding making ZnS-type structure and X being the most electropositive element goes to the octahedral sites of the YZ framework, having a relatively ionic bonding with the Z atoms. For the latter model, X and Z atoms can be understood to carry an ionic type of bonding between them and Y atoms are situated at half of the tetrahedral sites. The crystal structure of half-Heusler compounds is presented in Figure 2.1. In the crystal structure, the X and Z atoms are situated at $4a$ (0, 0, 0) and $4b$ ($\frac{1}{2}$, $\frac{1}{2}$, $\frac{1}{2}$) sites, respectively. They form a NaCl-type structure X being at the place of Na and Z at the place of Cl. The Y atoms occupy half of the tetrahedral voids with the Wyckoff position of $4c$ ($\frac{1}{4}$, $\frac{1}{4}$, $\frac{1}{4}$). The schematic relation between NaCl-type and ZnS-type structures with half-Heusler structure is presented in Figure 2.1.

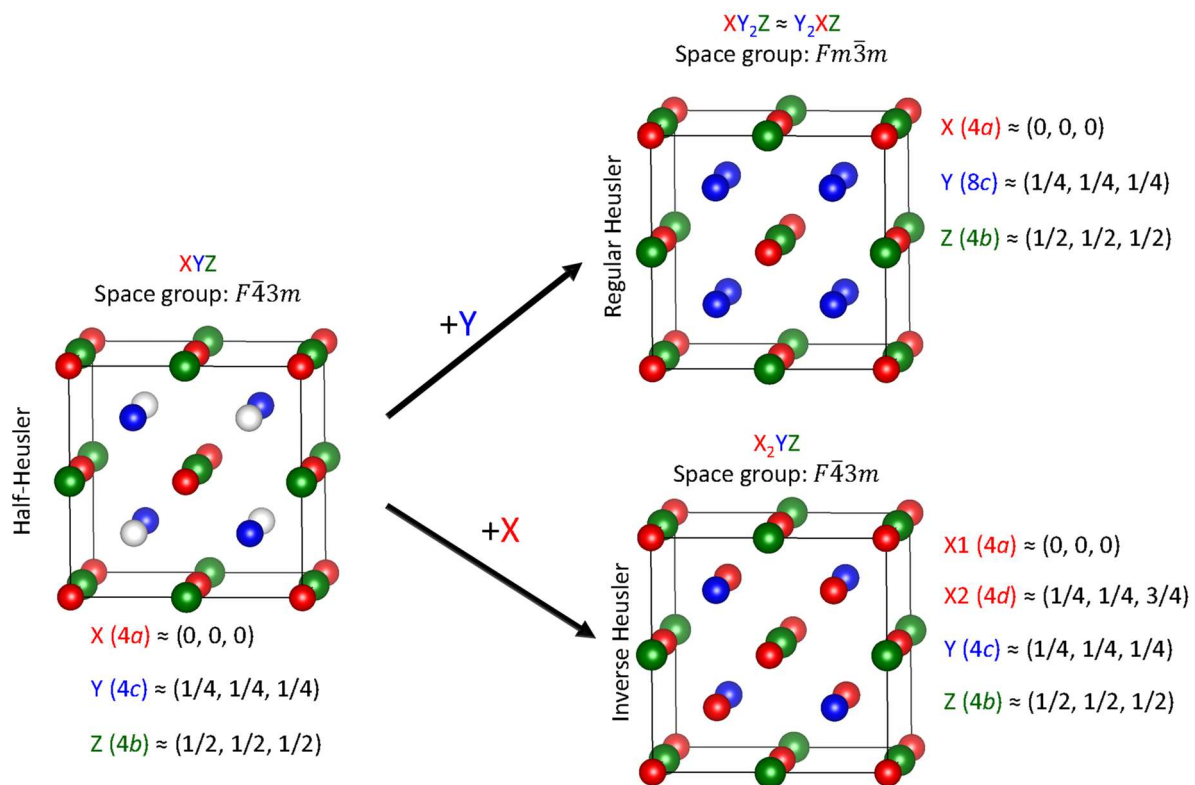


Figure 2.2. Evolution of regular and inverse Heusler structure from half-Heusler structure.

Now, the structure of full Heusler compounds can easily be derived by filling rest of the tetrahedral voids in the unit cell of half-Heusler compounds. For the case of regular Heusler compounds (Y_2XZ), the Y atoms further occupy rest half of the tetrahedral vacancies making the Wyckoff position of Y as $8c$ ($\frac{1}{4}$, $\frac{1}{4}$, $\frac{1}{4}$). However, in the case of inverse Heusler compounds (X_2YZ), the other half of the tetrahedral voids are filled with X atoms with the Wyckoff position of $4d$ ($\frac{1}{4}$, $\frac{1}{4}$, $\frac{3}{4}$). The crystal structures of regular and inverse Heusler compounds as well as their relation to the crystal structure of half-Heusler compounds are shown in Figure 2.2.

The regular Heusler compounds have space group $Fm\bar{3}m$ with a structure prototype as Cu_2MnAl . The inverse Heusler compounds crystallize in the space group $F\bar{4}3m$ with the structure prototype of CuHg_2Ti . In the regular Heusler compounds (Cu_2MnAl structure prototype which is often referred to as $L2_1$ structure), the Y atoms occupy $8c$ ($\frac{1}{4}, \frac{1}{4}, \frac{1}{4}$) site, while X and Z atoms occupy $4a$ ($0, 0, 0$) and $4b$ ($\frac{1}{2}, \frac{1}{2}, \frac{1}{2}$) sites, respectively. In the inverse Heusler compounds, X atoms are situated at two Wyckoff positions, $4a$ ($0, 0, 0$) and $4d$ ($\frac{1}{4}, \frac{1}{4}, \frac{3}{4}$) while Y and Z atoms are present at $4c$ ($\frac{1}{4}, \frac{1}{4}, \frac{1}{4}$) and $4b$ ($\frac{1}{2}, \frac{1}{2}, \frac{1}{2}$) positions, respectively³⁴. Few other types of crystal structure can be obtained when there is an interatomic mixing at a particular atomic site³⁴.

Structural distortion:

Most of the Heusler compounds crystallize in cubic structures but when the crystal field effect (Jahn-Teller distortion) becomes large then the cubic structure undergoes structural distortion^{39,40} and forms tetragonal or hexagonal structure, depending upon the distortion direction. For the cubic structure, if the distortion direction is $[111]$, the resultant structure is hexagonal with a space group $P6_3/mmc$ or $P6_3mc$ ⁴¹ and if the distortion direction is $[001]$, the resultant structure is tetragonal. In the case of tetragonal distortion, regular Heusler ($Fm\bar{3}m$) and inverse Heusler ($F\bar{4}3m$) compounds transform to tetragonal compounds having space group $I4/mmm$ and $I\bar{4}m2$, respectively^{29,30,32}. The schematic for the structural transformation is shown in Figure 2.3.

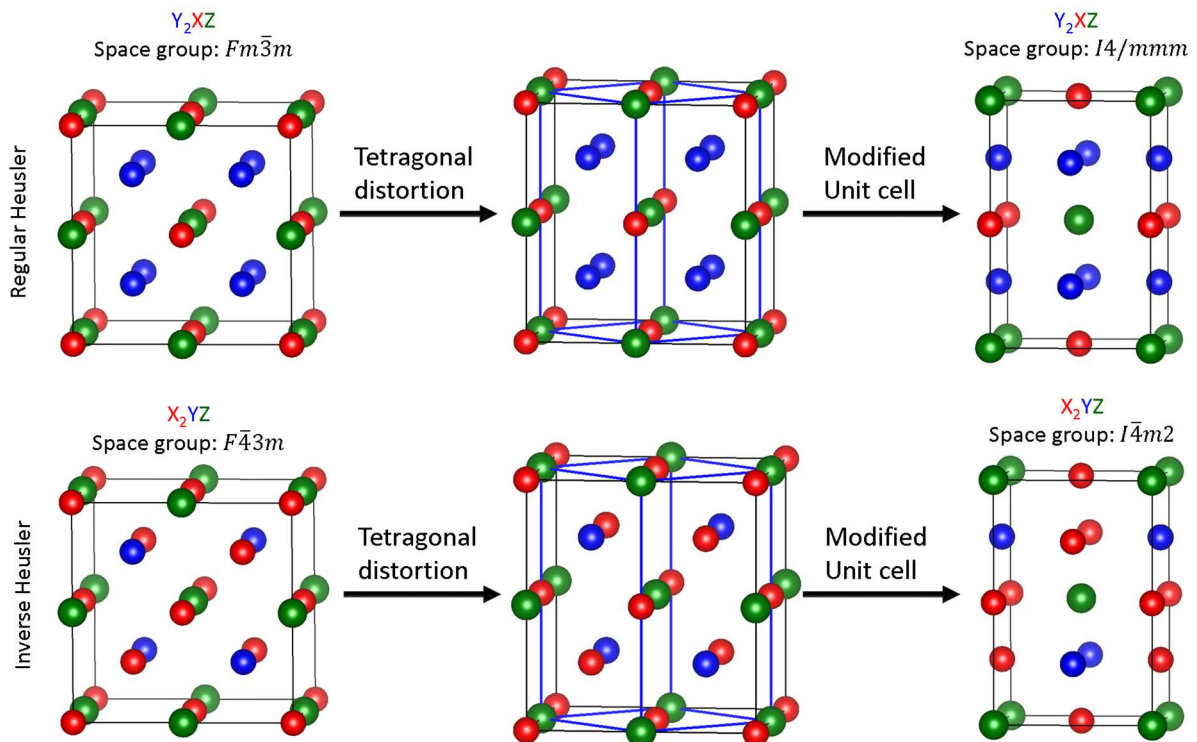


Figure 2.3. Schematic for the formation of tetragonal structure from regular and inverse cubic Heusler structure.

Heusler family, therefore, consists of a variety of compounds showing different types of crystal structures that are both centro- and noncentrosymmetric. The compounds in this family are known to show a range of interesting physical properties such as the magnetic shape-memory effect^{42,43}, thermoelectric properties^{44,45}, magnetic antiskyrmions^{27,46}, half-metallicity^{47,48}, compensated ferrimagnetism^{49–52}, superconductivity^{53,54}, Weyl topology^{55,56} and topological insulator^{57,58}. One of the most important advantages of Heusler compounds is that the physical properties can mostly be predicted by simply counting the number of electrons present in the compound. For example, the compounds with either 18 or 24 valence electrons (VE) are semiconductors. However, most of these predictions are limited to the cubic structure so far. The physical properties can be tuned with simply changing the number of VE. This trend is set to follow the Slater-Pauling (SP) rule, which states that the magnetic moment of 3d elements and their alloys can be estimated with the number of VE³⁴. Therefore, the Heusler compounds have always been fascinating to both the scientific and industrial communities due to their multifunctional properties.

One of the most recently discovered properties in the Heusler family is magnetic antiskyrmions²⁷. They were predicted to exist in the compound having D_{2d} symmetry²⁶. Therefore, the tetragonal inverse Heusler compounds are very interesting as they crystallize in the space group $I\bar{4}m2$ with D_{2d} symmetry.

2.2. Superstructure

A superstructure is a derived structure from a pristine crystal structure, called as substructure, under certain conditions. The symmetry of the superstructure is the subgroup of the substructure^{59–62}. They can be obtained in numerous ways, for example, a set of different atoms are substituted for a set of like atoms or some ordered vacancies are created in the substructure. The superstructure can be obtained by suppressing any kind of crystallographic operation or a combination of operations in the substructure⁶¹. The most commonly recognized link between the derived superstructure and its substructure is their relation between unit cell parameters. The cell edge of the superstructure is multiples of the corresponding substructure⁶⁰. The driving force for the formation of superstructure might be the change in the chemical environment around an atom.

The superstructure can easily be discerned from X-ray⁶³ or electron diffraction patterns⁶⁴, where additional peaks or diffraction spots appear compared to the numbers of peaks corresponding to the pristine substructure. In this case, the unit cell of the supercell would be different from the subcell. However, for some of the cases, extra peaks are not present; rather, there appears a change in the peak intensity only. In such a case, the unit cell lattice parameters would be the same as the subcell but the crystal symmetry will change⁵⁹. Other than the diffraction patterns, a supercell can also be observed through a transmission electron microscopy in real space⁶⁵.

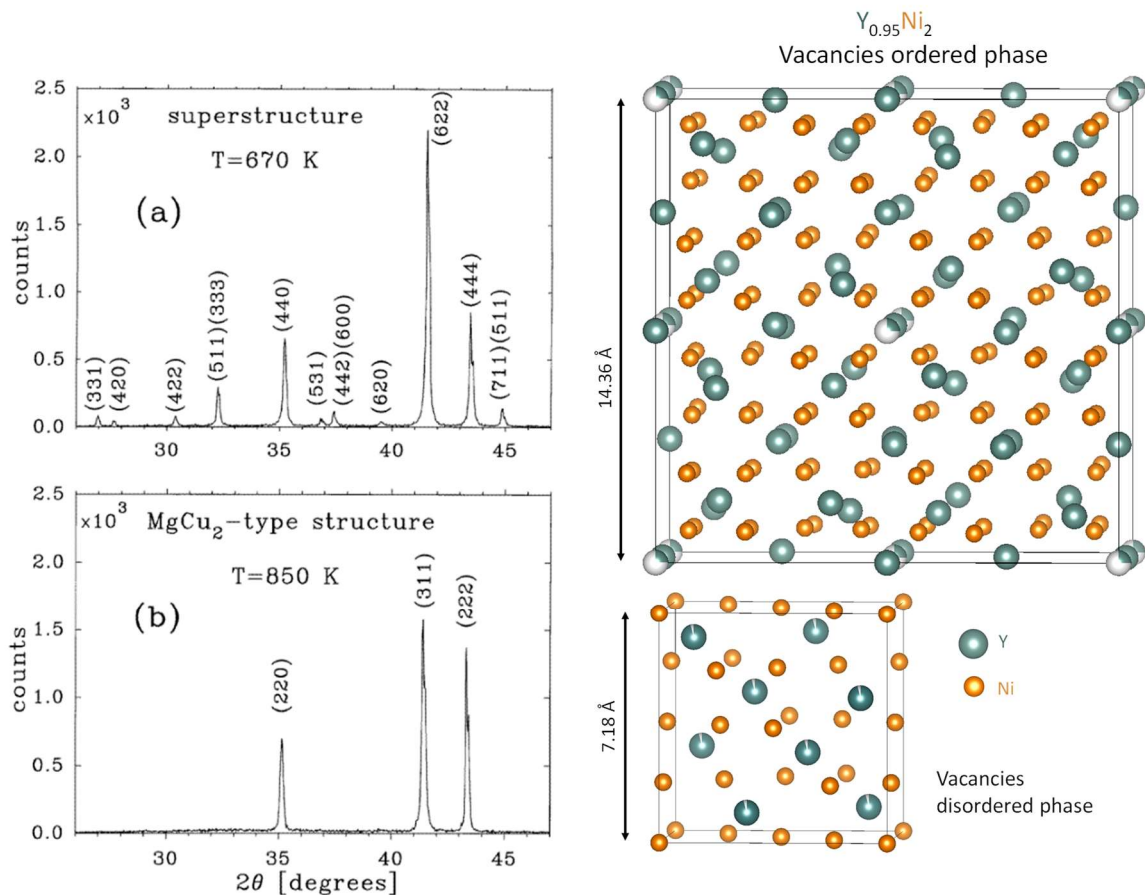


Figure 2.4. Powder X-ray diffraction patterns of (a) superstructure (b) substructure and their respective crystal structures of $Y_{0.95}Ni_2$. (Figure adapted from Ref. 63).

So far, various types of superstructures have been discovered in many compounds such as Cu_2Se ⁶⁶, RNi_2 (R : rare-earth elements, Laves phase)^{63,67}, and Heusler compounds³⁵. These supercells are mostly created by the ordering of the vacancies present in the unit cell. Here, an example of a superstructure in YNi_2 is given⁶³. $Y_{0.95}Ni_2$ is supposed to crystallize in the cubic Laves phase with the structure type of $MgCu_2$ and space group of $Fd\bar{3}m$. However, the vacancies present in the unit cell are ordered. These ordered vacancies at the Y sites lead to doubling of the cubic unit cells and change of space group to $F\bar{4}3m$ ⁶³. The conforming superstructure reflection peaks are observed in the powder X-ray diffraction patterns (Figure 2.4(a)), and such peaks are absent in the disordered vacancy phase (Figure 2.4(b)). The crystal structure for both superstructure and substructure are shown in Figure 2.4.

Superstructures in Heusler compounds:

Besides the ordering of vacancies, a superstructure can also be formed if the position of atoms is interchanged with the position of other atoms or vacancies. This might lead to a change in the unit cell and the crystal symmetry. For example, CoMnSb (written as $\text{Co}_8\text{Mn}_8\text{Sb}_8$ in superstructure form) shows such type of superstructure³⁵. In Figure 2.5, the crystal structures of CoMnSb with both half-Heusler structure and superstructure are shown. The crystal structure of the superstructure of $\text{Co}_8\text{Mn}_8\text{Sb}_8$ can be viewed as alternating MnSb (NaCl type structure) and Co_2MnSb (regular full-Heusler structure). Moreover, it can be understood in term of shifting of cobalt atoms to the neighboring unit cell, resulting in doubling of the unit cell as well as changing the crystal symmetry from noncentrosymmetric space group $F\bar{4}3m$ to centrosymmetric space group $Fm\bar{3}m$. CoMnSb exists in both the substructure and superstructure form depending upon the sample preparation methods. At high-temperature annealing, it crystallizes in $F\bar{4}3m$ with half-Heusler structure while at low-temperature annealing, the cobalt atoms are in favor to rearrange themselves, consequently a $2 \times 2 \times 2$ superstructure is formed^{34,35}.

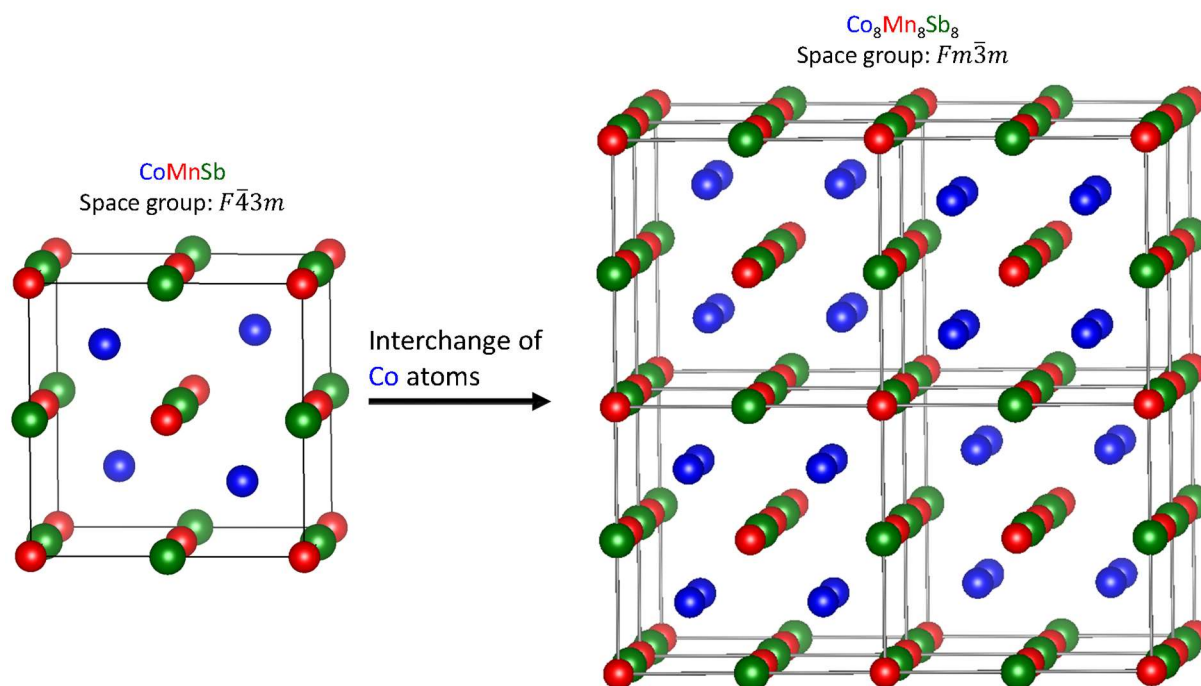


Figure 2.5. Evolution of superstructure in $\text{Co}_8\text{Mn}_8\text{Sb}_8$ from half-Heusler structure CoMnSb.

Another related compound with a $2 \times 2 \times 2$ superstructure form is $\text{Ru}_9\text{Zn}_7\text{Sb}_8$ ³⁶. Soon after its discovery, many other compounds with chemical formula $\text{X}_9\text{Y}_7\text{Z}_8$ (X = Fe, Ru, Co, Rh, or Ir; Y=Zn; Z = Sn or Sb) have been synthesized. The reason for having the unique chemical formula as $\text{X}_9\text{Y}_7\text{Z}_8$ is that some of the X atoms replace Y atoms in the crystal structure^{36,37}. A schematic for the relation between crystal structures of half-Heusler CoMnSb, $\text{Co}_8\text{Mn}_8\text{Sb}_8$, and $\text{X}_9\text{Y}_7\text{Z}_8$ is presented in Figure 2.6. However, the crystal symmetry remains the same after the replacement of these atoms.

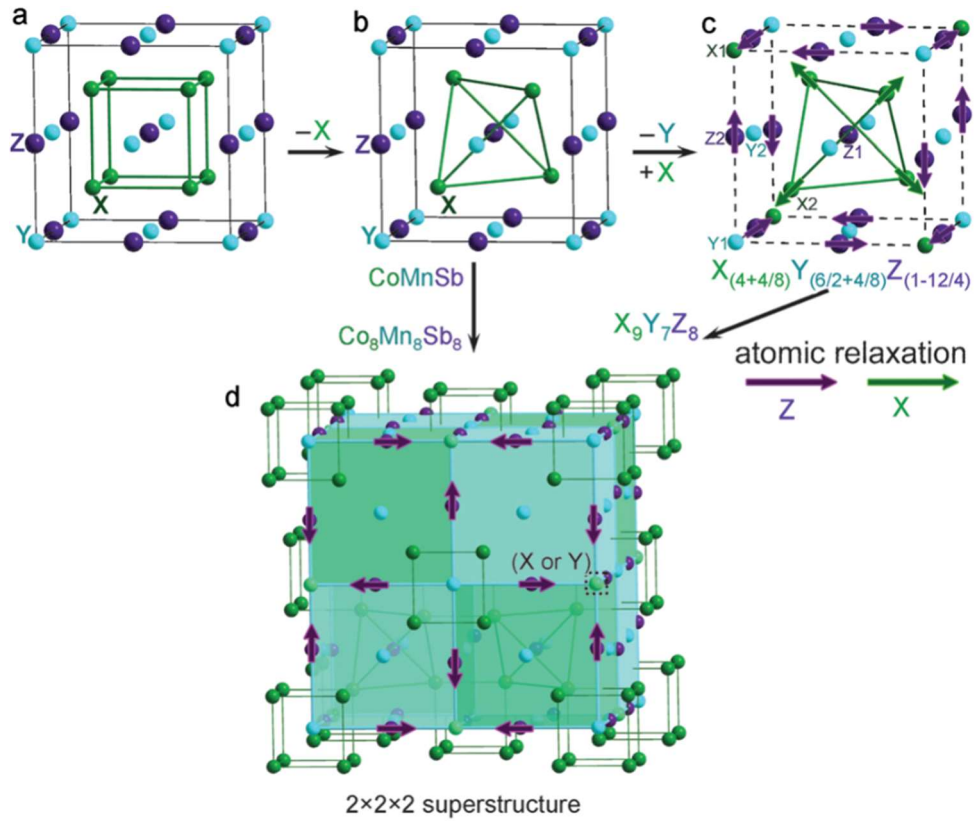


Figure 2.6. The relation between half-Heusler structure and the superstructures of $\text{Co}_8\text{Mn}_8\text{Sb}_8$ and $\text{X}_9\text{Y}_7\text{Z}_8$. (Figure adapted from Ref. 37).

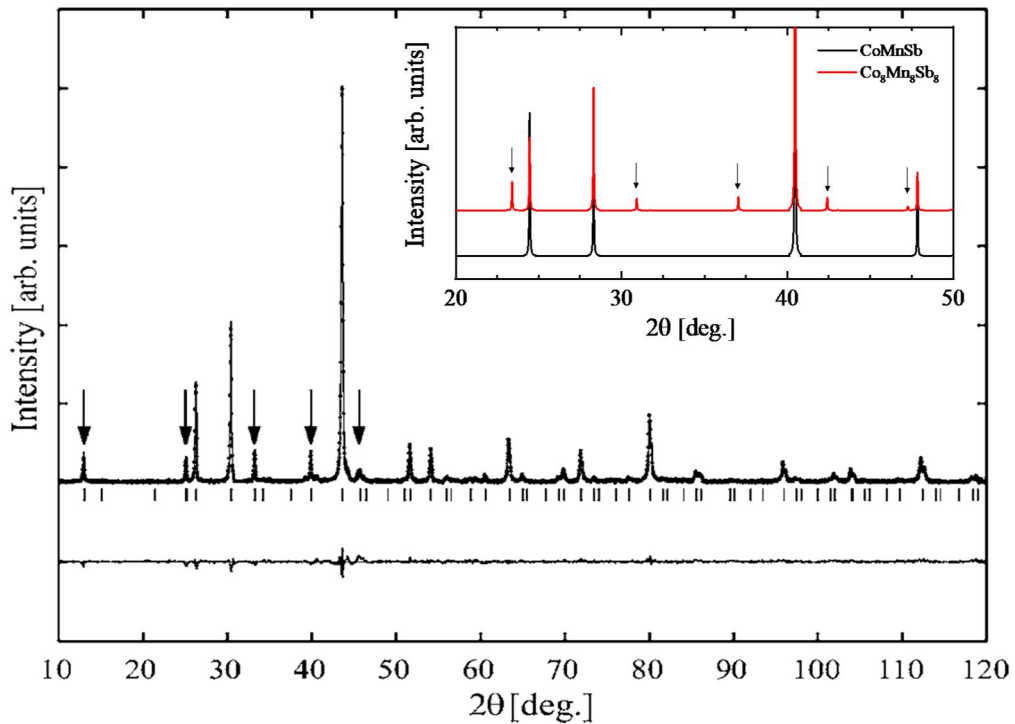


Figure 2.7. Experimental powder XRD pattern of $\text{Co}_8\text{Mn}_8\text{Sb}_8$. The inset shows the comparison between XRD patterns of the superstructure (red) and the substructure (black). Arrows in this Figure correspond to the superstructure reflections. (Figure adapted from Ref. 35).

Figure 2.7 shows the powder X-ray diffraction pattern of $\text{Co}_8\text{Mn}_8\text{Sb}_8$. As it can be seen in the diffraction pattern, there are several extra peaks present along with the peaks corresponding to the half-Heusler substructure. These extra peaks (indicated by arrows) are referred to as superstructure peaks and marked with arrows in the diffraction pattern. A similar pattern is also obtained for the related compounds $\text{X}_9\text{Y}_7\text{Z}_8$ ³⁷.

2.3. Magnetic skyrmions and antiskyrmions

Skyrmion was originally modeled by Tony Skyrme in 1962⁶⁸ as a topological particle that can not be changed by continuous deformation of fields. The magnetic analog, magnetic skyrmions and antiskyrmions are a topological arrangement of magnetic spins and were modeled by Bogdanov *et al.*^{9,15,26}. These are now very promising candidates for efficient future memory devices because they can be driven using an ultralow current density^{19,24}. These spin structures can stabilize mainly due to four kinds of mechanisms. One of the most known mechanisms is through a collective competition of Heisenberg interaction, Dzyaloshinskii-Moriya interaction, dipole interaction, and Zeeman effect. The spins in skyrmions can be wrapped around a unit sphere and this cannot be unbound into a trivial spin structure such as ferromagnetic spin structure^{10,17,69}. The spatial rotation of spins in skyrmions is given as follows,

$$N_{Sk} = \frac{1}{4\pi} \int \hat{m} \cdot (\partial_x \hat{m} \times \partial_y \hat{m}) dx dy \quad 2.1$$

where, \hat{m} in the normalized local magnetization and N_{Sk} is called as skyrmion topological charge.

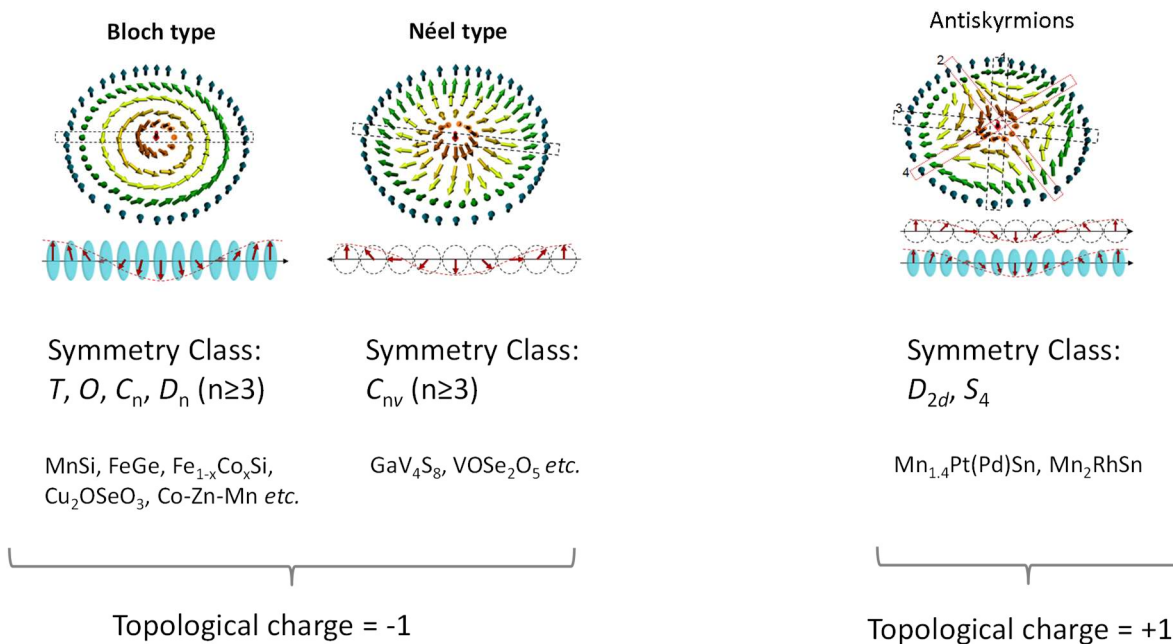


Figure 2.8. The relation between crystal symmetry and type of skyrmion and their existence in the real compounds. (Figure adapted from Ref. 27).

So far, three types of skyrmions texture have been experimentally observed with various techniques, and these are Bloch type²¹, Néel type^{12,22}, and antiskyrmions^{27,28,46}. The Bloch and Néel type skyrmions have a topological charge -1 while the antiskyrmions have a topological charge of +1¹⁷. Having opposite topological charge, skyrmions and antiskyrmions are considered as antiparticle to each other²⁵. The existence of these skyrmion textures are mainly determined by the crystal symmetry of a magnetic compound. The Bloch type may be found in all the magnetic materials with chiral crystal structure with O , T , C_n , and D_n ($n \geq 3$), the Néel type can be found in the compound with C_{nv} symmetry⁷⁰. The existence of antiskyrmions was predicted in a material with D_{2d} and S_4 symmetry²⁶. The different types of skyrmions and their relation to the crystal symmetry are summarized in Figure 2.8.

The skyrmion lattice, a regular arrangement of skyrmions, can lead to interesting physical properties, such as the topological Hall effect⁷¹ and the generation of spin-transfer torque⁷². They can be observed in both real and inverse space with various techniques. For real space observation, magnetic force microscope^{73,74} and Lorentz transmission electron microscope (LTEM)^{13,21,27,75-77} are employed while for inverse space, small-angle neutron scattering (SANS)^{12,16,78,79} and small-angle resonant X-ray scattering⁸⁰⁻⁸³ are used. However, the indication of the presence of skyrmion lattice can also be found in some common measurements such as magnetic and electrical transport measurements. Here, mainly signatures of magnetic skyrmions in magnetic and transport measurements are presented.

DC and AC susceptibility measurements:

The magnetic phase diagram of a material can be mapped most easily with DC magnetization or AC susceptibility measurements. The magnetic phase diagram of MnSi¹⁶ is shown in Figure 2.9. The phase diagram is similar for most of the skyrmion hosting compounds¹³. In the case of MnSi, skyrmions only exist in a few K temperature ranges close to the magnetic ordering temperature. In the measurements of DC magnetization as a

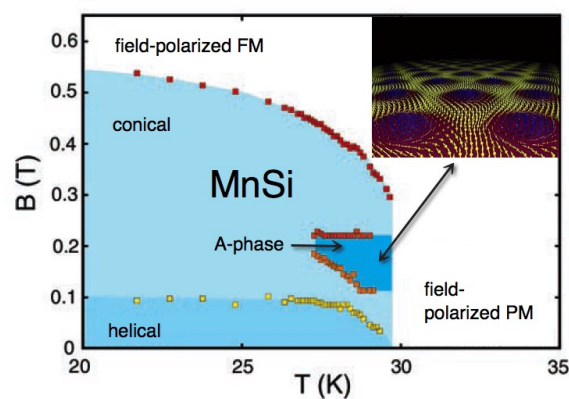


Figure 2.9. The magnetic phase diagram of skyrmions hosting B20 compound MnSi. (Figure adapted from Ref. 16).

function of the magnetic field, a sharp change in the magnetization appears at a magnetic phase boundary. The first derivative of the magnetization shows the peaks at these phase boundaries. Similarly, in the AC susceptibility measurements, a slope change in the real part of susceptibility (Figure 2.10(a)) and a peak in the imaginary part of susceptibility are observed (Figure 2.10(b))⁸⁴.

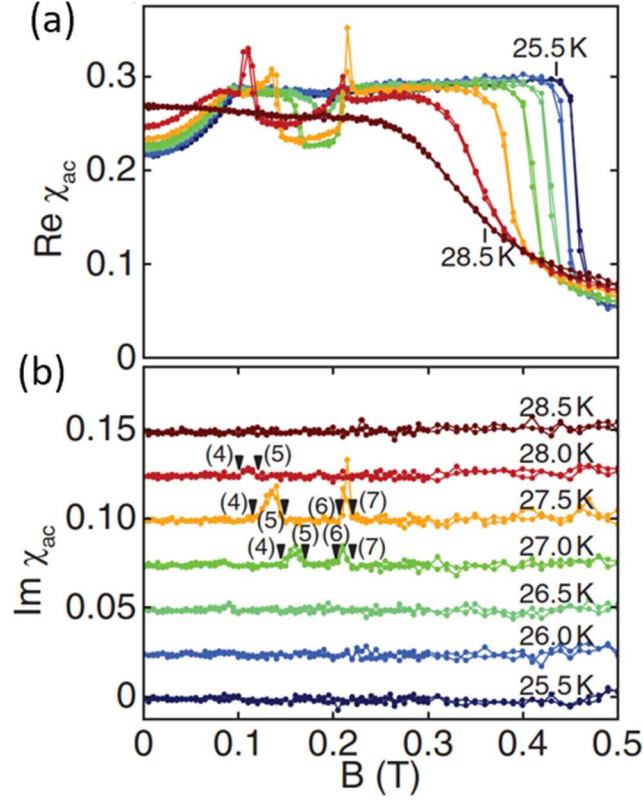


Figure 2.10. (a) Real part (b) imaginary part of susceptibility as a function of the field at different temperatures of B20 compound MnSi. (Figure adapted from Ref. 84).

Anomalous and Topological Hall effects:

In general, the measured Hall resistivity, ρ_{yx} of a magnetic material can be expressed by an empirical relation as,

$$\begin{aligned} \rho_{yx} &= \rho_{yx}^N + \rho_{yx}^A + \rho_{yx}^T \\ &= R_0 \mu_0 H + ((\alpha + S_A \rho_{xx})M) \rho_{xx} + R^T B_{em} \end{aligned} \quad 2.2$$

where, $\rho_{yx}^N = R_0 \mu_0 H$ is the normal Hall resistivity, due to the Lorentz force in which R_0 is the normal Hall coefficient and $\mu_0 H$ is the applied external magnetic field. The anomalous Hall resistivity in a magnetic material is given by the relation $\rho_{yx}^A = ((\alpha + S_A \rho_{xx})M) \rho_{xx}$ where α , and S_A correspond to the extrinsic contributions from the skew and

impurity density-independent scatterings, respectively. M is the magnetization and ρ_{xx} is the longitudinal resistivity. ρ_{yx}^T is the topological Hall resistivity⁸⁵ and is given by the relation $R^T B_{em}$, where R^T is the topological Hall coefficient and B_{em} is the emergent magnetic field due to real-space Berry curvature⁸⁶.

Magnetic skyrmions and antiskyrmions have a topological charge, therefore, they can exhibit extraordinary electrical phenomena. When an electron passes through the magnetic skyrmions, it aligns itself to the local magnetic moment, thereby acquiring an additional phase, called Berry phase^{19,71,87} (Figure 2.11(a)). A non-zero Berry phase acts like a fictitious magnetic field, thus resulting in an additional contribution in Hall effect. This additional contribution is termed as topological Hall effect (THE). The THE has been observed in many skyrmions^{71,88–95} and antiskyrmions⁹⁶ hosting magnetic phases. For example, the observation of THE in B20 compound MnSi⁷¹ is shown in Figure 2.11(b).

The THE is quite cumbersome to extract from the total Hall resistivity and it becomes even more difficult to distinguish between momentum and real space contributions^{97,98}. The understanding of the real space and momentum space contributions are better understood in the limit where the spin-orbit coupling (SOC) goes to zero and dependent on the electron scattering rate with respect to the length scale of the magnetic structure. In the case of large topological magnetic structures such as skyrmions where the scattering rate is much lower, the THE is due to the continuum limit of the scalar spin chirality or the so-called topological winding number. The size and direction of B_{em} are determined by the external magnetic field for the skyrmions hosting systems and is an approximately linear variation of the external magnetic field at a given temperature.

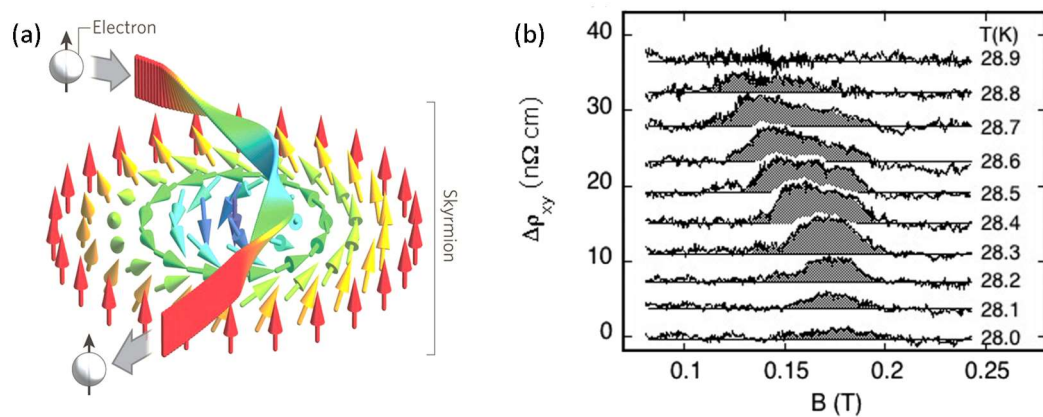


Figure 2.11. (a) Emergence of real-space Berry curvature generated by an electron passing through skyrmions (Figure adapted from Ref. 87) (b) topological Hall effect in A-phase of B20 compound MnSi. (Figure adapted from Ref. 71).

In the case of a magnetic texture such as a non-coplanar spin structure, in which the order of the crystal structure is much smaller than the mean free path of the electron, the

momentum space Berry curvature (BC) dominates in the absence of SOC^{99,100}. This type of BC is mainly due to the noncollinear and non-coplanar magnetic structure in the low external field regime, where the internal emergent field dominates¹⁰¹. This emergent field is the result of the cone angle subtended by three spins that give rise to the scalar spin chirality:

$$\chi_{ij} = \sum \hat{S}_i \cdot (\hat{S}_j \times \hat{S}_k) \quad 2.3$$

where, and S_i is the spin vector of the moment.

A non-coplanar spin structure can lead to the emergent magnetic field that can give rise to the additional contribution in the Hall effect (Figure 2.12(a)). Such arranged spins make a non-zero scalar spin chirality^{99,101,102}. This additional contribution in Hall, THE, has been observed in Mn_5Si_3 ¹⁰³, Mn_2RhSn ¹⁰⁴, Mn_xPtSn ($x = 1.5, 1.8$)^{105,106}, $NiMnGa$ ¹⁰⁷ *etc.* The presence of THE due to the non-coplanar spin structure of Mn_5Si_3 ¹⁰³ is shown in Figure 2.12(b).

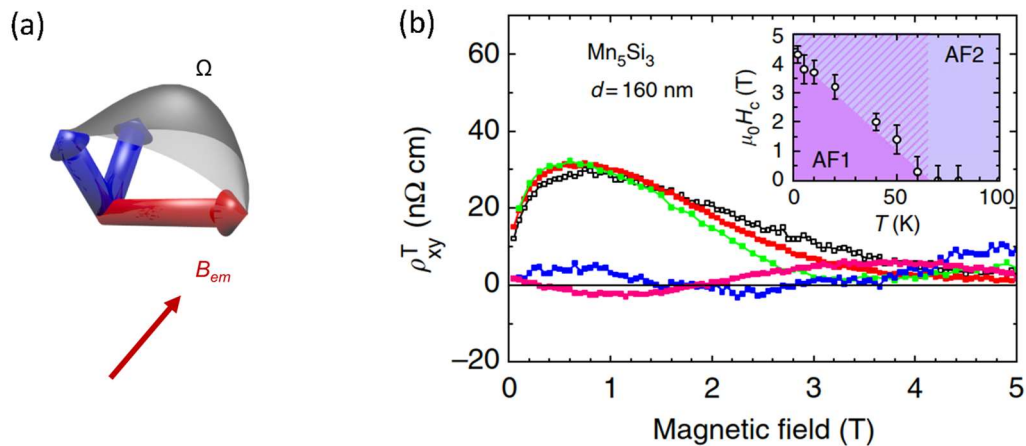


Figure 2.12. (a) The emergence of magnetic field due to the non-coplanar spin structure making a solid angle Ω (b) topological Hall effect due to non-coplanar scalar spin chirality. (Figure adapted from Ref. 103).

3. Techniques

3.1. Arc melting

Arc melting is one of the most widely used techniques to prepare polycrystalline samples of intermetallic compounds. The laboratory customized experimental setup of arc melting is shown in Figure 3.1, which can achieve temperature as high as 2773 K. The working principle is that all consequent elements are melted together by generating heat through an electric arc. This electric arc is produced by flowing high electric current between a tungsten electrode and a copper hearth. The elements are put together in grooves in the copper hearth. The copper hearth is kept cold during the melting process by running water to prevent melting itself as well as protect the loss of materials. To prevent oxidation, the chamber is isolated from the environment and is filled with purified argon gas. For further minimization of residual oxygen, titanium ingot is melted before the sample. The sample is melted multiple times (minimum three times) by flipping the sample ingot to achieve better homogeneity.

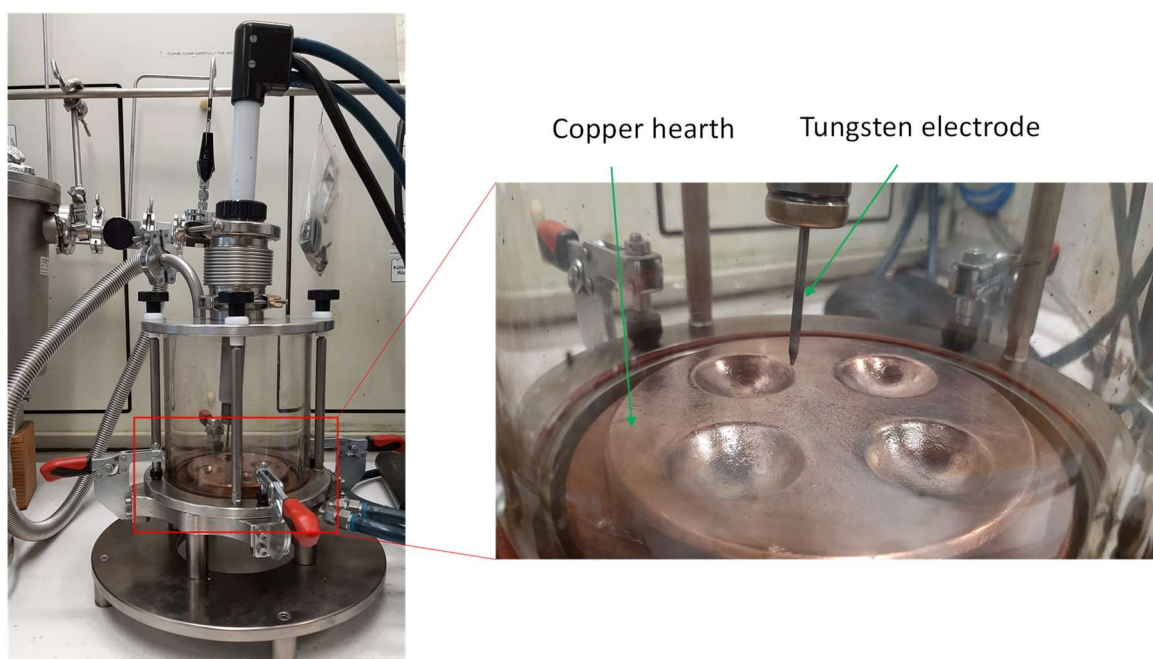


Figure 3.1. Laboratory customized experimental setup of arc melting. The set-up is built by the mechanical workshop at MPI-CPfS.

3.2. Induction melting

Induction melting is a rather quick method to prepare polycrystalline samples. This method is more suitable for a compound having high vapor pressure as well as conducting property. The main advantage of this method is the good control of the melting process, resulting in negligible weight loss due to the application of rather a low temperature. A nonconducting

crucible *e.g.*, alumina or quartz is used as a container for the melting elements. The crucible containing elements is put at the center of the induction copper coil and alternating current is passed through the coil. This generates a magnetic flux that penetrates through the elements and produces eddy current by electromagnetic induction. The dissipative eddy current through the elements leads to Joule heating. When this heating is sufficient enough, the elements turn into melt and get mixed. The experimental setup of induction melting is shown in Figure 3.2 wherein the copper coil is located inside the glove box. Such design does not need extra protection from other atmosphere and the melting procedure is carried out in a controlled atmosphere of argon.



Figure 3.2. The experimental setup of induction melting present inside the glove box.

3.3. Flux method

Flux method is a method to grow single crystals and it is advantageous in various ways as no specialized equipment is needed, and the crystal can be grown at relatively low temperatures. To grow single crystals of a compound having multiple structural transitions, the flux method is quite useful because the crystal growth temperature region can easily be controlled^{108–111}.

In the flux method, for reaction having temperatures below 1473 K, the reactants are sealed in a quartz tube with a partial argon atmosphere to provide a protective environment during the reaction. As a flux, any element or intermetallic with a low melting point can be used. The commonly used elemental flux are tin, gallium, antimony, bismuth, tellurium, aluminium and indium. The flux, along with other constituent elements or compounds, are put together in a nonreactive crucible. Afterward, it is put in a quartz tube along with some quartz wool (acts as a filter) on the top of the crucible and then sealed in 0.2 bar pressure of argon. The whole reaction mixture is heated above the melting point of the flux, where it turns into the liquid solution. At this temperature, the reaction mixture is kept for few hours to make a homogeneous mixture. After that, the crystal growth process is started by slow cooling up to the temperature above the melting point of flux, at which the extra flux is removed with centrifugation. The grown crystals are left on the other side

of quartz wool. A schematic representation of the steps involved in the flux method is shown in Figure 3.3.

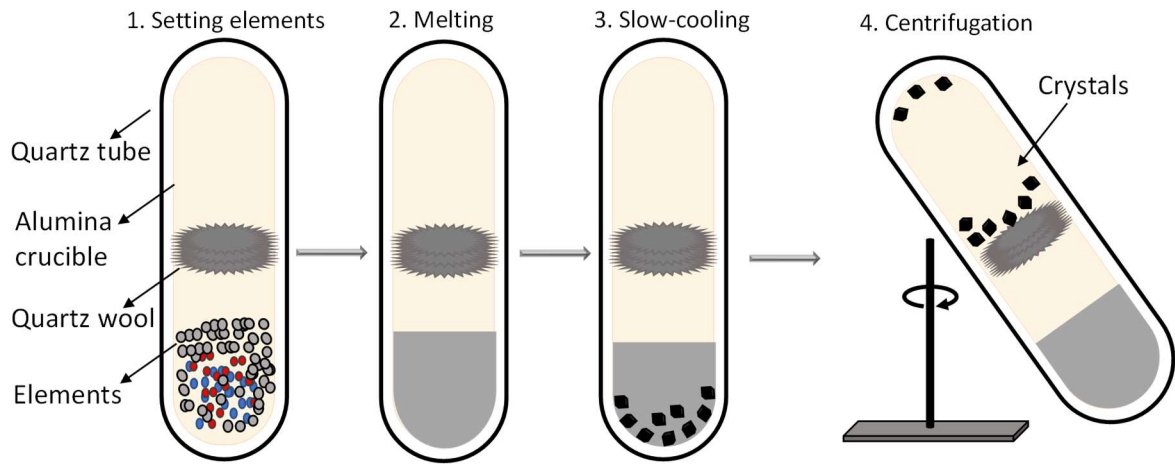


Figure 3.3. Schematic of crystal growth processes or steps involved in the flux method.

3.4. Bridgman method

The Bridgman technique (also known as Bridgman-Stockbarger method) is one of the most commonly used techniques to grow large single crystals¹¹². Similar to the floating zone and Czochralski technique, the Bridgman technique also employs the crystal growth from the melt. In this technique, the crucible containing the molten material is translated along the axis of a temperature gradient in the furnace. The principle of the Bridgman technique is the directional solidification by translating a melt from hot zone to cold zone of the furnace. Initially, the polycrystalline material is put in the crucible that is unreactive to the melt. Then the temperature of the furnace is increased above the melting temperature of the sample. After melting, the crucible is then translated slowly to the cooler zone of the furnace. When the bottom temperature of the crucible falls below the solidification temperature, the crystal growth is initiated by the seed at the melt-seed interface. After the complete transfer of crucible out of the hot zone to the cold zone, the entire melt normally converts to a solid single-crystalline ingot.

Figure 3.4(a) and (b) show the experimental setup and the schematic diagram of the Bridgman furnace, which has been used to grow crystals mentioned in this thesis. The maximum temperature reached in this furnace is 1973 K. The environment inside the furnace is protected by a continuous flow of argon gas. An electric motor is attached to the bottom of the furnace. After the melting of the sample, this motor pulls the sample downward to get it out of the furnace, creating the temperature gradient in the growth condition. Thus, leading to the formation of single crystals.

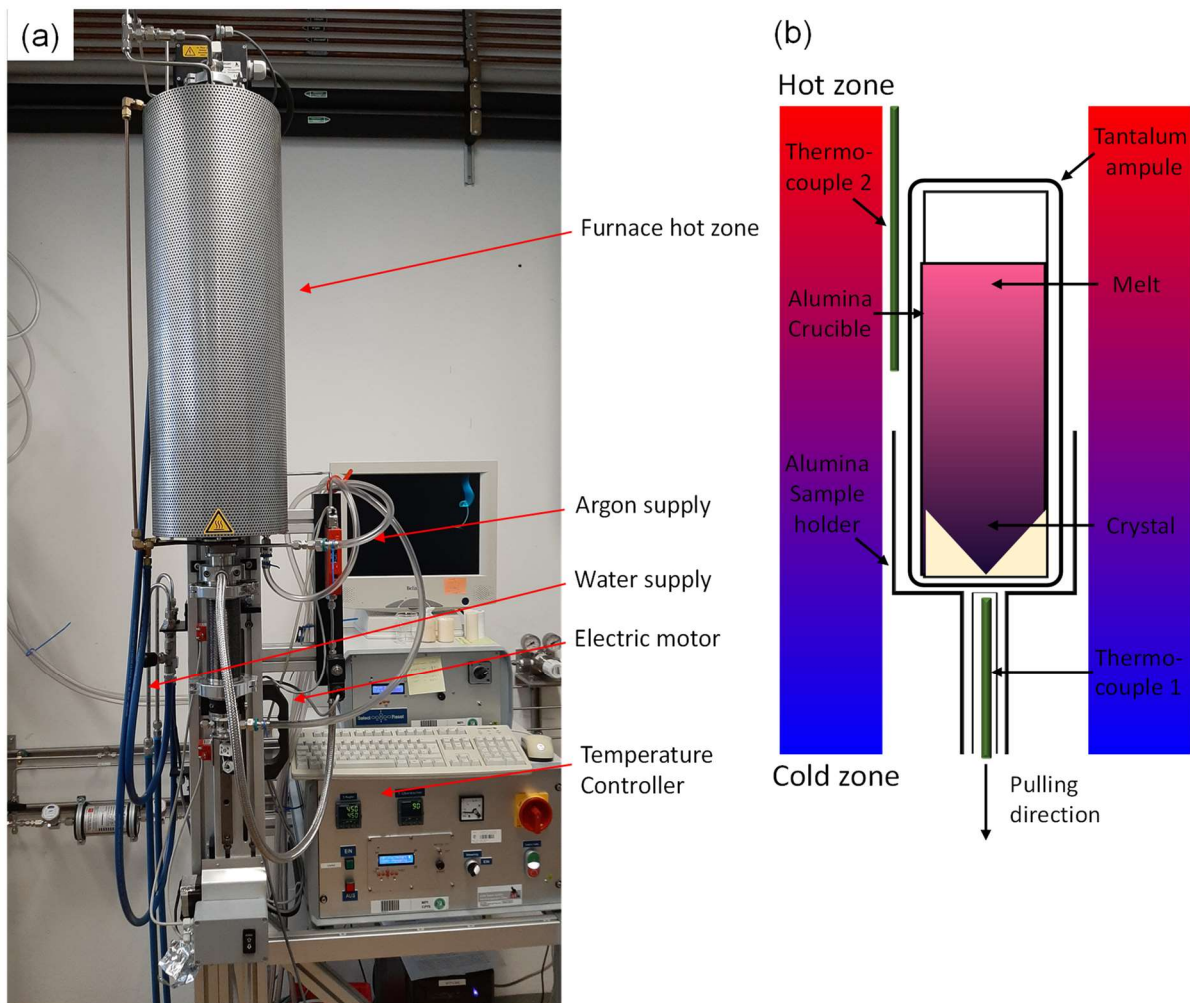


Figure 3.4. (a) Experimental setup and (b) schematic diagram of the vertical Bridgman furnace.

3.5. X-ray diffraction

3.5.1. Powder X-ray diffraction

Powder X-ray diffraction (XRD) is a rapid analytical technique mainly used for phase identification of a crystalline material and provides information on unit cell dimensions and crystal structure. For all the samples, the diffraction patterns were collected at room temperature using Cu $K\alpha_1$ radiation in the range of $3^\circ \leq 2\theta \leq 100.3^\circ$ and steps of 0.005° . The samples were finely ground in an agate mortar, and then homogeneously dispersed powder on a Mylar foil was mounted on XRD sample holder for the measurements. Topas software and PowderCell 2.4 package¹¹³ were used for the refinement of the diffraction patterns.

3.5.2. Single-crystal X-ray diffraction

Single-crystal XRD is a fast, non-destructive technique to obtain a precise crystal structure of a material with details about atomic positions, lattice parameters, bond angles, and bond lengths. Single-crystal XRD data were collected by a Rigaku AFC7 diffractometer with Mo K α radiation and a Saturn 724 + CCD detector. The refinement of the structure was done by SHELX package^{114,115}.

3.5.3. Laue diffraction

Laue method is mainly used to know the orientation of a large single crystal. In this method, the sample is stationary and white radiation of X-ray is used. Such a beam contains a broad range of wavelengths, which covers all the crystallographic planes to satisfy the condition of Bragg's Law by choosing an appropriate X-ray wavelength. The radiation from the target element molybdenum is used in this method. Laue method can give preliminary information about the symmetry of the crystals. As an example of cubic crystals, the collected pattern for [111] is 3-fold and is 4-fold for [100].

3.6. Powder neutron diffraction

Powder neutron diffraction measurements were performed at Laboratoire Léon Brillouin, Saclay, France, using a two-axis diffractometer equipped with a vertical pyrolytic graphite monochromator and cold neutron source of wavelength 2.426 Å. The refinement of the diffraction patterns was done with Fullprof suite package¹¹⁶.

3.7. Physical properties measurements

3.7.1. Magnetic measurements

All the magnetic measurements were performed in a superconducting quantum interference device (SQUID) magnetometer (MPMS-3) from Quantum Design Inc. The temperature range of measurements was 1.8–400 K in standard option and 300–1000 K in the oven mode option. The magnetic field range of the measurements was -7 to 7 T.

3.7.2. Electric transport measurements

All the electrical transport measurements were done in physical property measurement system (PPMS) from Quantum Design Inc. Physical properties such as Hall resistivity and longitudinal resistivity of the compounds were measured in a five-probe or four-probe option. The standard temperature range is 1.8 K to 400 K and the applied field was +9 T to -9 T.

4. Mn_{1.4}PtSn

As discussed in the previous chapter, compounds with D_{2d} symmetry were predicted to host a vortex-type spin structure, called as antiskyrmions. Tetragonally distorted inverse Heusler compounds such as Mn₂RhSn, Mn₂PtSn, Mn₂IrSn belong to the space group of D_{2d} symmetry¹¹⁷. However, except Mn₂RhSn, none of these compounds form as single-phase unless some vacancies are introduced at Mn-sites¹¹⁸. One such compound is Mn_{1.4}PtSn, which is a relative of Mn₂PtSn but with some vacancies at Mn sites and also has D_{2d} symmetry^{27,119,120}. Recently, the existence of antiskyrmions was proven by Lorentz transmission electron microscopy (LTEM) in this compound²⁷. In order to study the bulk properties related to antiskyrmions through magnetic, electric transport and neutron diffraction measurements, large single crystals are required. In this chapter, the techniques employed to grow such single crystals of Mn_{1.4}PtSn and its magnetic and electrical properties are discussed. The detailed structural analysis reveals that Mn_{1.4}PtSn is the first observed tetragonal superstructure in the Heusler family of compounds. From magnetization and powder neutron measurements, the presence of a non-coplanar spin structure is revealed. Electrical transport measurement shows the presence of a large topological Hall effect (THE) in the system, a key signature of a non-coplanar spin structure.

The text and figures are taken from following publications,

P. Vir, N. Kumar, H. Borrmann, B. Jamijansuren, G. Kreiner, C. Shekhar, and C. Felser, *Chem. Mater.* **31**, 5876 (2019).

P. Vir, J. Gayles, A. S. Sukhanov, N. Kumar, F. Damay, Y. Sun, J. Kübler, C. Shekhar, and C. Felser., *Phys. Rev. B* **99**, 140406(R) (2019).

4.1. Single crystal growth

4.1.1. Bridgman method

To grow the crystals of intermetallic compounds either by Bridgman or optical floating zone method, it requires the preparation of the polycrystalline sample, first. The polycrystalline sample of Mn_{1.4}PtSn was prepared by the arc-melting process. The high purity elements Mn (Sigma-Aldrich, 99.999 %), Pt (Sigma-Aldrich, 99.999 %) and Sn (Sigma-Aldrich, 99.999 %) were taken into stoichiometric ratio. An additional 3 mg/g of Mn was added to the mixture to compensate the Mn loss during melting as Mn tends to evaporate due to its high vapor pressure. All the elements were melted together. Afterward, the ingot of Mn_{1.4}PtSn was flipped and remelted. This process was repeated three times to increase the homogeneity. The prepared polycrystalline sample was sealed in a quartz tube

with a partial argon atmosphere inside and annealed at 1073 K for 7 days in a box furnace. The sample was quenched from 1073 K into the ice-water mixture.

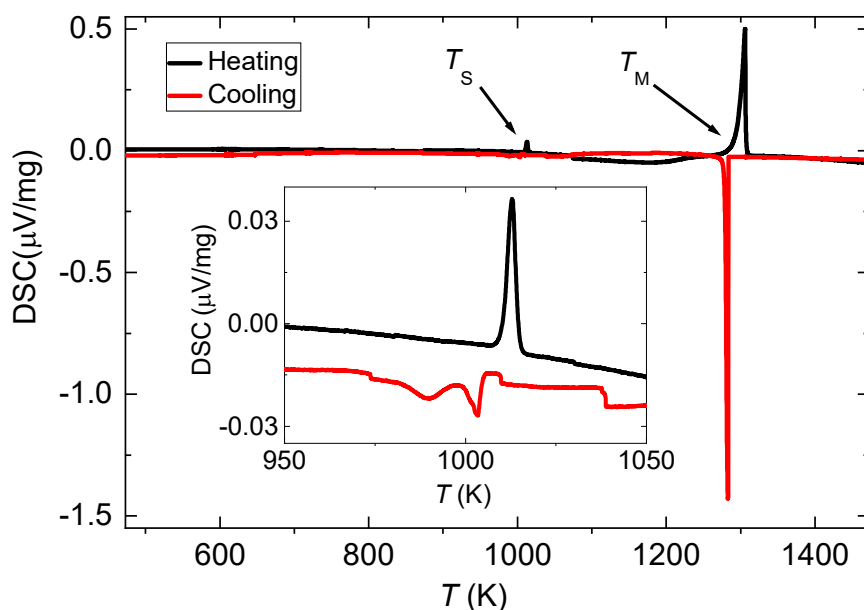


Figure 4.1. DSC measurement from 473 to 1473 K: inset shows enlarged view of the peak regions corresponding to structural transition, where T_S and T_M are at 1306 K and 1013 K, respectively (Figure adapted from our published work Ref. 119).

To know the melting point of $Mn_{1.4}PtSn$, the DSC measurement was performed on a small piece of annealed sample. In Figure 4.1, the DSC curve is shown as a function of temperature for both the cooling and the heating processes. Depending on heating and cooling processes, a large peak or dip appears at 1306 K, which corresponds to the melting point of the compound. The absence of any other peak nearby indicates that the compound melts congruently and does not decompose into other phases. Usually, for the intermetallic

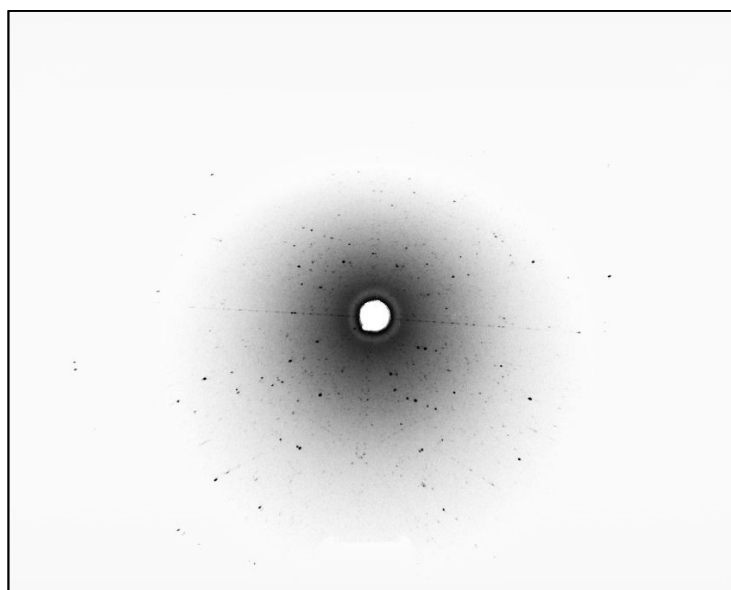


Figure 4.2. Laue diffraction pattern collected from single crystals of $Mn_{1.4}PtSn$ obtained by the Bridgman method.

compound that melts congruently, Bridgman or floating zone method yields rather high quality of the single crystal. Therefore, the single crystals of $\text{Mn}_{1.4}\text{PtSn}$ were grown by the above-described methods. Figure 4.2 shows a Laue diffraction pattern of $\text{Mn}_{1.4}\text{PtSn}$ crystals. Upon analyzing crystals with the Laue diffraction method, it appears that the crystal consists of several grains adjacent to each other.

To understand the reason behind this, the crystal was fine-polished and it was checked with a polarized light microscope. Since the structure of $\text{Mn}_{1.4}\text{PtSn}$ is tetragonal, it possesses crystallographic anisotropy. Therefore, twinning structures present in the crystal with different crystallographic orientations would be discernible under the polarized light with different contrasts. Figure 4.3 shows an image taken on the polished surface of the crystal, in which different contrasts correspond to crystal grains with different orientations. These grains are micro-sized twinned (or microtwinned) crystals that are oriented perpendicular to each other. Such type of micro-twinned grains have commonly been observed and studied in detail in the shape-memory Heusler compounds, for example, Ni_2MnGa ^{43,121}. These shape memory compounds show a structural transition from the high-temperature phase called as austenite phase to the low-temperature phase called as the martensitic phase. The structural transition is often referred as martensitic transition and the corresponding temperature is called martensitic transition temperature (T_S). Generally, the austenite phase has a cubic crystal structure while the martensitic phase has either tetragonal or orthorhombic crystal structure¹²². A closer look at the DSC curve of $\text{Mn}_{1.4}\text{PtSn}$ also reveals the presence of the martensitic transition in the compound (as shown in the inset of Figure 4.1). The martensitic transition temperature, T_S , of $\text{Mn}_{1.4}\text{PtSn}$ is found to be 1013 K.

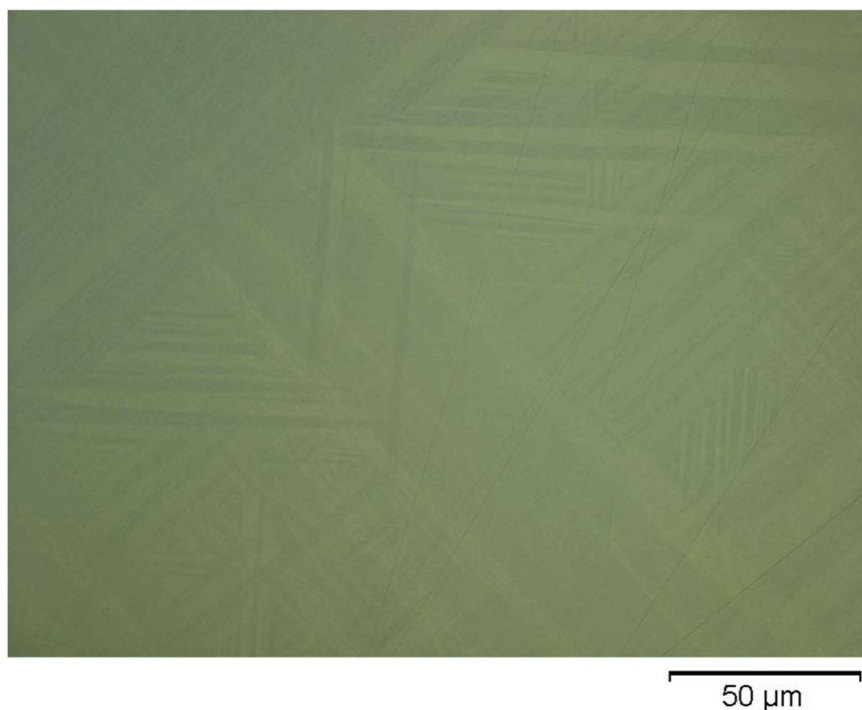


Figure 4.3. Polarized light microscopy image of the crystal grown by Bridgman method above martensitic transition temperature. Different contrast corresponds to microtwinned structure.

Figure 4.4 shows the schematic of the possible formation of microtwinned crystals obtained from the Bridgman method. The methods like Bridgman and optical floating zone require cooling directly from the melt, therefore, cooling from melt would first result in the formation of a single crystal of cubic phase of $\text{Mn}_{1.4}\text{PtSn}$. This cubic phase upon cooling below T_S would subsequently distort to the tetragonal phase. As there are three equivalent crystallographic directions ($[100]$, $[010]$, and $[001]$) in the cubic structure; the distortion results in three perpendicular microtwinned crystals.

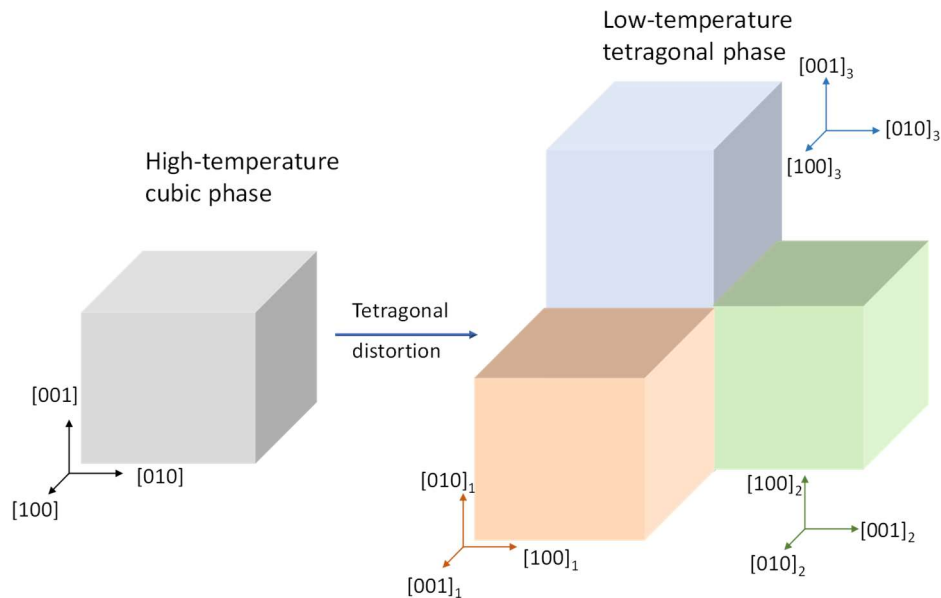


Figure 4.4. The schematic of formation of microtwinned structure. Different colors correspond to three perpendicular grains.

Such microtwinned crystals are used for studying the properties of antiskyrmions with LTEM, where a tiny piece of single crystal ($< 1 \mu\text{m}$) is enough. However, a large single crystal is required to study the bulk properties of antiskyrmions. A different crystal growth technique, the flux method, was employed to get microtwin free crystals. The flux method was chosen because the temperature range of crystal growth can easily be controlled, therefore, the crystal growth above T_S can be avoided.

4.1.2. Flux method

There is always a probability of flux inclusion in crystals grown by the flux method. Therefore, if possible, the use of external flux should be avoided. Fortunately, one of the constituent elements, Sn, has a low melting point of 505 K and can be used as a flux to grow single crystals of $\text{Mn}_{1.4}\text{PtSn}$. However, the major challenge is the unavailability of the ternary phase diagram of Mn-Pt-Sn. Therefore, several attempts with different elemental ratios were tried before getting a successful growth condition of single crystals.

The trial growth conditions confirmed that the formation of the desired phase $\text{Mn}_{1.4}\text{PtSn}$ is highly sensitive to the initial ratio of Mn and Pt during the crystal growth. In the first attempt, the elemental ratio of Mn:Pt = 1.4:1 was taken. The crystal obtained after the reaction had an undesired composition of $\text{Mn}_{22}\text{Pt}_{30}\text{Sn}_{48}$, in which Mn:Pt ratio was 0.73:1 and this was far below the desired ratio. Therefore, it seemed that a higher Mn:Pt ratio was needed to get the desired composition 1.4:1. To suppress the formation of $\text{Mn}_{22}\text{Pt}_{30}\text{Sn}_{48}$, a higher Mn to Pt ratio of 3:1 was taken, which resulted in the formation of $\text{Mn}_{1.4}\text{PtSn}$. In the flux growth, if the reaction mixture is cooled continuously from high temperatures (~ 1273 K), the obtained crystals are always microtwinned which can be verified by polarized light optical microscopy image of the surface of a crystal as shown in Figure 4.5 where regions with different contrasts correspond to different orientations. The size of the microtwinned grain of crystal grown by the flux method is larger than that of the Bridgman method.

Having known the structural transformation at 1013 K and the correct elemental ratio of Mn:Pt, the crystal growth below this temperature was performed. To achieve a homogeneous solution, the complete reaction mixture was heated to 1323 K, which was then cooled very rapidly to 923 K (below the structural transformation temperature) to avoid the growth of any cubic phase. Slow cooling from 923 to 723 K was adopted to grow single crystals with tetragonal structure. This cooling profile results in the formation of single crystals free from microtwins. Hence, the only successful method to grow crystals of $\text{Mn}_{1.4}\text{PtSn}$ free from microtwin is flux method wherein the growth process occurs far below the melting point as well as martensitic transition.

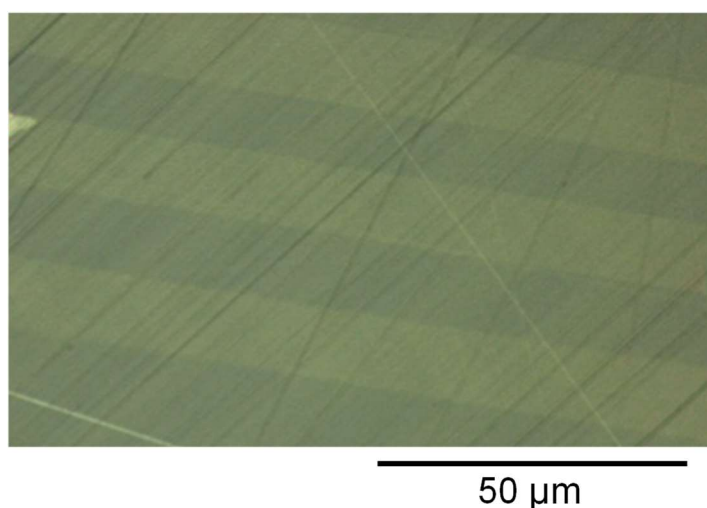


Figure 4.5. Polarized light microscopy image of the crystal grown by flux method above the martensitic transition temperature. Different contrast corresponds to microtwinned structure (Figure adapted from our published work Ref. 119).

A successful method and a detailed heating profile to grow the microtwin free single crystal of $\text{Mn}_{1.4}\text{PtSn}$ are summarized in this paragraph and Figure 4.6. Single crystals of $\text{Mn}_{1.4}\text{PtSn}$ were grown by flux method using tin as flux. Purification of Mn (Sigma-Aldrich, 99.999%) was done by heating the Mn pieces in a quartz tube at 1273 K for 24 hours. This

oxide free Mn and Pt (Sigma-Aldrich, 99.999%) were cut into very small pieces and weighed in 3:1 molar ratio with a total weight of 0.75 g. This was loaded in a dried alumina crucible along with 10 g of tin. The alumina crucible was then sealed in a quartz tube under 0.2 bar argon pressure. The sealed quartz tube was put in the box furnace and heated to 1323 K with a rate of 200 K/h. The whole content was kept at this temperature for 24 hours. Initially, a very fast cooling to 923 K was carried out and then followed by slow cooling to 723 K with a rate of 2 K/h. At 723 K, the tube was kept for 24 hours, where extra flux was removed by the centrifugation. Obtained single crystals of $Mn_{1.4}PtSn$ were of silvery metallic color and of 1–2 mm size. The crystals were stable in air and moisture and no decomposition was observed even after several months. Several crystals were separated for further characterizations. With the same experimental conditions, crystal growth was found to be completely reproducible.

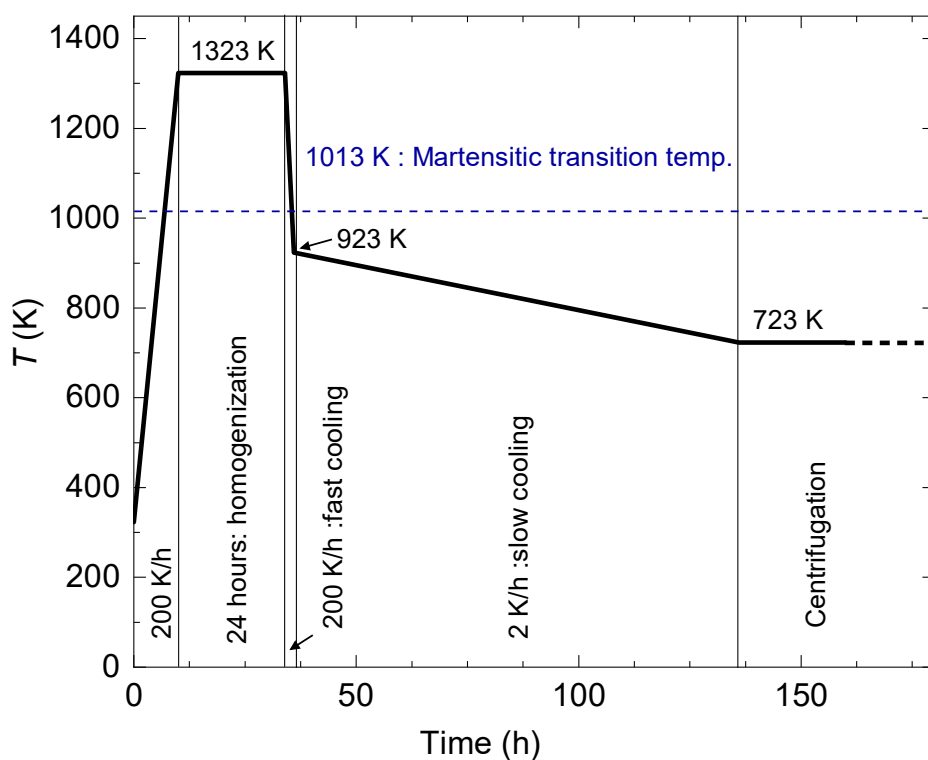


Figure 4.6. The heating profile involved in the synthesis of the microtwin free single crystals of $Mn_{1.4}PtSn$ by flux method.

Composition:

The composition of single crystals was checked with both EDX and chemical analysis methods.

Chemical analysis: Chemical analysis was carried out on as-grown crystals of $\text{Mn}_{1.4}\text{PtSn}$ in order to get a more accurate composition. The instrument used for this process was ICPOES S100 SUDV (Agilent) and the digestion process was done with Turbowave (MLS). The acidic solution used for dissolving crystals was 3 mL HCl and 0.5 mL HNO_3 . Independently, four sets of 5 mg crystals were used to get the standard deviation in the composition. The composition obtained is listed in the following table 4.1. The obtained composition $\text{Mn}_{1.43}\text{PtSn}$ from the chemical analysis is very close to the composition $\text{Mn}_{1.44}\text{PtSn}$ obtained from single-crystal XRD.

Table 4.1. The composition of flux-grown crystals from chemical analysis.

Elements	Composition (wt %) \pm deviation	Composition (molar ratio) \pm deviation
Mn	20.11 \pm 0.13	1.426 \pm 0.011
Pt	50.08 \pm 0.24	1 \pm 0.007
Sn	31.05 \pm 0.09	1.019 \pm 0.006

EDX: Figure 4.7 shows the EDX spectrum of $\text{Mn}_{1.4}\text{PtSn}$ single crystal. This spectrum was recorded on the crystal whose SEM image is shown in the inset of Figure 4.7. The

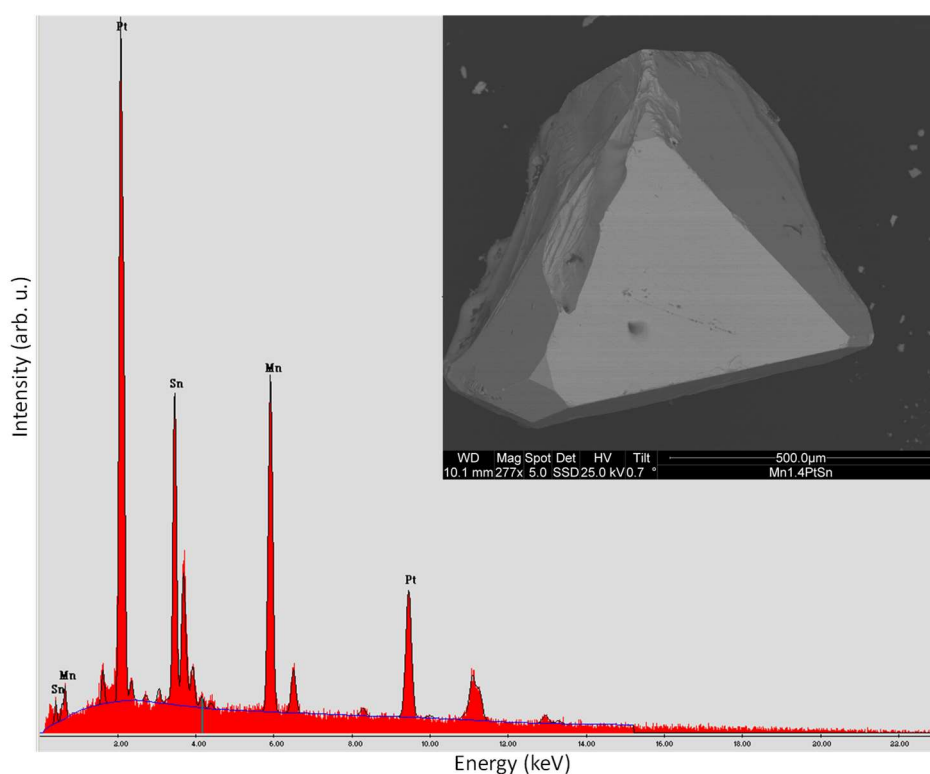


Figure 4.7. EDX spectrum along with SEM image (inset) of microtwin free crystal of $\text{Mn}_{1.4}\text{PtSn}$.

composition obtained by EDX analysis is 41% for Mn, 30% for Pt, and 29% for Sn, which formulates into $\text{Mn}_{1.39}\text{Pt}_{1.01}\text{Sn}_{0.98}$. This composition is very close to the one obtained from single-crystal XRD, which will be discussed further in this chapter.

Laue diffraction patterns:

The as-grown crystal obtained from the flux method is shown in Figure 4.8(a). Before measuring structural and direction-dependent physical properties, the directions of the crystals were analyzed by the Laue diffraction method. In the majority of the crystals, two types of facets exist i.e. rectangular and hexagonal. The rectangular facet is either (100) or (001) while the hexagonal one is always (112). Figures 4.8(b), (c) and (d) show the Laue diffraction patterns together with the superimposed simulated patterns along [001], [100] and [112], respectively. Laue pattern along [100] shows two-fold rotation symmetry while along [001], it shows four-fold rotation symmetry, which infers the presence of tetragonal symmetry in the crystal. Furthermore, the Laue pattern along [112] does not contain any rotational symmetry as expected in the tetragonal structure.

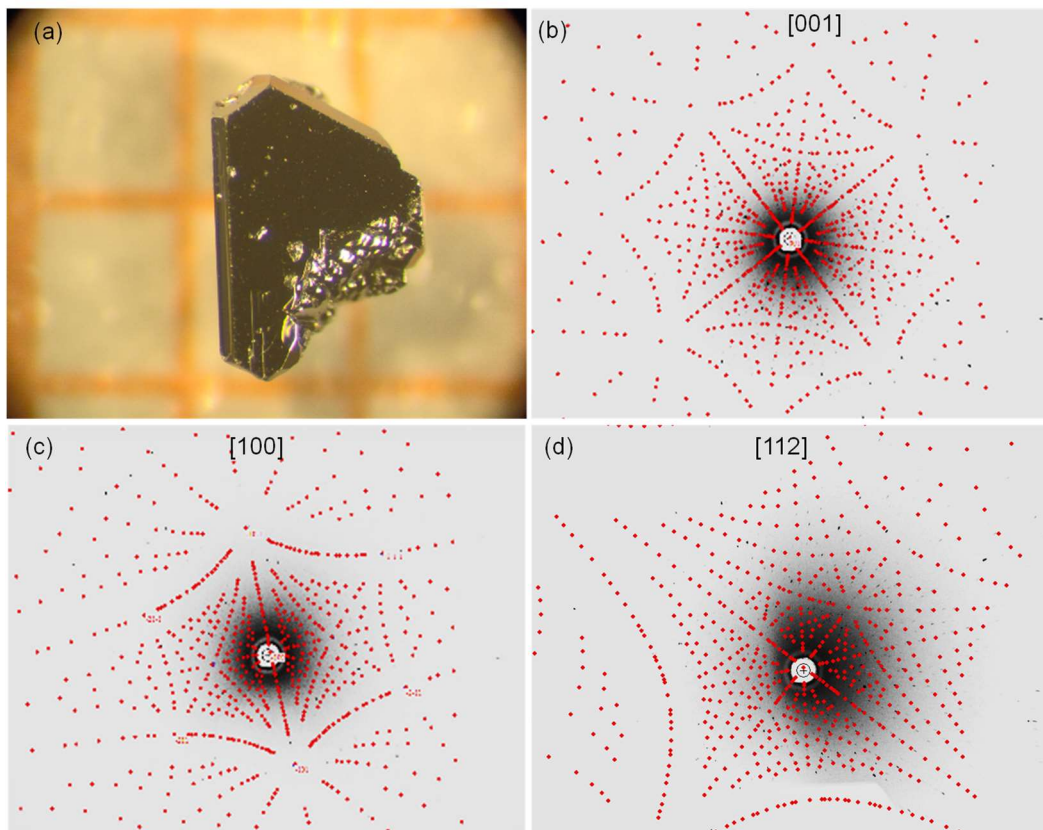


Figure 4.8. (a) Optical image of as-grown single crystal from flux method on mm-scale grid paper and corresponding Laue patterns for the crystallographic direction (b) [001] (c) [100], and (d) [112]. (Figure adapted from our published work Ref. 119).

4.2. Tetragonal superstructure

After understanding the crystal symmetry with Laue diffraction, a single crystal XRD was done to know the crystal structure precisely. A large crystal of $\text{Mn}_{1.4}\text{PtSn}$ was broken into many small pieces and a small piece was mounted for measurements. Three different data sets were collected on three different pieces.

Figure 4.9(a) shows the image of one of the crystal platelets used for the single crystal diffraction measurements. First, as a preliminary step, diffraction patterns were collected to know the lattice parameters and afterward, a data set containing a few thousand reflections were measured by rotating the crystal three-dimensionally. Figures 4.9(b), (c) and (d) show oscillation images around $[100]$, $[010]$ and $[001]$ directions, respectively.

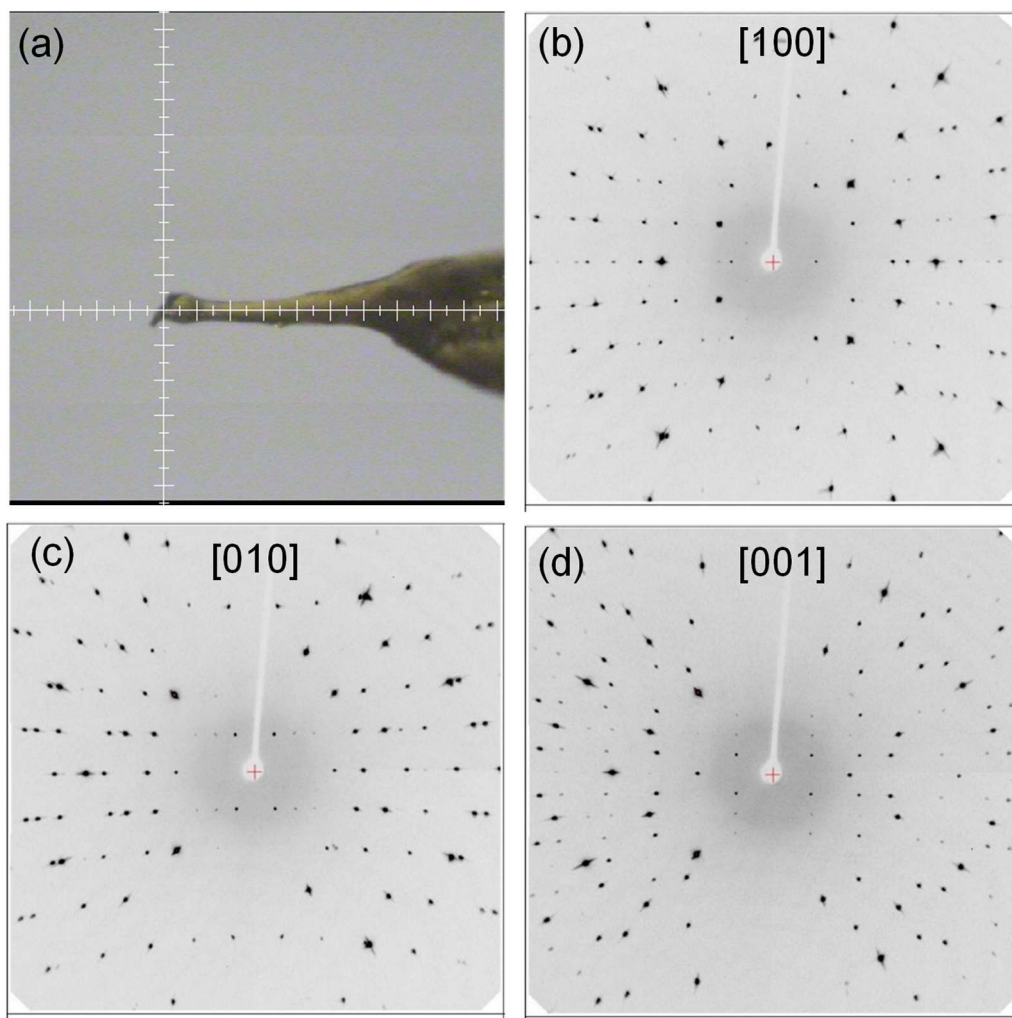


Figure 4.9. (a) The image of crystal platelet used for measuring single crystal diffraction and, diffraction pattern oscillating around (b) $[100]$ (c) $[010]$, and (d) $[001]$.

Result of refinements:

The crystal structure was refined with SHELX software¹¹⁴. The refined unit cell parameters are $a = 6.3651(4) \text{ \AA}$ and $c = 12.2205(11) \text{ \AA}$. The c/a ratio is 1.92, which is very close to 2. The structure refinements confirm the non-centrosymmetric model including the assignment of the absolute structure for the crystal investigated. There is little contribution due to twinning by inversion of 9(2) % accordingly and the Flack parameter is taken as 0.087(16). The complete single crystal refinement is summarized in table 4.2. In table 4.3, Wyckoff and atomic positions in the unit cell are presented along with the isotropic displacement parameters. The anisotropic displacement parameters and bond distances between each type of atoms are shown in table 4.4 and table 4.5, respectively. Through the single-crystal refinements, the resulting crystal structure is shown in Figure 4.10. In this structure, Mn atoms occupy $4a$ and $8d$ sites while Pt and Sn atoms occupy $8c$ and $8d$ sites, respectively. All the sites are fully occupied except Mn at $4a$ position. The nominal composition obtained from the single crystal refinement was $\text{Mn}_{1.44}\text{PtSn}$. For this composition, the $4a$ -Mn site is 88 percent occupied.

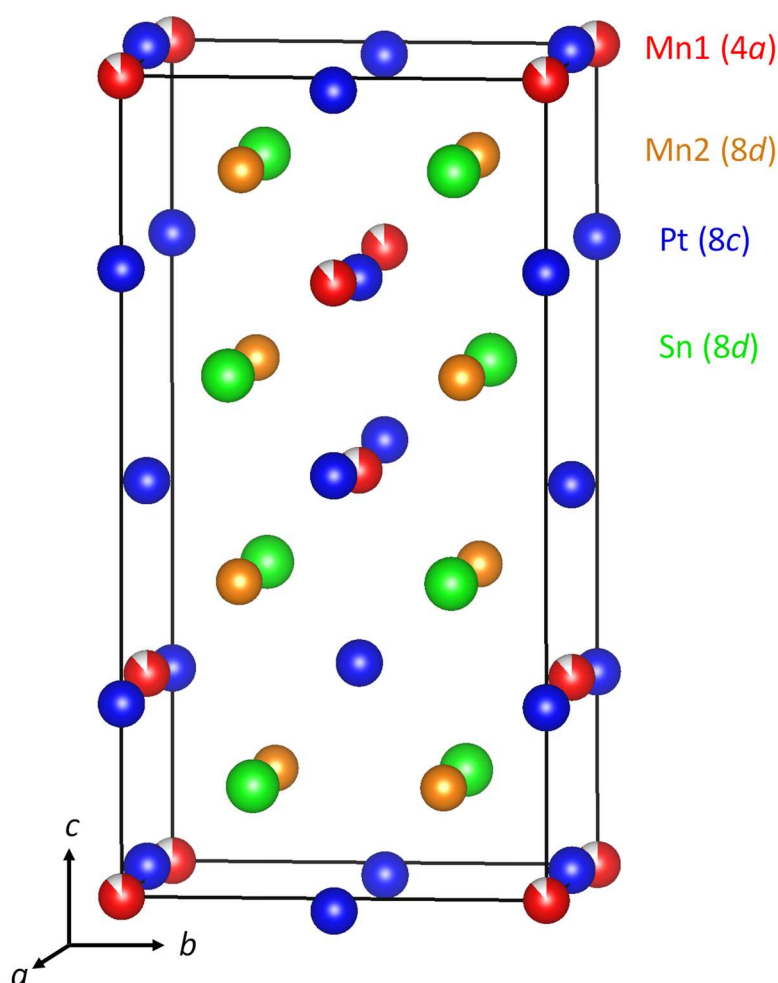


Figure 4.10. The crystal structure of $\text{Mn}_{1.44}\text{PtSn}$ obtained from single-crystal refinement.

Table 4.2: Crystal data and the detail of the structure refinement of Mn_{1.44}PtSn at 295(2) K.

Empirical formula	Mn _{1.44} PtSn
Formula weight	392.96
Temperature	295(2) K
Wavelength	0.71073 Å (Mo K α)
Crystal symmetry	tetragonal
Space group	$I\bar{4}2d$
Unit cell dimensions	$a = 6.3651(4)$ Å, $\alpha = 90^\circ$ $b = 6.3651(4)$ Å, $\beta = 90^\circ$ $c = 12.2205(11)$ Å, $\gamma = 90^\circ$
Cell volume	495.11(8) Å ³
Z	8
Density (experimental)	10.544 g/cm ³
Absorption coefficient	73.136 mm ⁻¹
$F(000)$	1312
Θ range for data collection	3.609 -36.964°
Index ranges	$-10 \leq h \leq 10$, $-9 \leq k \leq 9$, $-20 \leq l \leq 20$
Refinement method	full-matrix least-squares on F^2
Goodness of fit	0.954
No. of reflections	632
data/restraints/params	632/0/20
Final R indices [$>2\sigma(I)$]	$R_{\text{obs}} = 0.0203$, $wR_{\text{obs}} = 0.0377$
extinction coefficient	0.00026(5)
Abs structure Flack	0.087(16)

Table 4.3: Atomic coordinates and equivalent isotropic displacement parameters (in \AA^2) for $\text{Mn}_{1.44}\text{PtSn}$ at 295(2) K.^a

Label	Wyckoff	<i>x</i>	<i>y</i>	<i>z</i>	Occupancy	U_{eq}
Mn(1)	4 <i>a</i>	0	0	1/4	0.88	0.012
Mn(2)	8 <i>d</i>	1/4	0.2282	3/8	1	0.01
Pt(1)	8 <i>c</i>	0	1/2	0.48488	1	0.011
Sn(1)	8 <i>d</i>	0.27875	1/4	1/8	1	0.012

^a U_{eq} is defined as one-third of the trace of the orthogonalized U_{ij} tensor.

Table 4.4: Anisotropic displacement parameters (in \AA^2) for $\text{Mn}_{1.44}\text{PtSn}$ at 295(2) K with estimated standard deviations in paranthesis^a

Label	U_{11}	U_{22}	U_{33}	U_{12}	U_{13}	U_{23}
Mn(1)	0.0153(8)	0.0153(8)	0.0060(7)	0	0	0
Mn(2)	0.0089(7)	0.0119(9)	0.0075(5)	0	0	-0.0014(10)
Pt(1)	0.00968(16)	0.01545(17)	0.00811(12)	0.0006(2)	0	0
Sn(1)	0.0145(3)	0.0142(4)	0.0079(2)	0	0	0.0003(5)

^aThe anisotropic displacement factor exponent takes the form: $-2\pi^2 [h^2a^{*2}U_{11} + \dots + 2hka^*b^* U_{12}]$.

Table 4.5: Bond lengths (\AA) for $\text{Mn}_{1.44}\text{PtSn}$ at 295(2) K with estimated standard deviations in parentheses

Label	distances	Label	distances
Pt(1)- Mn(1)	2.7068(13) $\times 2$	Pt(1)- Mn(2)	3.1879(2) $\times 2$
Pt(1)- Sn(1)	2.7288(6) $\times 2$	Sn(1)- Mn(2)	2.8310(7) $\times 2$
Pt(1)- Sn(1)	2.7358(7) $\times 2$	Sn(1)- Mn(1)	2.8610(16)
Pt(1)- Mn(1)	2.7523(10) $\times 2$	Sn(1)- Mn(1)	3.0637(3) $\times 2$
Pt(1)- Mn(2)	2.8705(4)	Sn(1)- Mn(1)	3.1829(2) $\times 2$
Mn(1)- Mn(2)	2.8030(12) $\times 2$		

Relation to the Heusler structure:

The crystal structure of the inverse Heusler compound has been described previously in section 2.1. Here for a particular case of Mn_2PtSn , Mn and Sn atoms form NaCl-type structure with Wyckoff position of $4a$ and $4b$, respectively while other Mn and Pt atoms sit at tetrahedral sites with Wyckoff position $4c$ and $4d$. In order to relate the crystal structure of $\text{Mn}_{1.4}\text{PtSn}$ with inverse Heusler structure, the structure of the inverse Heusler structure is modified by shifting its origin to $(\frac{1}{4}, \frac{1}{4}, \frac{1}{4})$. A schematic of this operation is presented in Figure 4.11 in which the Wyckoff positions of these elements are interchanged. In the newly modified structure, Mn and Pt occupy $4a$ and $4b$ sites while other Mn and Sn are at $4c$ and $4d$ sites, respectively.

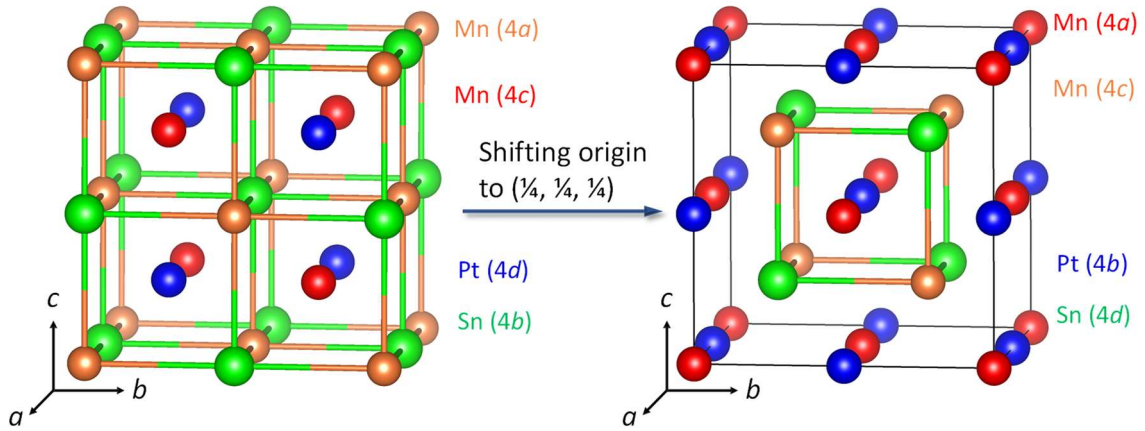


Figure 4.11. Schematic for the change in the crystal structure of inverse Heusler compound Mn_2PtSn after shifting its origin.

The crystal structures of different space groups are shown in Figure 4.12. It describes how structural evolution occurs from inverse cubic Heusler structure to inverse tetragonal Heusler structure, and then upon vacancy formation, the inverse tetragonal Heusler structure transforms into a superstructure form of another inverse tetragonal structure. The cubic structure of Mn_2PtSn supposedly has space group $F\bar{4}3m$ and the lattice parameter is approximately 6.25 \AA . When such a cubic crystal structure leads to tetragonal distortion, the new cell parameters of the tetragonal structure become $a_t = a_c/\sqrt{2}$ and $c_t = c_c$, changing the volume of the unit cell to half; the subscripts correspond to the tetragonal and cubic structure, respectively. Upon introducing the vacancies at Mn sites in Mn_2PtSn , the target compound is $\text{Mn}_{1.4}\text{PtSn}$. If vacancies are statistically distributed (hypothetical situation), the crystal symmetry and lattice parameters would be the same as Mn_2PtSn . However, in reality, the vacancies created at Mn sites are ordered and therefore, leads to change in the space group from $I\bar{4}m2$ to $I\bar{4}2d$ as well as the change in the lattice parameters. The new lattice parameters of $\text{Mn}_{1.4}\text{PtSn}$ becomes $a_T = \sqrt{2}a_t$ and $c_T = 2c_t$, enlarging the volume of the unit cell by 4 times; the subscripts correspond to the vacancy-ordered and vacancy-disordered structures, respectively. Thus, the relation between the volume of involved structures can be given as, $V_T = 4V_t = 2V_c$.

In Figure 4.13(a), the crystal structure of $\text{Mn}_{1.4}\text{PtSn}$ with space groups of $I\bar{4}m2$ (hypothetical, black line) and $I\bar{4}2d$ (red line) as a subcell and a supercell, respectively, along $[001]$ zonal axis is shown. The ‘a’ cell parameter of the supercell, a_T , is equal to the diagonal of the old sub-unit cell, which is $\sqrt{2}a_t$. Figure 4.13(c) shows the corresponding experimental single-crystal XRD pattern obtained in the reciprocal space. The black square connecting the intensities of 220 , $\bar{2}20$, $2\bar{2}0$, and $\bar{2}\bar{2}0$ represents the subcell, while the red square connecting the intensities of 200 , $\bar{2}00$, 020 , and $0\bar{2}0$ represents the supercell. Figures 4.13(b) and (d) show the crystal structure and the experimental single-crystal XRD patterns, respectively, along the $[100]$ zonal axis.

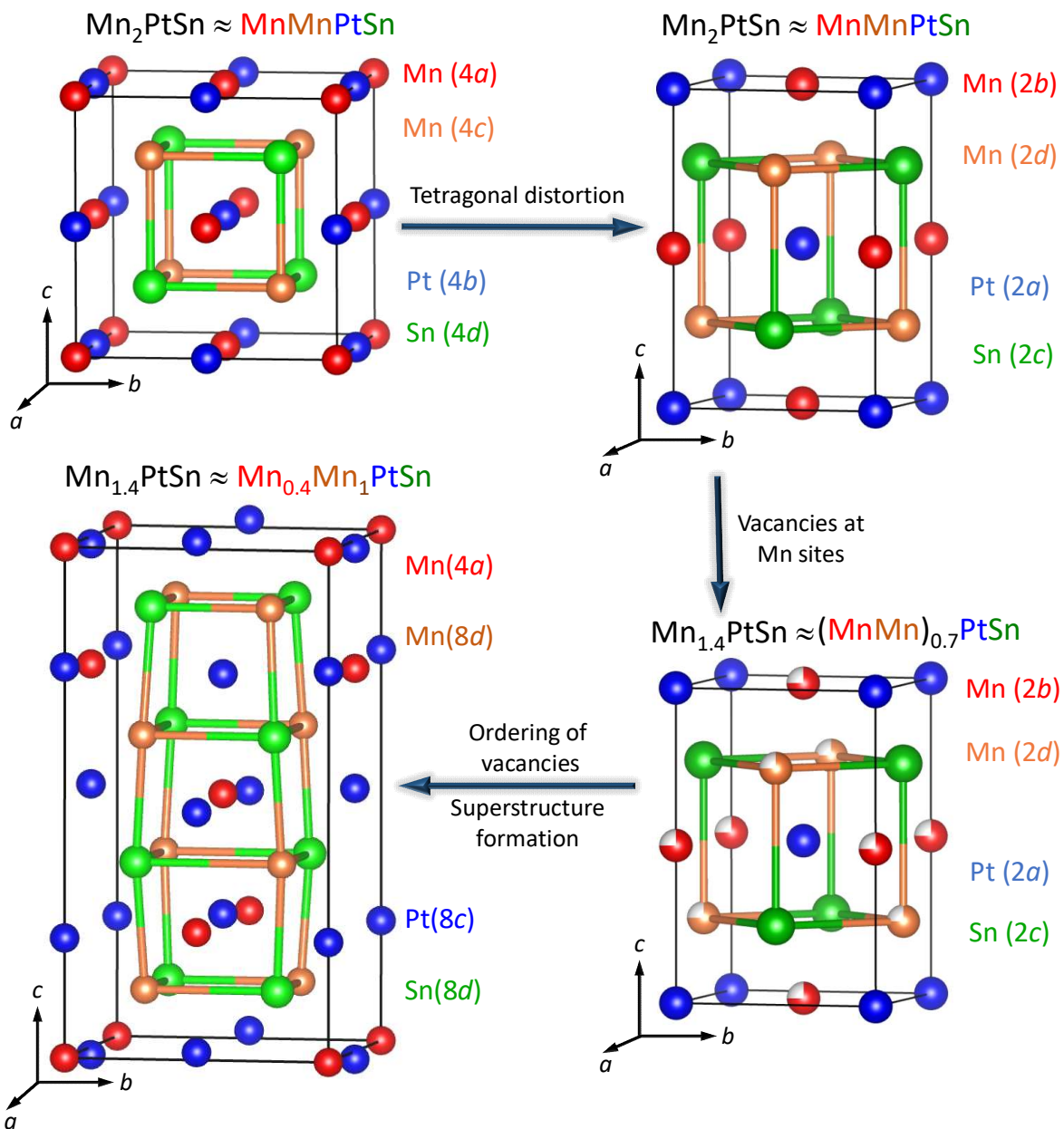


Figure 4.12. Schematic evolution of the superstructure induced by ordering of the Mn-vacancies in $\text{Mn}_{1.4}\text{PtSn}$. The Mn–Pt substructure is shown by black solid lines, whereas the Mn–Sn substructure is shown by green-orange solid lines. (Figure adapted from our published work Ref. 119).

The observed and calculated powder XRD patterns for $\text{Mn}_{1.4}\text{PtSn}$ by considering the ordered superstructure with the space group of $I\bar{4}2d$ are shown in Figure 4.14. The inset shows an expanded view of the pattern in the low angle range with indices hkl for the highest superstructure reflections. In the inset, the blue curve represents the simulated XRD pattern for the disordered crystal structure with space group $I\bar{4}m2$. Upon comparing the simulated XRD patterns for both space groups with the experimental XRD patterns, the experimental patterns match accurately only with the superstructure space group $I\bar{4}2d$, and thus rules out the possibility of the disordered crystal structure with space group $I\bar{4}m2$.

The crystal structure of $\text{Mn}_{1.4}\text{PtSn}$ can be described as a superstructure of the inverse Heusler structure (Mn_2PtSn) or the half-Heusler structure (MnPtSn). In the case of the cubic inverse or tetragonal inverse Heusler structures, the former with $c/a = 0.95$, the structure is

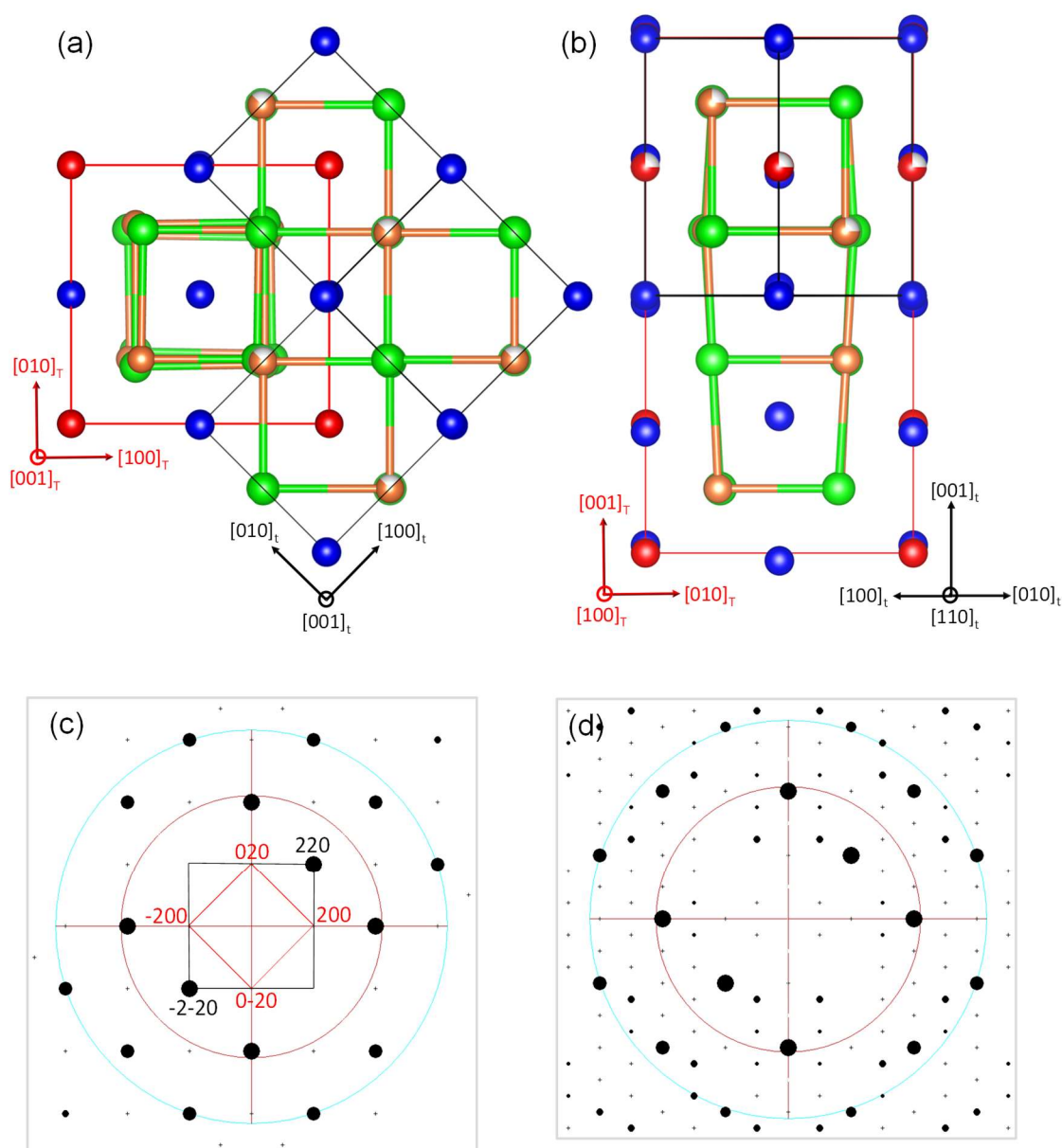


Figure 4.13. (a), (b) Crystal structure and (c), (d) single crystal diffraction patterns for the zone axis $[001]$ and $[100]$, respectively. (Figure adapted from our published work Ref. 119).

obtained by doubling the c -axis, forced by an ordered arrangement of vacancies in the Pt–Mn partial structure of inverse Mn_2PtSn . Alternatively, the structure of $\text{Mn}_{1.4}\text{PtSn}$ is obtained by partly filling the vacancies in MnPtSn . The created vacancies starting from Mn_2PtSn or the remaining vacancies starting from MnPtSn are equally distributed in Pt–Mn layers (for $\text{Mn}_{1.5}\text{PtSn}$: Pt–(0.4Mn/0.6□), which are alternately stacked with Mn–Sn layers along the c -axis. Here, □ is the place holder for a vacancy. In each Pt–(Mn/□) layer, the vacancies are arranged to have maximal distances from each other.

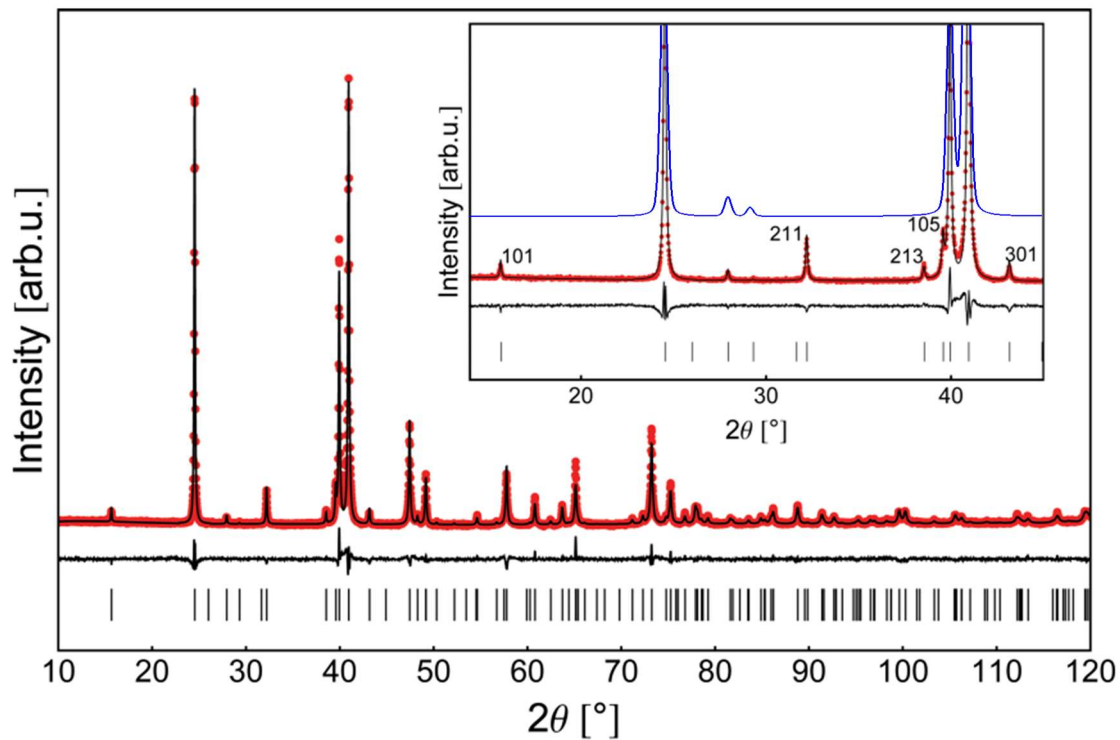


Figure 4.14. Observed and calculated powder XRD patterns. The inset shows the pattern with hkl indexed peaks for the higher superstructure reflections. For comparison, the simulated pattern corresponding to the disordered crystal structure in space group $I\bar{4}m2$ with missing superstructure reflections is shown (blue color). (Figure adapted from our published work Ref. 119).

The atomic environments of the atoms and the vacancy in the asymmetric part of the unit cell are shown for $\text{Mn}_{1.4}\text{PtSn}$, Mn_2PtSn , and MnPtSn in Figure 4.15. Here, it is shown that two vacancies are created in the first shell of Mn (Mn1) and Sn atoms of the Mn–Sn partial substructure. There is no vacancy in the atomic environment of the remaining Mn atoms (Mn2), but there are three vacancies in the octahedral shell of Pt. In addition, there are no vacancies in the atomic environment of a vacancy. This arrangement allows further Mn2 to be removed under the condition that no vacancies are created with vacancies in the first and second shells, as observed in the crystal structure of MnPtSn .

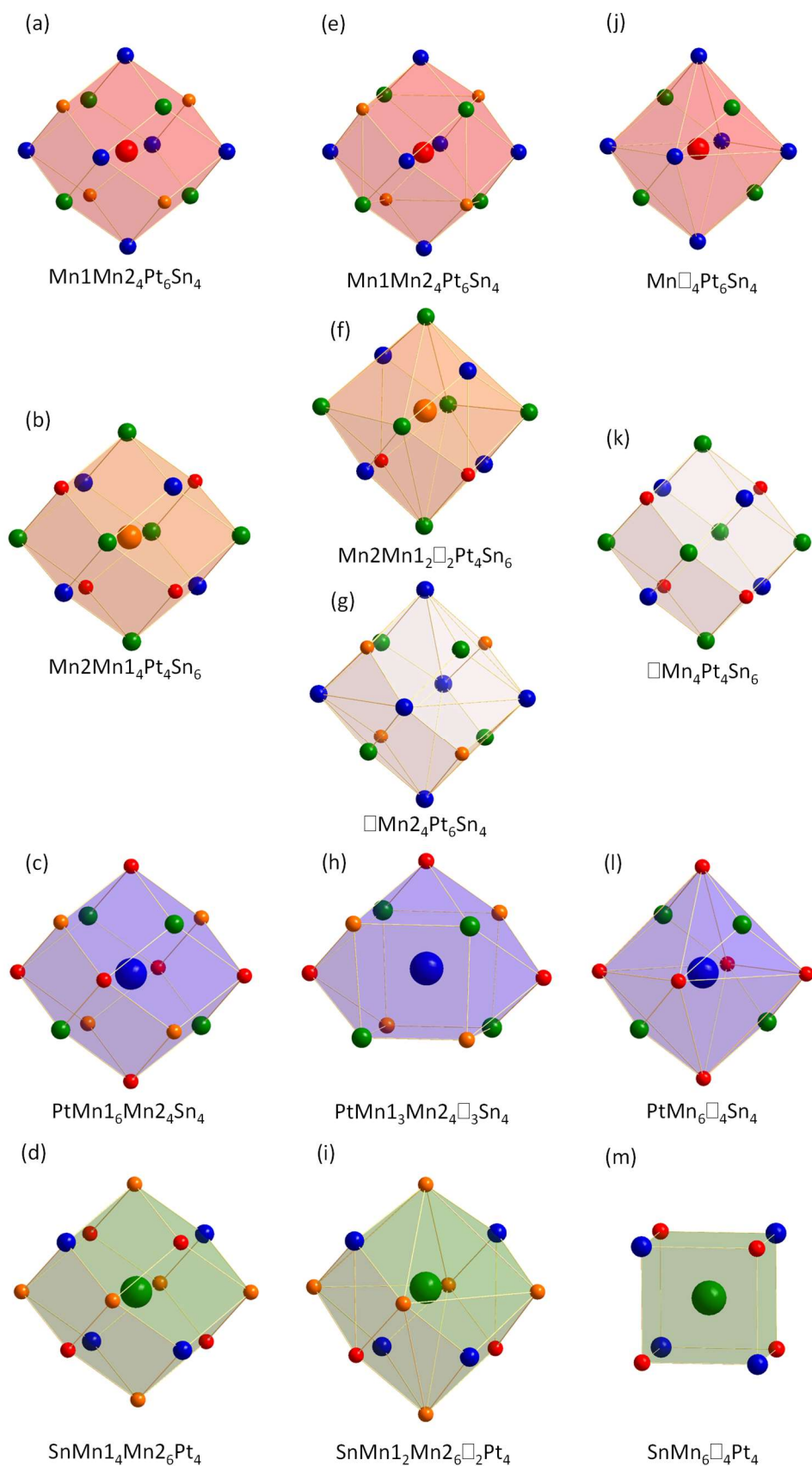


Figure 4.15. Atomic environments of the atoms in the asymmetric part of the unit cell and vacancy sites for a–d) tetragonal inverse Mn_2PtSn , e–i) $\text{Mn}_{1.4}\text{PtSn}$, and j–m) cubic half-Heusler MnPtSn . (Figure adapted from our published work Ref. 119).

4.3. Magnetic properties

The magnetization was measured in a commercial magnetometer (MPMS-3, Quantum Design) between 2 to 400 K for the magnetic field up to 7 T. For AC susceptibility measurement, the applied AC field 0.001 T and the frequency 93 Hz was used.

Magnetization measurement of single crystals of $\text{Mn}_{1.4}\text{PtSn}$ shows a rich magnetic temperature–field phase diagram. At high temperatures in the absence of external fields, the magnetic structure is collinear ferromagnetic aligned along [001]. As the temperature is decreased the system undergoes a spin-reorientation transition around 170 K to a magnetic phase having a non-coplanar spin arrangement. In the non-coplanar spin arrangement, the moments at $4a$ site align antiparallel with a small canting angle to the moment present at other $4a$ Mn-site, keeping net moment along [001] direction. Moments present at $8d$ site are parallel to each other. The existence of a non-coplanar spin structure is confirmed by refinement of powder neutron diffraction (see section 4.5) and first-principle theoretical calculations (see section 4.6).

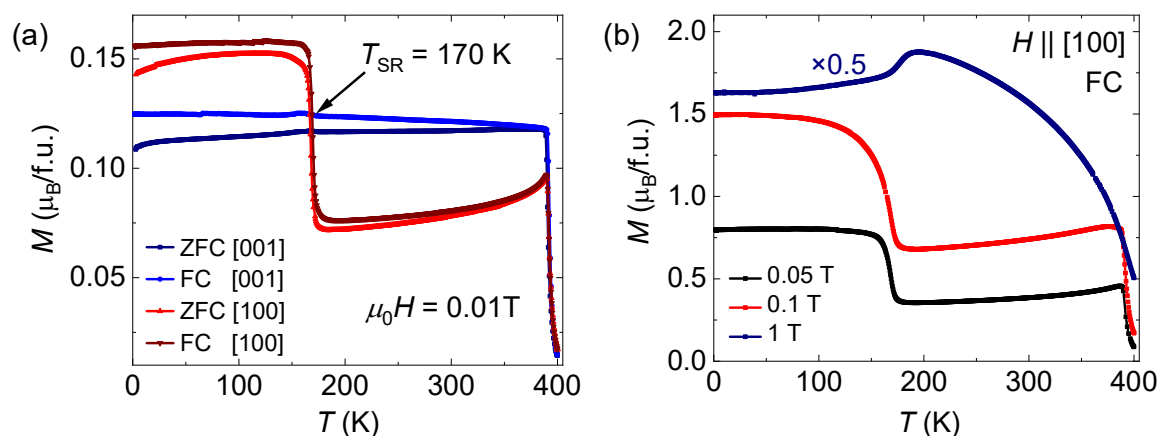


Figure 4.16. (a) Magnetization vs temperature at 0.01 T in different directions (b) Magnetization vs temperature at 0.05 T, 0.1 T, and 1 T for $H \parallel [100]$. (Figure adapted from our published work Ref. 119).

A large magnetocrystalline anisotropy is expected in $\text{Mn}_{1.4}\text{PtSn}$ because of the tetragonal superstructure and the involvement of heavy elements Pt and Sn. Figure 4.16(a) shows the magnetization versus temperature measurements in an applied external field of 0.01 T for two crystallographic axes, namely [100] and [001], in zero field cooled (ZFC) and field cooled (FC) conditions. A transition from paramagnetic to ferromagnetic transition observed at 392 K. On decreasing the temperature further, the sharp increase in the magnetic moment, around 170 K, is observed. This is attributed to a spin-reorientation transition (T_{SR}). The absence of any hysteresis in magnetization under warming and cooling conditions rules out the structural origin of this transition. To check the dependency of these transitions on the magnetic field, magnetic measurements in various higher applied fields along [100] are measured (Figure 4.16(b)). T_{C} and T_{SR} are almost unaffected with the

applied magnetic field. For 0.05 and 0.1 T, the moment values for $T < T_{\text{SR}}$ is higher than for $T > T_{\text{SR}}$.

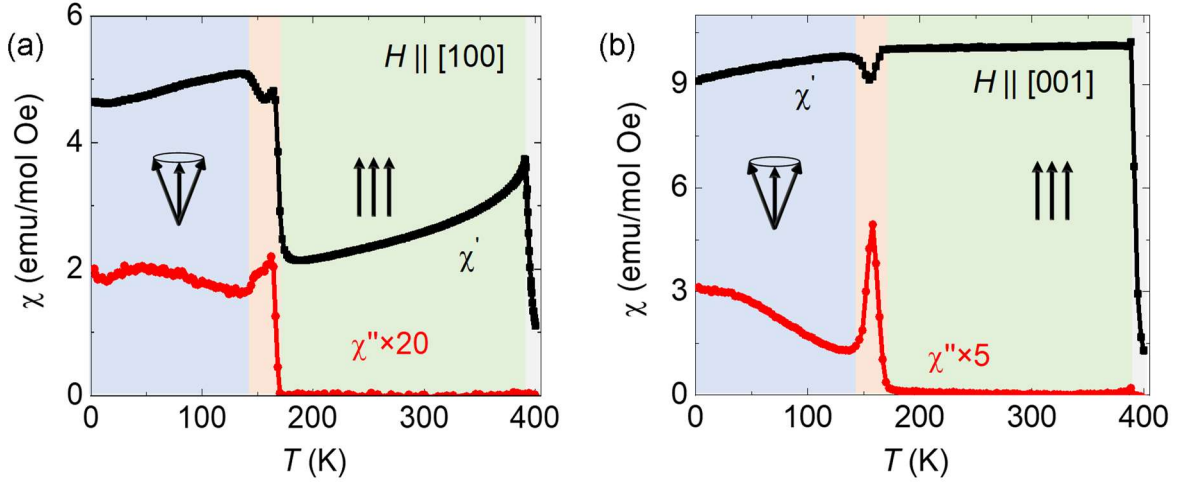


Figure 4.17. Real (black) and imaginary (red) part of AC susceptibility measured along (a) [100] and (b) [001]. The shaded regions visualize the magnetic structure, blue for non-coplanar, green for ferromagnetic, and the orange for a mixed state. (Figure adapted from our published work Ref. 120).

Figures 4.17(a) and (b) show both real (χ') and imaginary (χ'') parts of the AC susceptibility as a function of temperature for the directions $H \parallel [100]$ and $H \parallel [001]$, respectively. It clearly shows that there are two sharp changes in χ' at 392 K and 170 K independent of the direction. The peak at higher temperatures corresponds to the transition from a paramagnetic to a collinear ferromagnetic state while the lower regime corresponds to the spin-reorientation transition temperature (T_{SR}). Below T_{SR} , the spins get canted and stabilize themselves in a non-coplanar structure. A dip in the χ' is also observed in the vicinity of T_{SR} extending from 170 K to 135 K. This dip corresponds to a magnetic structure evolution from a collinear ferromagnet to a non-coplanar spin structure i.e. an intermediate region and the magnetic structure has smaller canting angle than that of low temperatures as revealed by neutron measurements (discussed later in this chapter). For $H \parallel [001]$, the value of χ' remains almost constant, indicating the magnetization along c -direction does not change below and above T_{SR} . For both the field directions, the imaginary part of the susceptibility (χ'') also displays spin reorientation transition. For the $H \parallel [100]$, there is a steep increase in the value of χ' , while going from above T_{SR} to below T_{SR} . This is evidence of the evolution of an in-plane magnetic moment below T_{SR} . Above the T_{SR} , the moment in the ab -plane is very small and it suddenly develops in the ab -plane as the temperature is reduced below T_{SR} .

Figure 4.18(a) and (b) show the isothermal magnetization at 2 K, 170 K, and 300 K for the $H \parallel [100]$ and $H \parallel [001]$, respectively. The saturation moment is found to be 4.7 μ_{B} /f.u. at 2 K for both the directions. For $H \parallel [100]$, the moment varies non-linearly with the applied magnetic field below the saturation, indicating the non-coplanar magnetic

structure. In the region of collinear magnetic order, the moment varies linearly with the magnetic field. The easy axis of the magnetization is [001] in both the magnetic regions.

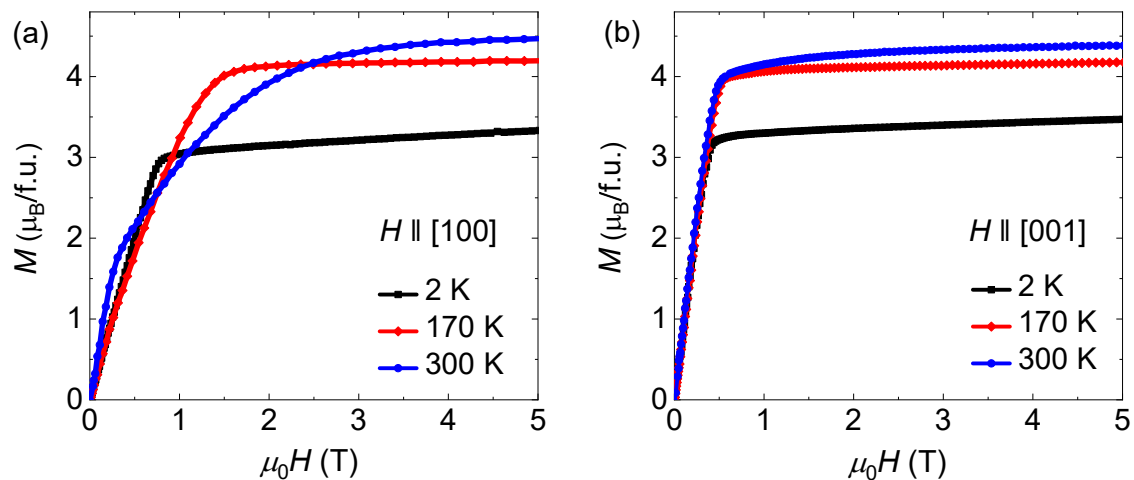


Figure 4.18. The isothermal magnetization curve for temperatures 2 K (black), 170 K (red) and 300 K (blue) for field along (a) [100] and (b) [001]. (Figure adapted from our published work Ref. 120).

Due to the tetragonal structure of the compound, the application of the external field may display anisotropic properties along the different crystal axes. Isothermal magnetization measurements performed on single crystals of $\text{Mn}_{1.4}\text{PtSn}$ confirm that the easy axis is c -axis for both below and above T_{SR} while a -axis is the hard axis. Isothermal magnetization at 2 K and 300 K for both the directions are compared in Figures 4.19(a) and (b). At 2 K (well below T_{SR}), the magnetization along [001] saturates at 0.3 T, and the saturation magnetization is $4.7 \mu_{\text{B}}/\text{f.u.}$, while along [100], the saturation is rather slow and is achieved at 3 T. Thus, below T_{SR} , the easy axis is [001]. The negligible coercivity shows that the compound is a soft magnet. At 300 K, which is above T_{SR} , [001] is still the easy axis, as shown in Figure 4.19(b). Unlike at 2 K, the magnetization at 300 K along both [001] and [100] varies rather linearly with the magnetic field.

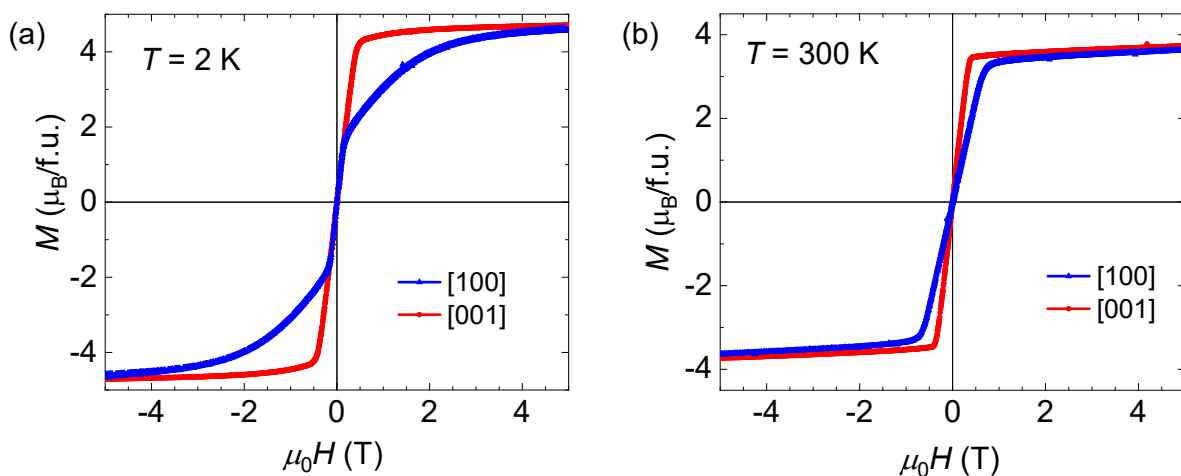


Figure 4.19. Isothermal magnetization at (b) 2 K and (c) 300 K for $H \parallel [100]$ (blue curve) and $H \parallel [001]$ (red curve). (Figure adapted from our published work Ref. 119).

4.4. Electrical transport properties

Resistivity measurements:

All transport measurements were carried out in a commercial physical properties measurement system (PPMS, Quantum Design) for a field up to 9 T in the temperature range of 2 to 300 K. A crystal was cut in a rectangular bar with edges corresponding to [100], [010] and [001]. The dimension of the sample was $0.25 \times 1 \times 0.35 \text{ mm}^3$.

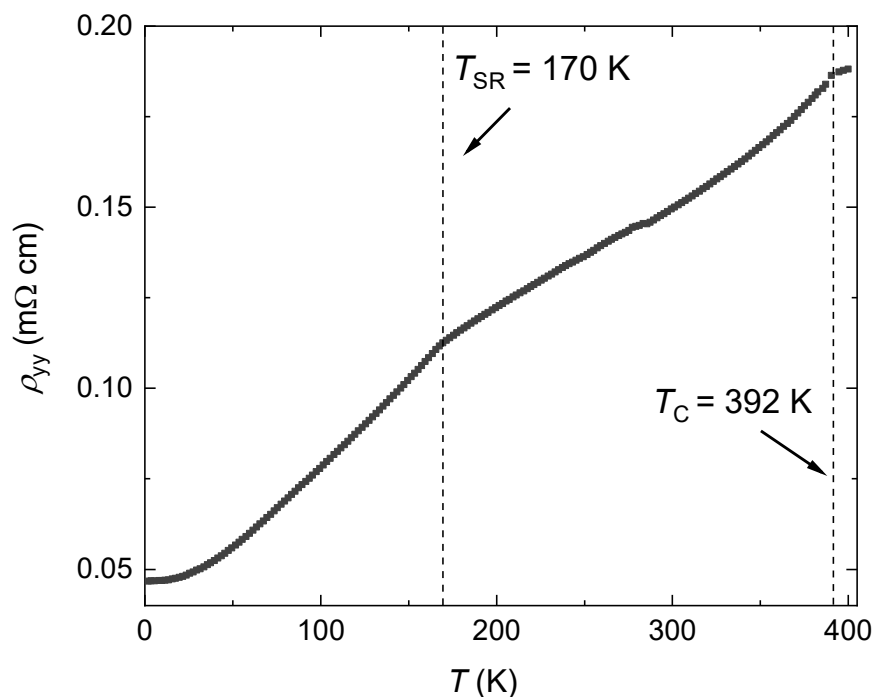


Figure 4.20. The longitudinal resistivity as a function of temperature for applied current along [010] between 2 K to 400 K. (Figure adapted from our published work Ref. 119).

Four-probe transport measurements were performed in two configurations $H \parallel [100]$; $I \parallel [010]$ and $H \parallel [001]$; $I \parallel [010]$, where applied current and frequency were 2 mA and 93 Hz, respectively, in ACT option. The Hall resistivity and magnetoresistance (MR) are performed in four-probe geometry. These contacts were made by silver paint with 25 μm diameter Pt wire.

The longitudinal resistivity with the current along [010] of $\text{Mn}_{1.4}\text{PtSn}$ as a function of temperature is shown in Figure 4.20. The resistivity decreases with decreasing the temperature, which indicates that the compound is metallic in nature. The slope changes twice at 392 K and 170 K in the resistivity, corresponding to the paramagnetic to ferromagnetic and T_{SR} transitions, respectively, which are consistent with magnetic measurements. The values of resistivity at 300 K and 2 K are 0.15 mΩ cm and 0.046 mΩ cm, respectively, giving a residual resistivity ratio of 3.3 ($RRR = R_{300\text{K}}/R_{2\text{K}}$).

Hall resistivity and magnetoresistance:

Figure 4.21(a) and (b) show the measured Hall resistivity for the configurations $H \parallel [100]$; $I \parallel [010]$ and $H \parallel [001]$; $I \parallel [010]$, respectively. In Figure 4.21(a) the Hall resistivity as a function of the magnetic field is plotted for temperatures 2 K, 170 K and 300 K. For the temperatures below T_{SR} (2 K and 170 K), there is an extra contribution to the normal Hall effect (NHE) and anomalous Hall effect (AHE) which cannot be attributed to the magnetization. This extra contribution in the Hall resistivity is a clear indication of the topological Hall effect (THE) in this compound. In the measured Hall resistivity above T_{SR} (300 K), there is no such observation of additional contribution to the NHE and AHE. The Hall resistivity for another configuration $H \parallel [001]$; $I \parallel [010]$ is shown in Figure 4.21(b). At 2 K, the Hall resistivity shows a nonlinear behavior, even after the saturation field associated with magnetization saturation. This is an indication that an extra contribution to NHE and AHE is present. It means that THE is also present at low temperatures in this configuration. For 300 K (temperature above T_{SR}), Hall resistivity follows magnetization and no additional contribution is observed.

The magnetoresistance (MR) is calculated using the formula,

$$MR (\%) = \frac{\rho(H) - \rho(0)}{\rho(0)} \times 100 \quad 4.1$$

where, $\rho(H)$ and $\rho(0)$ are the resistivities at applied field H and zero field, respectively.

In Figures 4.21(c) and (d), MR at temperatures 2 K, 170 K and 300 K for the configurations $H \parallel [100]$; $I \parallel [010]$ and $H \parallel [001]$; $I \parallel [010]$, respectively are shown. Below the T_{SR} , a negative MR of 3% is observed for both directions. There are several ups and downs in the MR observed at 170 K. These features are prominent for the temperature range of 130–170 K. This temperature range lies in the vicinity of T_{SR} . For the configuration $H \parallel [100]$ and above T_{SR} , the MR increases parabolically up to the saturation field, required for the formation of the single magnetic domain. After reaching the saturation field, MR is found to be negative. The increase in MR below saturation field can be understood as a continuous rotation of magnetic moment with the magnetic field, causing more electron-magnon scattering.

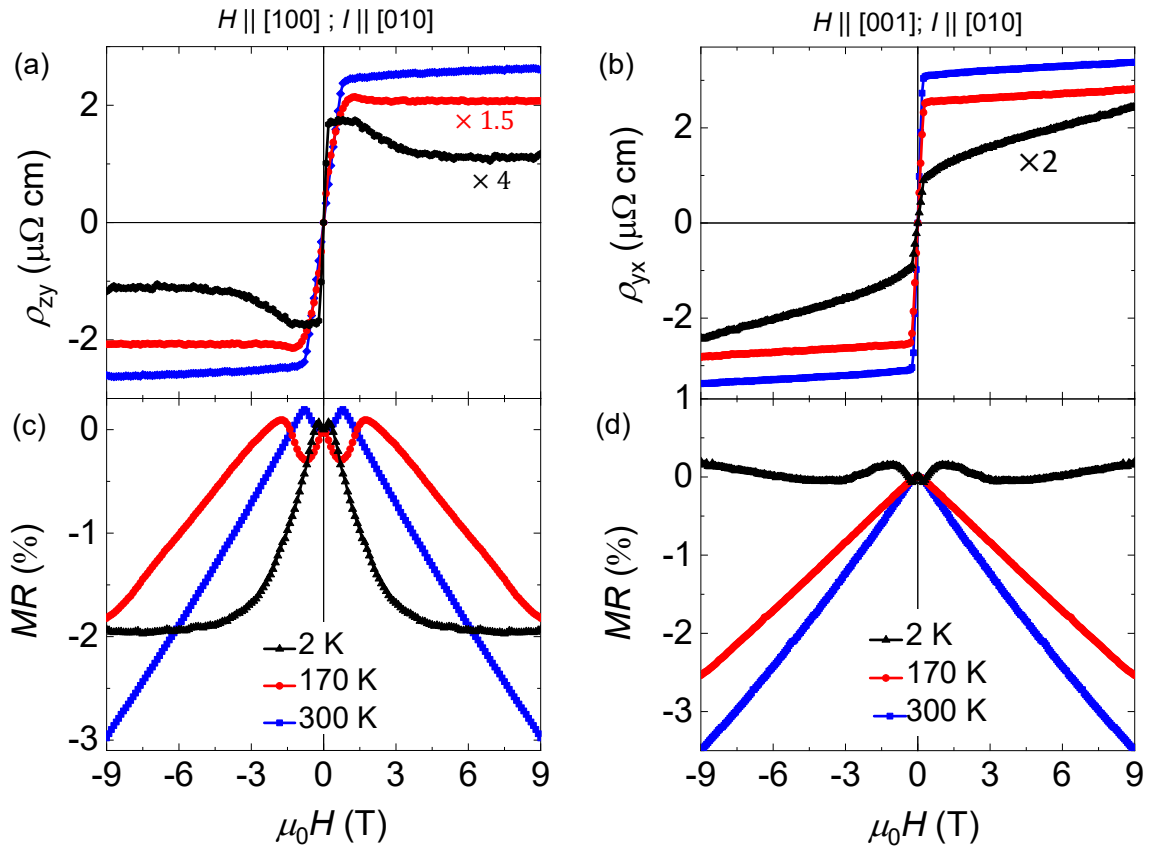


Figure 4.21. (a) and (b) The measured Hall resistivity, (c) and (d) the measured magnetoresistance at temperatures 2 K (black), 170 K (red), and 300 K (blue). (Figure adapted from our published work Ref. 120).

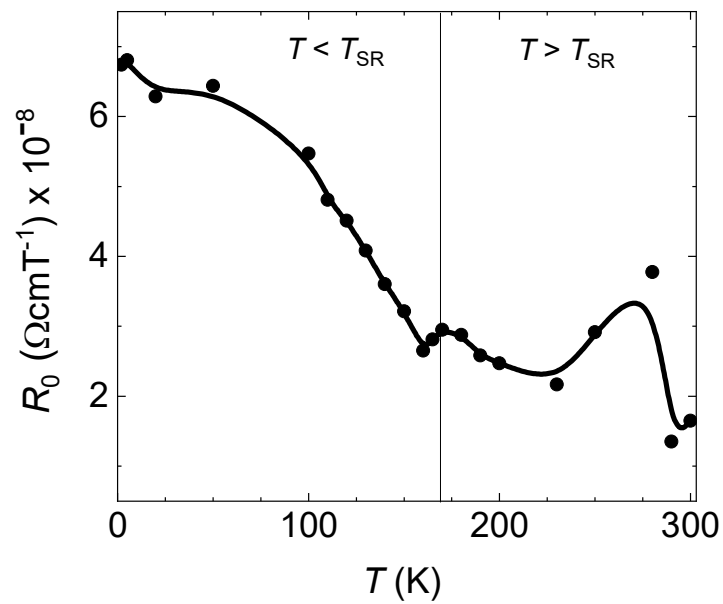


Figure 4.22. The normal Hall coefficient as a function of temperature for $H \parallel [001]$. (Figure adapted from our published work Ref. 120).

To calculate the charge carrier concentration, Drude model¹²³ with a single charge carrier was applied. According to this model, a charge carrier is related as follows,

$$n = \frac{1}{R_0 \cdot e} \quad 4.2$$

where, n is charge carrier concentration, R_0 is the normal Hall coefficient and e is the charge of an electron. According to the convention, the positive and negative values of R_0 determines the majority charge carriers as holes and electrons, respectively. R_0 was calculated from linear fitting the ρ_{yx} vs H curves of magnetic field range of 5 to 9 T. The lower magnetic field region was avoided for calculation of R_0 because there might be still some contributions from magnetization in case of a non-coplanar spin structure that contributes an error to R_0 . Figure 4.22 shows the variation of extracted R_0 with temperature for $H \parallel [100]$. The sign of R_0 is positive which indicates that the dominating charge carriers are holes.

Topological Hall effect:

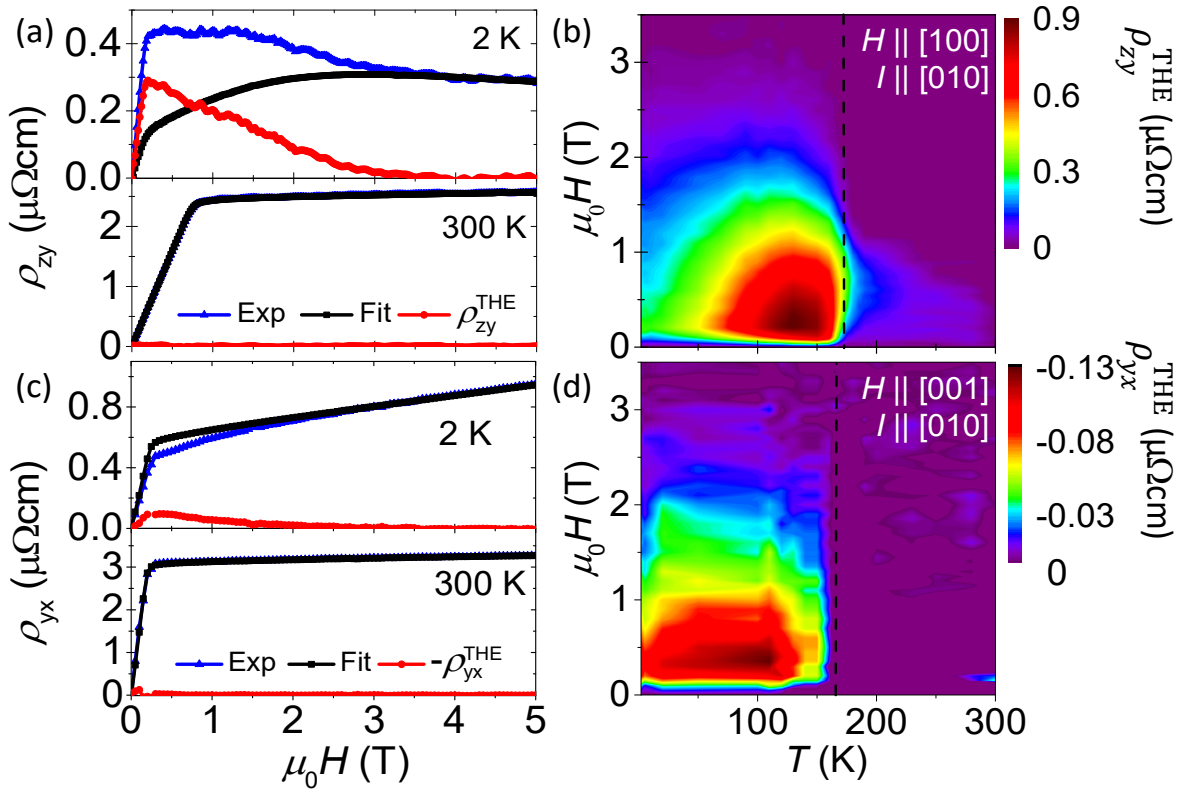


Figure 4.23. (a) and (c) The measured Hall resistivity (blue), the high field extrapolated AHE+NHE (black) and the subtraction of these two quantities resulting in THE (red) for temperature 2 and 300 K in the top and bottom panels, respectively. (b) and (d) contour plots of THE for temperature vs field. (Figure adapted from our published work Ref. 120).

THE can be obtained from the measured Hall resistivity after subtraction of NHE and AHE components. The upper and lower panels of Figure 4.23(a) show the measured Hall resistivity (blue curve), calculated NHE + AHE (black curve) and obtained THE (red curve) as a function of the magnetic field for temperatures of 2 K and 300 K, respectively for the configuration $H \parallel [100]$; $I \parallel [010]$. The similar data are shown in Figure 4.23(c) for the configuration $H \parallel [001]$; $I \parallel [010]$. A non-zero THE with the opposite sign exists below T_{SR} while it vanishes above T_{SR} for both the configurations. The contour plots of THE are shown in Figure 4.23(b) and (d) for all the temperatures. THE for both the directions exists only below T_{SR} that gives strong evidence that its origin is a non-coplanar spin structure. However, the value of THE differs by an order of magnitude between the directions.

Analysis of AHE and THE:

Figure 4.24 shows the analysis of AHE and THE in terms of the longitudinal resistivity (ρ_{yy}) for $H \parallel [100]$ and $H \parallel [001]$. Figures 4.24(a) and (c) show the experimentally measured anomalous Hall resistivity (black squares). Additionally, Figures 4.24(b) and (c) show the experimentally measured maximum value of the THE (red circles). As discussed

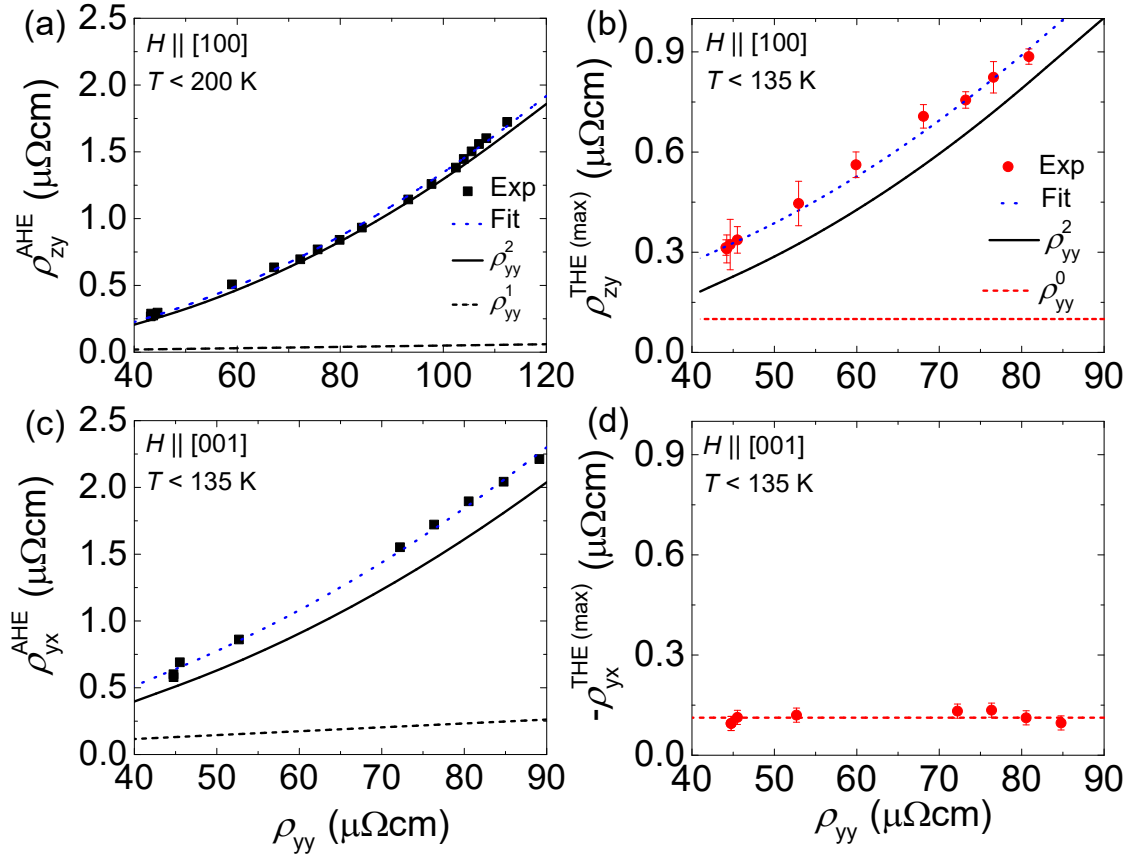


Figure 4.24. (a) and (c) The anomalous Hall resistivity as a function of the longitudinal resistivity, ρ_{yy} (black squares). The fitting in terms of (dashed black) ρ_{yy}^1 and ρ_{yy}^2 (solid black), and the summation (dashed blue). (b) and (d) The topological Hall resistivity as a function of the (red circles). The fitting in terms of (dashed red) ρ_{yy}^0 and ρ_{yy}^2 (solid red), and the summation (dashed blue). (Figure adapted from our published work Ref. 120).

at the beginning of section 2.3, a power-law fitting (Equation 2.2) is used to analyze the dominant contributions to the AHE. For both directions of the external field, a strong contribution from intrinsic-like mechanisms is seen that follows the square of the longitudinal resistivity. There is also anisotropic behavior with the field direction, which suggests an increase in the scattering mechanism that is linear in the longitudinal resistivity for the $H \parallel [001]$. The THE is also highly anisotropic and shows different mechanisms depending on the field direction. For $H \parallel [100]$, the THE shows mainly two contributions, one that follows the square of the longitudinal resistivity. Additionally, a component that is independent of the longitudinal resistivity. For $H \parallel [001]$, the THE shows no dependency on the longitudinal resistivity. Such a combination of the resistivity-independent and square of the resistivity-dependent of THE in a single material has not been seen before. Furthermore, the conclusion of our analysis can be clearly observed in the direct measurement. In the region of the spin reorientation transition, the THE scales linearly with the ρ_{yy} . This can be attributed to a skew scattering contribution analog in the AHE¹²⁴. In Figure 4.25, the analysis of the maximum value of THE in the temperature range of 135–170 K is shown. The overall variation of THE shows very good agreement with a fitted linear variation of longitudinal resistivity (ρ_{yy}). This is the indication that in this temperature range, skew scattering is the main contribution. Above T_{SR} (= 170 K), the value of THE is negligible.

The anomalous Hall conductivity (σ_{xy}^{AHE}) is extracted from the total conductivity, which is further estimated from measured ρ_{yx} and ρ_{xx} by using the formula,

$$\sigma_{xy}^{\text{AHE}} = \frac{\rho_{yx}^{\text{AHE}}}{\rho_{yx}^2 + \rho_{xx}^2} \quad 4.3$$

In Figures 4.26(a) and (b), the calculated anomalous Hall conductivity (σ_{xy}^{AHE} , black square) vs temperature for both $H \parallel [100]$ and $H \parallel [001]$, respectively. σ^{AHE} was calculated by extrapolating Hall conductivity data of 4 to 9 T to zero field. Figure 4.26(a) shows that for $H \parallel [100]$ configuration, σ^{AHE} has the highest value of $165 \Omega^{-1}\text{cm}^{-1}$ at 5 K and with increasing temperature, σ^{AHE} remains almost constant. In Figure 4.26(b), σ^{AHE} is shown for $H \parallel [100]$. σ^{AHE} remains almost constant of $250 \Omega^{-1}\text{cm}^{-1}$ up to T_{SR} then decreases continuously. Here, it is clearly seen that the Berry curvature is anisotropic in momentum space, as is expected for a tetragonal magnetic system.

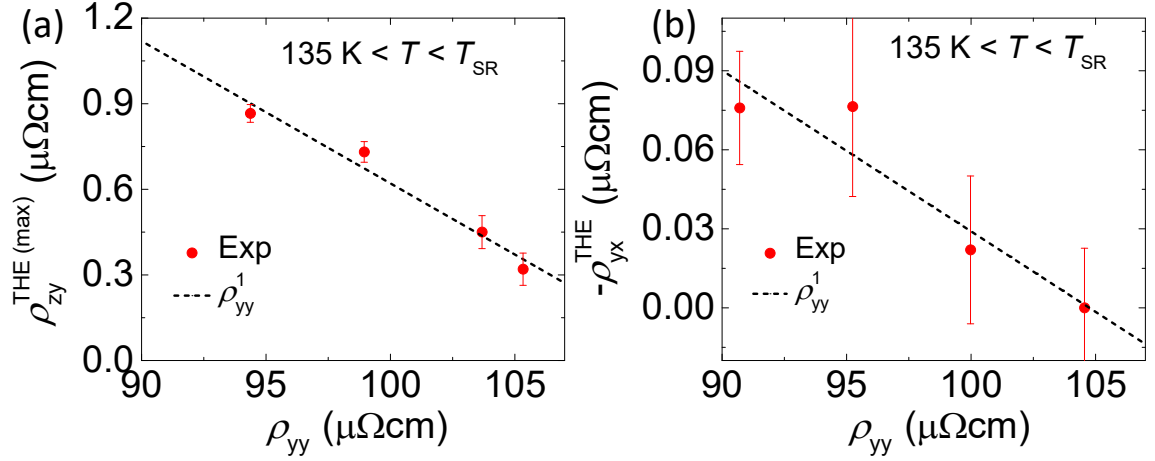


Figure 4.25. The fitting of THE in the temperature range of 135 K - 170 K for the configurations (a) $H \parallel [100]$ and (b) $H \parallel [001]$. (Figure adapted from our published work Ref. 120).

The topological Hall conductivity (σ^{THE}) can analogously be extracted using the same method (Equation 4.3) as anomalous Hall conductivity. In Figures 4.26(a) and (b), the temperature-dependent σ^{THE} (red curve) is shown for both $H \parallel [100]$ and $H \parallel [001]$. It is found that the σ^{THE} is of the same order of σ^{AHE} for $H \parallel [100]$ and indicates the main contribution is intrinsic for temperatures below T_{SR} . In contrast, σ^{THE} for $H \parallel [001]$ is strongly dependent on temperature and linearly decreases to zero at the T_{SR} .

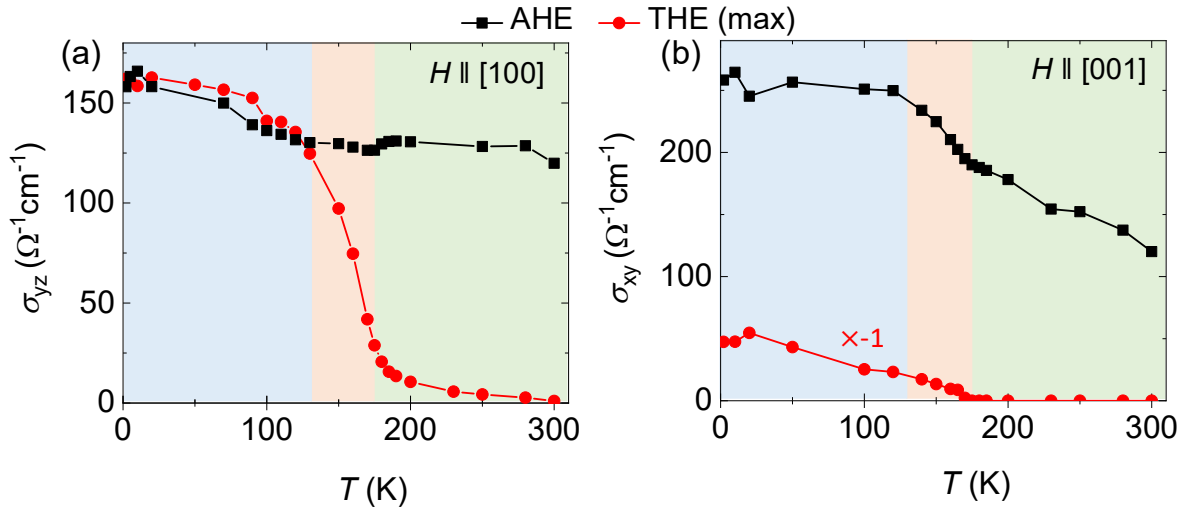


Figure 4.26. Anomalous and topological Hall conductivity for collinear (green) and non-coplanar (light blue, orange) magnetic regions for configurations (a) $H \parallel [100]$ and (b) $H \parallel [001]$. (Figure adapted from our published work Ref. 120).

4.5. Powder neutron diffraction

For the refinement procedure, the previously determined crystal structure parameters are used, namely, the space group $I\bar{4}2d$ and the following Wyckoff positions for the magnetic atoms: $4a$ (Mn1) with the x , y and z parameters (0, 1/2, 1/4) and $8d$ (Mn2) with (x , 1/4, 1/8); for the nonmagnetic atoms: $8c$ (Pt) with (0, 1/2, z) and $8d$ (Sn) with (x , 1/4, 1/8). The symmetry analysis of the magnetic structure was conducted by the BASIREPS tool included in the FullProf suite. The latter allows for the Mn2 site with two 1-dim irreducible representations (IRs) $\Gamma 1$ and $\Gamma 2$ contained one time, two 1-dim IRs $\Gamma 3$ and $\Gamma 4$ contained two times, and one 2-dim IRs $\Gamma 5$ contained three times. The decomposition of the magnetic representation for the Mn1 site yields two 1-dim IRs $\Gamma 1$ and $\Gamma 3$ contained one time and one 2-dim IRs $\Gamma 5$ contained two times. All the possible combinations of the IRs for Mn1 and Mn2 sites are tested and it is concluded that only the combination of $\Gamma 3$ (Mn1) and $\Gamma 3$ (Mn2) gives a satisfactory agreement with the experimentally observed magnetic structure above the T_{SR} . The corresponding model contains three free parameters that represent the M_z component on the Mn1 site — $M_z(\text{Mn1})$, alternating in-plane components M_x and M_y on the Mn2 site (in y , $-y$, $-x$, x sequence) — $M_{xy}(\text{Mn2})$, and M_z component on the Mn2 site — $M_z(\text{Mn2})$. The parameter $M_{xy}(\text{Mn2})$ was assumed to be zero, which in essence will result in a collinear ferromagnetic or a ferrimagnetic structure. As follows from our analysis, there exists no single-IR model that can describe the magnetic structure below the T_{SR} . Therefore, the models that include a superposition of two IRs on each Mn-sublattice were considered. Among those models, the combination of $\Gamma 3 + \Gamma 5$ (Mn1) and $\Gamma 3 + \Gamma 5$ (Mn2) was found to give the best agreement with the collected diffraction pattern. The model comprises a set of 13 parameters, of which only 6 parameters are assumed to have finite values and 2 parameters are constrained to the equal values and opposite signs. This restricts the model to the set of 5 effective parameters: $M_z(\text{Mn1})$, $M_x(\text{Mn1})$, $M_z(\text{Mn2})$, $M_x(\text{Mn2})$, and alternating $M_y(\text{Mn1})$ (in y , $-y$ sequence). The proposed model describes a noncollinear coplanar magnetic structure if the $M_y(\text{Mn1})$ is set to zero (referred hereafter as the Model 2) and a non-coplanar structure in the opposite case (referred hereafter as the Model 1).

Figures 4.27(a) and (b) show the experimental patterns observed at the base temperature of 1.5 K, which is plotted together with the results of the refinement using the magnetic model discussed above. The key signature of the noncollinear arrangement of the magnetic moments is the emerging intensity in the (004) Bragg peak, which is forbidden if all the magnetic moments in the unit cell strictly point along the crystallographic [001] direction. Furthermore, the presence of the (002) reflection would highlight the non-coplanar component of the magnetic structure. However, as discussed below, the non-coplanar component might result in only a very weak reflection that may remain undetectable on top of the background signal, when the exposition time of the diffraction pattern is limited. Figure 4.27(a) demonstrates an agreement between the data and Model 1 (non-coplanar structure) with the refined parameters: $M_z(\text{Mn2}) = (0.3 \pm 0.3) \mu_B$, $M_x(\text{Mn2}) = (2.6 \pm 0.2) \mu_B$, $M_z(\text{Mn1}) = (2.8 \pm 0.2) \mu_B$, $M_x(\text{Mn1}) = (-1 \pm 0.4) \mu_B$, and $M_y(\text{Mn1})$

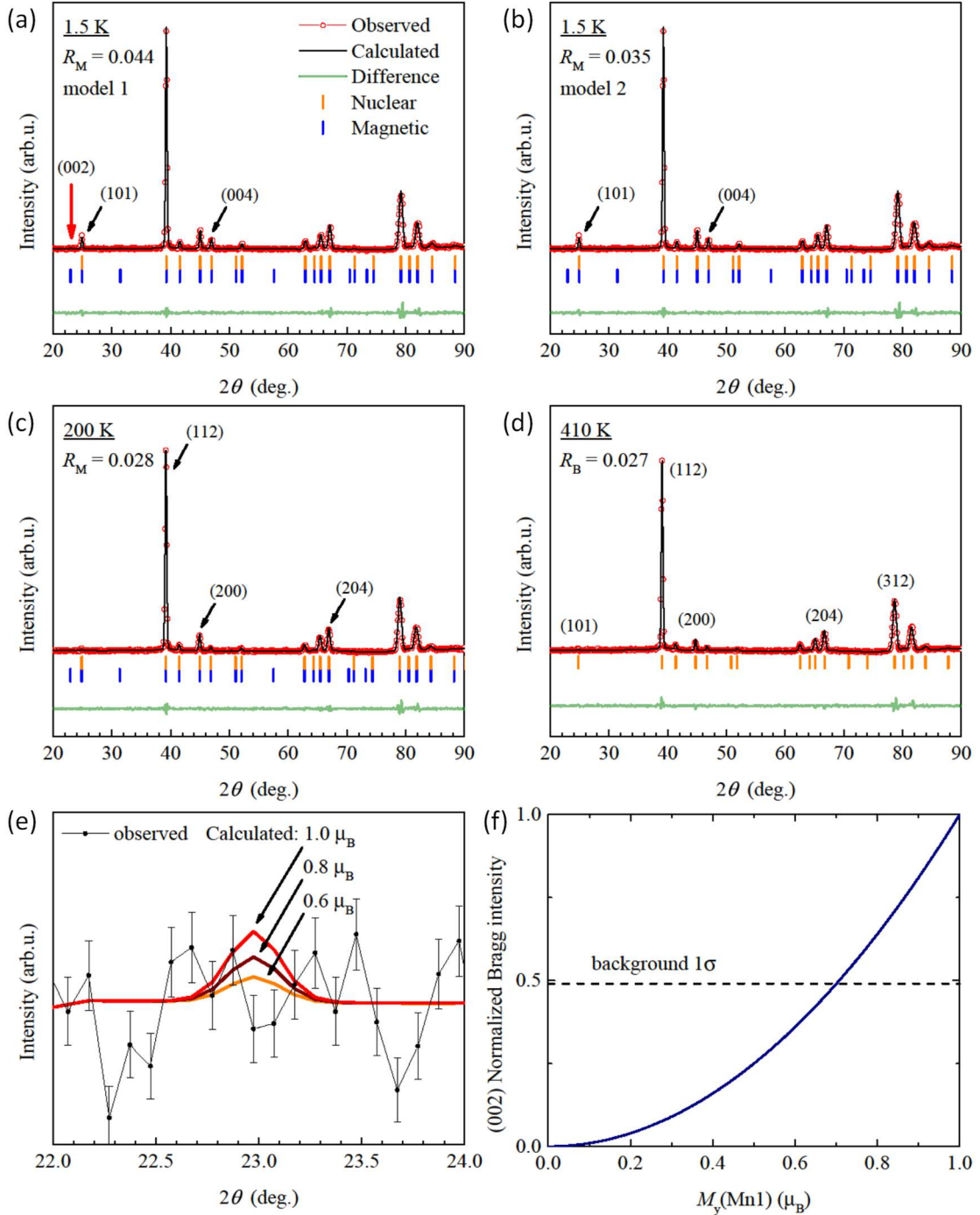


Figure 4.27. Results of the Rietveld refinement of the powder neutron diffraction data. (a) The model with the non-coplanar spin arrangement (model 1) in application to the data collected at $T = 1.5$ K. (b) The model with the coplanar magnetic structure (model 2) used to refine the same pattern. (c) The collinear spin structure at $T = 200$ K. (d) The pattern collected in the paramagnetic state at $T = 410$ K where only nuclear scattering is observed. The black solid lines represent the model fit, red opened circles are experimental data, green solid lines show the residue; vertical bars correspondingly mark the nuclear and magnetic Bragg reflections. (e) The calculated intensity of the magnetic (002) Bragg peak assuming different magnitudes of the non-coplanar component of the magnetic moment at the Mn1 site. (f) The intensity of the calculated (002) reflection as a function of the $M_y(\text{Mn1})$; the dashed line depicts the estimated error bars of the background present in the collected data. (Figure adapted from our published work Ref. 120).

$= 1 \mu_B$ (fixed). The refinement of the alternative model (Model 2) is shown in Figure 4.27(b). The Model 2, which is the coplanar noncollinear structure, converges to $M_z(\text{Mn2}) = (0.3 \pm 0.3) \mu_B$, $M_x(\text{Mn2}) = (2.6 \pm 0.2) \mu_B$, $M_z(\text{Mn1}) = (2.8 \pm 0.2) \mu_B$, $M_x(\text{Mn1}) = (-1.1 \pm 0.4) \mu_B$, and $M_y(\text{Mn1}) = 0 \mu_B$ (fixed). As can be seen, the two models give very similar results with the agreement factors (magnetic R-factors) $R_M = 0.044$ (Model 1) and $R_M = 0.035$ (Model 2).

The magnetic structure at $T = 200 \text{ K}$ (Figure 4.27(c)) was determined as the collinear ferromagnetic structure with the components of the magnetic moments $M_z(\text{Mn2}) = (2.5 \pm 0.1) \mu_B$ and $M_z(\text{Mn1}) = (1.1 \pm 0.2) \mu_B$. In this case, the magnetic contribution to the total scattering is mainly observed by the additional intensity in the (112), (200), and (204) Bragg peaks. Figure 4.27(d) shows the example of the diffraction pattern where only a nuclear contribution is present, i.e. above T_C . The refinement of the crystal structure at $T = 410 \text{ K}$ shows the Bragg R-factors $R_B = 0.027$. The agreement factors presented are defined as $R = \sum |I_{\text{obs}} - I_{\text{calc}}| / \sum |I_{\text{obs}}|$, where I_{obs} and I_{calc} correspond to observed and calculated intensity for the crystal and the magnetic structures, respectively in R_B or R_M . In order to quantify the potentially undetected (002) magnetic Bragg peak, its calculated intensity for different assumed values of $M_y(\text{Mn1})$ component is plotted in Figure 4.27(e). As can be seen, the non-coplanar magnetic component $M_y(\text{Mn1})$ smaller than $1 \mu_B$ predicts the Bragg intensity that is comparable with the background noise. To quantify the assumed component in a strict fashion (see Figure 4.27(f)), the normalized intensity of the (002) Bragg peak as a function of the $M_y(\text{Mn1})$ together with one standard deviation of the background intensity is plotted. Thus, the assumed value in Model 1 for $M_y(\text{Mn1}) = 1 \mu_B$ corresponds approximately to the background uncertainty ($\pm 1\sigma$). The magnetic structures for temperatures above and below T_{SR} , obtained from refinement of powder neutron diffraction, are shown in Figure 4.28.

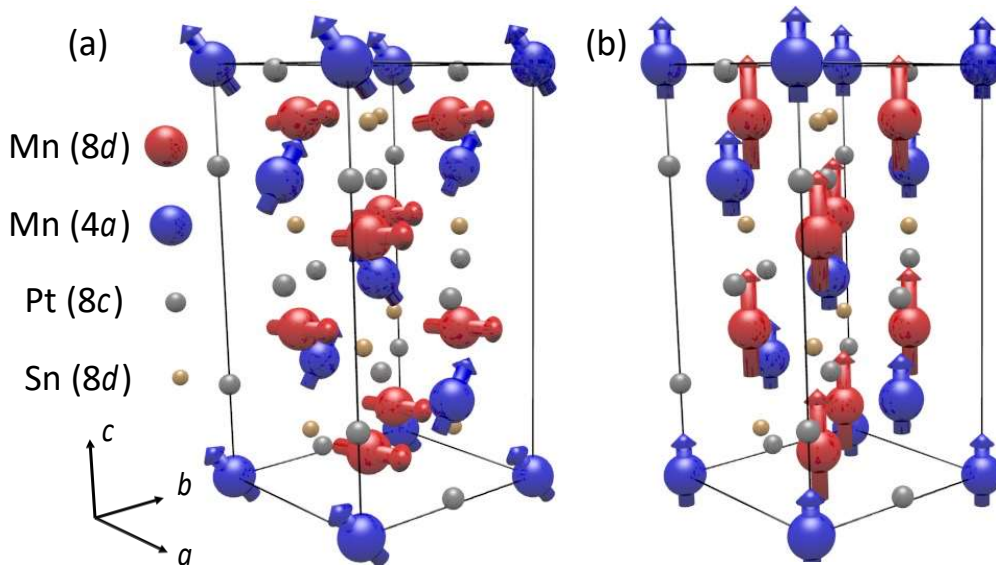


Figure 4.28. The magnetic structure for (a) $T < T_{SR}$ and (b) $T > T_{SR}$. (Figure adapted from our published work Ref. 120)

4.6. Theory

The magnetic ground state was calculated by first-principles calculations using the augmented spherical waves method^{125,126} in the superstructure of Mn_{1.5}PtSn. It is found that the relaxed non-coplanar spin structure has lower energy than the ferrimagnetic and ferromagnetic solution. The magnetic anisotropy between the *ab*-plane and the *c*-axis favors the *c*-axis by 4 meV/u.c. The weak anisotropy allows for the non-coplanar order. In the non-coplanar spin structure, the Mn ions at the *8d* Wyckoff position align collinearly in the *ab*-plane where the Mn atoms at the *4a* position order antiferromagnetically with an angle of $\sim 14^\circ$. Furthermore, a Wannier interpolated Hamiltonian of the collinear ferromagnet and the rigid band approximation is used to calculate the momentum space Berry curvature for the AHE in Mn_{1.4}PtSn, where the conductivity of 155 and 232 $\Omega^{-1}\text{cm}^{-1}$ for the magnetization along the *a*-axis and the *c*-axis, respectively is obtained. Using the method in Franz *et al.*⁸⁶, a topological Hall constant of -1.5 and $0.5 \times 10^{-8} \Omega\text{cmT}^{-1}$ for the field along the *a*-axis and the *c*-axis, respectively, is obtained. These calculations support the anisotropic behavior of the THE and AHE that are intrinsic due to the electronic structure.

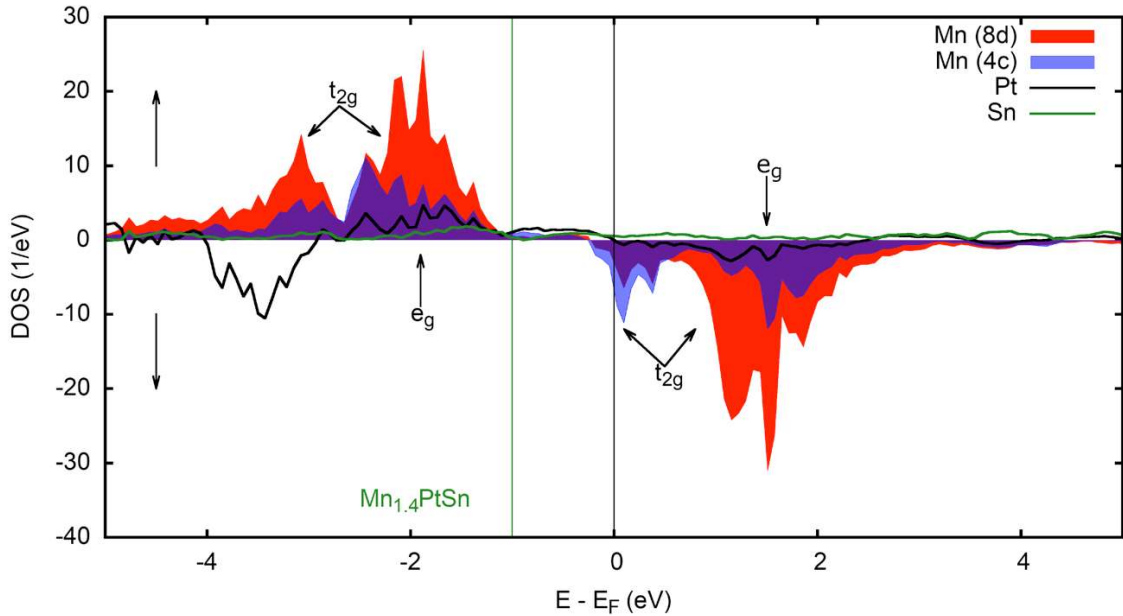


Figure 4.29. DFT calculation of the ferromagnetic projected density of states (DOS) in Mn_{1.4}PtSn. The red curve shows that of the Mn at the *8d* Wyckoff position and the blue of the Mn at the *4c* Wyckoff position. The black and green curves show the projected density of states for that of Pt and Sn. The splitting of the *e_g* and *t_{2g}* states of the Mn atoms are labeled in the graph. (Figure adapted from our published work Ref. 120).

Figure 4.29 shows the projected density of states (DOS) for each atom in Mn_{1.5}PtSn. From the DOS, it can be seen a large exchange splitting on the Mn elements that range from ≈ 2 – 4 eV. Furthermore, the large hybridization of the *e_g* states with the *t_{2g}* states leads

to a source for the DMI from the Mn elements. The DOS of the Pt elements gives the largest source for the DMI and is finite when the DOS is maximized. In Figure 4.29, the rigid band shift of the DOS to $\text{Mn}_{1.4}\text{PtSn}$ is represented as the vertical green line. Lastly, the Sn atoms also is a source for the DMI when the DOS is large at the Fermi energy.

The Fermi level dependence of the AHE in 4.30(a) and the THE in 4.32(b) are presented. The Wannier¹²⁷ interpolated Hamiltonian were extracted for a collinear ferromagnet from VASP¹²⁸, using the GGA pseudopotential¹²⁹. The Wannier functions from the concentration of $\text{Mn}_{1.5}\text{PtSn}$ with 196 valence electrons are taken and the rigid band approximation to calculate the properties at $\text{Mn}_{1.4}\text{PtSn}$ with 190.4 valence electrons is used. In Figure 4.30(a), AHE shows to be very anisotropic for different directions of the magnetization. The AHE with the xy component of the Berry curvature sum (shown in red) shows to vary from 800 to $-400 \text{ } \Omega^{-1}\text{cm}^{-1}$. Where the yz component is comparatively constant between -200 and $-400 \text{ } \Omega^{-1}\text{cm}^{-1}$. Compared to the AHE, the topological Hall constant shows to oscillate rapidly due to the changes in the spin Fermi surface as a function of the Fermi energy. The values are also found to be anisotropic for different directions.

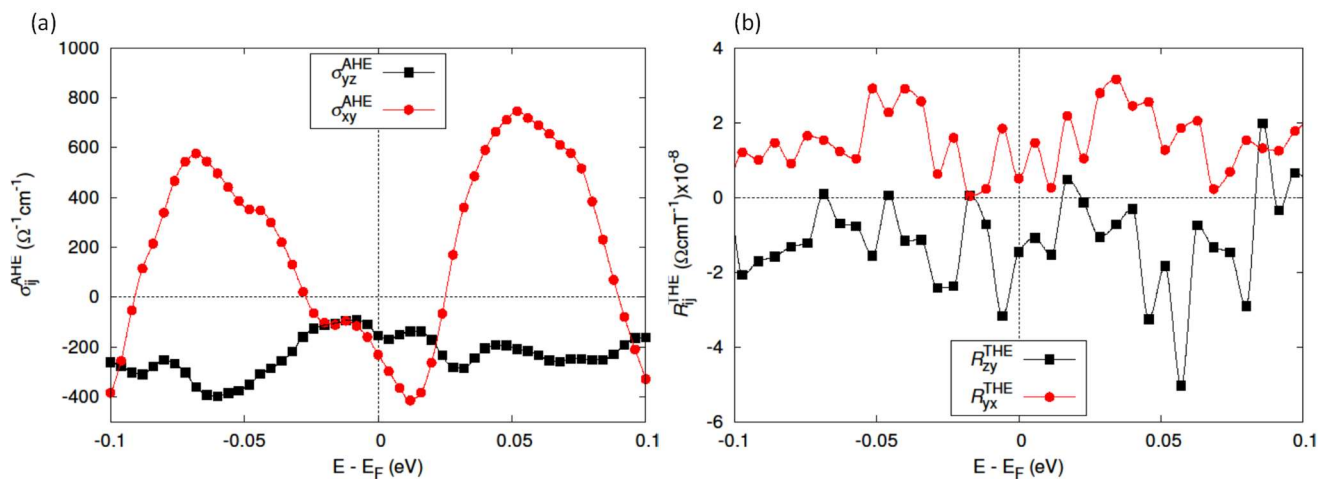


Figure 4.30. DFT calculations of the AHE and the THE. (a) the AHE is shown for the magnetization along the x -direction (σ_{yz}) in black squares and along the z -direction (σ_{xy}) in red dots. (b) the topological Hall constant is shown for the magnetization along the x -direction (R_{zy}^{THE}) in black squares and along the z -direction (R_{yx}^{THE}) in red dots. (Figure adapted from our published work Ref. 120).

5. $\text{Mn}_{1.4}\text{Pt}_{1-x}\text{Ir}_x\text{Sn}$ ($x = 0.1-1$)

As described in chapter 4, $\text{Mn}_{1.4}\text{PtSn}$ crystallizes in tetragonal superstructure with space group $I\bar{4}2d$, possessing D_{2d} symmetry¹¹⁹. The magnetic ordering above room-temperature and observation of antiskyrmion in this material makes it very interesting for application in spintronics devices. However, one of the major drawbacks of this material is having a high magnetic moment $4.7 \mu_B/\text{f.u.}$, resulting in a large stray magnetic field¹²⁰. Additionally, antiskyrmions do not move along a straight-line path due to its topological charge that limits particular device applications, for example, high-density skyrmion racetrack memory devices¹³⁰. Therefore, researchers are looking for materials that have very low or zero net moment and can host (anti)skyrmions, leading to the discovery of antiferromagnetic (anti)skyrmions¹³⁰⁻¹³⁴. Interestingly, $\text{Mn}_{1.4}\text{PtSn}$ belongs to the Heusler family of compounds and it is very well known that the magnetic moment of a Heusler compound can easily be tailored by playing with the number of valence electrons³⁴. Iridium (Ir) with one less electron than platinum (Pt) is a perfect choice of an element to replace Pt in $\text{Mn}_{1.4}\text{PtSn}$ to get a compound with a low magnetic moment. Therefore, a series of compounds of $\text{Mn}_{1.4}\text{Pt}_{1-x}\text{Ir}_x\text{Sn}$ with a systematic change of iridium concentration (in 0.1 steps) were prepared. A comprehensive study was performed on these compounds, which includes structural characterizations, magnetic and electric transport measurements as well as powder neutron diffraction. Several novel and interesting properties are discovered, which are discussed in this chapter.

5.1. Sample preparation

To check whether Ir goes completely in the unit cell and leads to the formation of single-phase, first polycrystalline samples of these compounds were prepared. All polycrystalline samples of $\text{Mn}_{1.4}\text{Pt}_{1-x}\text{Ir}_x\text{Sn}$ ($x = 0.1-1$) were prepared by the arc-melting method in the presence of an argon atmosphere, as described below.

First, high purity elements (Sigma-Aldrich, 99.999 %) Pt, Ir and Sn were taken into stoichiometric ratio without Mn and melted together in the arc melting with 200 A of current. The resulting ingot was melted five times followed by flipping it every time. This step makes sure to get Ir completely dissolved. Also, Sn brings down the melting temperature of the mixture, therefore leads to lesser evaporation of Mn during melting. In the second step, the stoichiometric amount of Mn with an additional 3 mg/g was added in the homogenized melted ingot of Pt, Ir, and Sn from the previous step. Now, all the components were again melted three times followed by flipping the ingot to get a homogenized mixture. After preparation of the polycrystalline sample, it was sealed in a quartz tube with a partial 0.2 bar argon atmosphere inside. The tube was then put in the box furnace and annealed at 1073 K for 7 days then it was quenched in ice-water mixture. The quality of polycrystalline samples was checked with powder XRD. These procedures are applied for each sample compositions.

5.2. Tetragonal superstructure

Figures 5.1 and 5.2 show the experimental powder XRD pattern (red open circle) of $\text{Mn}_{1.4}\text{Pt}_{1-x}\text{Ir}_x\text{Sn}$ ($x = 0.1-1.0$) compounds along with theoretical pattern (black), background (blue) and Bragg positions. Figures 5.1(a), (b), (c), (d) and (e) show individual diffraction patterns for $x = 0.1, 0.2, 0.3, 0.4,$ and $0.5,$ respectively while the corresponding measurements for $x = 0.6, 0.7, 0.8, 0.9$ and 1.0 are shown in Figures 5.2(a), (b), (c), (d), and (e), respectively. For all the compounds, the diffraction patterns reveal a single-phase with no existence of any impurity. A complete Rietveld refinement was done for all the compounds. From refinement, it is found that the crystal structure of all compounds is isotypic as $\text{Mn}_{1.4}\text{PtSn}$ with the space group of $I\bar{4}2d$ and D_{2d} symmetry. A schematic of the change in the crystal structure with Ir-substitution is shown in Figure 5.3. In the crystal structure, Mn atoms occupy $4a$ (Mn1) and $8d$ (Mn2) sites, Sn atoms are present at $8d$ site whereas $8c$ site is shared by both Pt and Ir. The refinement results indicate that the ratio of Pt:Ir at $8c$ site is very close to the nominal ratio in the respective compound. Also, for all the compounds, Mn2 ($8d$) and Sn ($8d$) sites are fully occupied while Mn1 ($4a$) site has occupancy close to 80 percent. The vacancies in the crystal are ordered as it was shown for the pristine compound $\text{Mn}_{1.4}\text{PtSn}$ (see section 4.2), superstructure reflections are observed in the diffraction patterns. This means that all the compounds of this series are tetragonal superstructure of Heusler compounds. In summary, new members, in addition to $\text{Mn}_{1.4}\text{PtSn}$, in the family of the tetragonal Heusler superstructure are discovered.

From refinement, the lattice parameters a ($= b$) and c are extracted and their variation with Ir-concentration (x) is shown in Figures 5.4(a) and (b), respectively. It is found that a initially increases up to $x = 0.3$ then it follows a decreasing trend. Whereas, c initially decreases up to $x = 0.5$ and remains unchanged with further Ir-substitution. The resultant c/a ratio is calculated for each compound (Figure 5.4(c)) and it is found that c/a decreases up to $x = 0.5$ then starts increasing. Since c/a ratio of $\text{Mn}_{1.4}\text{PtSn}$ is 1.94, close to 2, its tetragonal crystal structure can be assumed as a structure composed of two cubic unit cells or pseudo-cubic. As soon as c/a ratio starts decreasing or deviating from 2, the crystal structure of compounds moves away from the pseudo-cubic nature, therefore, the tetragonality of crystal increases. Thus, the compound with the lowest c/a ratio, $\text{Mn}_{1.4}\text{Ir}_{0.5}\text{Pt}_{0.5}\text{Sn}$, has the largest tetragonal distortion and moving on either side of the curve of c/a vs x leads to a reduction of tetragonality. Such variation in the c/a ratio has also been observed with Rh substitution at Pt site and is reported by Kumar *et al.*⁹⁶ The fact that the c/a ratio of $\text{Mn}_{1.4}\text{IrSn}$ is smaller than that of $\text{Mn}_{1.4}\text{PtSn}$, it possesses larger tetragonality. This effect of tetragonality with Ir-substitution is also reflected in magnetic properties and will be discussed later in this chapter. The unit cell volume of all the compounds is found to be decreasing almost linearly with x (Figure 5.4(d)).

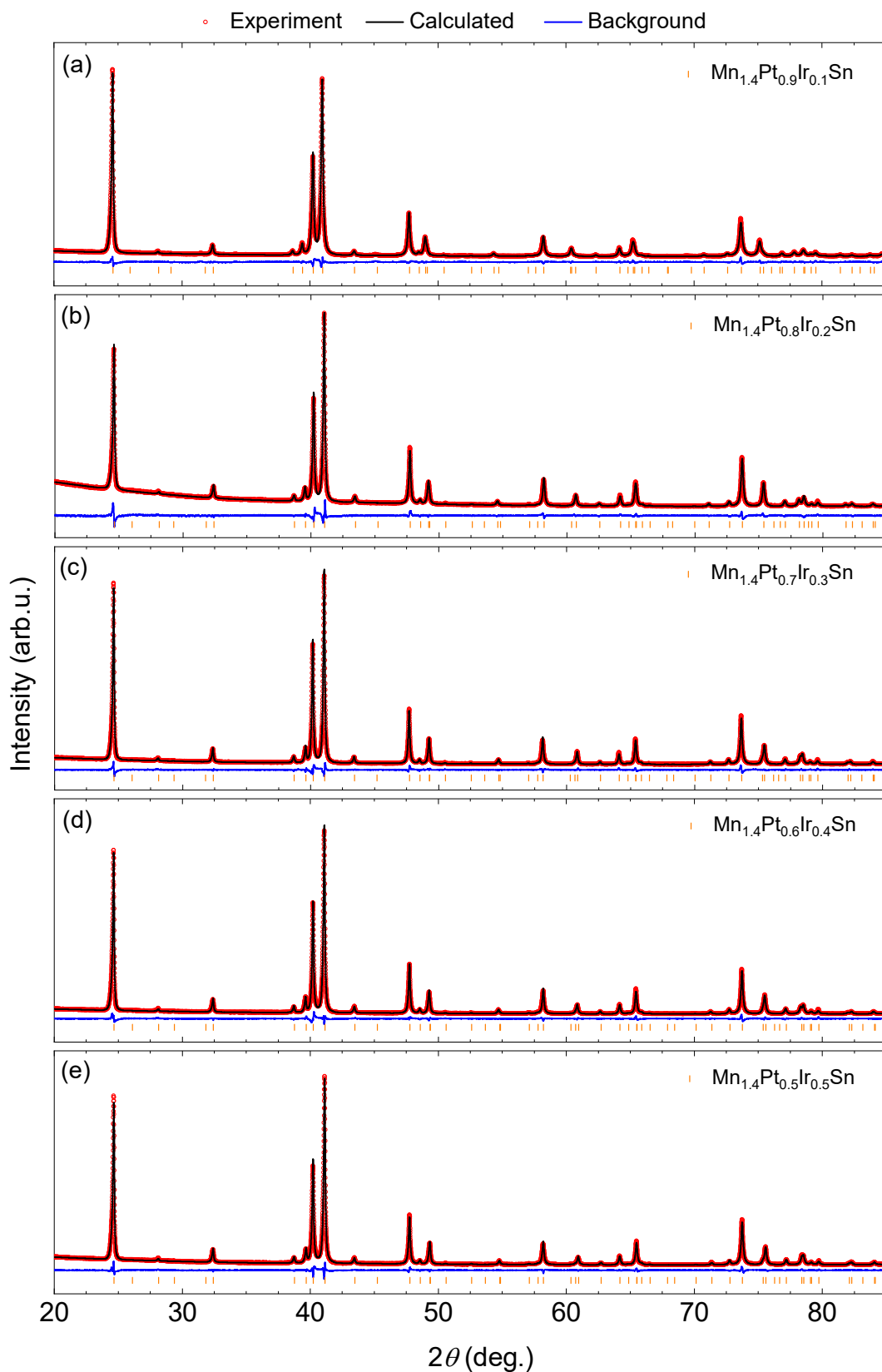


Figure 5.1. The experimental (red open circle), calculated (black) XRD pattern along with background (blue color) and the Bragg positions of compounds (orange) with Ir-substitution $x = 0.1-0.5$.

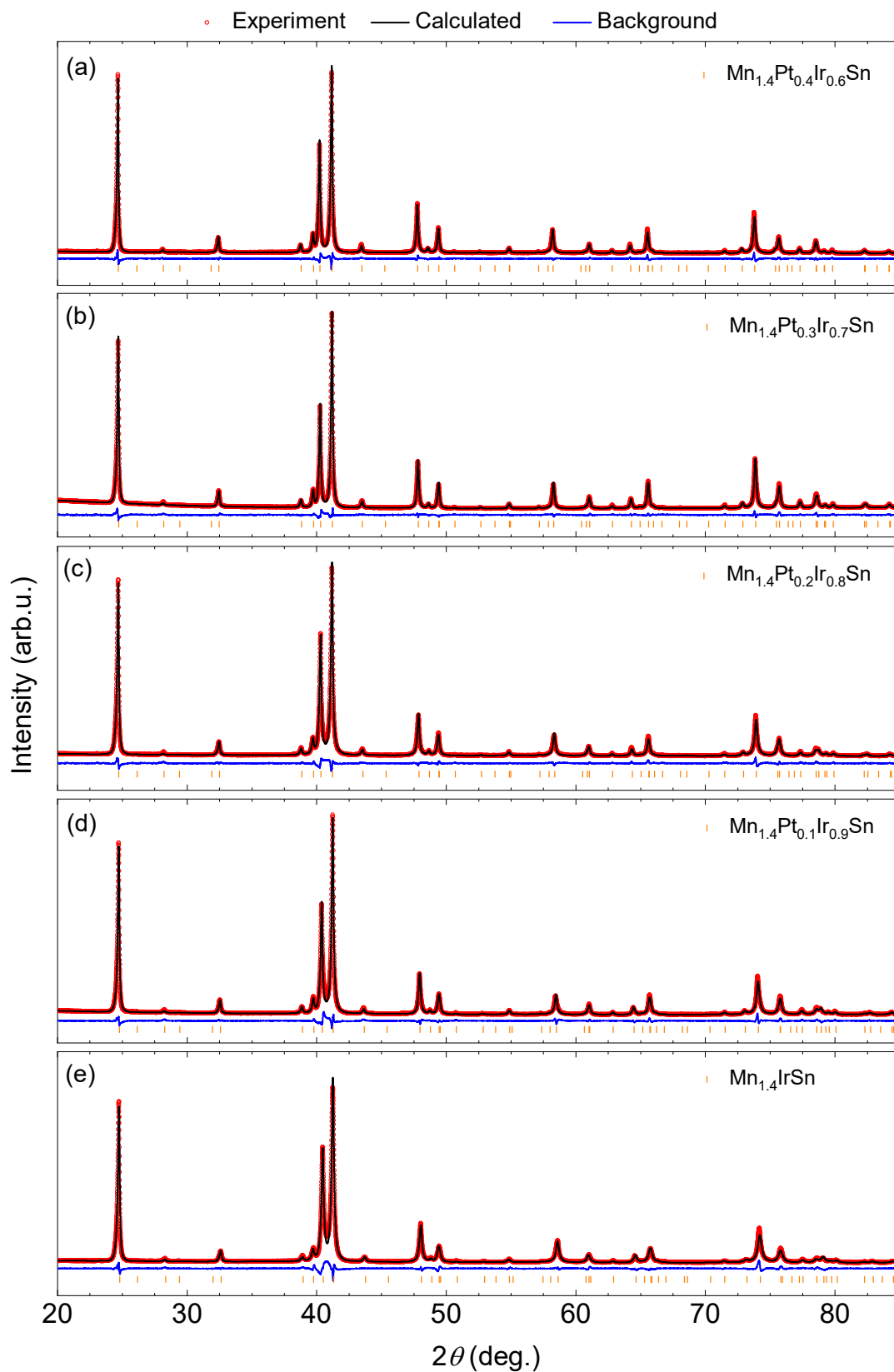


Figure 5.2. The experimental (red open circle), calculated (black) XRD pattern along with background (blue color) and the Bragg position of compounds (orange) with Ir-substitution $x = 0.6-1.0$.

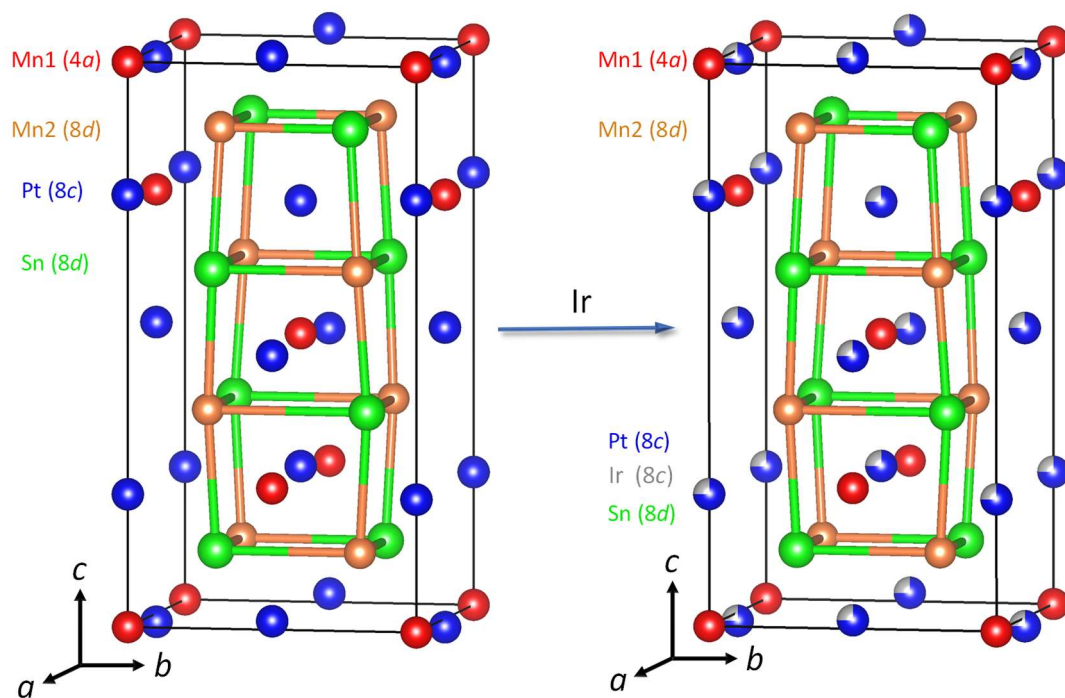


Figure 5.3. The Schematic of change in the crystal structure of $\text{Mn}_{1.4}\text{PtSn}$ upon Ir-substitution.

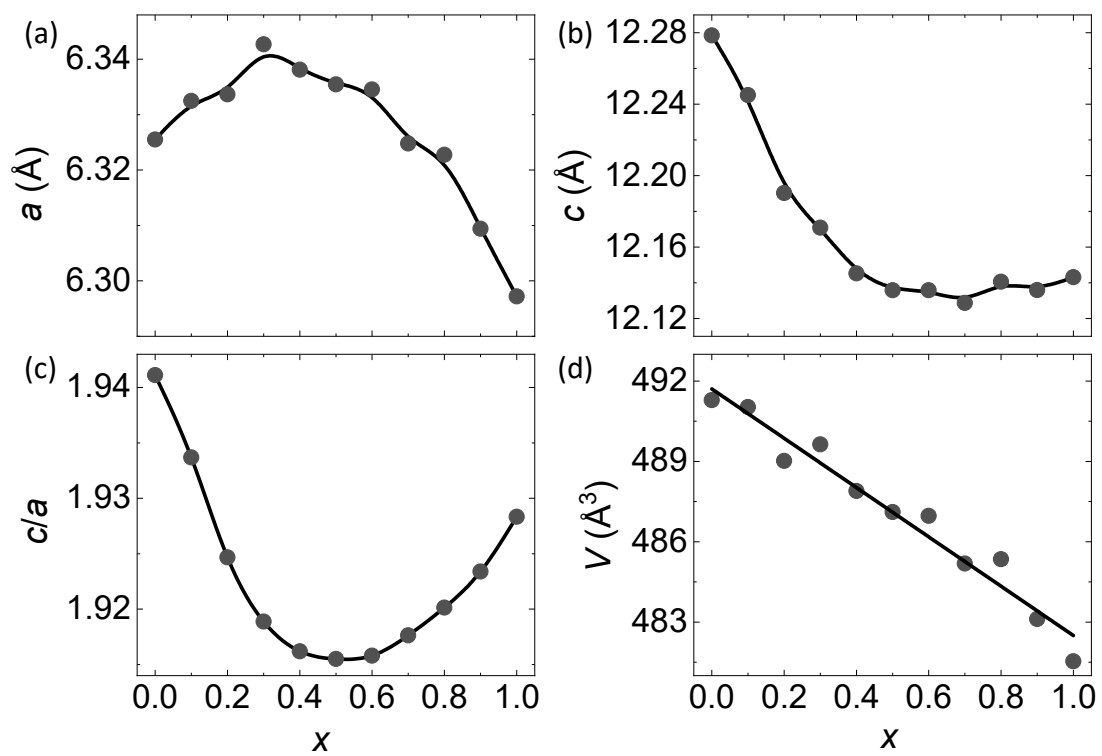


Figure 5.4. The lattice parameters (a) a (b) c (c) c/a , and (d) volume obtained from refinement of Ir-substituted compounds.

5.3. Magnetic properties

To explore the magnetic properties of compounds of $\text{Mn}_{1.4}\text{Pt}_{1-x}\text{Ir}_x\text{Sn}$, magnetization (M) was measured in commercial Quantum Design, MPMS-3. The magnetization as a function of temperature is measured for the applied external field of 0.01, 0.1, 1 and 7 T in zero-field cooling (ZFC) and field cooling (FC) mode. The magnetization as a function of the magnetic field is measured for temperatures with 50 K steps. From Figure 5.5 to 5.14, the magnetic properties corresponding to each compound are presented.

$\text{Mn}_{1.4}\text{Pt}_{0.9}\text{Ir}_{0.1}\text{Sn}$:

Figure 5.5(a) shows the M vs T curve of $\text{Mn}_{1.4}\text{Pt}_{0.9}\text{Ir}_{0.1}\text{Sn}$ for the applied external field of 0.01, 0.1, 1 and 7 T. The magnetization curves for 0.01 T and 0.1 T are multiplied with factors of 12 and 2 to have a visible comparison with the higher field. Upon decreasing temperature from 400 K, a sharp jump in the magnetization, observed at 375 K that corresponds to T_C . Upon decreasing the temperature further, another magnetic transition at 125 K is observed corresponding to the spin-reorientation transition temperature (T_{SR}). For the applied field of 7 T, the transition at 125 K is smeared out, possibly due to the complete field-polarization of magnetic moments. Similar behavior in the magnetization is observed for parent compound $\text{Mn}_{1.4}\text{PtSn}$. This indicates that the magnetic structure for $x = 0.1$ could be the same as the parent compound.

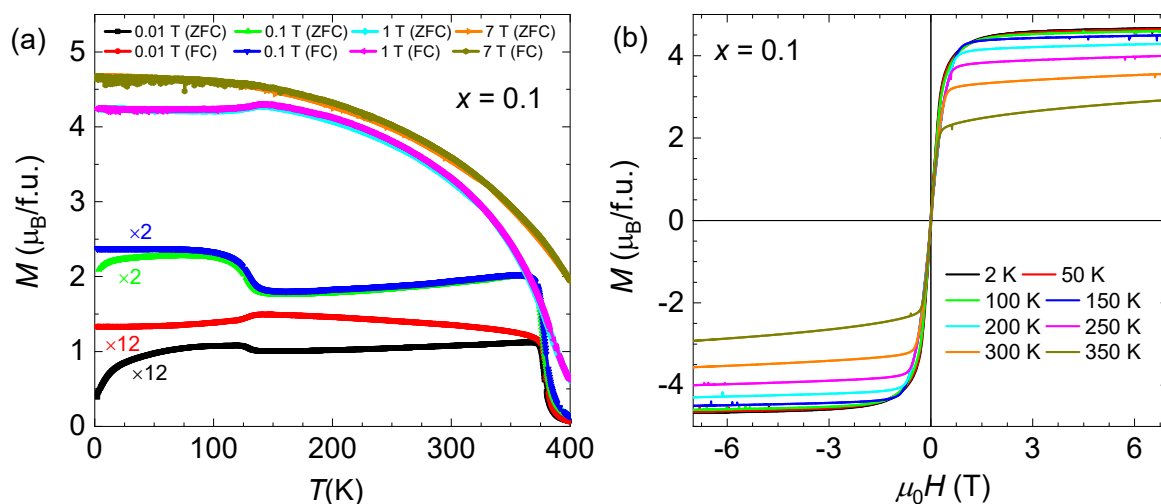


Figure 5.5. (a) M vs T for applied field of 0.01, 0.1, 1, and 7 T (b) M vs H at different temperatures of $\text{Mn}_{1.4}\text{Pt}_{0.9}\text{Ir}_{0.1}\text{Sn}$.

Figure 5.5(b) shows the magnetization as a function of the magnetic field at different temperatures. For temperatures below T_{SR} , the magnetization varies non-linearly up to the saturation field of 2 T. The requirement of a large saturation field is due to the presence of a non-coplanar spin structure as it was observed for $\text{Mn}_{1.4}\text{PtSn}$ (see section 4.3). The magnetization above T_{SR} varies almost linearly and becomes constant after magnetic

saturation indicating the magnetic structure above T_{SR} is collinear. The saturation magnetization at 2 K and 300 K is found to be 4.6 and 3.31 $\mu_B/f.u.$, respectively. The compound is a soft magnet as a negligible coercivity is observed.

Mn_{1.4}Pt_{0.8}Ir_{0.2}Sn:

Figure 5.6(a) shows the M vs T curves for the applied fields of 0.01, 0.1, 1 and 7 T measured in ZFC and FC mode. The observed value of T_C and T_{SR} are 355 and 125 K, respectively. The overall variation in the magnetization for Mn_{1.4}Pt_{0.8}Ir_{0.2}Sn is similar to the parent compound Mn_{1.4}PtSn and Mn_{1.4}Pt_{0.9}Ir_{0.1}Sn. Therefore, the magnetic spin structure of this composition could be the same as Mn_{1.4}PtSn.

Figure 5.6(b) shows the magnetization as a function of the magnetic field for different temperatures. Again, at $x = 0.2$ composition, magnetization varies non-linearly below T_{SR} and linearly above T_{SR} . This means the magnetic structure below T_{SR} is non-coplanar and above T_{SR} collinear ferromagnet. The saturation magnetic moment at 2 K is 4.5 $\mu_B/f.u.$

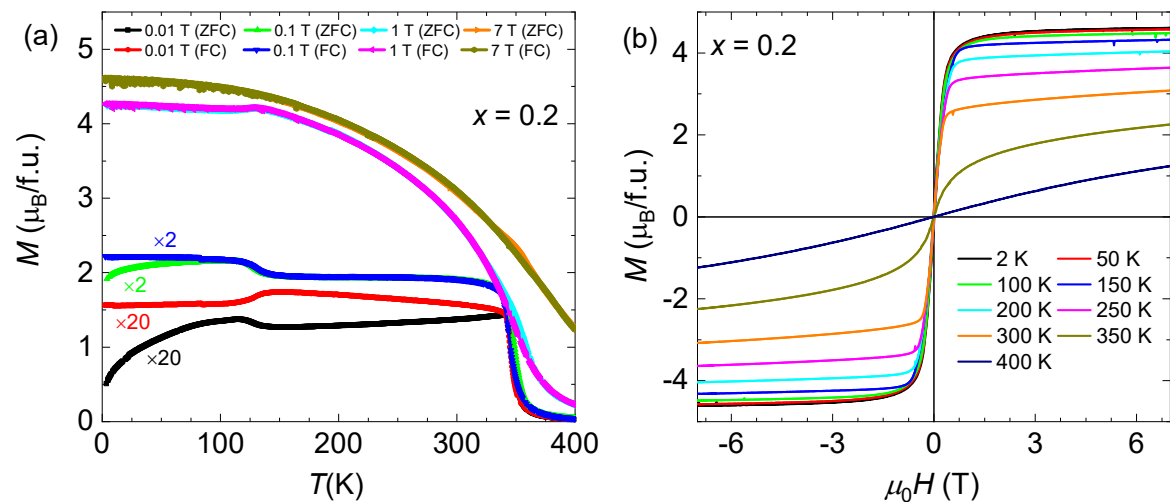


Figure 5.6. (a) M vs T for applied field of 0.01, 0.1, 1, and 7 T (b) M vs H at different temperatures of Mn_{1.4}Pt_{0.8}Ir_{0.2}Sn.

Mn_{1.4}Pt_{0.7}Ir_{0.3}Sn:

Figure 5.7(a) shows the M vs T for the applied fields of 0.01, 0.1, 1 and 7 T in ZFC and FC mode. T_C and T_{SR} of this compound are found to be 305 K and 150 K, respectively. The value of T_{SR} is higher than that of $x = 0.2$. This could be due to the possible change in the magnetic structure. For $x = 0.3$, the high-temperature magnetic structure is collinear in-plane ferrimagnetic as obtained from refinement of powder neutron diffraction pattern (see

section 5.4.) while for up to $x = 0.2$, the magnetic structure is collinear ferromagnetic (same as $\text{Mn}_{1.4}\text{PtSn}$). The low-temperature magnetic structure for compounds up to $x = 0.3$ is non-coplanar. This means that the Ir-substitution of $x = 0.3$ leads to a change in the magnetic structure at higher temperatures from out-of-plane ferromagnet to in-plane ferrimagnet.

Figure 5.7(b) shows the M vs H for different temperatures. The observed saturation magnetic moment at 2 K is $4.6 \mu_{\text{B}}/\text{f.u.}$ A negligible coercivity is also observed at all the temperatures.

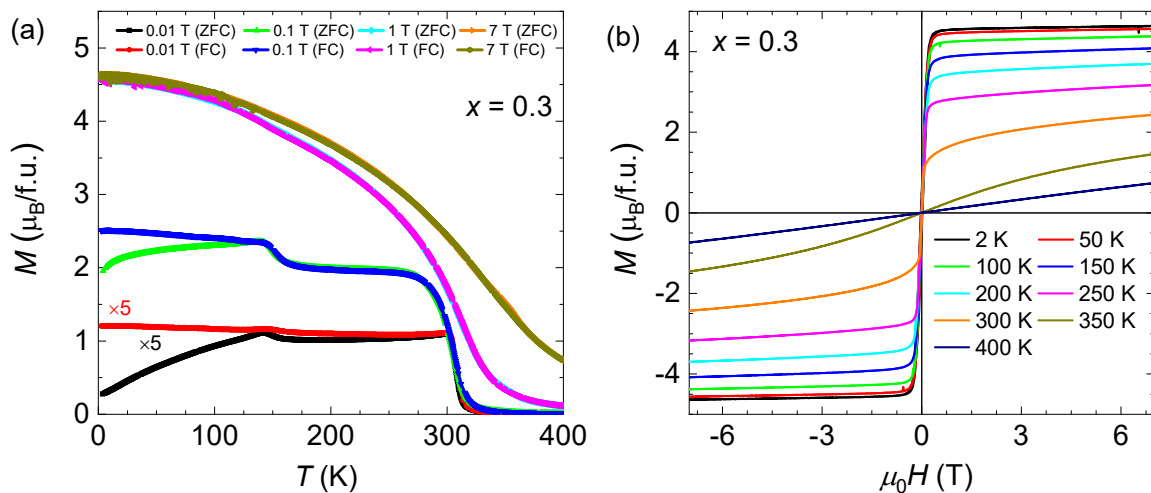


Figure 5.7. (a) M vs T for the applied field of 0.01, 0.1, 1, and 7 T (b) M vs H at different temperatures of $\text{Mn}_{1.4}\text{Pt}_{0.7}\text{Ir}_{0.3}\text{Sn}$.

$\text{Mn}_{1.4}\text{Pt}_{0.6}\text{Ir}_{0.4}\text{Sn}$:

Figure 5.8(a) shows the M vs T curve of $\text{Mn}_{1.4}\text{Pt}_{0.6}\text{Ir}_{0.4}\text{Sn}$ compound for the applied external field of 0.01, 0.1 and 7 T in ZFC and FC mode. T_{C} and T_{SR} are observed at 280 K and 100 K, respectively. The variation in the magnetization for $x = 0.4$ is marginally different from that of lower Ir-substitution i.e. $x = 0.1, 0.2$ and 0.3 . For the applied field of 0.1 T, the magnetization for $x = 0.4$ tends to decrease whereas it increases in the case of $x = 0.1, 0.2, 0.3$ below T_{SR} . The magnetic transition around 100 K is smeared out for the applied field of 7 T, possibly due to the complete field polarization of the magnetic moment.

Figure 5.8(b) shows the magnetization as a function of the field at various temperatures. The saturation magnetic moment at 2 K is $3.5 \mu_{\text{B}}/\text{f.u.}$ The magnetization curve at 2 K shows a significant value of coercivity of 0.3 T. A linear increase in the magnetization even after the saturation field indicates that the magnetic structure is possibly ferrimagnet, which is also confirmed by the refinement of powder neutron diffraction (see section 5.4).

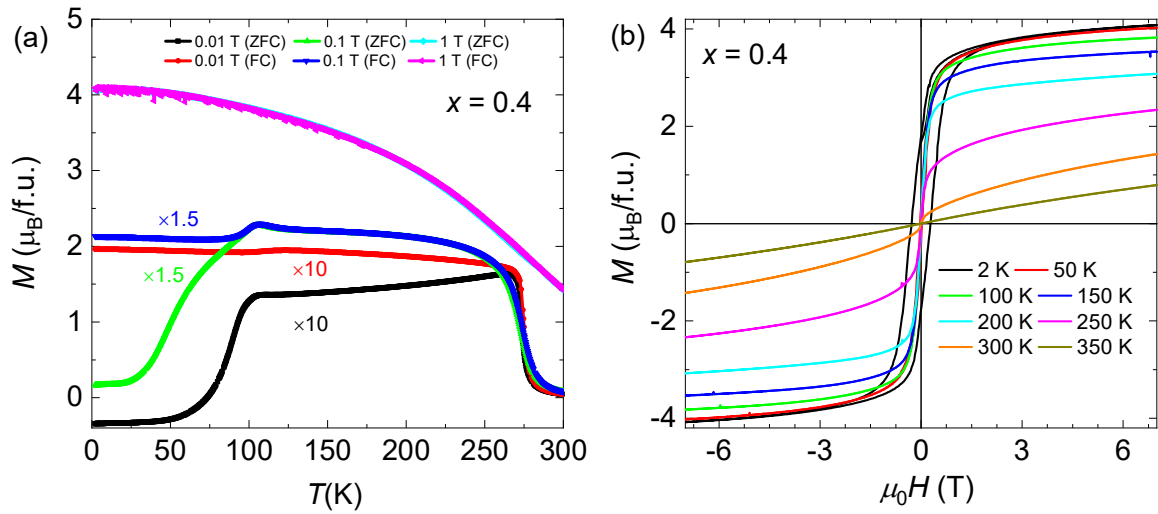


Figure 5.8. (a) M vs T for the applied field of 0.01, 0.1, and 7 T (b) M vs H at different temperatures of $\text{Mn}_{1.4}\text{Pt}_{0.6}\text{Ir}_{0.4}\text{Sn}$.

$\text{Mn}_{1.4}\text{Pt}_{0.5}\text{Ir}_{0.5}\text{Sn}$:

Figure 5.9(a) shows the M vs T curve of $\text{Mn}_{1.4}\text{Pt}_{0.5}\text{Ir}_{0.5}\text{Sn}$ compound for the applied external field of 0.01, 0.1, 1 and 7 T in ZFC and FC mode. A sharp increase in the magnetization at 250 K, corresponds to the T_C while T_{SR} of this compound is observed at 80 K. The variation in the magnetization is similar to $x = 0.4$, indicating the presence of the same magnetic structure.

Figure 5.9(b) shows the magnetization as a function of the field for different temperatures. The compound exhibits $3.25 \mu_B/\text{f.u.}$ of saturation magnetization and the coercivity value is 0.42 T at 2 K.

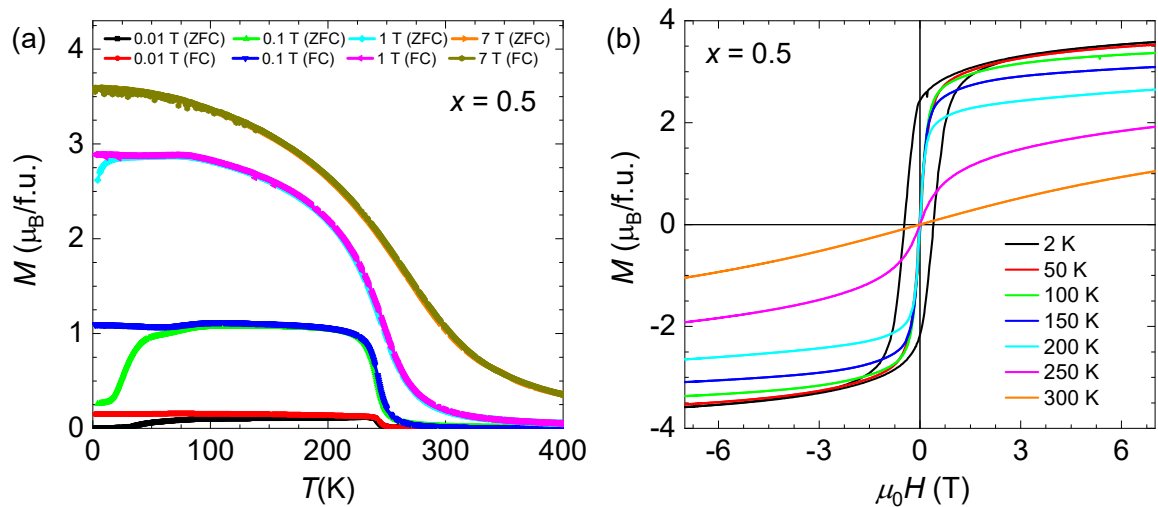


Figure 5.9. (a) M vs T for the applied field of 0.01, 0.1, 1, and 7 T (b) M vs H at different temperatures of $\text{Mn}_{1.4}\text{Pt}_{0.5}\text{Ir}_{0.5}\text{Sn}$.

For the higher Ir-concentration compounds ($0.7 \geq x \geq 0.4$), the variation in the magnetization is again similar. However, the value of T_C and T_{SR} decreases with increasing Ir-concentration. Also, the saturation magnetic moment decreases with increasing Ir-concentration. The M vs T and M vs H curves are presented in Figures 5.10 and 5.11 for $x = 0.6$ and 0.7 , respectively.

Mn_{1.4}Pt_{0.4}Ir_{0.6}Sn:

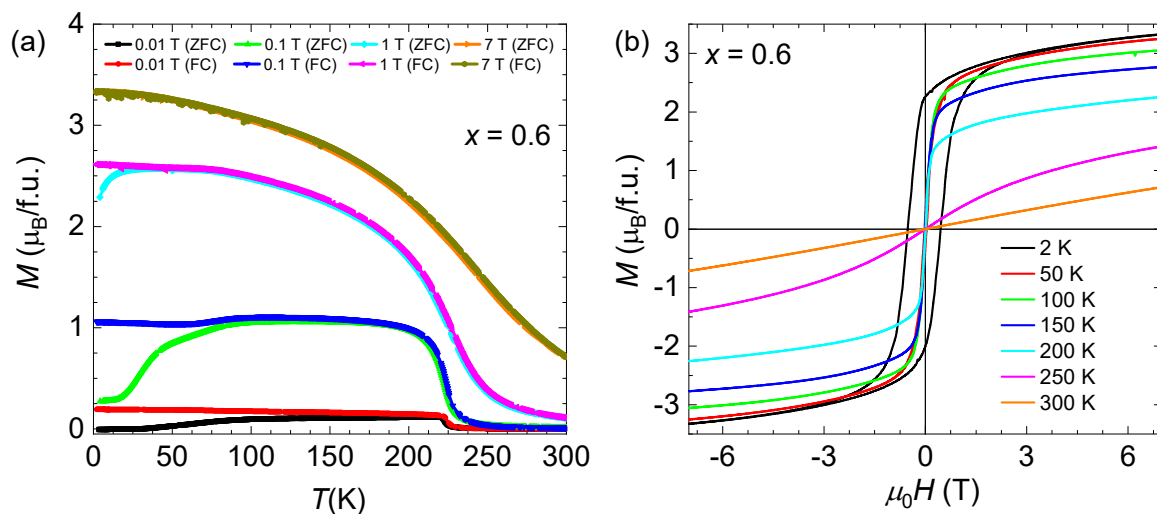


Figure 5.10. (a) M vs T for the applied field of 0.01, 0.1, 1, and 7 T (b) M vs H at different temperatures of Mn_{1.4}Pt_{0.4}Ir_{0.6}Sn.

Mn_{1.4}Pt_{0.3}Ir_{0.7}Sn:

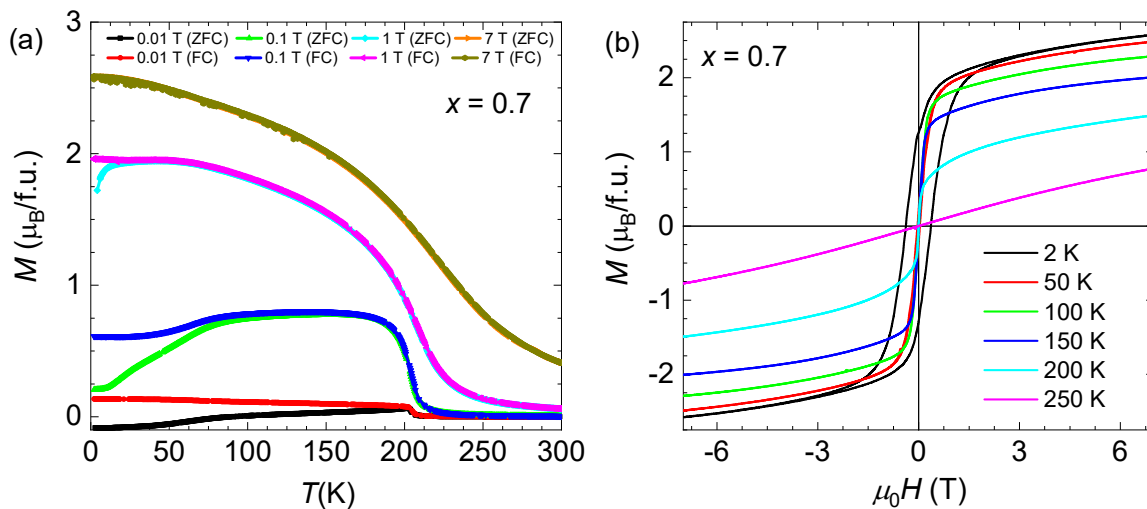


Figure 5.11. (a) M vs T for the applied field of 0.01, 0.1, 1, and 7 T (b) M vs H at different temperatures of Mn_{1.4}Pt_{0.3}Ir_{0.7}Sn.

For the compounds with higher Ir-concentration than $x = 0.8$, only one magnetic transition (T_C) is observed and the T_{SR} is absent. From the refinement of powder neutron diffraction, the magnetic structure is found to be collinear ferrimagnet in all the temperature range. M vs T and M vs H curves of $x = 0.8, 0.9$ and 1.0 are presented in Figures 5.12, 5.13, and 5.14, respectively.

Mn_{1.4}Pt_{0.2}Ir_{0.8}Sn:

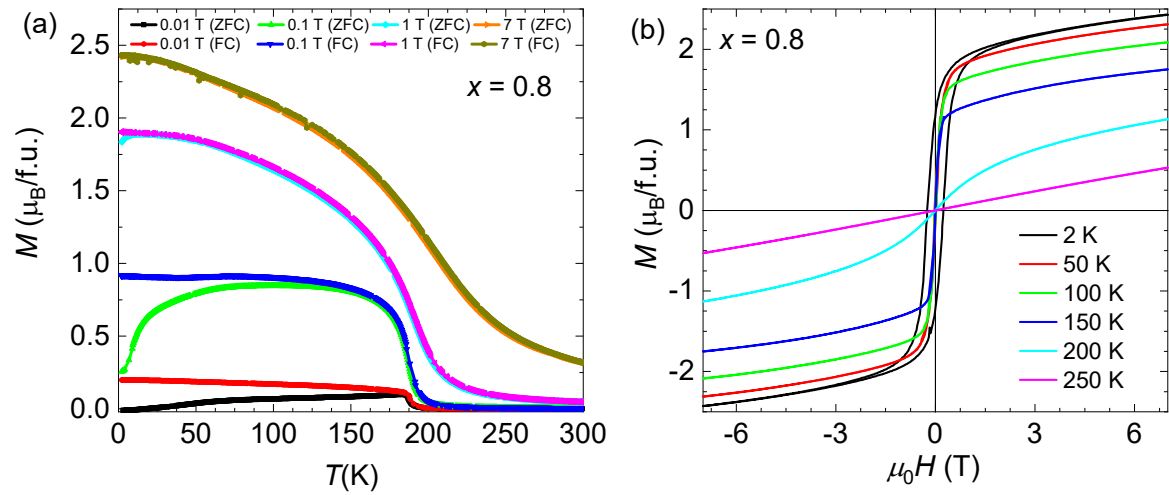


Figure 5.12. (a) M vs T for the applied field of 0.01, 0.1, 1, and 7 T (b) M vs H at different temperatures of Mn_{1.4}Pt_{0.2}Ir_{0.8}Sn.

Mn_{1.4}Pt_{0.1}Ir_{0.9}Sn:

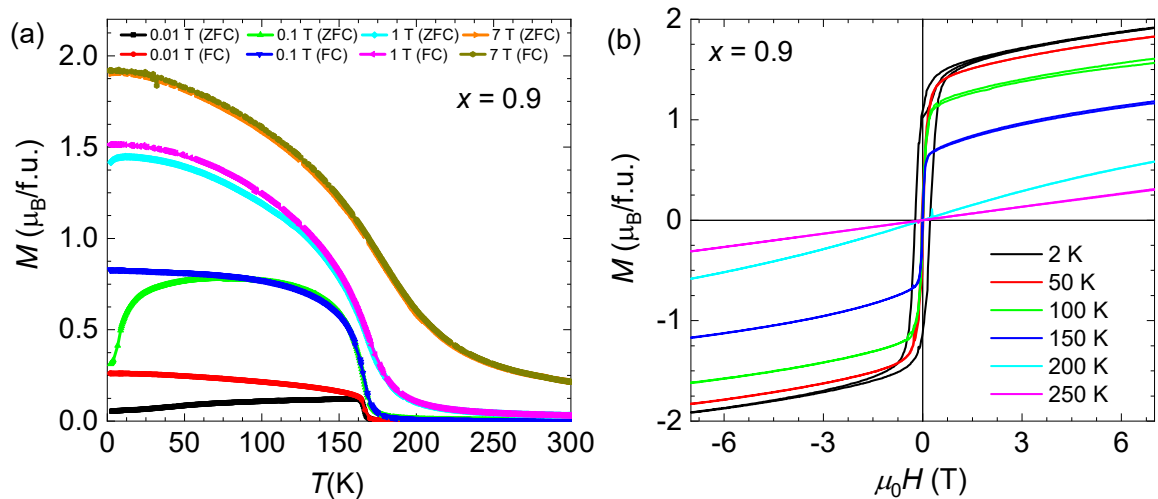


Figure 5.13. (a) M vs T for the applied field of 0.01, 0.1, 1, and 7 T (b) M vs H at different temperatures of Mn_{1.4}Pt_{0.1}Ir_{0.9}Sn.

Mn_{1.4}IrSn:

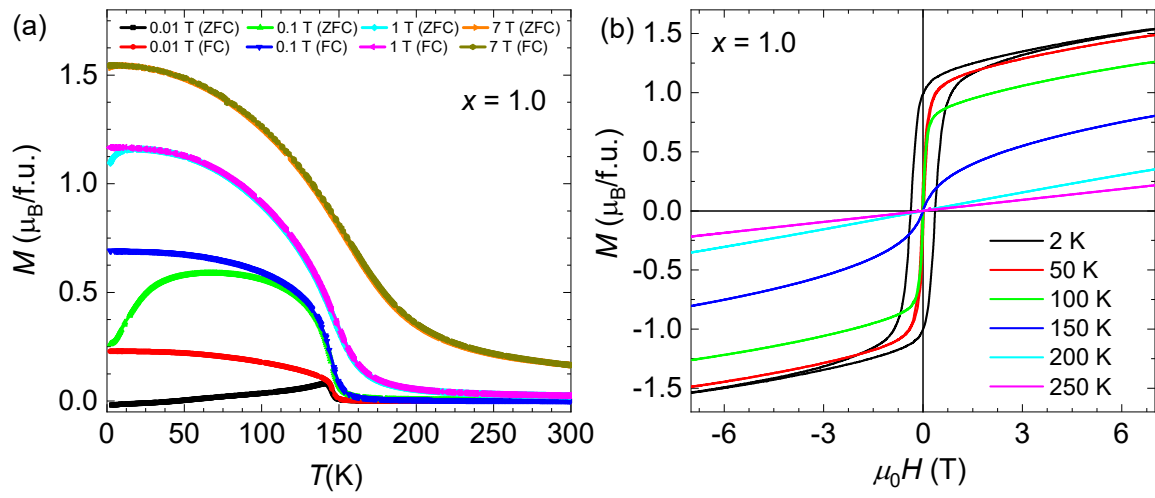


Figure 5.14. (a) M vs T for the applied field of 0.01, 0.1, 1, and 7 T (b) M vs H at different temperatures of Mn_{1.4}IrSn.

Combined property of the series:

Curie temperature (T_C) for all the compounds is calculated from the position of minima in dM/dT vs T plot for the applied field of 0.01 T. It can be seen in the Figure 5.15(a) that the variation of T_C with x is almost linear which proves the tunability nature of magnetic properties in this series of Heusler compounds. This linear reduction in T_C can be explained in terms of decreasing direct exchange interaction between two Mn moments. Ir has one less valance electron than Pt and continuous substitution leads to the reduction of conduction electrons mediating between Mn-moments. The spin-reorientation transition (T_{SR}) is also found to be decreasing continuously with Ir-concentration up to $x = 0.7$ and is absent for higher Ir-concentrations ($x \geq 0.8$).

The saturation magnetic moment (M_S) is calculated from the isothermal magnetization curve of 2 K by extrapolating the moment of 4–7 T to zero field. The variation of M_S as Ir-concentration (x) is shown in Figure 5.15(b). As can be seen in the graph, the magnetic moment is almost constant up to $x = 0.3$ while for Ir-concentration higher than $x = 0.4$, it decreases linearly with x . This can be understood in terms of the change in the magnetic structure, evidencing from the refinement of powder neutron diffraction (see section 5.4). The low-temperature magnetic structure up to $x = 0.3$ is the same as the parent compound $Mn_{1.4}PtSn$, possibly leading to the approximately same saturation moment. The linear decrease in the magnetic moment might be due to continuous change in the values of antiparallely aligned magnetic moments of ferrimagnetic spin structure. In addition to that, a notable observation is that the compounds tend to become hard magnet upon increasing Ir-concentration due to the increase in the tetragonality, as demonstrated from the refinement of XRD patterns.

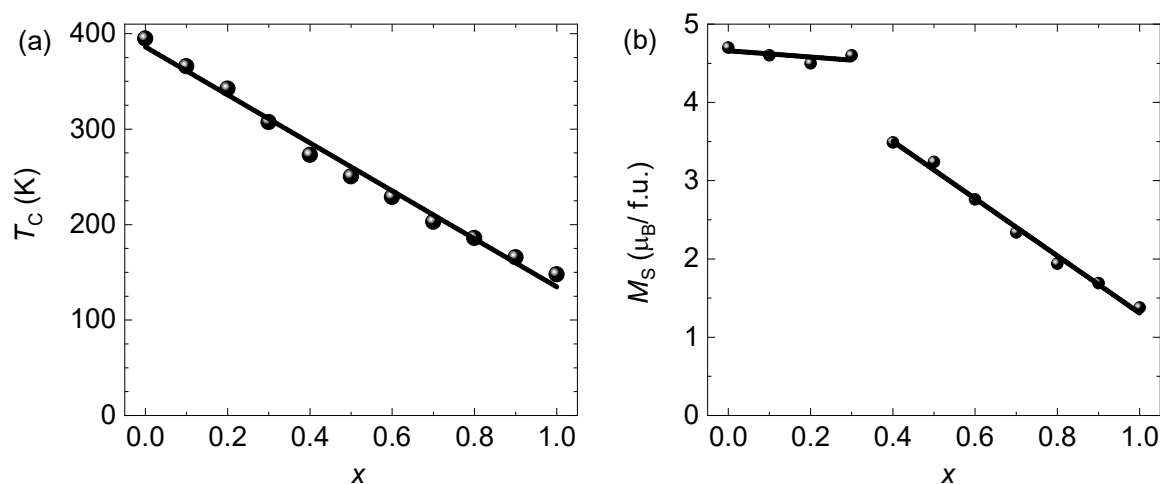


Figure 5.15. (a) Curie temperature (T_C) and (b) saturation moment (M_S , 2 K) as function of Ir-concentration (x).

5.4. Powder neutron diffraction

For the parent compound $\text{Mn}_{1.4}\text{PtSn}$, the magnetic structure is collinear ferromagnet above T_{SR} while it is non-coplanar below T_{SR} . The variation in the magnetization of compounds with $x = 0.1, 0.2$ is the same as parent compound $\text{Mn}_{1.4}\text{PtSn}$, reflecting a similarity in the magnetic spin structure. However, the magnetization variation is different for higher Ir-concentration compounds. Therefore, powder neutron diffraction measurements were done for Ir-concentrations $x = 0.3, 0.4, 0.5, 0.6,$ and 0.7 for several temperatures including $T < T_{\text{SR}}, T_{\text{SR}} < T < T_{\text{C}}$ and $T > T_{\text{C}}$.

The crystal structure used for neutron refinement is the same as obtained from the refinement of XRD patterns. The refinement of the magnetic structure was done using the Fullprof suite. The symmetry analysis model used for refinement is the same as used for parent compound $\text{Mn}_{1.4}\text{PtSn}$ (see section 4.6). The corresponding model contains three free parameters that represent the M_z component on the Mn1 site — $M_z(\text{Mn1})$, alternating in-plane components M_x and M_y on the Mn2 site (in $y, -y, -x, x$ sequence) — $M_{xy}(\text{Mn2})$, and M_z component on the Mn2 site — $M_z(\text{Mn2})$. Whereas for temperatures below T_{SR} , a combination of irreducible representation was used.

Figure 5.16 shows the powder neutron diffraction pattern of compound $\text{Mn}_{1.4}\text{Pt}_{0.7}\text{Ir}_{0.3}\text{Sn}$ ($x = 0.3$) for temperatures 1.5 K (Figure 5.16(a)), 200 K (Figure 5.16(b)) and 320 K (Figure 5.16(c)). In Figure 5.16(c), the diffraction pattern is shown for 320 K, which corresponds to the temperature in the paramagnetic phase. This diffraction pattern (nuclear pattern) can be successfully fitted with the crystal structure obtained from XRD refinement. For high-temperature magnetic structure ($T > T_{\text{SR}}$), the diffraction pattern for 200 K was refined. All the magnetic reflections are found to be superimposed with nuclear reflections, indicating that the propagation vector of the magnetic structure is $k = 0$. There is a significant enhancement in the intensity of 112, 200, 004, and 211 reflections observed while the intensity of 103 remains unchanged. The observation of magnetic intensity at 004 peaks indicates that the magnetic moment could be in-plane. From complete refinement, it is found that the structure is in-plane ferrimagnetic above T_{SR} with moment present at Mn1 (4a) and Mn2 (8d) align antiparallel in the ab -plane of tetragonal structure. To get the magnetic structure below T_{SR} , refinement of the pattern collected at 1.5 K was done. At 1.5 K, a spontaneous increase in the intensity of 101 peak is seen in addition to the enhancement in the intensity of 112, 200, 004 and 112 peaks. A similar enhancement in the peak intensity is observed for the parent compound, $\text{Mn}_{1.4}\text{PtSn}$. In $\text{Mn}_{1.4}\text{PtSn}$, the canting angle between the moments of Mn1 (4a) and Mn2 (8d) is close to 90 degrees. The moment residing at Mn1 (4a) align close to c -direction with a small component in ab -plane. Whereas, the moment at Mn2 (8d) is close to the ab -plane with a small component along c -direction. To simplify the model, the magnetic moment of Mn1 (4a) was considered along c -direction with no component in ab -plane and for Mn2 (8d), it was considered in ab -plane with no component along c -direction. This slight modification in the magnetic structure does not lead to any significant change in the R -value but simplifies the refinement to a great extent. From refinement, the obtained magnetic structure is the same

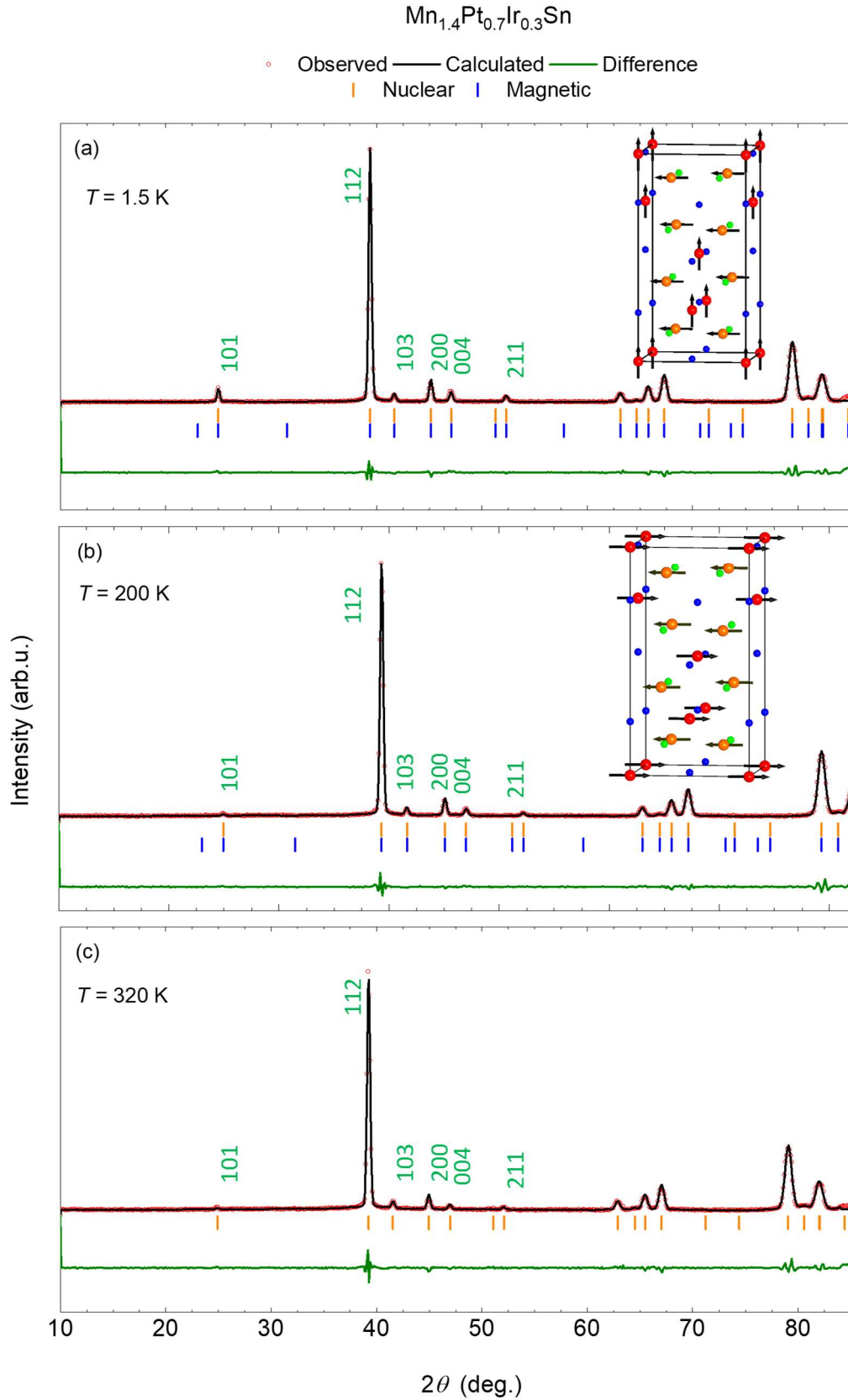


Figure 5.16. Experimental powder neutron diffraction pattern (red open circle), theoretical pattern (black line) and background (green line) along with nuclear (orange) and magnetic (blue) reflections. Inset picture represents the magnetic structure at that particular temperature of $\text{Mn}_{1.4}\text{Pt}_{0.7}\text{Ir}_{0.3}\text{Sn}$.

as the low-temperature magnetic structure of the parent compound $\text{Mn}_{1.4}\text{PtSn}$ *i.e.* non-coplanar spin structure. Therefore, with Ir-substitution, the magnetic structure below T_{SR} remains the same up to $x = 0.3$. Whereas for temperatures above T_{SR} , it changes from out-of-plane ferromagnet to in-plane ferrimagnet. The magnetic structures of respected temperatures are shown in the inset of powder neutron diffraction pattern in Figure 5.16.

Figure 5.17 shows the powder diffraction pattern of Ir-substituted compound with composition $x = 0.4$. The refinement was done for temperatures 1.5 K ($T < T_{\text{SR}}$), 120 K ($T_{\text{SR}} < T < T_{\text{C}}$) and $T > T_{\text{C}}$. From the refinement of the diffraction patterns of temperatures above T_{SR} , it is found out that the magnetic structure remains in-plane ferrimagnetic, the same as $x = 0.3$. The refinement of the diffraction patterns for 1.5 K results in the magnetic structure to be in-plane ferrimagnetic, unlike the compounds with lower Ir-concentration ($x \leq 0.3$), where the low-temperature magnetic structure is non-coplanar. However, a slight amount of moment (up to $0.5 \mu_{\text{B}}$) along c -direction can be considered within limited statistics of powder neutron diffraction data. The inclusion of magnetic moment along c -direction gives rise to a canted magnetic structure *i.e.* canted in-plane ferrimagnet. The refinement of higher Ir-concentration compounds ($x = 0.5, 0.6, 0.7$) leads to the same magnetic structure. The diffraction patterns of compounds with $x = 0.5, 0.6$ and 0.7 are shown in Figures 5.18, 5.19 and 5.20, respectively. Thus, it can be summarized that the magnetic structure is canted in-plane ferrimagnetic below T_{SR} and collinear in-plane ferrimagnet above T_{SR} .

From magnetization measurements (see section 5.3), it was evidenced that T_{SR} decreases with increasing Ir-concentration and is zero for the compounds with $x = 0.8, 0.9$, and 1.0 . Assuming that the same magnetic structure as $x = 0.4$ continues in these compounds, the possible magnetic structure would be collinear in-plane ferrimagnetic in all the temperature ranges for compounds with $x = 0.8, 0.9$, and 1.0 .

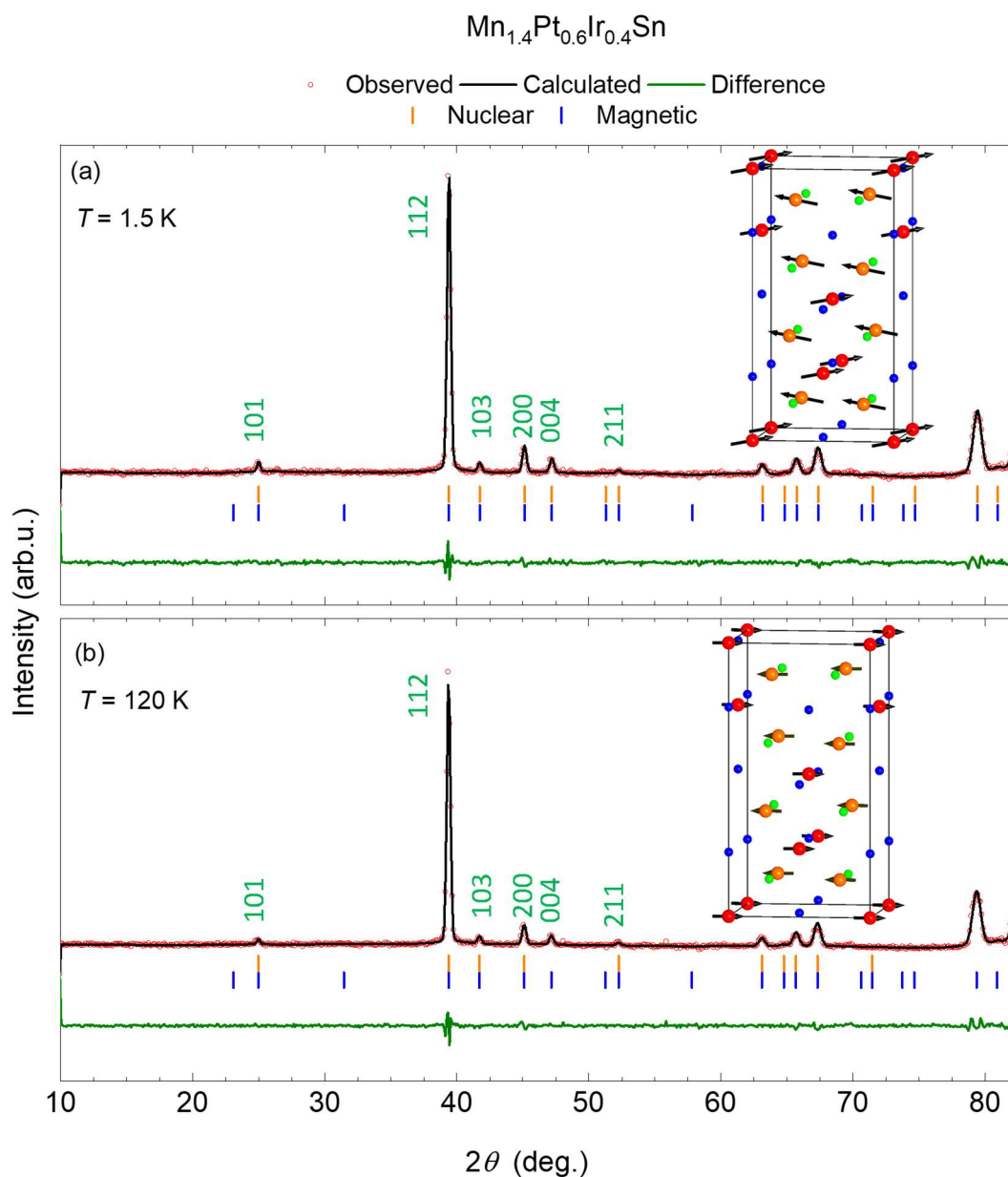


Figure 5.17. Experimental powder neutron diffraction pattern (red open circle), theoretical pattern (black line) and background (green line) along with nuclear (orange) and magnetic (blue) reflections. Inset picture represents the magnetic structure at that particular temperature of $\text{Mn}_{1.4}\text{Pt}_{0.6}\text{Ir}_{0.4}\text{Sn}$.

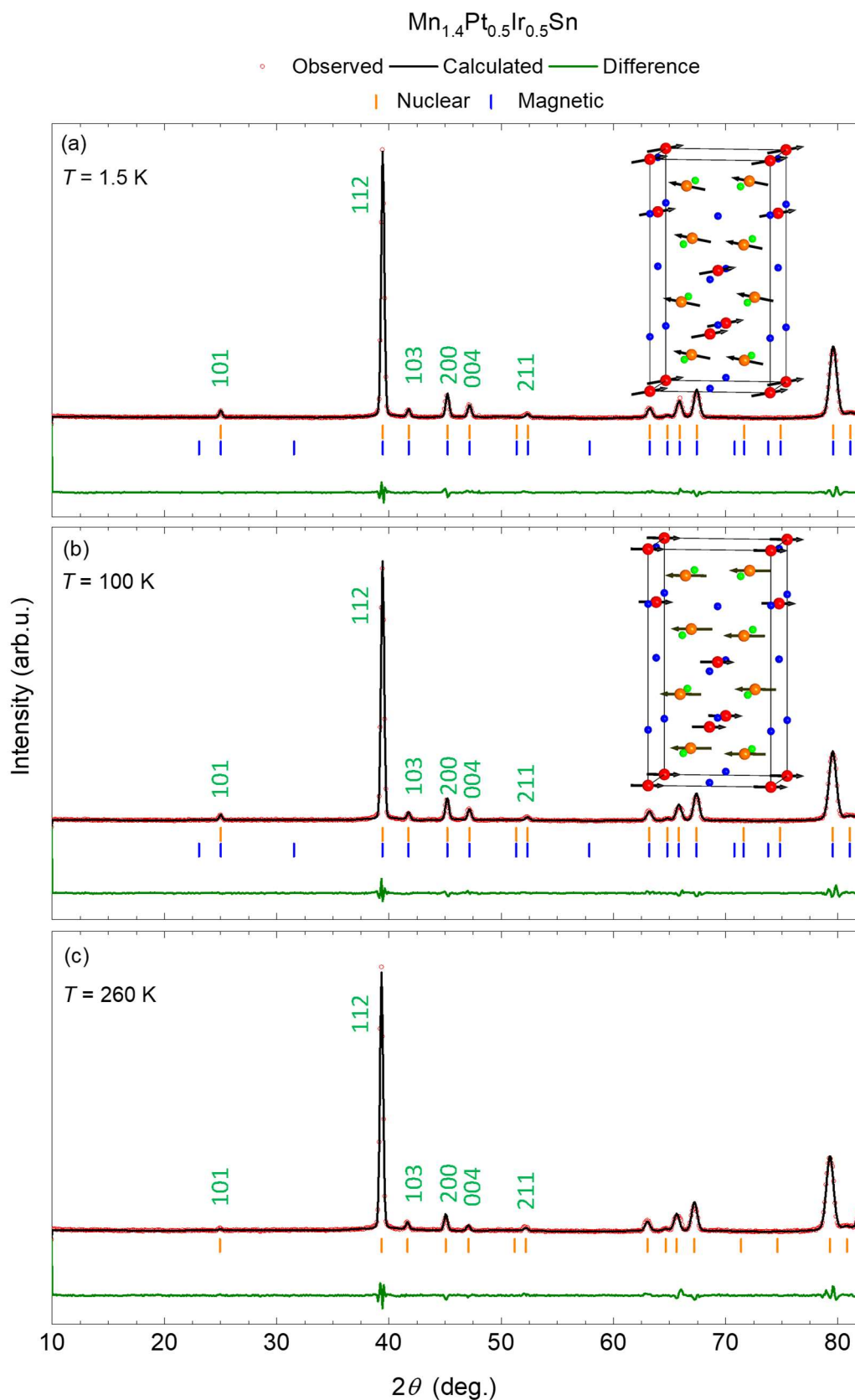


Figure 5.18. Experimental powder neutron diffraction pattern (red open circle), theoretical pattern (black line) and background (green line) along with nuclear (orange) and magnetic (blue) reflections. Inset picture represents the magnetic structure at that particular temperature of $\text{Mn}_{1.4}\text{Pt}_{0.5}\text{Ir}_{0.5}\text{Sn}$.

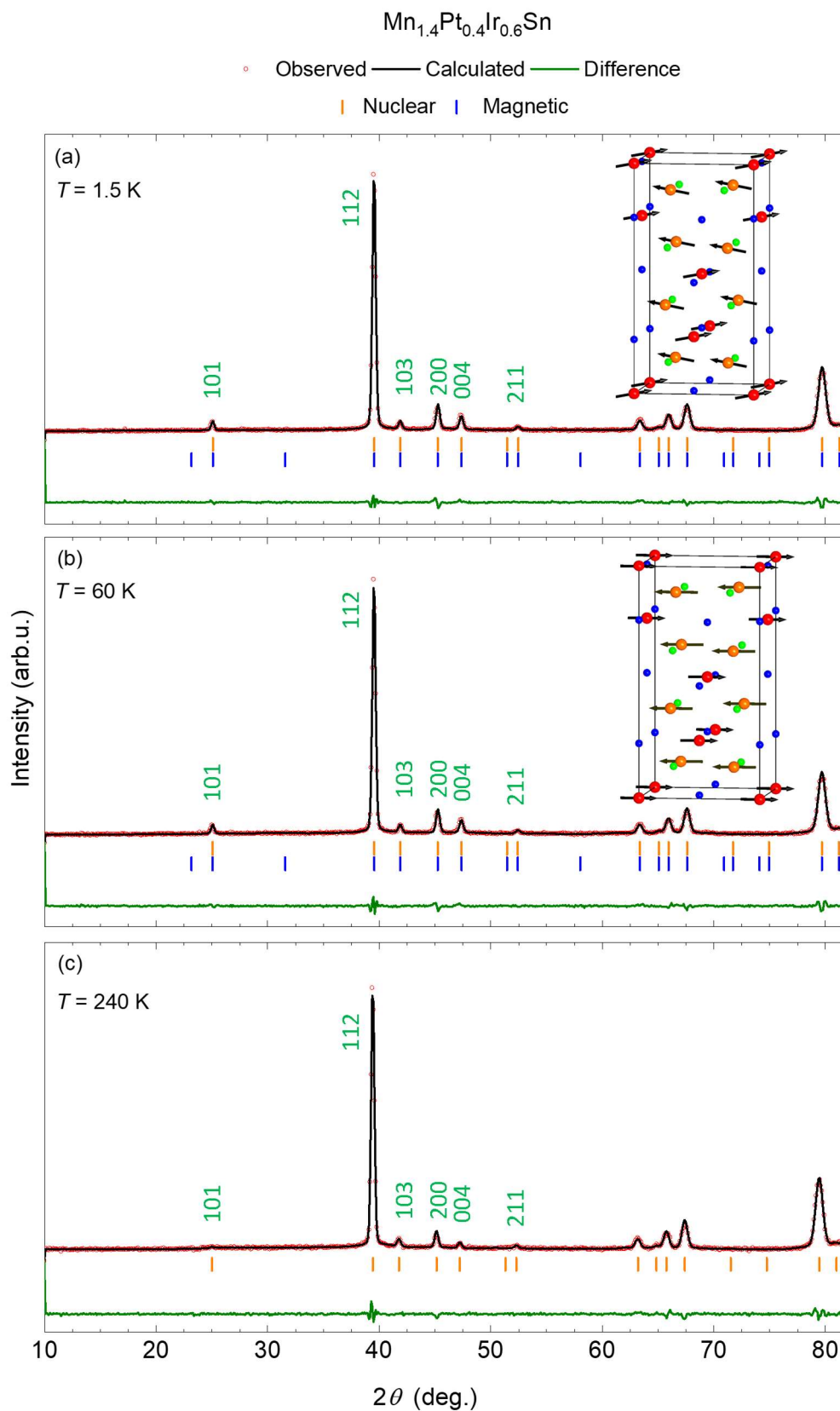


Figure 5.19. Experimental powder neutron diffraction pattern (red open circle), theoretical pattern (black line) and background (green line) along with nuclear (orange) and magnetic (blue) reflections. Inset picture represents the magnetic structure at that particular temperature of $\text{Mn}_{1.4}\text{Pt}_{0.4}\text{Ir}_{0.6}\text{Sn}$.

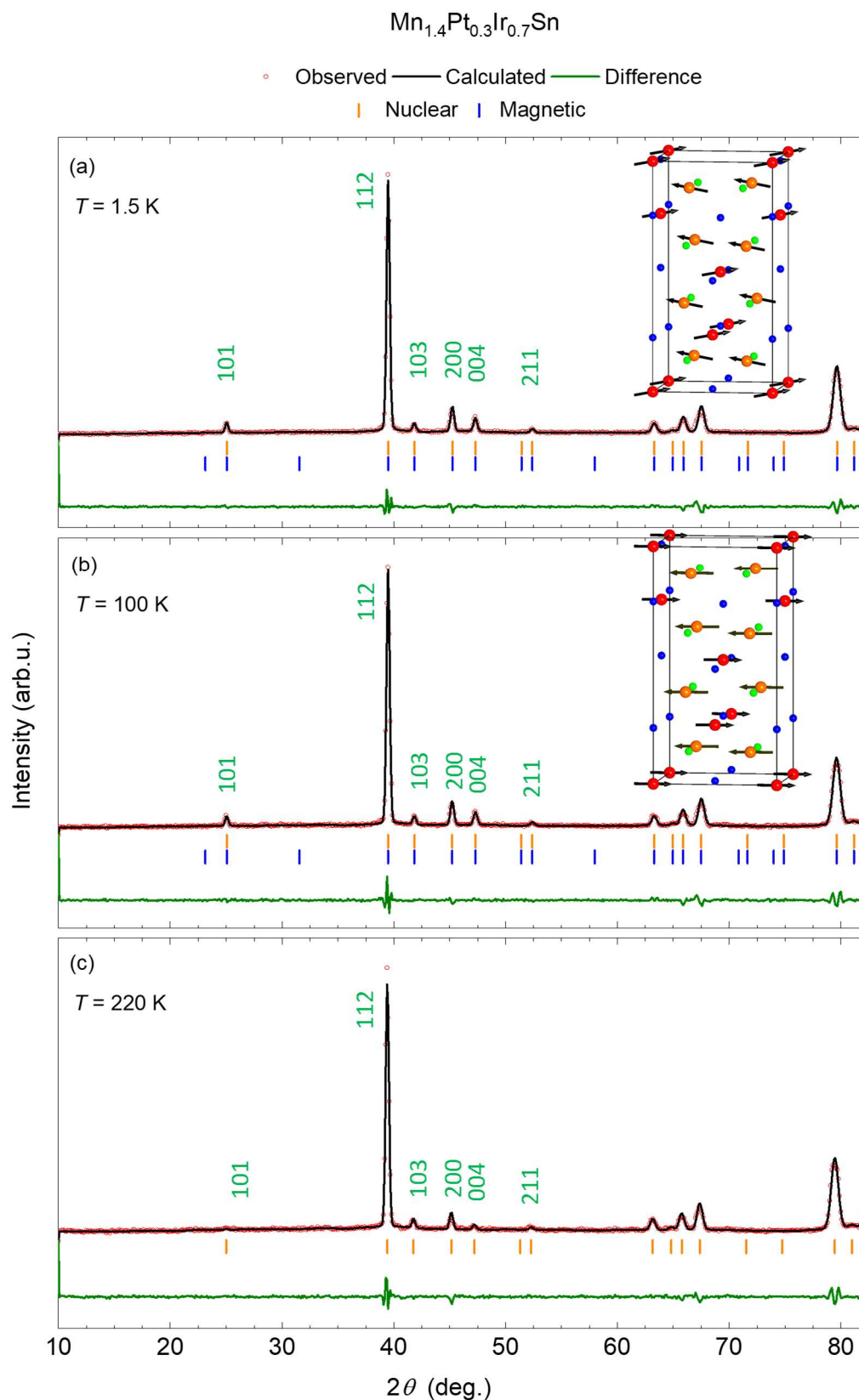


Figure 5.20. Experimental powder neutron diffraction pattern (red open circle), theoretical pattern (black line) and background (green line) along with nuclear (orange) and magnetic (blue) reflections. Inset picture represents the magnetic structure at that particular temperature of $\text{Mn}_{1.4}\text{Pt}_{0.3}\text{Ir}_{0.7}\text{Sn}$.

5.5. Electrical transport properties

To gain insight into electronic properties, electrical transport properties were measured. For the measurements, a rectangular-shaped piece was cut from the polycrystalline sample. The electric contact was made with silver paint with 25 μm diameter Pt wire. The measurements were done in AC transport mode using 5 mA current and 93 Hz frequency. The temperature and magnetic field range of measurements were 2–300 K and -9 to 9 T, respectively. Since the polycrystalline sample was used for measurements, a general convention was used for the direction of electric current, Hall voltage and magnetic field, which are along x -, y -, and z -directions, respectively. Following this convention, the longitudinal resistivity is ρ_{xx} , Hall resistivity is ρ_{yx} and the resultant Hall conductivity (using Equation 4.3) is σ_{xy} .

Figures 5.21 to 5.30 show the resistivities measurements of the compounds belonging to the series $\text{Mn}_{1.4}\text{Pt}_{1-x}\text{Ir}_x\text{Sn}$. For all the compounds, the same representation format is used. In all the Figures, (a) Magnetoresistance (MR) (b) ρ_{xx} vs T (c) ρ_{yx} vs H (d) charge carrier concentration, n , vs T (e) σ_{xy} vs H , and (f) anomalous Hall conductivity, σ_{xy}^{AHE} , vs T are presented

Magnetoresistance: For all the compositions, a negative MR (calculated using Equation 4.1) is observed at 9 T (Figures 5.21–5.30(a)). For the temperatures below T_{SR} , the resistivity first increases with the magnetic field up to the field required for magnetization saturation. After saturation, the resistivity starts decreasing. For the temperatures above T_{SR} , the resistivity continuously decreases with the magnetic field without showing upturn. In lower Ir-concentration ($x < 0.3$), the negative MR of 3 % and for compounds with high Ir-concentration ($x > 0.3$), a negative MR of 1.5 % is observed. This indicates that the longitudinal resistivity is not very sensitive to the applied external field in these compounds.

Longitudinal resistivity: For all the compounds, the resistivity decreases with decreasing temperature, revealing a metallic character (Figures 5.21–5.30(b)). Depending on the resistivity and magnetic structure at 2 K, the compounds can widely be divided into three categories. First, from $x = 0.1$ to 0.3, where ρ_{xx} is approximately 100 $\mu\Omega$ cm at 2 K and from the refinement of neutron diffraction patterns, it is evidenced that the magnetic spin structure of these three compounds is non-coplanar. Second, from $x = 0.4$ to 0.7, where ρ_{xx} is approximately 160 $\mu\Omega$ cm at 2 K and for these compounds, the possible spin structure is canted in-plane ferrimagnetic. The third category is the compounds with $x = 0.8, 0.9$ and 1.0, where ρ_{xx} is approximately 250 $\mu\Omega$ cm at 2 K and the magnetic structure is collinear in-plane ferrimagnetic. Overall, the resistivity shows an increasing trend with Ir-concentration by contributing one less electron as compared to Pt. Therefore, it seems the Ir-substitution plays a significant role in determining the electrical and magnetic properties.

Mn_{1.4}Pt_{0.9}Ir_{0.1}Sn

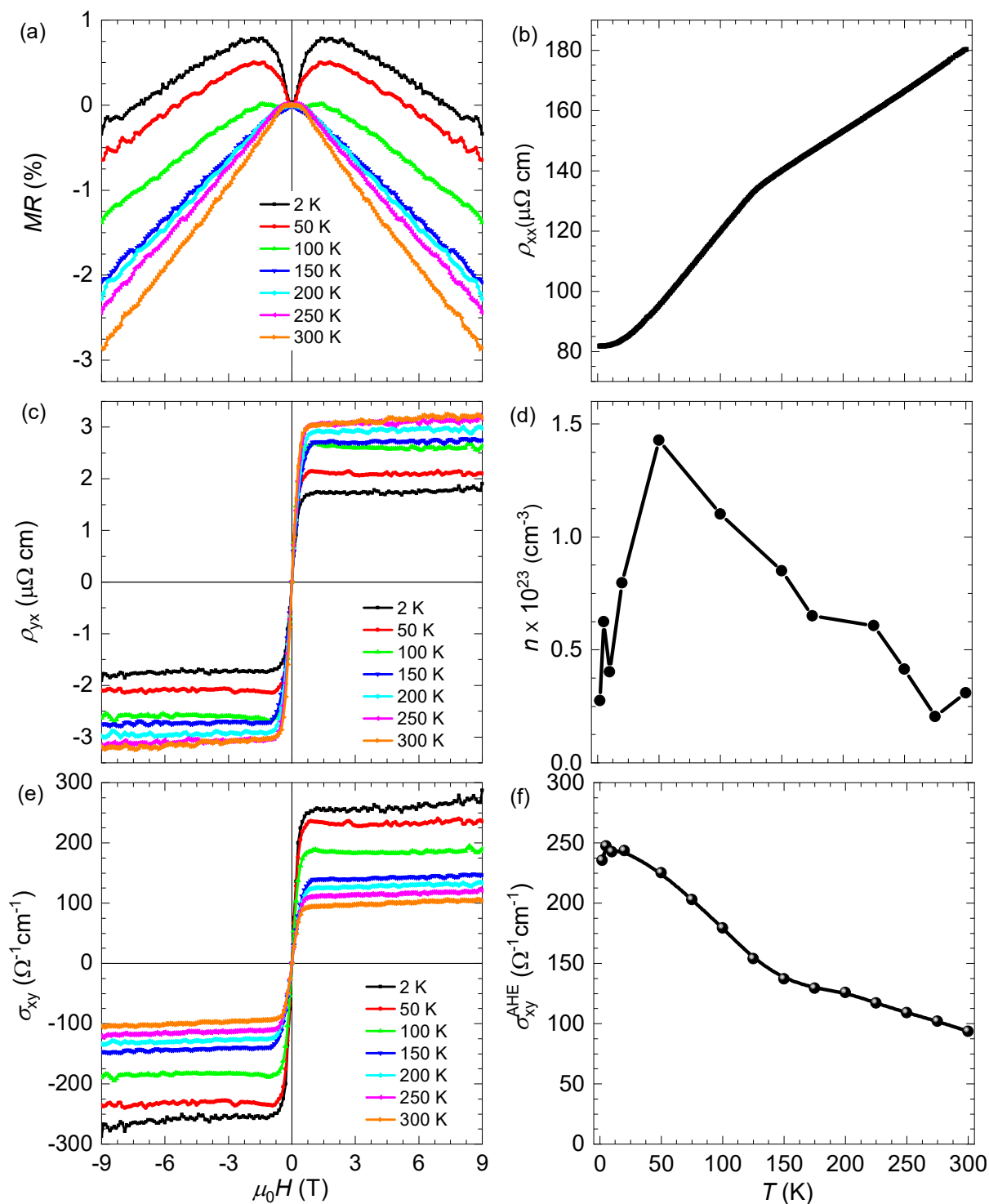


Figure 5.21. (a) Magnetoresistance (MR) (b) ρ_{xx} vs T (c) ρ_{yx} vs H (d) charge carrier concentration, n , vs T (e) σ_{xy} vs H , and (f) anomalous Hall conductivity, σ_{xy}^{AHE} , vs T of Mn_{1.4}Pt_{0.9}Ir_{0.1}Sn.

Naturally, defects also alter the resistivity at the lowest temperature. However, considering the fact that these samples have been prepared in similar conditions, the probable amount of defect could be the same. Noticeably, the resistivity of these compounds changes much between the magnetic categories, signifying the role of magnetic structure over the defects in these polycrystalline samples. A magnetic transition can be evidenced as a change of slope in the resistivity curve. For composition $x = 0.1, 0.2,$ and $0.3,$ the slope changes in the resistivity corresponding to T_C is not visible as T_C is above 300 K. However, the transition corresponding to T_{SR} is clearly seen and coincides with the value obtained from magnetic measurements. For compounds with lower Ir-concentration ($x < 0.4$), the slope-change related to T_{SR} is very sharp while for higher Ir-concentration ($0.7 \geq x \geq 0.4$), it is smeared. This is quite reasonable as for the compounds up to $x = 0.3,$ there is a transition from non-coplanar spin structure to a collinear spin structure and affects the electronic properties more as compared to the compounds ($0.7 \geq x \geq 0.4$), where magnetic structure changes from canted in-plane ferrimagnet to in-plane ferrimagnet. For the compounds with $x = 0.8, 0.9,$ and $1.0,$ the resistivity shows no transition related to $T_{SR},$ revealing the absence of low-temperature magnetic phase in these compounds.

Hall resistivity: In Figures 5.21–5.30(c), the measured Hall resistivity as a function of the magnetic field is shown for different temperatures. As can be seen in the Figures, the Hall resistivity follows the magnetization of that particular compound. For temperatures below $T_C,$ Hall resistivity increases very sharply till the saturation magnetic field and then is almost constant for $x = 0.1–0.3$ and increases for $x = 0.4–1.0.$ In the paramagnetic phase, the variation of ρ_{yx} is linear as expected. For the compounds with lower Ir-concentration ($x = 0.1–0.3$), ρ_{yx} increases with increasing temperature, whereas for high Ir-concentration ($x = 0.4–1.0$), ρ_{yx} is found to follow the opposite behavior, where it decreases with increasing temperature. As similar to magnetization, the coercivity in the ρ_{yx} is also observed. For the compounds with a non-coplanar spin structure ($x = 0.1–0.3$), an additional contribution to normal Hall and anomalous Hall resistivity is observed at low temperature, which is a signature of topological Hall effect as it was observed for parent compound $Mn_{1.4}PtSn.$

Charge carrier concentration: The charge carrier concentration, $n,$ (calculated using Equation 4.2) as a function of temperature is shown in Figures 5.21–5.30(d). In all Ir-substituted compounds, the majority charge carrier is hole-type. For compounds with lower Ir-concentration ($x = 0.1–0.3$), n is quite high of the order of $10^{23},$ while for higher Ir-concentration ($x \geq 0.4$), it decreases quite drastically by a factor $10^2.$ In the particular composition, the n also varies slightly with temperature. For lower Ir-concentration, n shows an overall decreasing behavior while it increases for higher substitution.

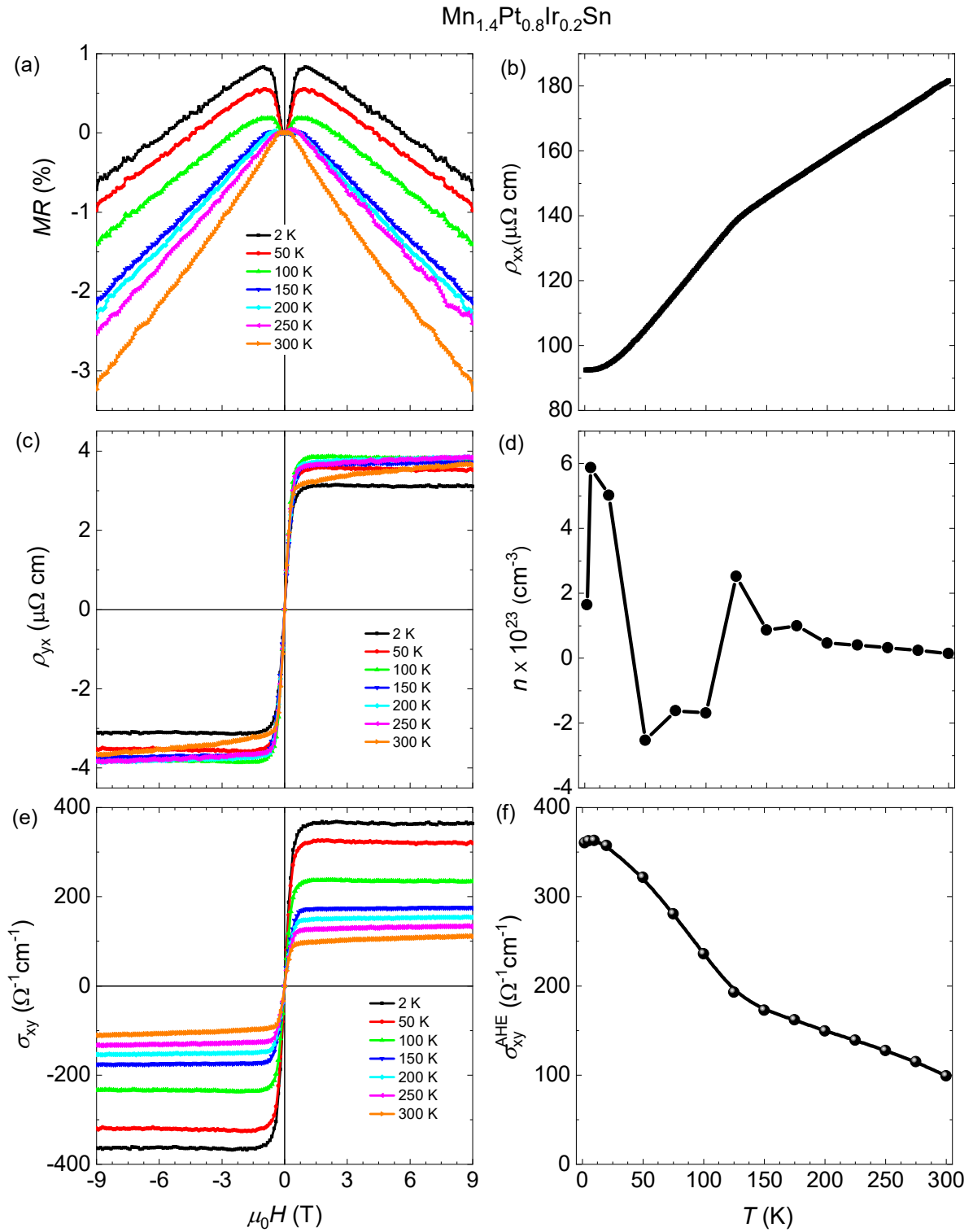


Figure 5.22. (a) Magnetoresistance (MR) (b) ρ_{xx} vs T (c) ρ_{yx} vs H (d) charge carrier concentration, n , vs T (e) σ_{xy} vs H , and (f) anomalous Hall conductivity, σ_{xy}^{AHE} , vs T of $\text{Mn}_{1.4}\text{Pt}_{0.8}\text{Ir}_{0.2}\text{Sn}$.

Hall conductivity: σ_{xy} as a function of the field for different temperatures is presented in Figure 5.21–5.30(e). The variation in σ_{xy} is almost similar to the magnetization. However, σ_{xy} is found to be decreasing with increasing temperature irrespective of composition. The coercivity observed matches well with the coercivity observed in the magnetization.

Anomalous Hall conductivity: The anomalous Hall conductivity (σ_{xy}^{AHE}) as a function of temperature is shown in Figure 5.21–5.30(f). It is calculated by extrapolating 5 to 9 T curve of σ_{xy} vs H to zero field. As expected, σ_{xy}^{AHE} decreases with increasing temperature for all the compounds due to increasing thermal fluctuation. Ambiguously, the presence of T_{SR} and T_C is also reflected in the σ_{xy}^{AHE} vs T plots. At T_{SR} , a slope change is observed while the value of σ_{xy}^{AHE} becomes close to zero at T_C . The almost linear decrement in the value of σ_{xy}^{AHE} indicates that the skew-scattering is also contributing significantly in addition to its intrinsic part⁸⁵. The significant skew-scattering can be anticipated in a polycrystalline sample, originating from defects and grain boundaries scatterings.

$\text{Mn}_{1.4}\text{Pt}_{0.7}\text{Ir}_{0.3}\text{Sn}$

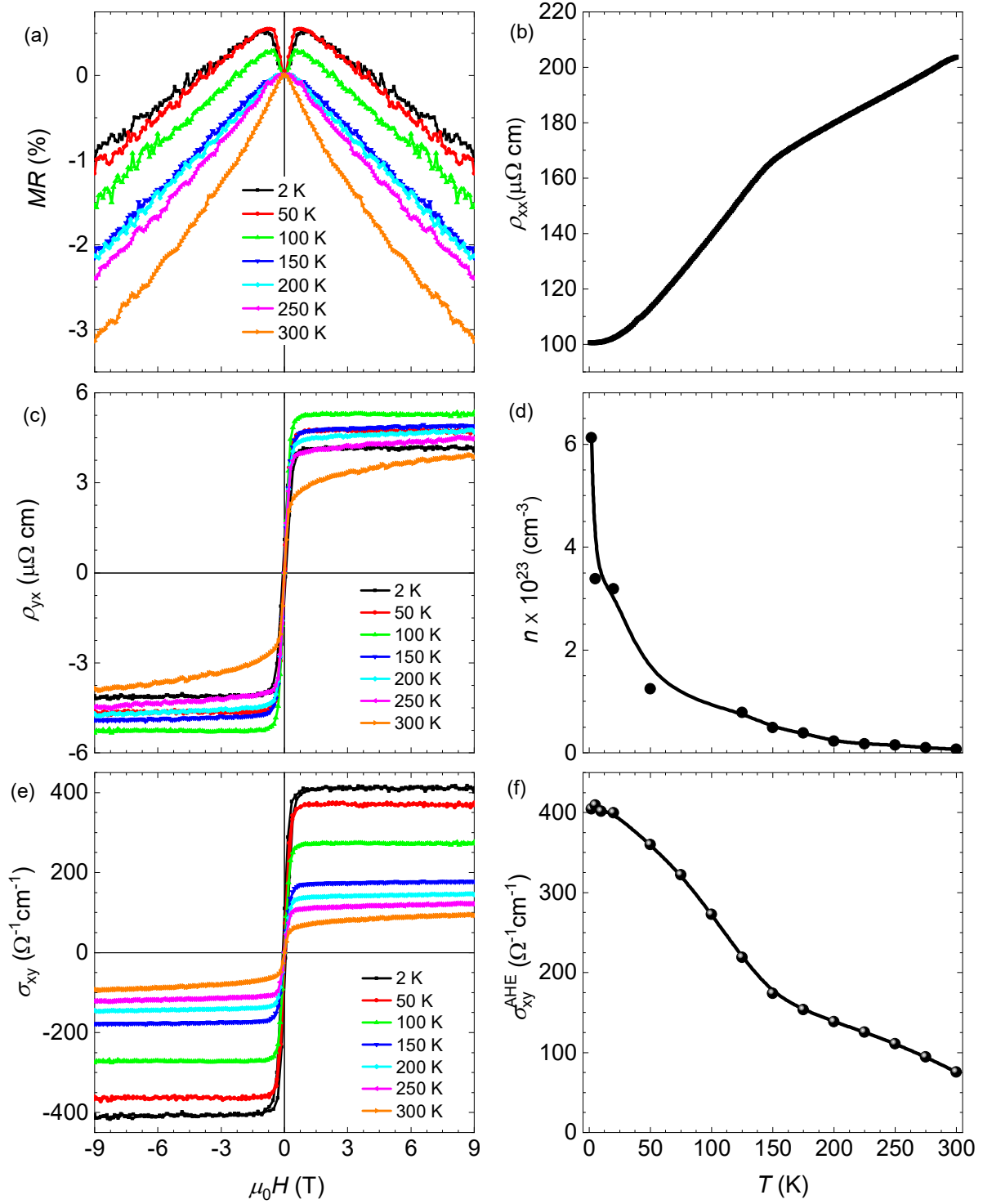


Figure 5.23. (a) Magnetoresistance (MR) (b) ρ_{xx} vs T (c) ρ_{yx} vs H (d) charge carrier concentration, n , vs T (e) σ_{xy} vs H , and (f) anomalous Hall conductivity, σ_{xy}^{AHE} , vs T of $\text{Mn}_{1.4}\text{Pt}_{0.7}\text{Ir}_{0.3}\text{Sn}$.

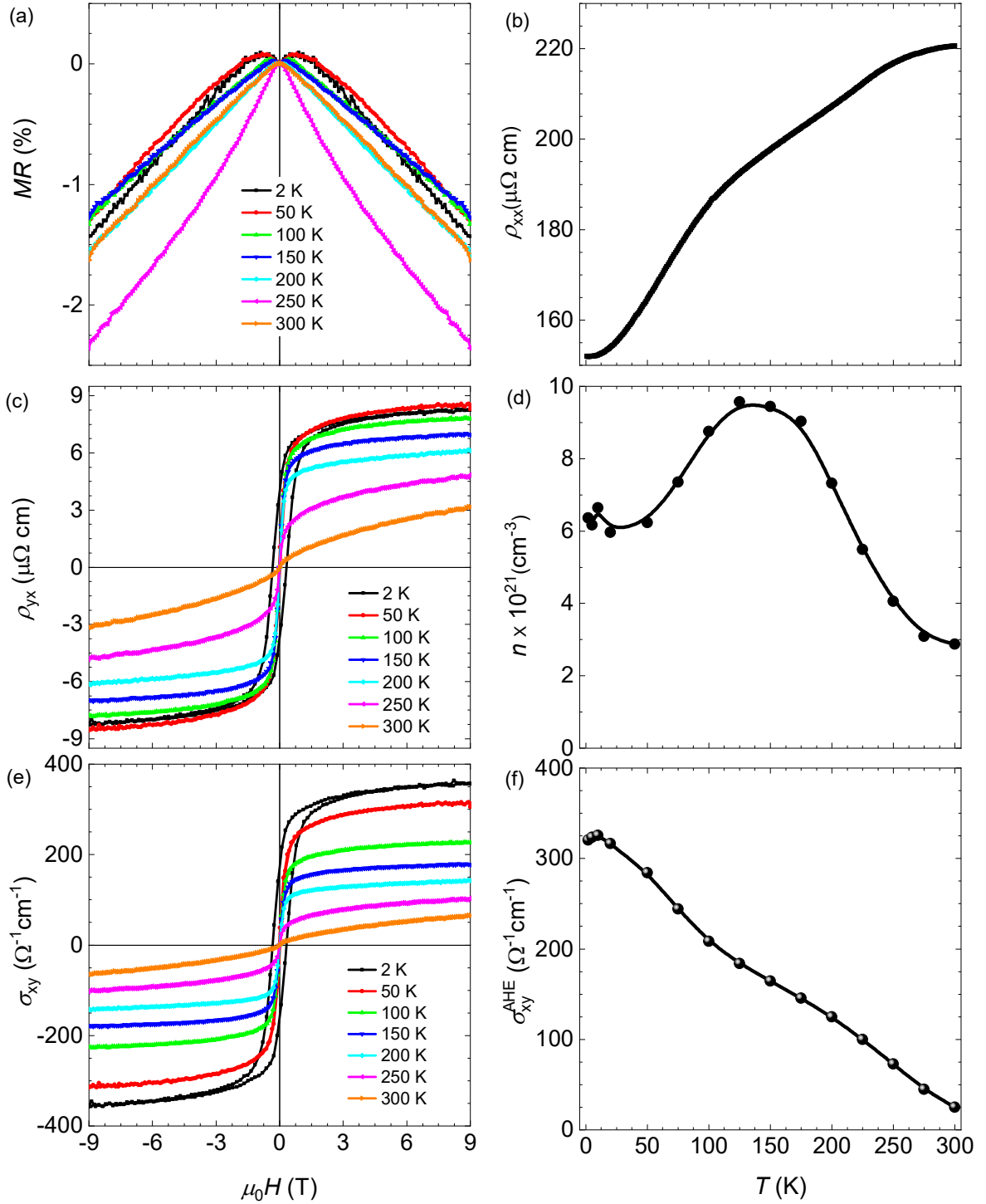
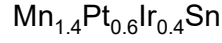


Figure 5.24. (a) Magnetoresistance (MR) (b) ρ_{xx} vs T (c) ρ_{yx} vs H (d) charge carrier concentration, n , vs T (e) σ_{xy} vs H , and (f) anomalous Hall conductivity, σ_{xy}^{AHE} , vs T of $\text{Mn}_{1.4}\text{Pt}_{0.6}\text{Ir}_{0.4}\text{Sn}$.

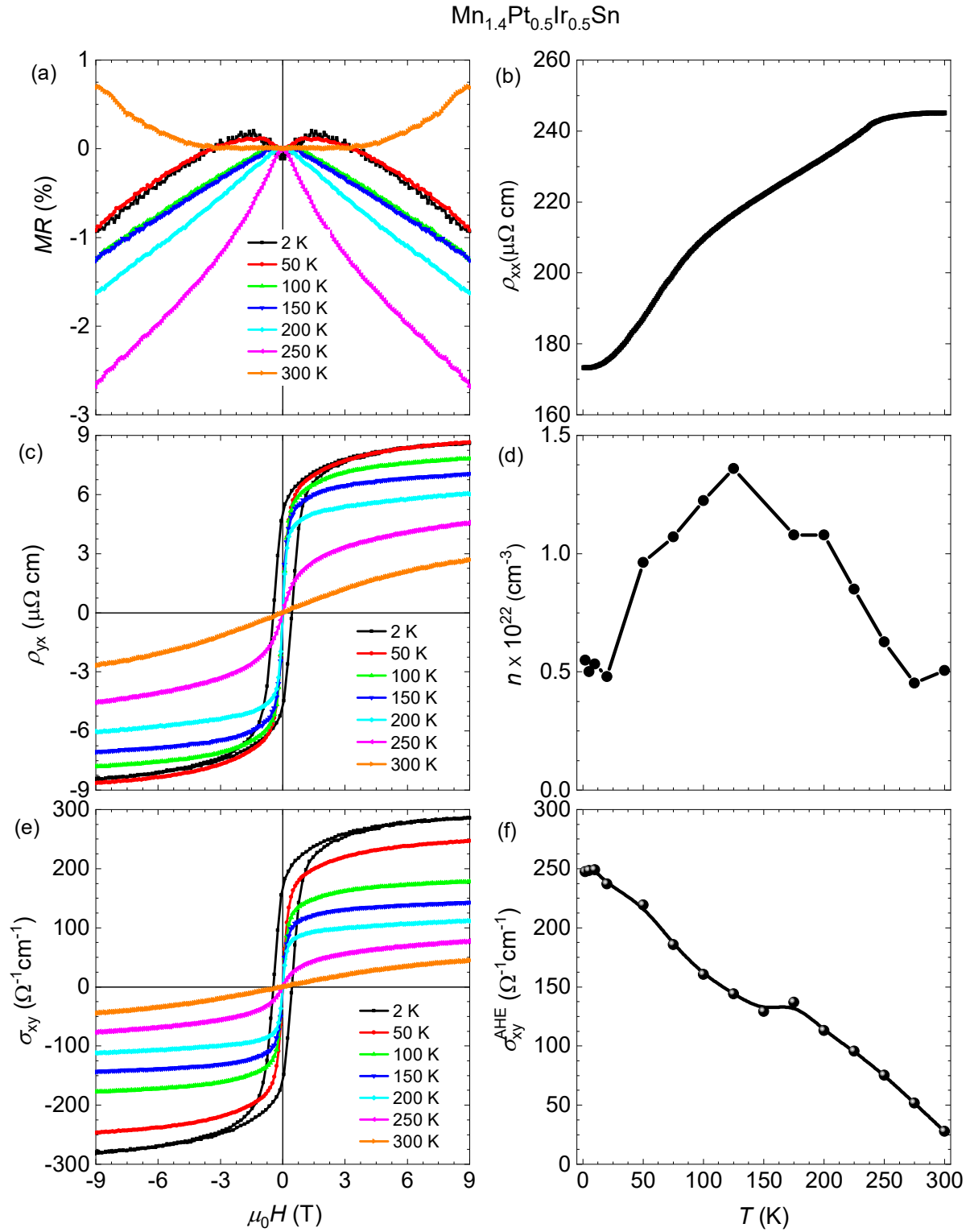


Figure 5.25. (a) Magnetoresistance (MR) (b) ρ_{xx} vs T (c) ρ_{yx} vs H (d) charge carrier concentration, n , vs T (e) σ_{xy} vs H , and (f) anomalous Hall conductivity, σ_{xy}^{AHE} , vs T of $\text{Mn}_{1.4}\text{Pt}_{0.5}\text{Ir}_{0.5}\text{Sn}$.

Mn_{1.4}Pt_{0.4}Ir_{0.6}Sn

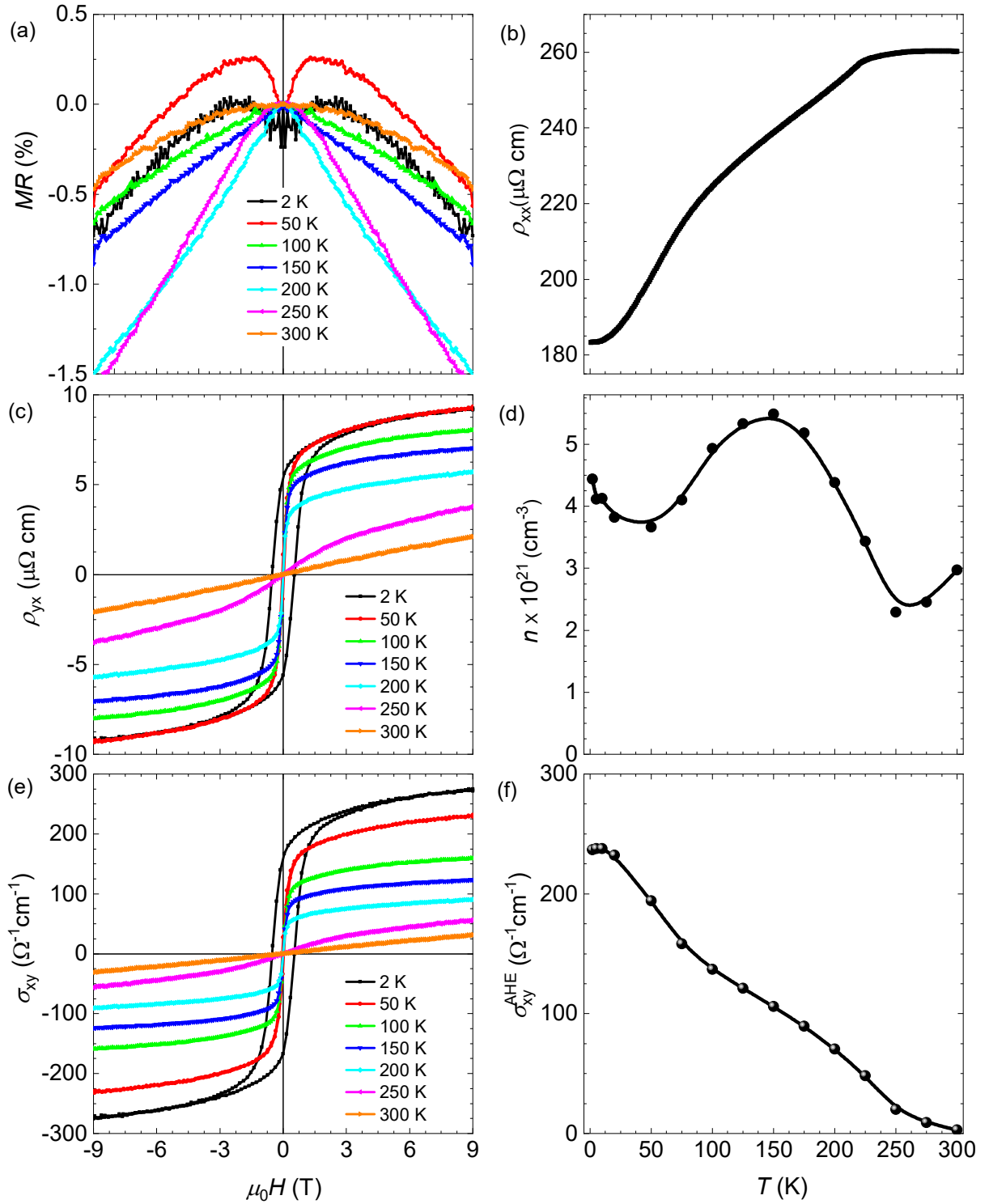


Figure 5.26. (a) Magnetoresistance (MR) (b) ρ_{xx} vs T (c) ρ_{yx} vs H (d) charge carrier concentration, n , vs T (e) σ_{xy} vs H , and (f) anomalous Hall conductivity, σ_{xy}^{AHE} , vs T of Mn_{1.4}Pt_{0.4}Ir_{0.6}Sn.

Mn_{1.4}Pt_{0.3}Ir_{0.7}Sn

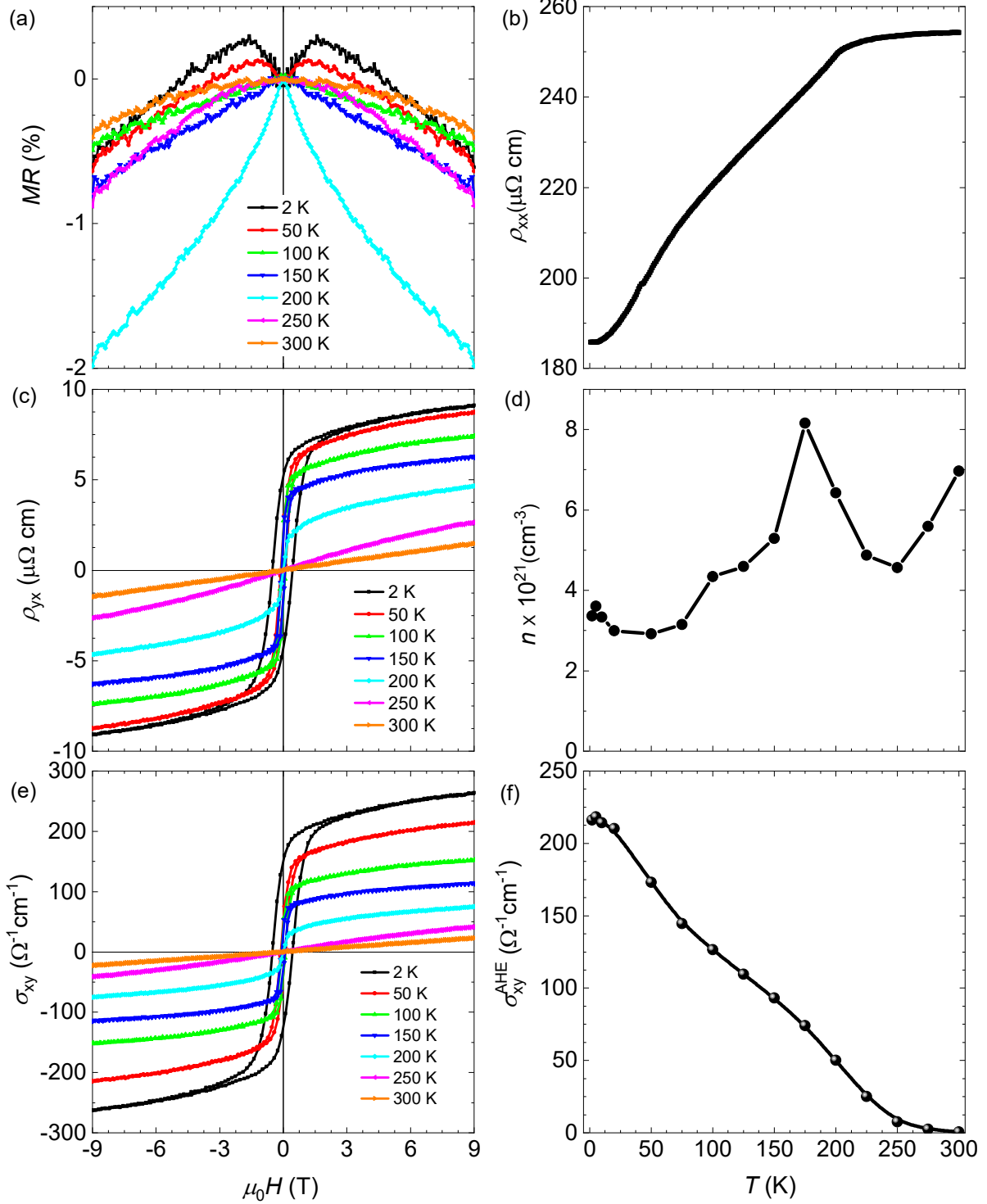


Figure 5.27. (a) Magnetoresistance (MR) (b) ρ_{xx} vs T (c) ρ_{yx} vs H (d) charge carrier concentration, n , vs T (e) σ_{xy} vs H , and (f) anomalous Hall conductivity, σ_{xy}^{AHE} , vs T of Mn_{1.4}Pt_{0.3}Ir_{0.7}Sn.

Mn_{1.4}Pt_{0.2}Ir_{0.8}Sn

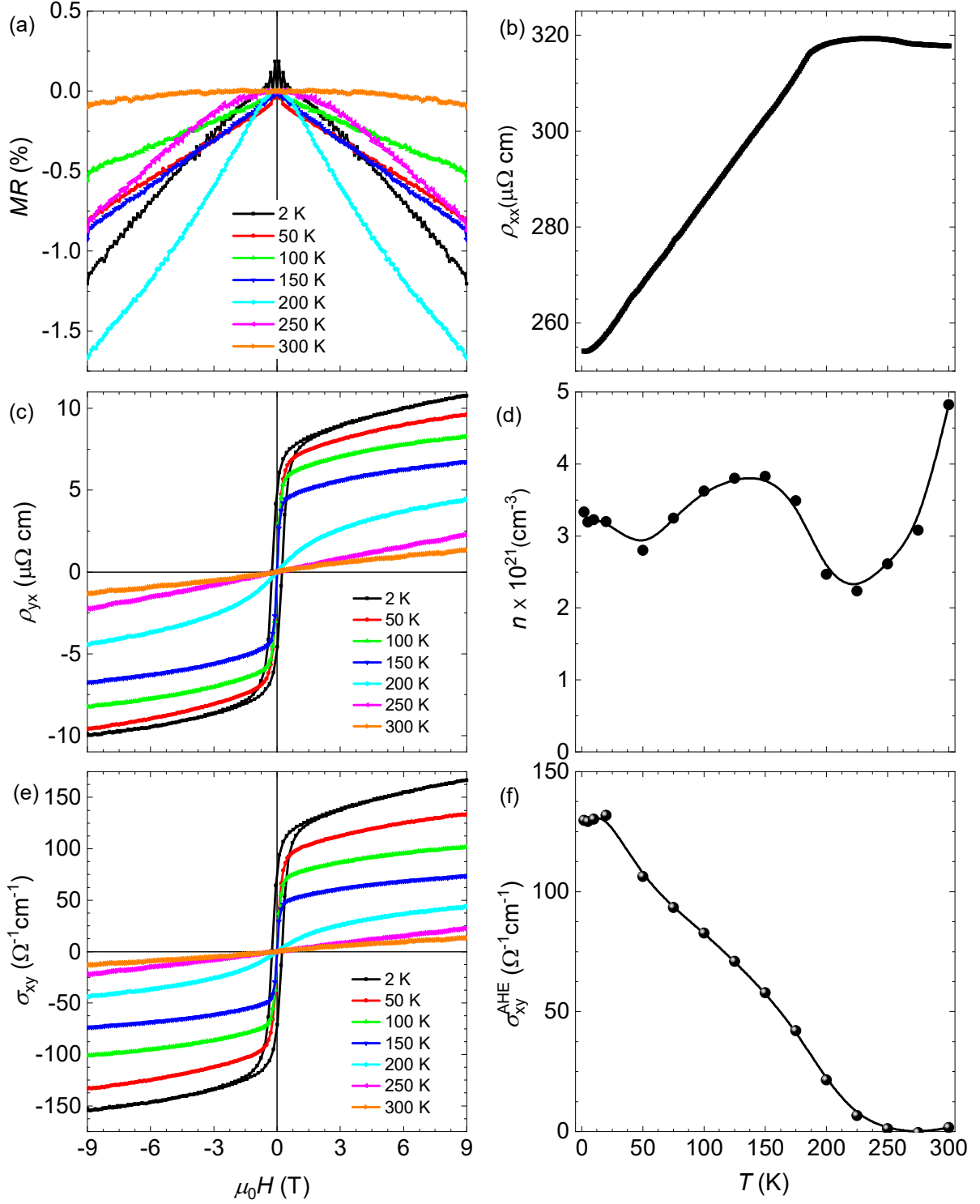


Figure 5.28. (a) Magnetoresistance (MR) (b) ρ_{xx} vs T (c) ρ_{yx} vs H (d) charge carrier concentration, n , vs T (e) σ_{xy} vs H , and (f) anomalous Hall conductivity, σ_{xy}^{AHE} , vs T of Mn_{1.4}Pt_{0.2}Ir_{0.8}Sn.

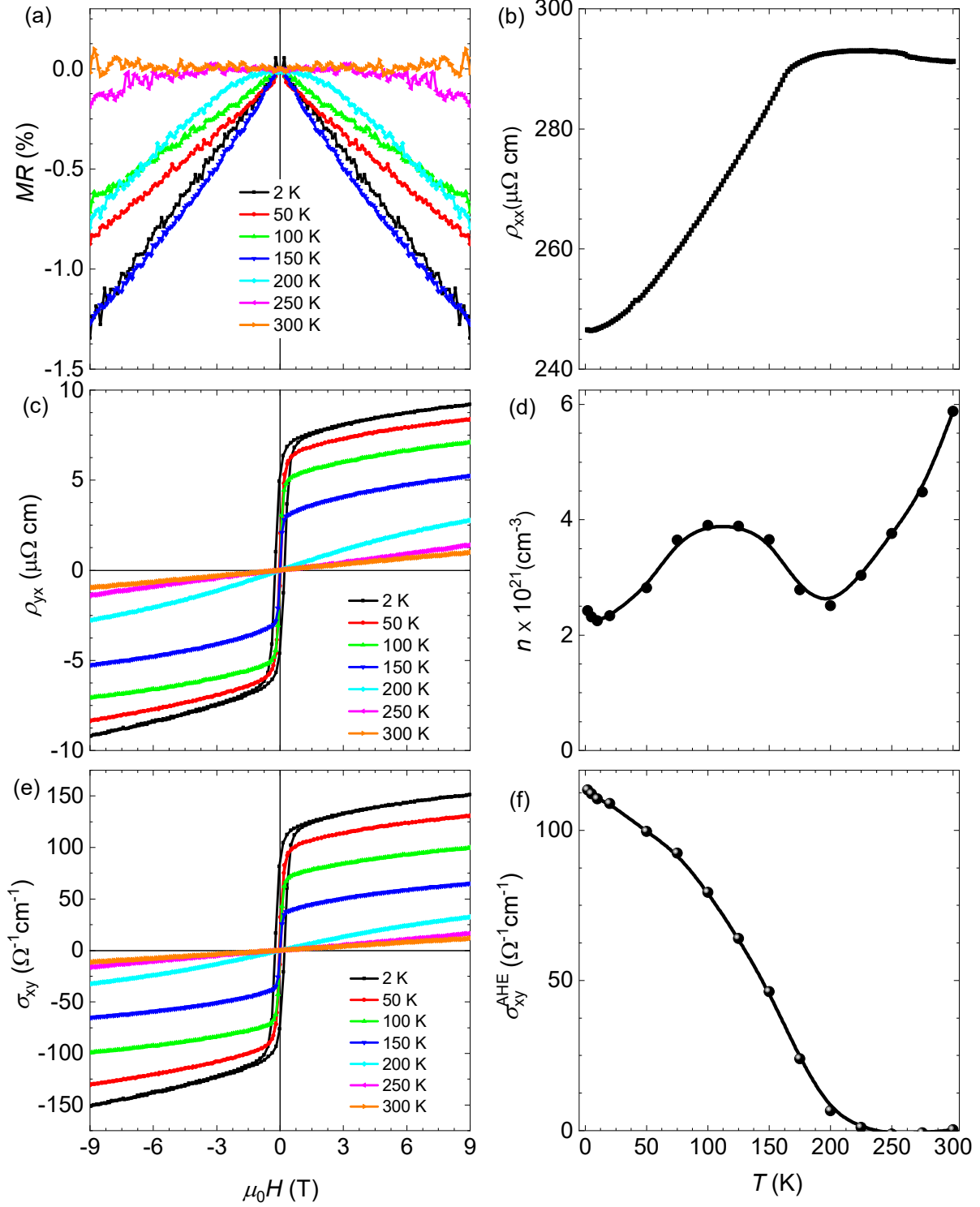
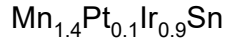


Figure 5.29. (a) Magnetoresistance (MR) (b) ρ_{xx} vs T (c) ρ_{yx} vs H (d) charge carrier concentration, n , vs T (e) σ_{xy} vs H , and (f) anomalous Hall conductivity, σ_{xy}^{AHE} , vs T of $\text{Mn}_{1.4}\text{Pt}_{0.1}\text{Ir}_{0.9}\text{Sn}$.

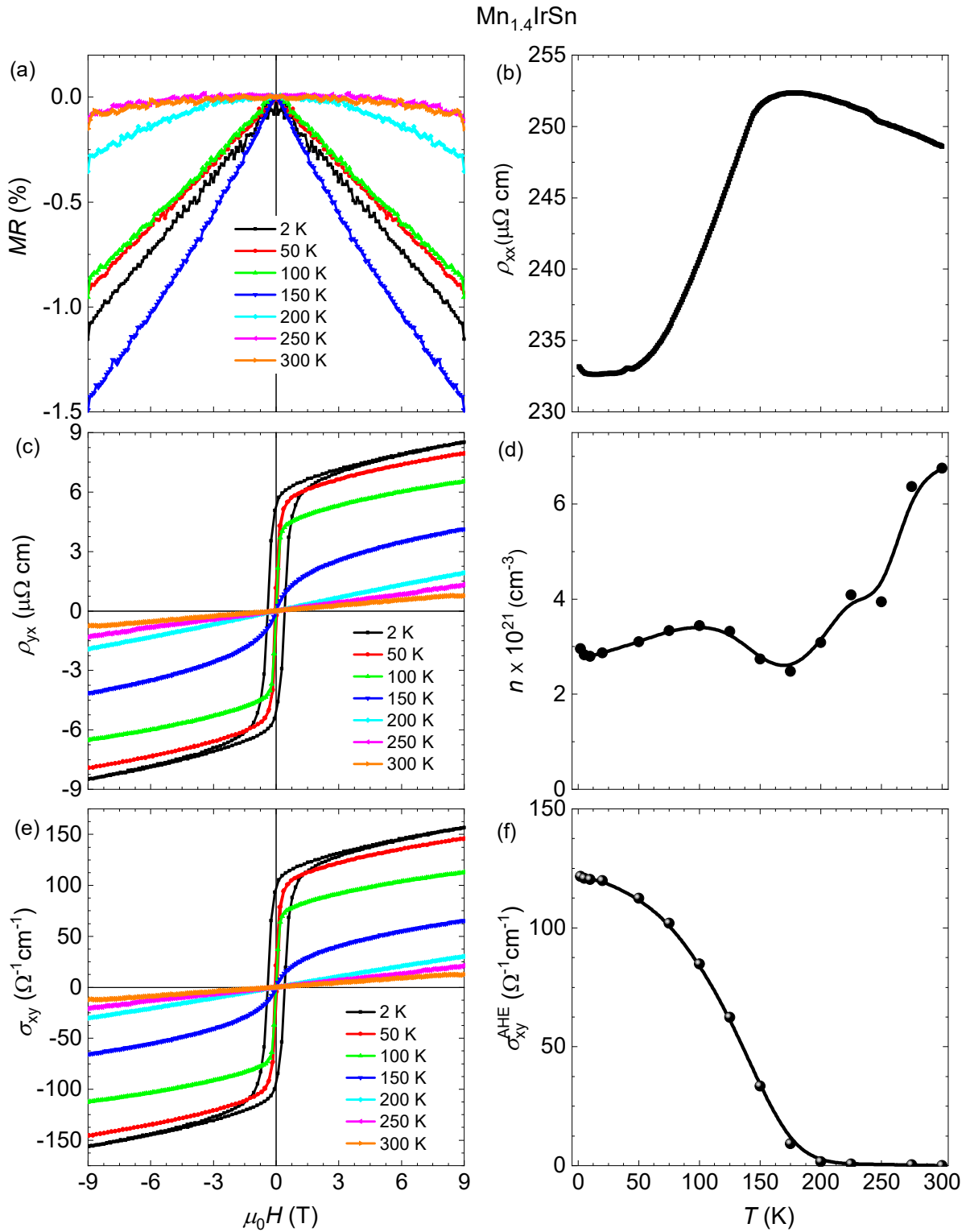


Figure 5.30. (a) Magnetoresistance (MR) (b) ρ_{xx} vs T (c) ρ_{yx} vs H (d) charge carrier concentration, n , vs T (e) σ_{xy} vs H , and (f) anomalous Hall conductivity, σ_{xy}^{AHE} , vs T of $\text{Mn}_{1.4}\text{IrSn}$.

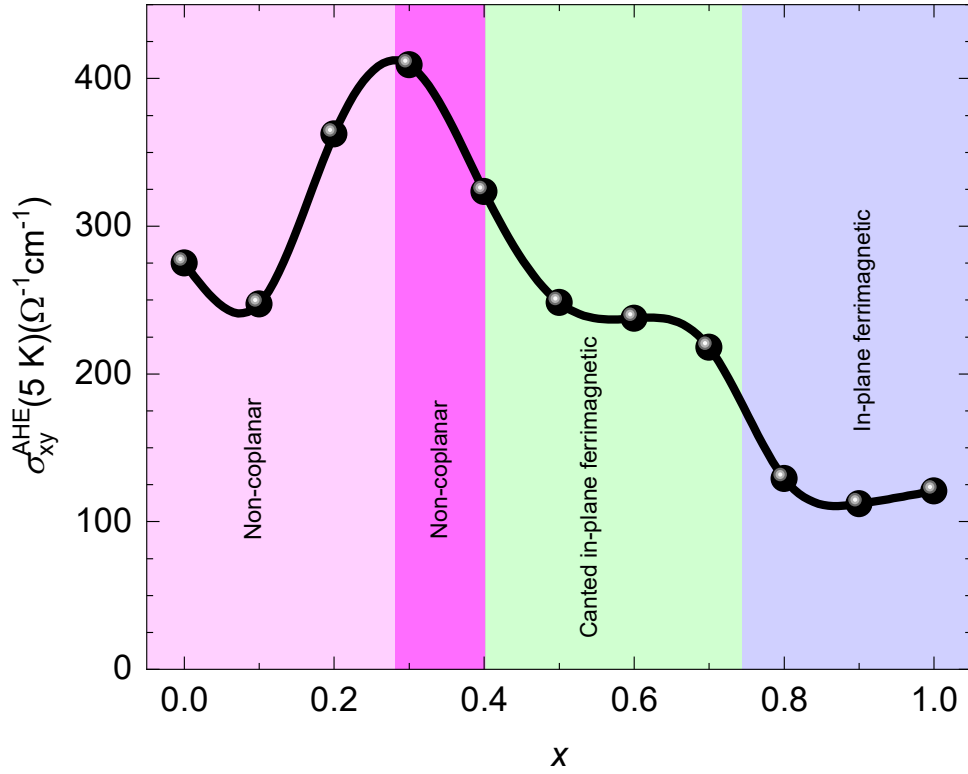


Figure 5.31. The variation of σ_{xy}^{AHE} at 5K as a function of Ir-concentration (x).

Figure 5.31 shows the variation of σ_{xy}^{AHE} as a function of Ir-concentration (x). σ_{xy}^{AHE} first increases and reaches to a maximum value of $405 \Omega^{-1}\text{cm}^{-1}$ for the compound $\text{Mn}_{1.4}\text{Pt}_{0.7}\text{Ir}_{0.3}\text{Sn}$ and then starts to decrease up to $x = 0.5$. From $x = 0.5$ to 0.7 , it is almost constant. A higher Ir-substitution leads to a reduction in σ_{xy}^{AHE} and becomes constant from $x = 0.8$ to 1.0 . The variation σ_{xy}^{AHE} as a function of Ir-concentration indicates that σ_{xy}^{AHE} does not depend on the magnetic moment. For $x = 0.1$ – 0.3 , it increases while the magnetic moment is constant and for $x = 0.5$ – 0.7 and 0.8 – 1.0 , it is constant while their magnetic moment displays a decreasing trend. Therefore, it can be concluded that the role of the magnetic structure is reflected in the variation of σ_{xy}^{AHE} and the same type of magnetic structure exhibits nearly the same value of σ_{xy}^{AHE} .

5.6. Single crystal growth

After studying the structural and the physical properties of polycrystalline samples of $\text{Mn}_{1.4}\text{Pt}_{1-x}\text{Ir}_x\text{Sn}$, the preparation of single crystals was attempted. The single crystals of these compounds would allow to investigate the anisotropy related properties and properties related to antiskyrmions. The single crystals were tried to grow with flux method following a similar method as described for single crystals of $\text{Mn}_{1.4}\text{PtSn}$. Several attempts were made with varying elements and flux ratios. In each trial, the reactions resulted in large single crystals but with a composition of $\text{Mn}_{22}(\text{Pt}_{1-x}\text{Ir}_x)_{30}\text{Sn}_{48}$. This particular problem was also observed while growing $\text{Mn}_{1.4}\text{PtSn}$. For $\text{Mn}_{1.4}\text{PtSn}$, even slightly varied composition other than $\text{Mn}:\text{Pt} = 3:1$ always leads to the crystals of $\text{Mn}_{22}\text{Pt}_{30}\text{Sn}_{48}$. Using a different element to flux ratio, the crystal growth of $\text{Mn}_{1.4}\text{Pt}_{0.9}\text{Ir}_{0.1}\text{Sn}$ was successful but for higher Ir-concentration, it was not successful even after several attempts. The results of $\text{Mn}_{1.4}\text{Pt}_{0.9}\text{Ir}_{0.1}\text{Sn}$ composition will be discussed at the end of this chapter.

Another way to get microtwin free crystals is detwinning of the micro-twinned crystals obtained from either optical floating zone method or Bridgman method. The detwinning of these crystals can be done by either application of uniaxial pressure or the external magnetic field¹²¹. Detwinning with the magnetic field has been successful for compounds having the martensitic transition temperature below the magnetic ordering temperature. This detwinning procedure is used very frequently in the shape-memory

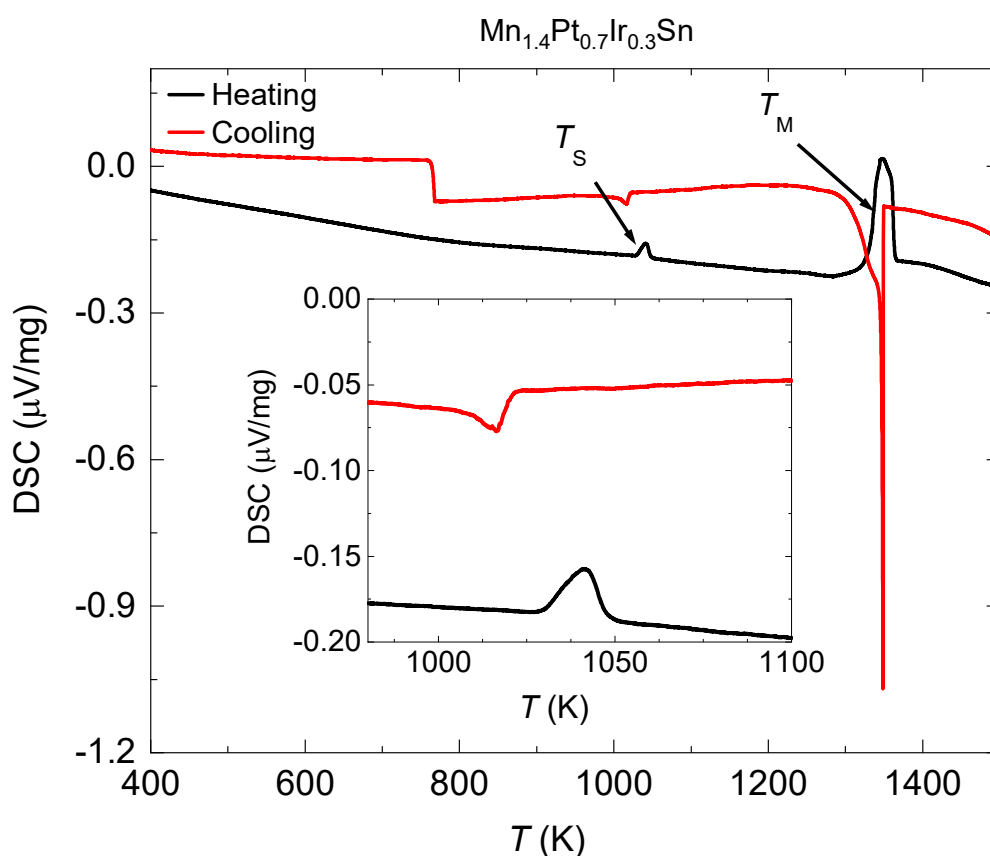


Figure 5.32. DSC measurement from 400 to 1500 K: inset is enlarged part of region having peaks corresponding to structural transition of $\text{Mn}_{1.4}\text{Pt}_{0.7}\text{Ir}_{0.3}\text{Sn}$.

compounds^{121,135–140}. From the DSC analysis of Ir-substituted compounds, the martensitic transition temperature is found to be close to 1073 K. Whereas, all the compounds belonging to this series have Curie temperature below 400 K. Therefore, the application of the magnetic field to detwin does not follow pre-criteria and it does not work. The only way left is then the application of uniaxial pressure at a temperature close to the martensitic transition temperature. At this temperature, a large movement of twin-boundary is expected. For this purpose, a holder was designed to apply uniaxial pressure but the crystal was broken in many pieces. Another attempt to apply uniaxial pressure was used by putting the microtwinned crystal in the spark plasma sintering method, but the quality of the resulting crystal became worse due to unknown reasons. This method can further be optimized by varying the temperature and pressure and might result in microtwin free crystals of $\text{Mn}_{1.4}\text{Pt}_{1-x}\text{Ir}_x\text{Sn}$.

Figure 5.32 shows the DSC curve measured for $x = 0.3$ Ir-concentration compound. A peak at 1350 K is observed, which corresponds to the melting point. The presence of a single peak without any splitting indicates the compound melts congruently and does not decompose into any other phase. The martensitic transition temperature observed of this compound is at 1045 K (the inset of Figure 5.32). Most of the compounds melt congruently, and both melting point and martensitic transition temperature increase with increasing Ir-concentration.

To grow the crystals from the Bridgman method, the polycrystalline samples were first prepared by the arc-melting process (see section 5.1). They were grounded into small pieces and loaded in the cone-shaped alumina crucible. This was put in a tantalum tube and then sealed with arc melting. The whole reaction mixture was put in the Bridgman furnace and heated to almost 100 K above the melting point to get a homogeneous liquid phase. It was kept there for 12 hours before starting the crystal growth process. After 12 hours, the crucible was slowly pulled out from furnace with a rate of 1 mm/h until the temperature of the sample gets at least 100 K lower than the martensitic transition temperature. At this temperature, the sample was kept for an additional few hours before switching off the furnace. The optical images of resulting crystals by this method are presented in Figure 5.33.

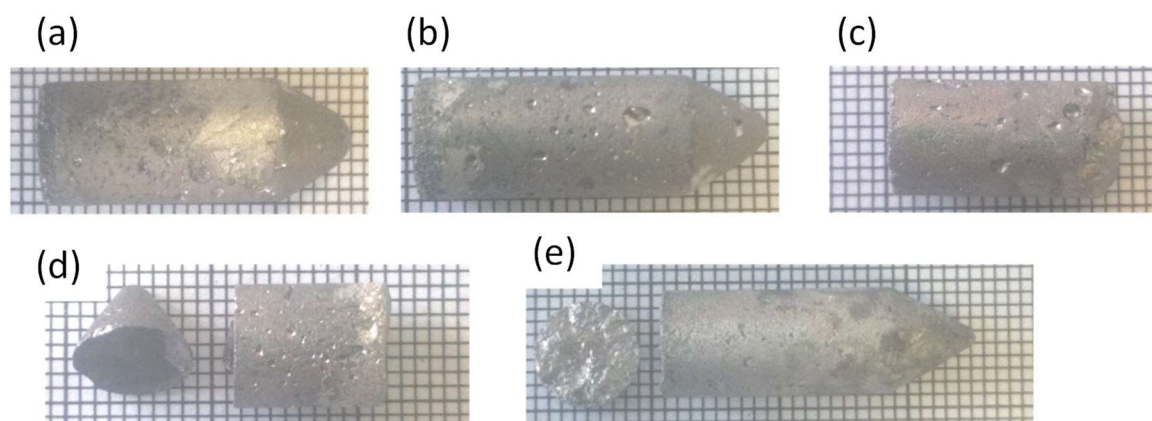


Figure 5.33. The optical picture of crystals grown by Bridgman method of compounds with Ir-concentration (a) $x = 0.1$ (b) $x = 0.2$ (c) $x = 0.3$ (d) $x = 0.4$, and (e) $x = 0.6$.

Figure 5.34 shows the Laue diffraction pattern of the compound $\text{Mn}_{1.4}\text{Pt}_{0.4}\text{Ir}_{0.6}\text{Sn}$. Upon analyzing these crystals with Laue diffraction patterns, the crystals were not a single crystal; instead they were twinned. As can be seen in the diffraction pattern, the diffraction pattern does not correspond to any single orientation. Moreover, there are four spots (inside of marked a red circle) present instead of a single spot. This means that in addition to the perpendicularly oriented microtwinned structure, each oriented grain also has a small degree misoriented crystal with mosaicity of 2–3 degree. Similar findings are observed for all the crystals grown by Bridgman method.

To know the size and morphology of the microtwinned crystals, the sample was polished and analyzed with polarized light microscopy. Figures 5.35(a), (b) and (c) show such images taken by the polarized light microscope. It can be clearly seen that different crystal grains display different contrasts. Some of the grains are quite large (of 50 μm) and are big enough to study the properties of antiskyrmions with LTEM by preparing thin lamella. Therefore, a piece of lamella was prepared from the largest grain using focused ion beam (FIB). Upon closely looking in transmission electron microscopy, it is found that these large grains are also microtwinned and composed of the smaller twin grains. The image taken by TEM is shown in Figure 5.35(d).

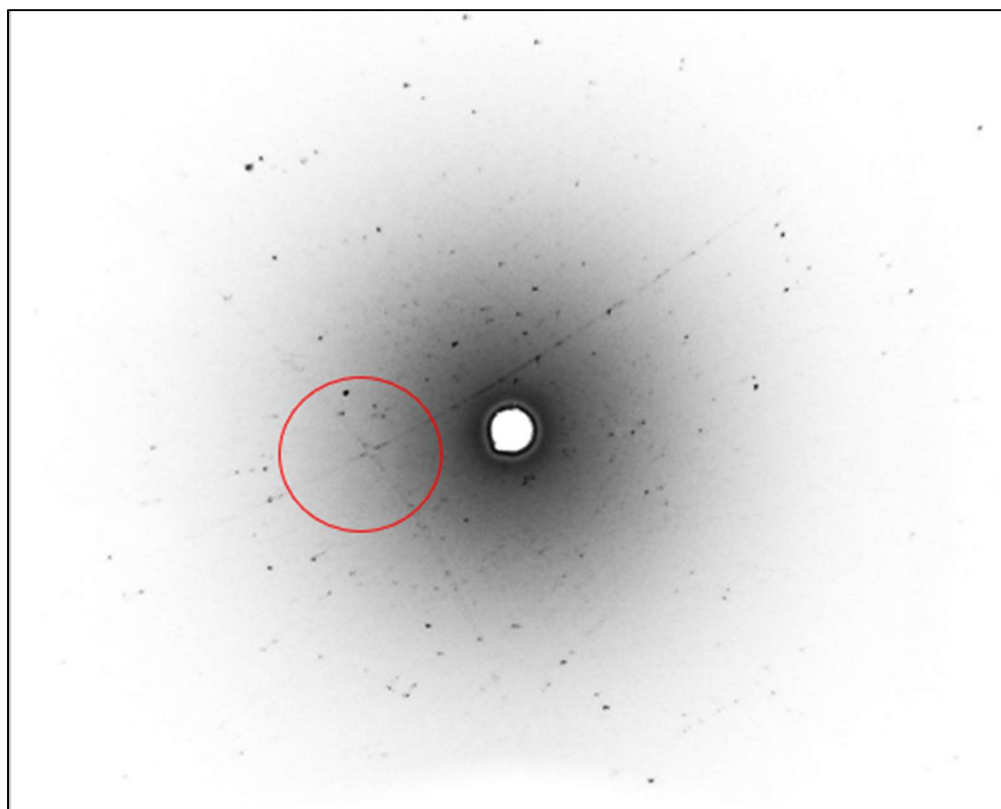


Figure 5.34. Laue diffraction pattern collected from the crystal of $\text{Mn}_{1.4}\text{Pt}_{0.4}\text{Ir}_{0.6}\text{Sn}$ obtained by the Bridgman method.

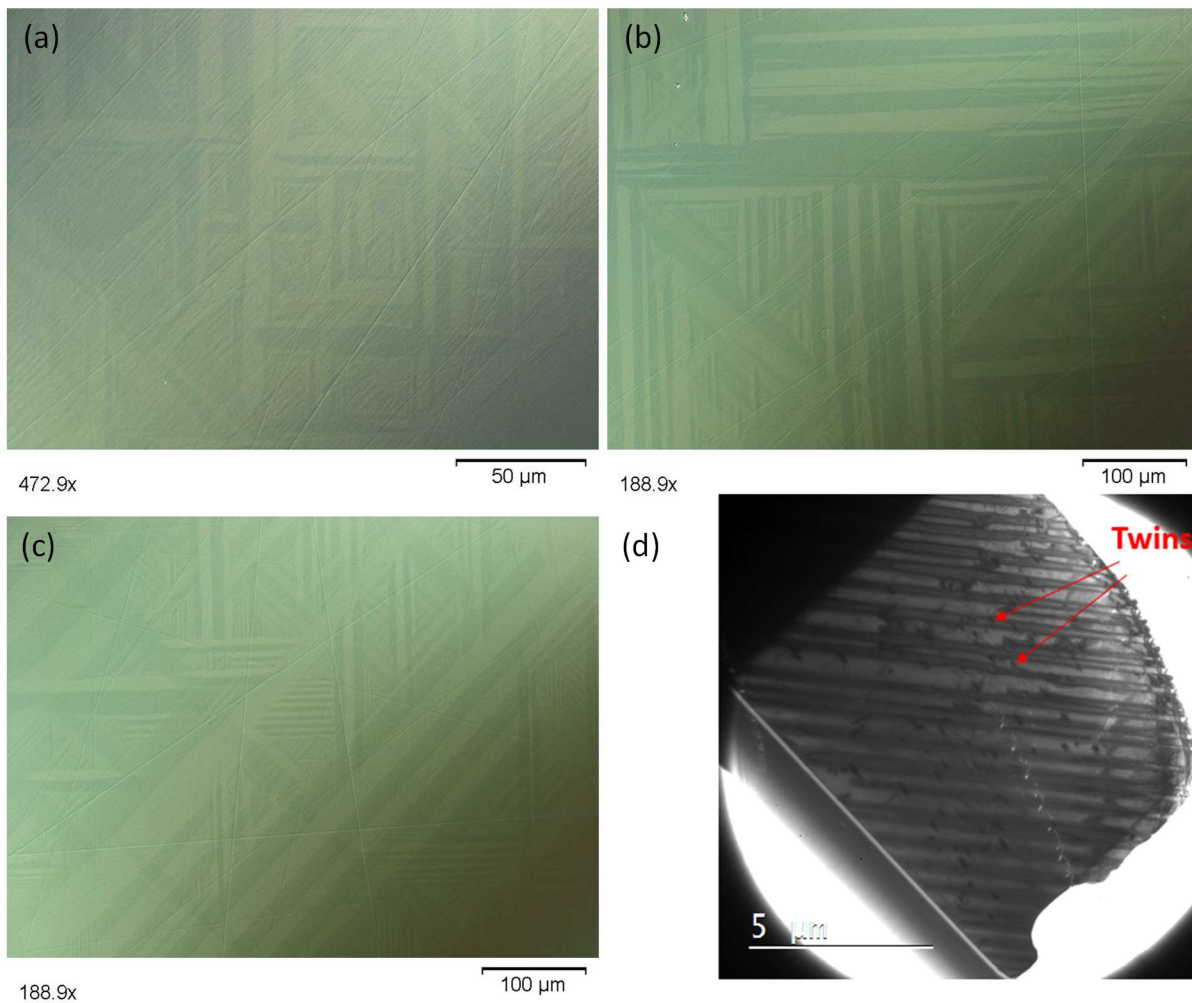


Figure 5.35. Polarized light microscope image of the crystal of compounds with Ir-concentration (a) $x = 0.2$ (b) $x = 0.3$ (c) $x = 0.6$. Different contrast corresponds to microtwinning structure. (d) transmission electron microscope image of a thin lamella prepared from the largest grain of compound $\text{Mn}_{1.4}\text{Pt}_{0.4}\text{Ir}_{0.6}\text{Sn}$.

Microtwin free single crystal of $\text{Mn}_{1.4}\text{Pt}_{0.9}\text{Ir}_{0.1}\text{Sn}$:

Following the same method to grow microtwin free crystals of $\text{Mn}_{1.4}\text{PtSn}$ from flux method, microtwin free single crystals of the compound with $x = 0.1$ can be grown by taking a higher amount of flux. High-purity elements Mn (Sigma-Aldrich, 99.999 %), Pt (Sigma-Aldrich, 99.999 %) and Ir (Sigma-Aldrich, 99.999 %) were taken into 3:0.9:0.1 ratio and weighed accordingly for 0.5 g. They were put in a dried alumina crucible along with 10 g of Sn (Sigma-Aldrich, 99.999 %). A higher ratio of Sn flux was needed, probably due to the limited solubility of Ir in Sn. The alumina crucible was sealed in the quartz tube with 0.2 bar argon atmosphere inside. The quartz tube was put in the box furnace and heated to 1323 K with the rate of 200 K/h and it was held for 24 hours to get a homogenized mixture. After 24 hours, the mixture was cooled rapidly to 923 K with a rate of 200 K/h and then slowly cooled to 723 K with a rate of 2 K/h. The excess flux was removed by centrifugation. A chunk of many small jointed crystals together was obtained and bigger crystals were separated mechanically. Some Sn flux was present on the surface of crystals and removed by putting the crystals in dilute HCl for few hours. The obtained crystals were silvery shiny with the same morphology as the parent compound $\text{Mn}_{1.4}\text{PtSn}$. Optical images of as-grown crystals are presented in Figure 5.36(a). The facets with rectangular shape correspond to [100] and [001] and triangular facet corresponds to [112]. The Laue diffraction pattern of [001] is shown in Figure 5.36(b) in which the four-fold pattern indicates a tetragonal symmetry of the compound.

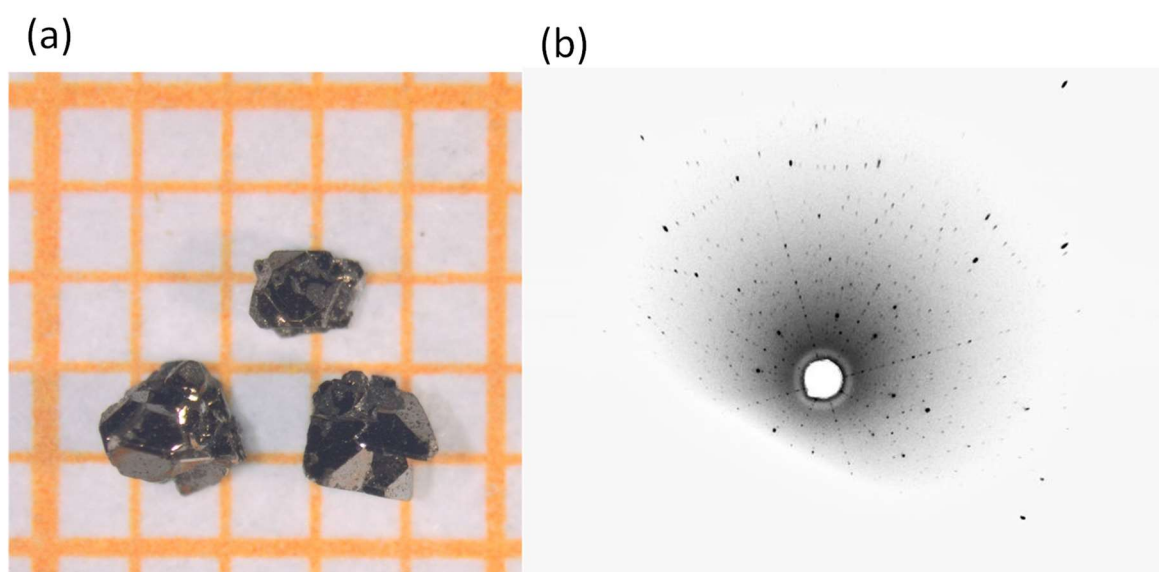


Figure 5.36. (a) As-grown single crystal from flux method on mm-scale grid paper (b) Laue Pattern for the crystallographic direction [001].

The magnetic properties of $\text{Mn}_{1.4}\text{Pt}_{0.9}\text{Ir}_{0.1}\text{Sn}$ single crystals were measured in an unknown direction. The magnetization as a function of the temperature is shown in Figure 5.37(a). The T_C was observed at 365 K which is slightly lowered compared to T_C obtained in the polycrystalline sample. However, T_{SR} is found to be 170 K, which is higher than its

polycrystalline sample (125 K). The increase in the T_{SR} value might be due to different Mn concentration in the single crystal. A detailed single-crystal refinement is needed to support the chemical composition precisely.

Due to large enough size of the single crystals, the transport properties and LTEM study for antiskyrmions can be done in the future. The flux method might be a good option to get microtwin free crystals with higher Ir-concentration by selecting an appropriate ratio of Mn, Pt, Ir, and Sn. This series of compounds provides an interesting playground of both out-of-plane and in-plane anisotropy. The out-of-plane anisotropy (moments along c -direction) along with DMI stabilize the antiskyrmions, whereas, in-plane anisotropy may give rise to a new type of topological spin textures such as magnetic bimerons^{141,142}.

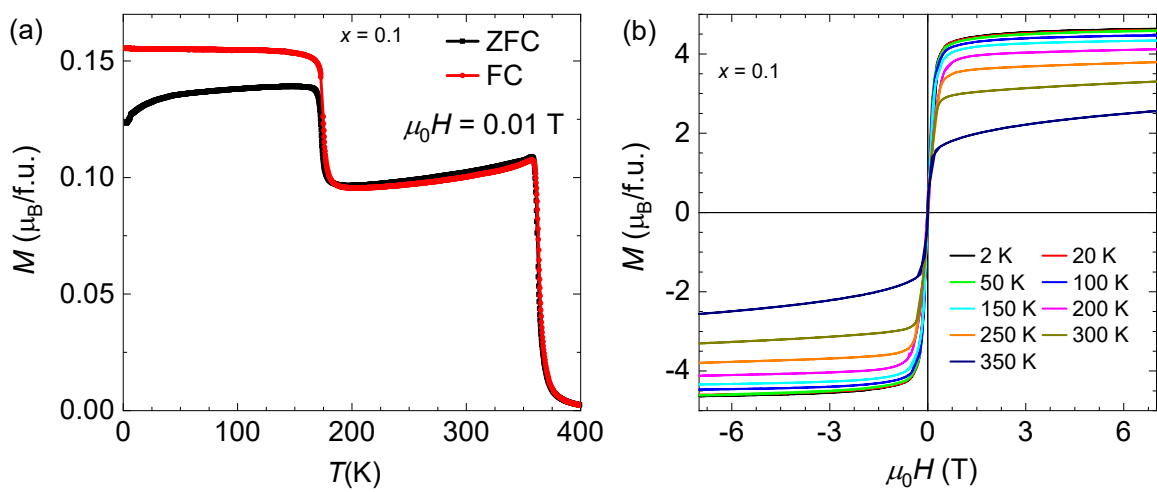


Figure 5.37. (a) M vs T for applied field of 0.01 T (b) M vs H at different temperatures of $Mn_{1.4}Pt_{0.9}Ir_{0.1}Sn$.

6. $\text{Mn}_{1.4}\text{Y}_x\text{PtSn}$ ($\text{Y} = \text{Co, Ni, Cu}$; $x = 0.1\text{--}0.6$)

Besides hosting antiskyrmions²⁷, $\text{Mn}_{1.4}\text{PtSn}$ is also structurally enriched and forms a superstructure of the tetragonal Heusler compound with ordered vacancies¹¹⁹. The attempts to fill these vacancies with Mn atoms (formation of $\text{Mn}_{1.4+x}\text{PtSn}$) lead to the segregation of Mn in the form of secondary phases with Pt or Sn^{93,94}. Therefore, the maximum Mn concentration in this compound as a single-phase is 1.4. Since Mn cannot go to the vacancies sites, it is an important question, can other transition-metal atoms be filled at these vacancies? If so, how the structural and physical properties will be modified? To address these questions, three series of polycrystalline compounds were prepared by adding cobalt, nickel, and copper at the place of vacancies in $\text{Mn}_{1.4}\text{PtSn}$. In this chapter, the effects of the addition of these transition metals in the crystal structure and magnetic properties are discussed.

6.1. Sample preparation

All the polycrystalline samples of $\text{Mn}_{1.4}\text{Y}_x\text{PtSn}$ ($\text{Y} = \text{Co, Ni, Cu}$; $x = 0.1\text{--}0.6$) were prepared by the induction melting process in an argon atmosphere. Highly pure elements (Sigma-Aldrich, 99.999 %) were weighed into a stoichiometric ratio and put in an alumina crucible. An additional 1 mg/g Mn element was taken to compensate the weight loss during the melting. The alumina crucible containing all the elements was then put at the center of the copper coil of the induction melting setup. The high-frequency current was applied in the copper coil and slowly increased to heat the elements. After sufficient current, all the elements turned into liquid and got mixed together (as described in section 3.2). At this condition (same value of electric current), the melt was kept for few minutes to achieve good homogeneity. Afterward, the current was switched off and the sample was allowed to cool down. The ingot was then flipped and melted again. This procedure was repeated three times to increase homogenization. The prepared polycrystalline sample was sealed in a quartz tube with a partial argon atmosphere and annealed at 1073 K for 7 days. After that, it was quenched in an ice-water mixture.

The quality of the obtained materials was characterized by powder X-ray diffraction (PXRD) (Huber Guinier G670 with $\text{CuK}\alpha 1$ radiation, $\lambda = 1.5406 \text{ \AA}$) while the composition was measured with EDX attached with SEM. XRD patterns were refined by Topas software for structural analysis.

6.2. Tetragonal superstructure

6.2.1. Cobalt addition

Figure 6.1 shows the powder XRD patterns of $\text{Mn}_{1.4}\text{Co}_x\text{PtSn}$ ($x = 0.1\text{--}0.6$). From the XRD patterns, it can be seen that the compounds with cobalt addition up to $x = 0.2$ exist in the tetragonal crystal structure (Figures 6.1(a), (b)). Further addition of cobalt leads to the

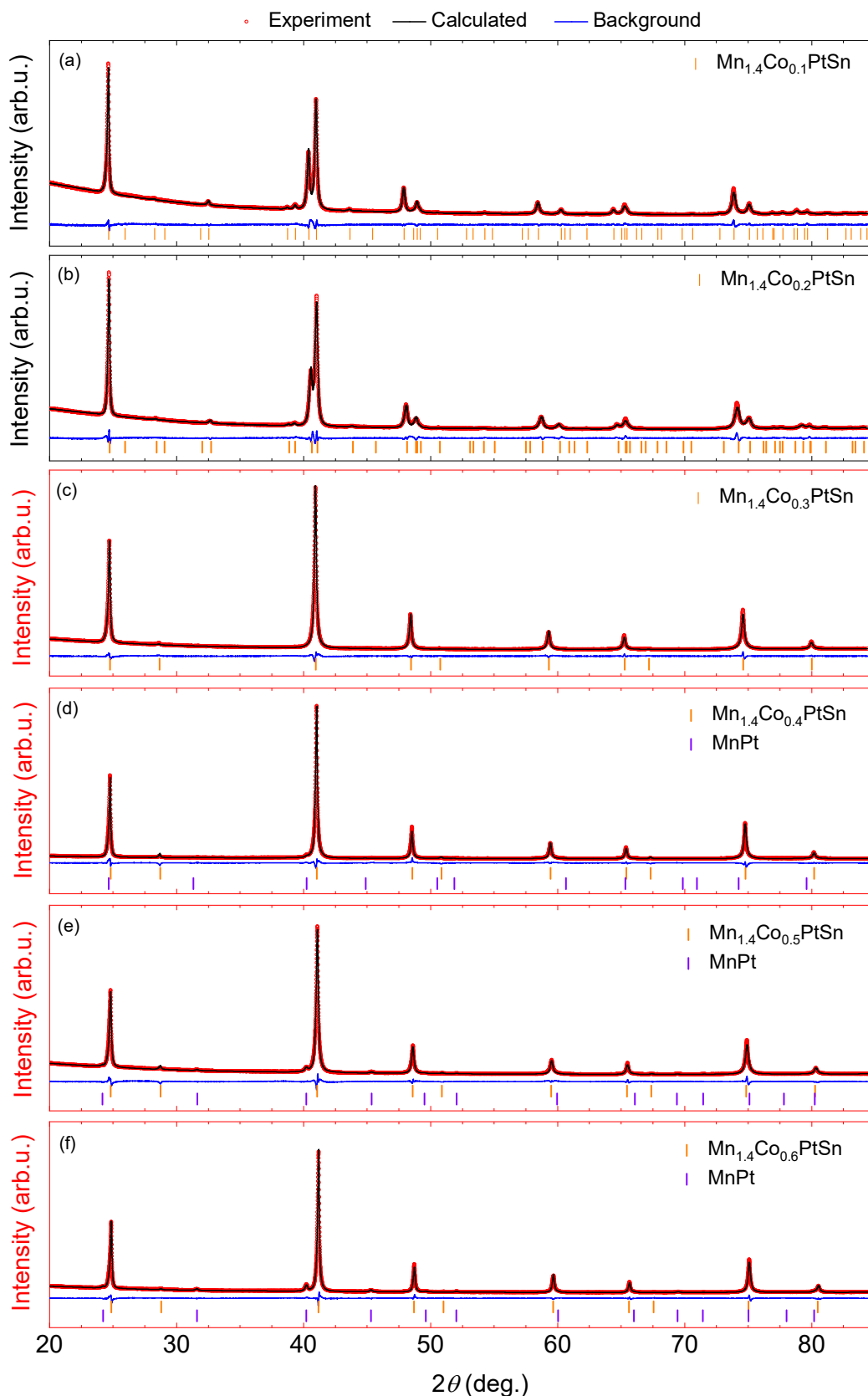


Figure 6.1. The experimental (red open circle), calculated (black) XRD pattern along with background (blue color) and the Bragg position of majority phase (orange) and minority phase (purple) for the compounds belonging to series $\text{Mn}_{1.4}\text{Co}_x\text{PtSn}$. Plots with black and red color box are representation of tetragonal and cubic crystal structure, respectively.

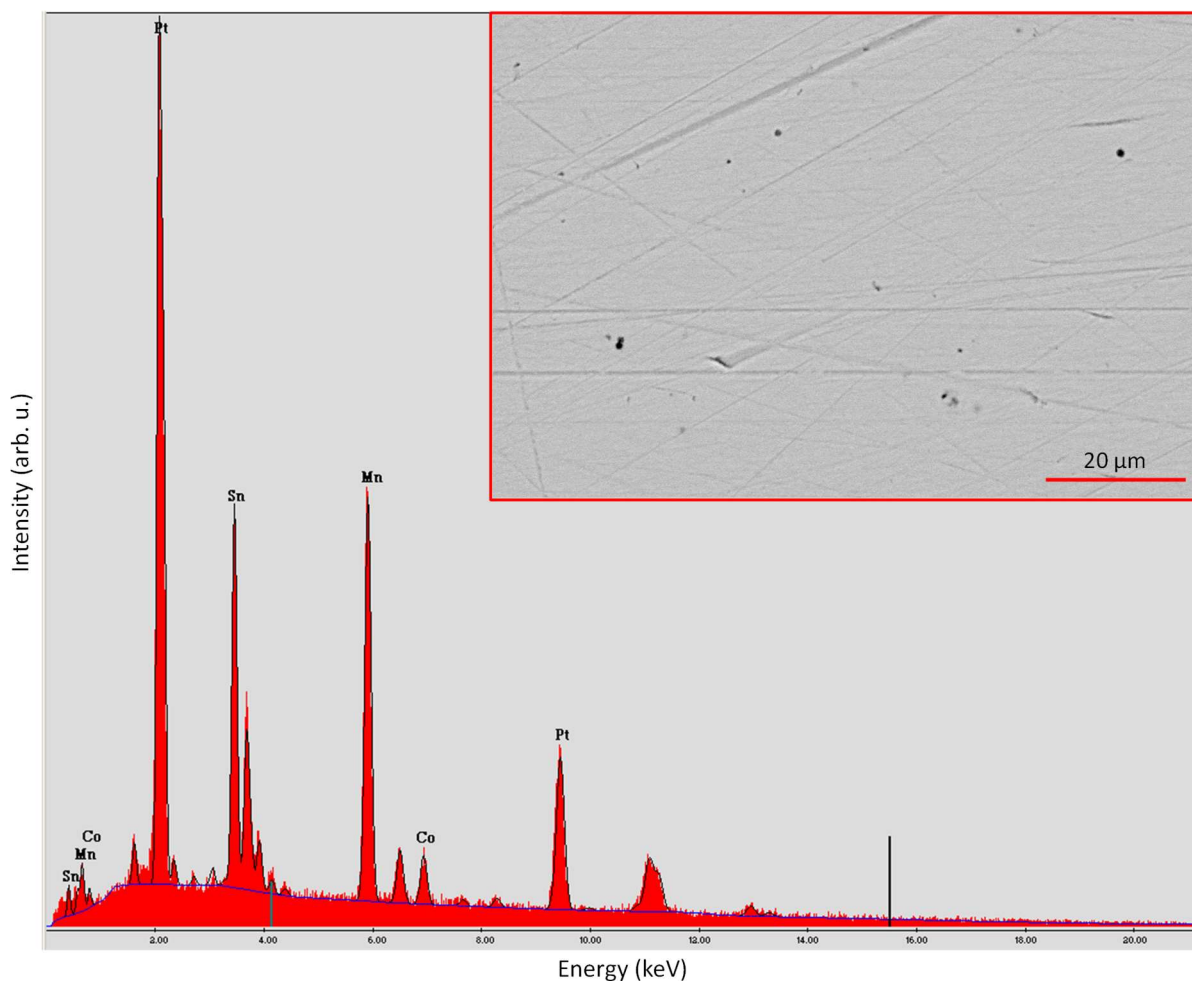


Figure 6.2. EDX spectrum along with SEM image as inset of compound $\text{Mn}_{1.4}\text{Co}_{0.2}\text{PtSn}$.

transformation from tetragonal to the cubic structure as evidence of the peak splitting corresponding to the tetragonal structure is absent for $x = 0.3$ – 0.6 (Figures 6.1(c)–(f)).

Figure 6.1(c) shows the XRD pattern of $\text{Mn}_{1.4}\text{Co}_{0.3}\text{PtSn}$ ($x = 0.3$). It can be seen that the compound exists as a single phase with a cubic structure as no foreign peaks are identified. For higher Co-concentration compounds ($x \geq 0.4$), the presence of extra impurity peaks is identified in the diffraction patterns. Regardless of different crystal structures and the presence of a secondary phase, complete Reitvald refinement was done for all the compounds. The results of the refined patterns showing the agreement between experiment and calculated patterns are presented in Figure 6.1. For the compounds $\text{Mn}_{1.4}\text{Co}_{0.1}\text{PtSn}$ (Figure 6.1(a)) and $\text{Mn}_{1.4}\text{Co}_{0.2}\text{PtSn}$ (Figure 6.1(b)), the diffraction patterns show that the compounds are in single-phase with no detectable impurities. The presence of the superstructure peaks in the diffraction patterns indicates that the crystal structure of these two compounds is related to the tetragonal superstructure of $\text{Mn}_{1.4}\text{PtSn}$. The refinement reveals that the addition of Co atoms goes to the vacancies site (4b) with a small chemical disordering with Mn present at 4a site (Mn1). The occupancies of the Wyckoff positions 8d (Mn2), 8c (Pt) and 8d (Sn) are close to 100 percent.

For the compounds with higher Co-concentration ($x \geq 0.3$), the obtained crystals structure is cubic. The refinement reveals that the cubic structure corresponds to the inverse Heusler structure with the space group of $F\bar{4}3m$. The addition of Co goes to $4a$ site which is shared with Mn element.

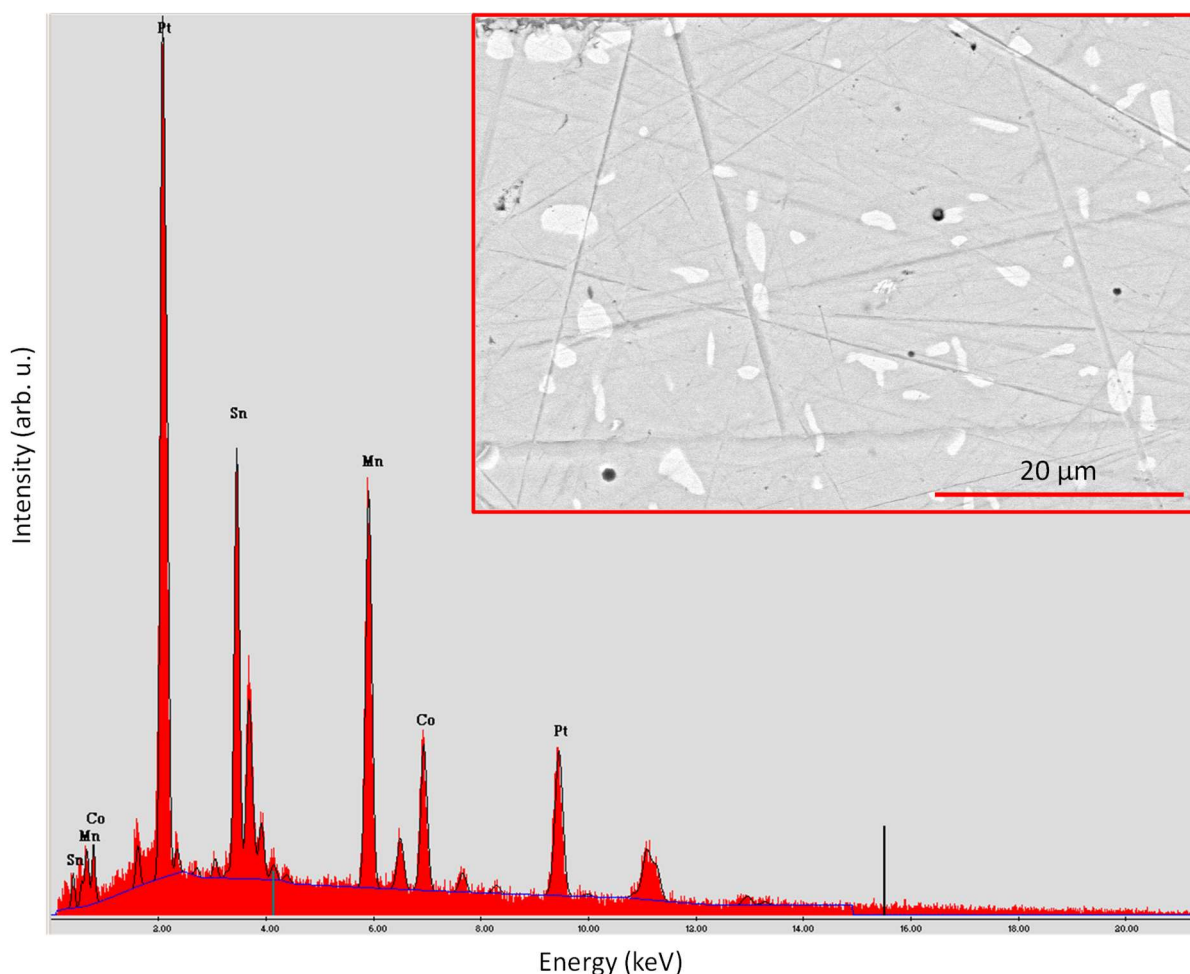


Figure 6.3. EDX spectrum along with SEM image as an inset of compound $Mn_{1.4}Co_{0.6}PtSn$.

As discussed above, the XRD patterns of the compound $Mn_{1.4}Co_{0.3}PtSn$ show a single-phase cubic structure without any detectable of impurity while for compounds with higher Co-concentration, there are extra impurity peaks in the diffraction patterns. The intensity of the peaks increases with increasing Co content, which indicates that the more impurity phase gets formed with increasing Co-concentration. Refinement, together with the support of EDX, reveals that the impurity phase corresponds to MnPt. For $Mn_{1.4}Co_{0.4}PtSn$, $Mn_{1.4}Co_{0.5}PtSn$, and $Mn_{1.4}Co_{0.6}PtSn$, the amount of MnPt phase is 1, 3 and 8 percent, respectively.

Figures 6.2 and 6.3 show the EDX spectra of the compound $Mn_{1.4}Co_{0.2}PtSn$ and $Mn_{1.4}Co_{0.6}PtSn$, respectively. The inset in these Figures shows the SEM images of the polished surface. As can be seen in Figure 6.2 inset ($Mn_{1.4}Co_{0.2}PtSn$), there is no extra impurity visible as contrasts throughout the sample is the same. Whereas, for Figure 6.3 inset ($Mn_{1.4}Co_{0.6}PtSn$), two different contrasts are clearly discernable in the SEM image,

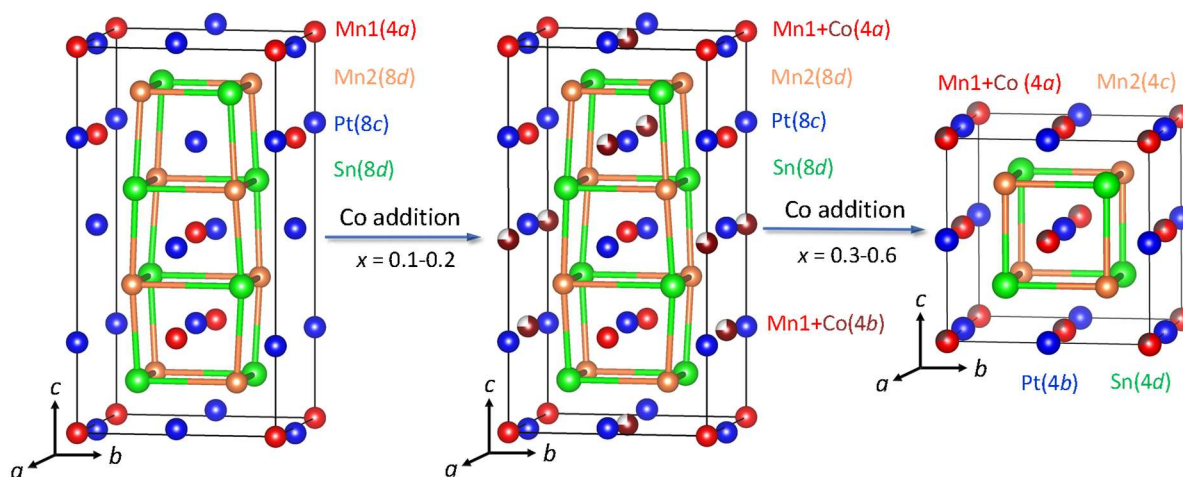


Figure 6.4. The schematic of change in the crystal structure with cobalt addition.

indicating the presence of two different phases. The dark and the bright contrasts in the image correspond to the majority phase and MnPt, respectively. The composition of the majority phase obtained by EDX on $\text{Mn}_{1.4}\text{Co}_{0.6}\text{PtSn}$ (with the highest impurity phase) is $\text{Mn}_{1.33}\text{Co}_{0.6}\text{Pt}_{0.97}\text{Sn}_{1.1}$. This indicates that the cobalt atoms completely go into the crystal lattice and do not appear in the form of the secondary phase. The reduction in Mn and Pt amount in the majority phase is due to the formation of MnPt impurity. The schematic of change in the crystal structure with the addition of cobalt atoms is shown in Figure 6.4.

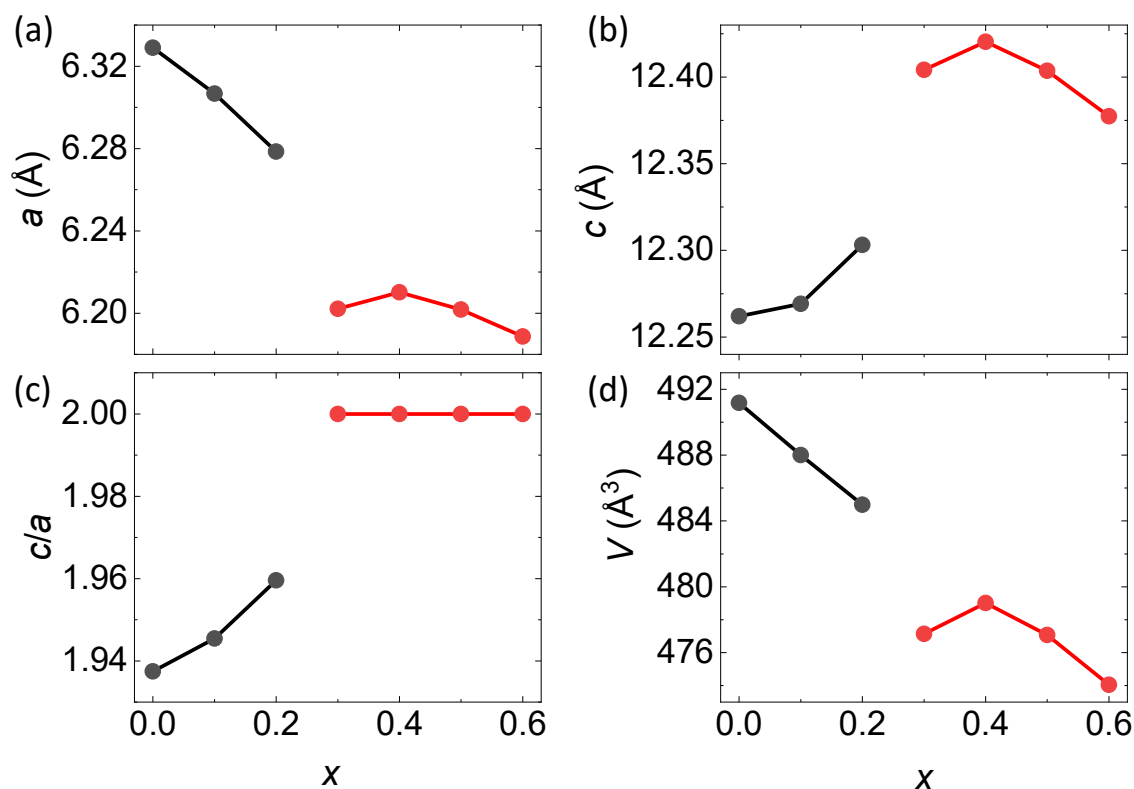


Figure 6.5. The lattice parameters as a function of cobalt addition for $\text{Mn}_{1.4}\text{Co}_x\text{PtSn}$. The black and red color curves are representation of tetragonal and cubic crystal structure, respectively.

The lattice parameters of the compounds of $\text{Mn}_{1.4}\text{Co}_x\text{PtSn}$, obtained from XRD refinement, are presented in Figure 6.5. For the comparison of the lattice parameters of the cubic phase with the tetragonal phase, c of the cubic phase is presented by $2c$. For the tetragonal structure ($x \leq 0.2$), a decreases while c increases monotonically (Figure 6.5(a), (b)). The resultant c/a ratio, therefore, increases with the addition of Co element (Figure 6.5(c)). This indicates that the tetragonality nature decreases with the addition of Co atoms in the crystal structure. For the cubic phase ($x > 0.3$), $a (= c)$ does not change significantly. Figure 6.5(d) shows the change in the unit cell volume as a function of Co-concentration (x) and it decreases with increasing Co-concentration.

6.2.2. Nickel addition

Figure 6.6 shows the powder XRD patterns of $\text{Mn}_{1.4}\text{Ni}_x\text{PtSn}$ ($x = 0.1-0.6$). From the diffraction patterns, it can be seen that the tetragonal phase exists up to $x = 0.4$ as the peak splitting corresponding to the tetragonal structure is present. Whereas further addition of Ni element in the compound leads to the stabilization of cubic structure with a small amount of additional impurity phase of MnPt. For all the compounds belonging to this series, complete Reitvald refinement was performed. From the refinement of the tetragonal phase, it is found that the structure of the compounds is analogous to $\text{Mn}_{1.4}\text{PtSn}$ superstructure. In the tetragonal crystal structure, the occupancy of Mn ($8d$), Pt ($8c$), and Sn ($8d$) are close to 100 percent, which means that these sites are fully occupied without any chemical disordering. Whereas, the $4a$ site is found to be shared by both Mn and Ni atoms.

From the refinement of cubic phase ($x \geq 0.4$), it is found that the structure is related to inverse cubic Heusler structure with space group $F\bar{4}3m$. In the framework of the inverse full-Heusler structure, Mn, Pt and Sn atoms occupy at $4c$, $4b$, and $4d$ sites without any chemical disordering. While at site $4a$, the position is shared by both Ni and Mn atoms.

Figures 6.7 and 6.8 show the EDX spectra along with inset SEM images of the polished surface of the compound $\text{Mn}_{1.4}\text{Ni}_{0.2}\text{PtSn}$ and $\text{Mn}_{1.4}\text{Ni}_{0.6}\text{PtSn}$, respectively. In Figure 6.7 inset, as it can be seen, the most part of the surface shows same contrast. However, there is a presence of a very small amount of impurities seen in the SEM image, which is undetectable in XRD patterns. For $x = 0.6$, the SEM image (inset, Figure 6.8) shows a clear presence of the impurity phase, in which dark and bright contrasts correspond to the majority phase and the minority phase (MnPt), respectively. The composition of the majority phase of the compound with the highest impurity concentration ($x = 0.6$) found to be $\text{Mn}_{1.1}\text{Ni}_{0.6}\text{PtSn}$. This means that the addition of Ni element in the compound leads to the replacement of some amount of Mn in the unit cell. The replaced Mn amount combines with Pt and leads to the formation of minority phase MnPt. For the cubic structure, the maximum Mn+Ni concentration in the majority phase is 1.7. A schematic of the crystal structure evolution with Ni addition is presented in Figure 6.9.

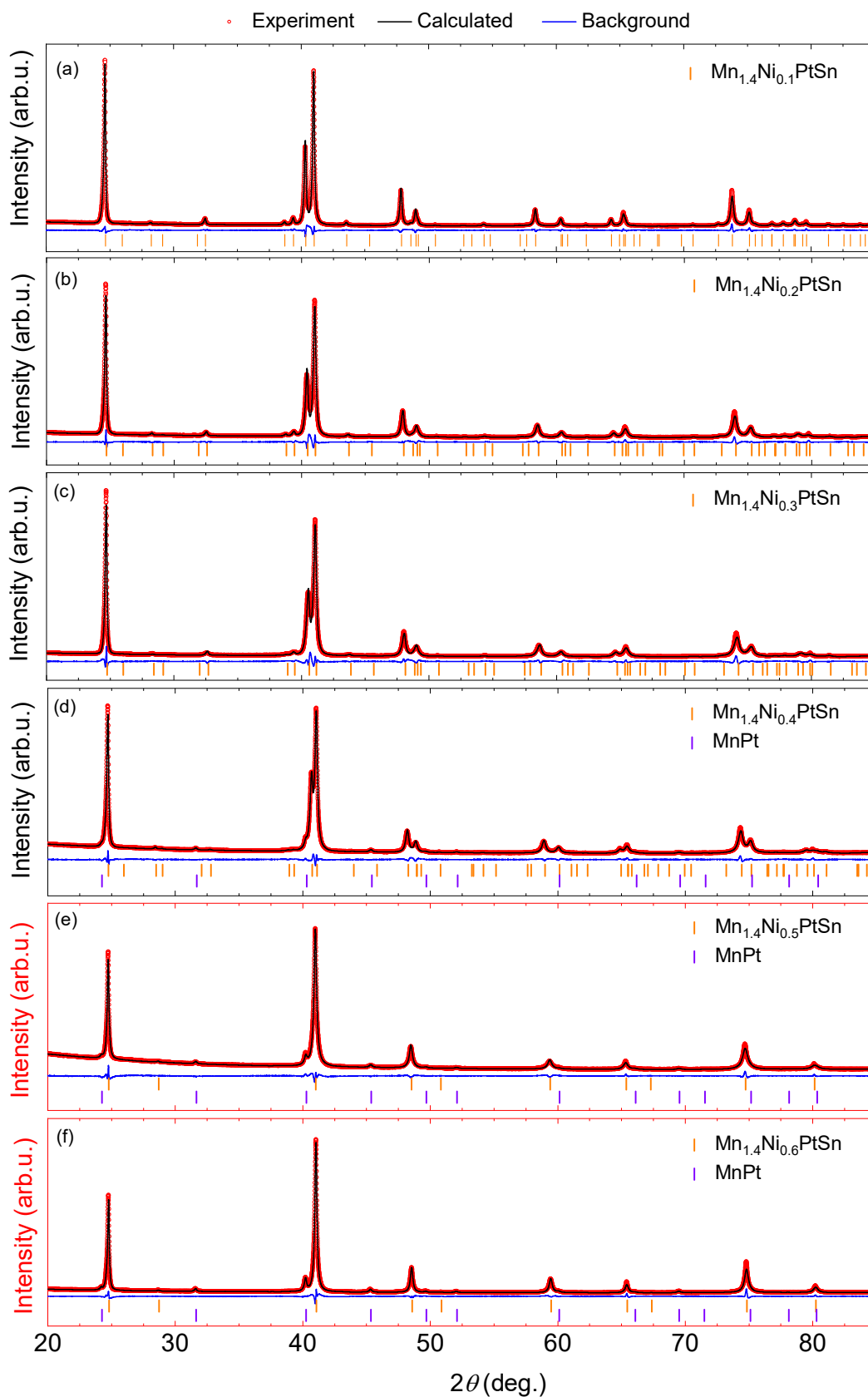


Figure 6.6. The experimental (red open circle), calculated (black) XRD pattern along with background (blue color) and the Bragg position of majority phase (orange) and minority phase (purple) for the compounds belonging to series Mn_{1.4}Ni_xPtSn. Plots with black and red color box are representation of tetragonal and cubic crystal structure, respectively.

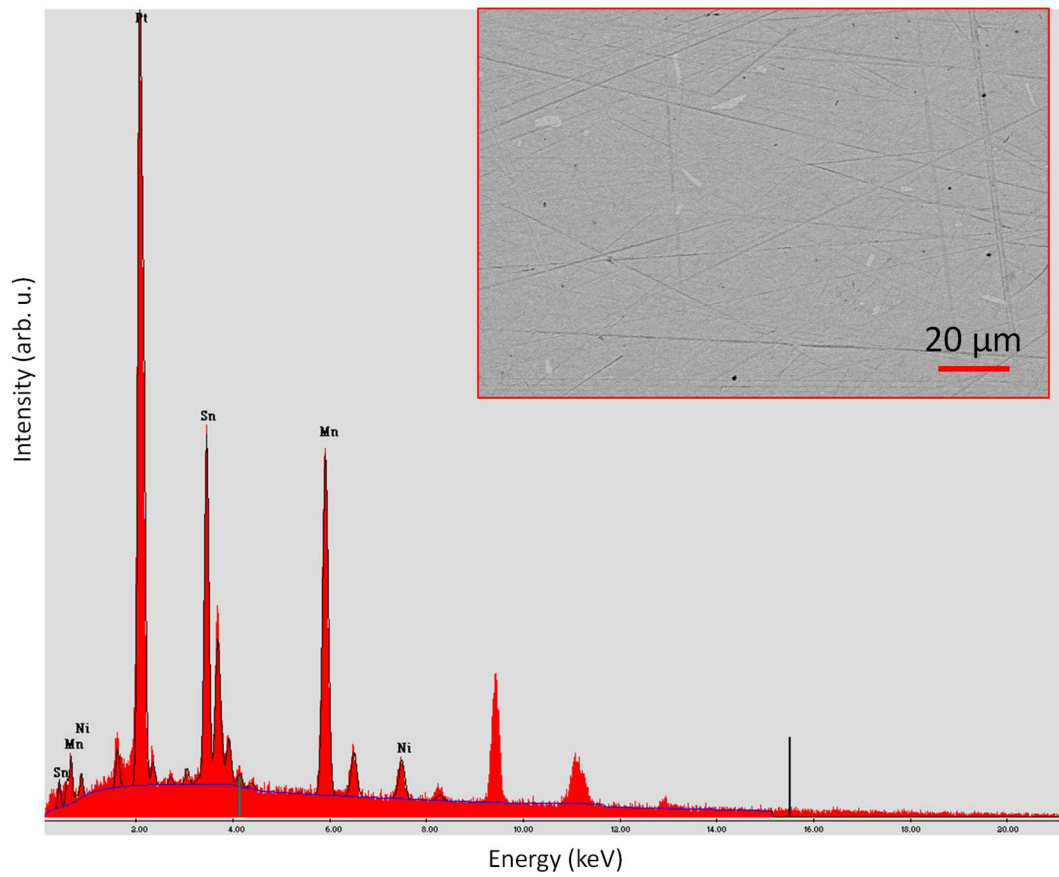


Figure 6.7. EDX spectrum along with SEM image as inset of compound $\text{Mn}_{1.4}\text{Ni}_{0.2}\text{PtSn}$.

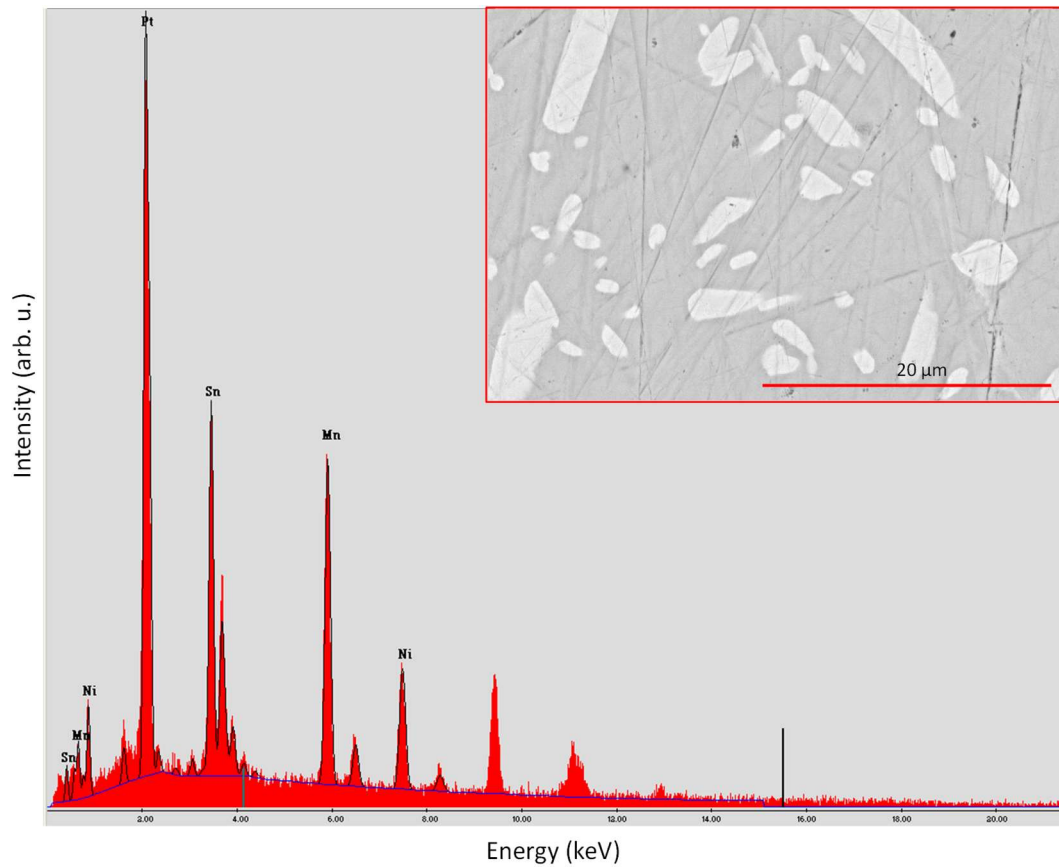


Figure 6.8. EDX spectrum along with SEM image as inset of compound $\text{Mn}_{1.4}\text{Ni}_{0.6}\text{PtSn}$.

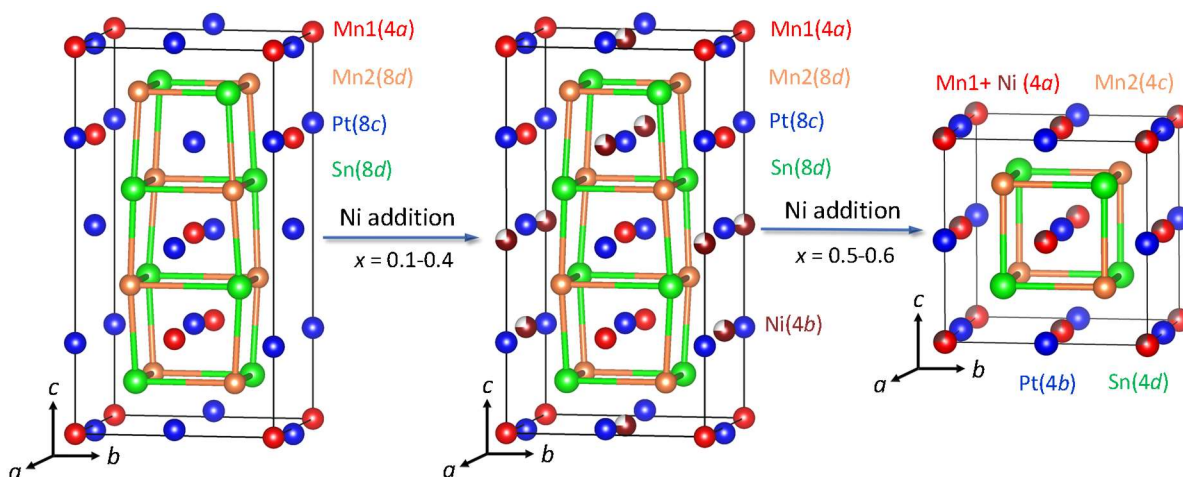


Figure 6.9. The schematic of change in the crystal structure with Ni addition in $\text{Mn}_{1.4}\text{Ni}_x\text{PtSn}$.

The lattice parameters, extracted from the refinement of the compounds of $\text{Mn}_{1.4}\text{Ni}_x\text{PtSn}$ series, are plotted in Figure 6.10. It is observed that the lattice parameter a decreases linearly with x up to $x = 0.4$ and upon further addition of Ni, the slope of decrement changes in the cubic phase (Figure 6.10(a)). The lattice parameter c starts decreasing very slowly up to $x = 0.3$ and then starts increasing (Figure 6.10(b)). The resultant c/a ratio increases monotonically with x , reflecting the tetragonality of the unit

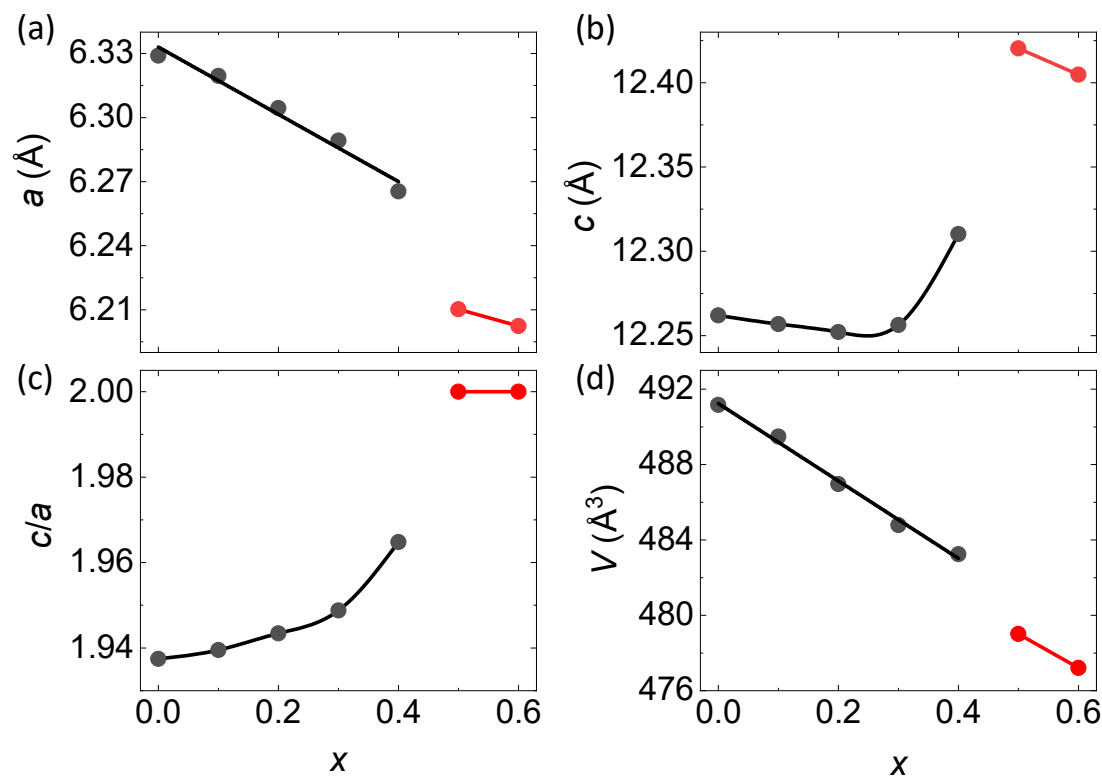


Figure 6.10. The lattice parameters as a function of Ni addition in $\text{Mn}_{1.4}\text{Ni}_x\text{PtSn}$, black curve represents the tetragonal phase while red represents the cubic phase. The black and red color curves are representation of tetragonal and cubic crystal structure, respectively.

cell decreases with the addition of the nickel element in the unit cell. Independent of structures, the unit cell volume decreases linearly with the addition of Ni (Figure 6.10(d)).

6.2.3. Copper addition

The XRD patterns for all the compounds of the series $Mn_{1.4}Cu_xPtSn$ are shown in Figure 6.11. The diffraction patterns of all the compounds show the presence of peak splitting. This indicates that all the compounds belonging to this series crystallize in a tetragonal structure. Additionally, the presence of superstructure peaks in all the diffraction patterns concludes that these compounds also have superstructure form the same as $Mn_{1.4}PtSn$ (space group $I\bar{4}2d$). The complete Reitvald refinement was done for all compositions. The presence of superstructure reflections even in zero vacancy system $Mn_{1.4}Cu_{0.6}PtSn$ indicates that copper goes exactly at the place of vacancy without any chemical disordering with Mn atoms. If there would be any chemical disordering between Mn and Cu, the symmetry of the compound would change to inverse tetragonal Heusler structure with space group of $I\bar{4}m2$. Furthermore, there would not be any superstructure reflection present in the diffraction patterns as the case for Mn_2RhSn . However, this is not the case here and Cu is very well ordered in the unit cell, maintaining the same crystal structure to $Mn_{1.4}PtSn$.

Figures 6.12 and 6.13 show the EDX patterns while insets show corresponding SEM image for the compound $Mn_{1.4}Cu_{0.2}PtSn$ and $Mn_{1.4}Cu_{0.6}PtSn$, respectively. In both the SEM images, there are no extra phases present in the compounds and display a homogeneous contrast throughout the image. This is also compatible with the XRD patterns, wherein no extra peaks are detected. The compositions obtained from EDX analyses of these compounds are $Mn_{1.34}Cu_{0.21}PtSn$ and $Mn_{1.35}Cu_{0.61}Pt_{1.04}Sn_{0.99}$ for $Mn_{1.4}Cu_{0.2}PtSn$ and $Mn_{1.4}Cu_{0.6}PtSn$, respectively. Considering the error in the analysis of composition from EDX spectra, the targeted and the actual compositions are very close. The schematic of structural evolution with copper addition is shown in Figure 6.14.

The existence of a single phase in the fully occupied compounds indicates that the Cu atoms can easily be incorporated in the unit cell. While for Co and Ni added compounds, there exists a significant amount of impurity for the high concentration of added elements. This might be due to the smaller atomic radii of Cu compared to Mn, Co or Ni. Additionally, for Cu added compounds, the tetragonal structure survives up to $x=0.6$ while for Co and Ni added compound, higher addition of either Co or Ni leads to the formation of inverse cubic Heusler structure. The reason for the existence of a tetragonal structure for a high amount of Cu could be due to the presence of d^9 electronic configuration of Cu^{2+} and d^4 electronic configuration of Mn^{3+} . Both d^9 and d^4 electronic configurations are very much prone to Jahn-Teller distortion, especially in an octahedral chemical environment. The $Mn_{0.5}$ and $Cu_{0.5}$ or vacancies occupy in an octahedral environment of Sn (see Figure 4.15), leading to the octahedral splitting of d -orbitals of Mn and Cu.

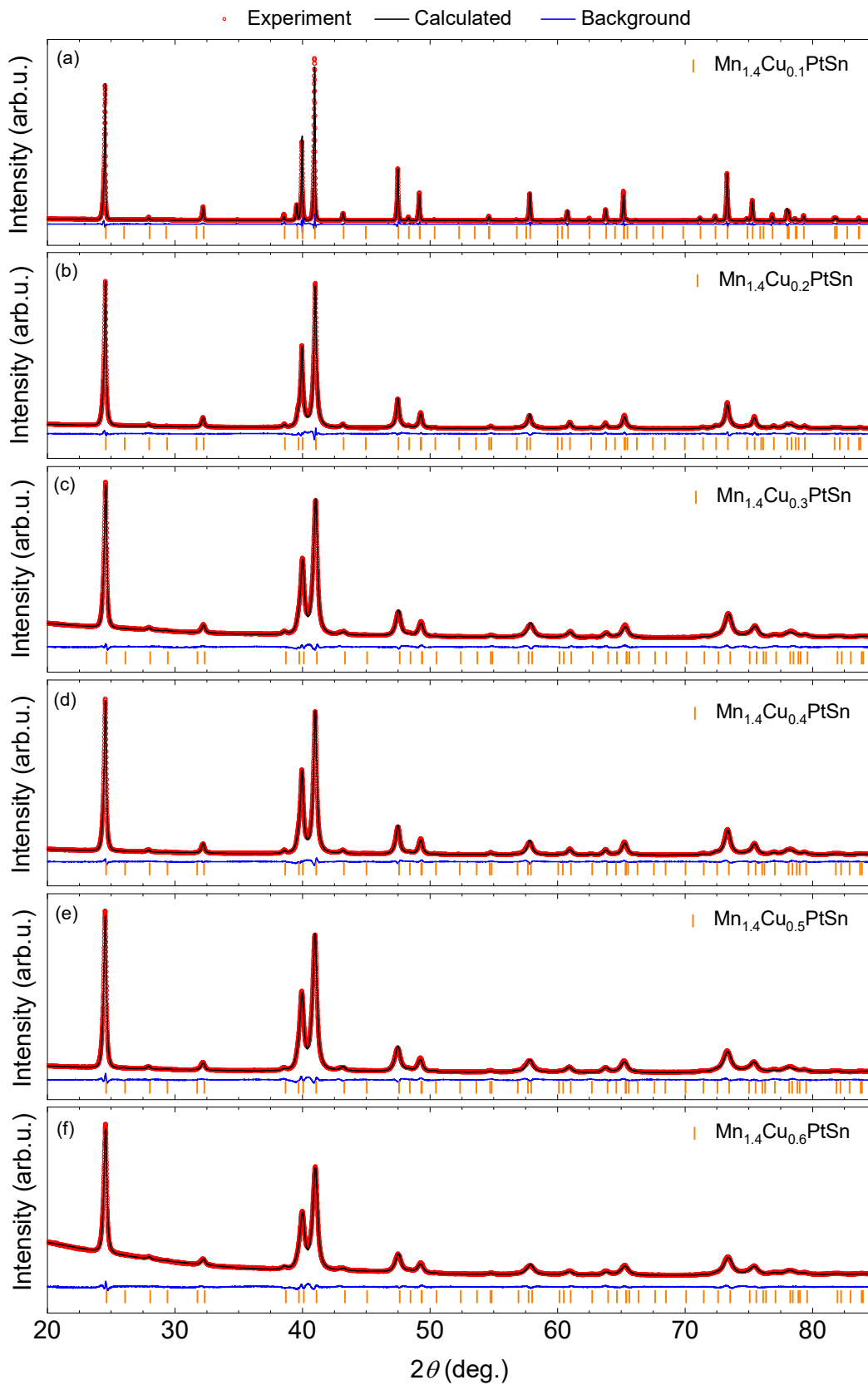


Figure 6.11. The experimental (red open circle), calculated (black) XRD pattern along with background (blue color) and the Bragg position (orange for the compounds belonging to series $Mn_{1.4}Cu_xPtSn$). Plots with black and red color box are representation of tetragonal and cubic crystal structure, respectively.

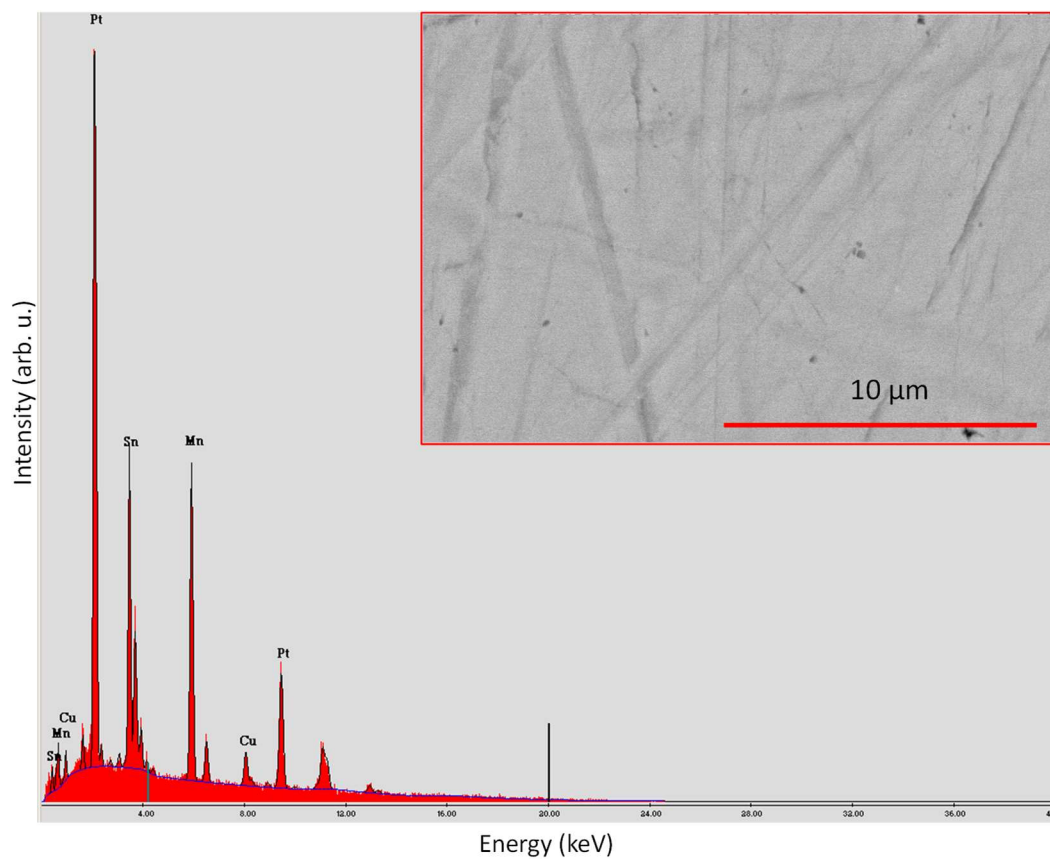


Figure 6.12. EDX spectrum along with SEM image as inset of compound $\text{Mn}_{1.4}\text{Cu}_{0.2}\text{PtSn}$

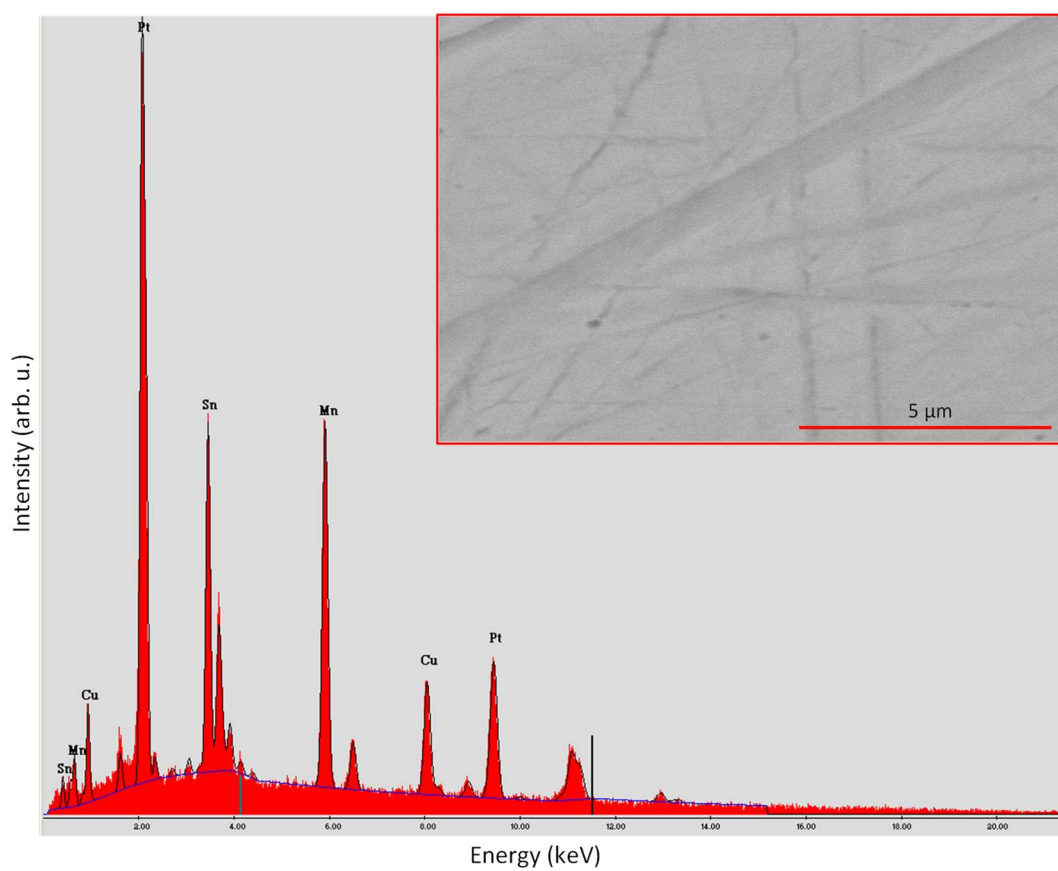


Figure 6.13. EDX spectrum along with SEM image as inset of compound $\text{Mn}_{1.4}\text{Cu}_{0.6}\text{PtSn}$.

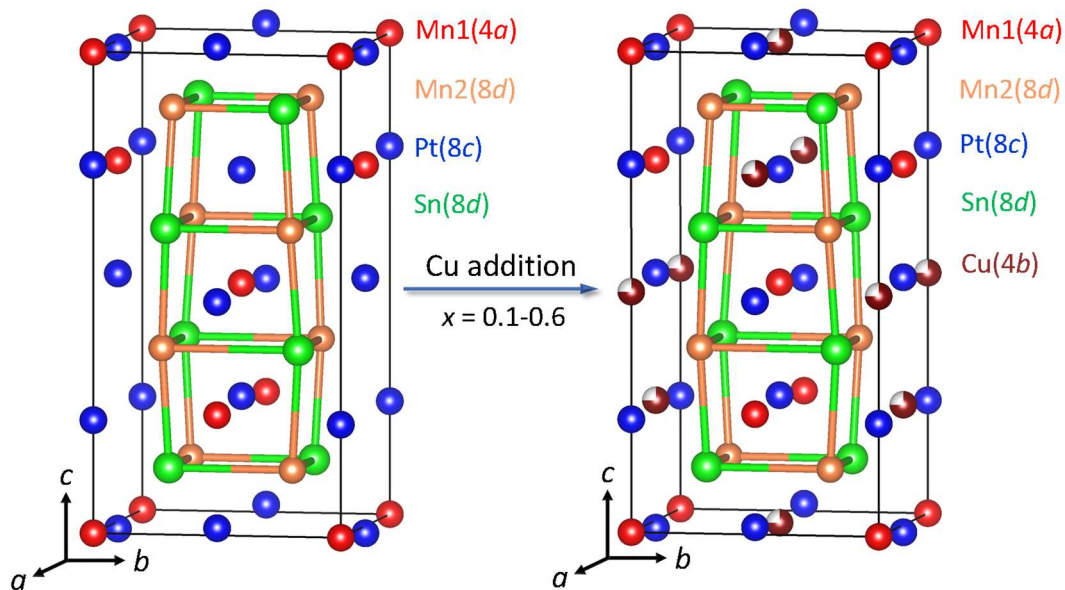


Figure 6.14. The schematic of change in the crystal structure with Ni addition in $\text{Mn}_{1.4}\text{Cu}_x\text{PtSn}$.

In Figure 6.15, the lattice parameters extracted from the refinement of XRD patterns are shown. Figure 6.15(a) shows the variation of unit cell parameter a as a function of Cu addition and it initially increases with x and then it remains almost unchanged. However, in Figure 6.15(c), the lattice parameter c initially decreases and then is almost constant. Similarly, c/a ratio initially decreases and then it becomes unchanged after $x = 0.2$ while the unit cell volume is found to be nearly unchanged with x .

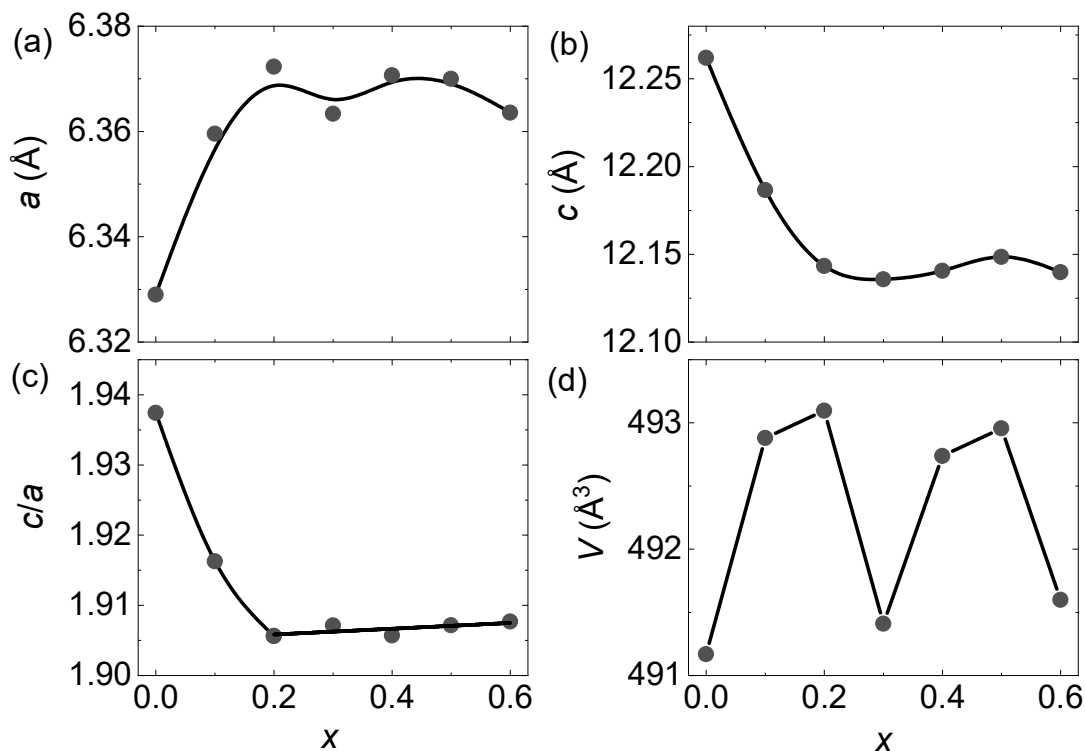


Figure 6.15. The lattice parameters as function of copper addition in the $\text{Mn}_{1.4}\text{Cu}_x\text{PtSn}$.

6.3. Magnetic properties

6.3.1. Cobalt addition

The magnetic properties of compounds of the series $\text{Mn}_{1.4}\text{Co}_x\text{PtSn}$ ($x = 0.1-0.6$) have been studied. In Figure 6.16(a), the magnetization as a function of temperature for field cooling curve (FC) in the applied external field of 0.01 T. The Curie temperature was calculated from the derivative of the magnetization curve. T_C is found to be increasing with cobalt addition in the unit cell. A linear variation of T_C for both tetragonal and cubic phase is found but they vary in two different slopes as it can be seen in Figure 6.16(c). The increment in the T_C can be originated by the increase in the direct exchange interaction. Similar to the parent compound, all the compounds belonging to $\text{Mn}_{1.4}\text{Co}_x\text{PtSn}$, only Mn and Co are magnetic while Pt and Sn are nonmagnetic. Interestingly, the compounds having tetragonal crystal structure exhibit a spin-reorientation transition at the low temperature, which indicates that the magnetic structure is realigned and forms a canted spin structure below this temperature. On the other side, for the compounds possessing cubic crystal structure, the spin-reorientation transition is absent.

In Figure 6.16(b), the isothermal magnetization curves measured at 2 K for different Co-concentration are presented and the magnetic moment is calculated. Their magnetic

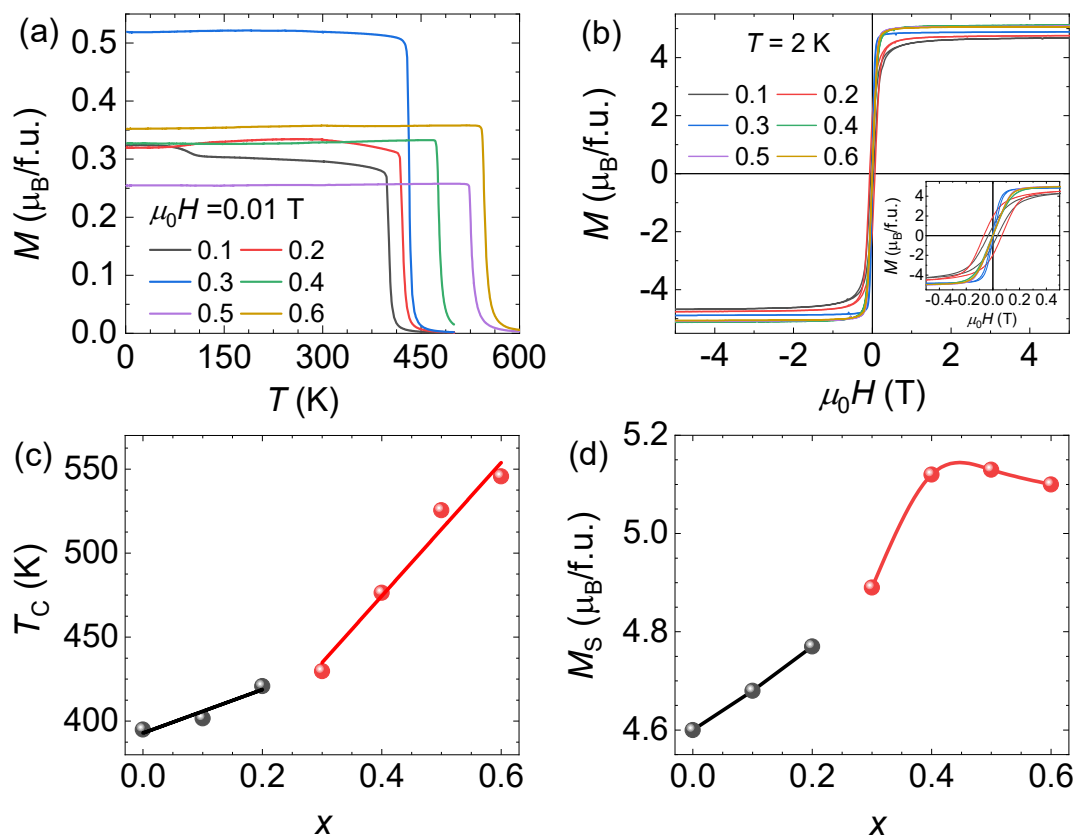


Figure 6.16. (a) M vs T (b) M vs H (c) T_C vs x and (d) M_S (2 K) vs x for compounds $\text{Mn}_{1.4}\text{Co}_x\text{PtSn}$. The black and red color curves are representation of tetragonal and cubic crystal structure, respectively.

moment variation with cobalt addition is given in Figure 6.16(d). The moment for the tetragonal phase is found to be continuously increasing while it is almost constant for the cubic phase ($x \geq 0.4$). As described previously in the crystal structure section, the majority amount of cobalt goes to the vacancy site with a slight amount of chemical disordering on the Mn site in the unit cell. It is well in the Co-based Heusler compounds that Co atoms have ferromagnetic exchange interactions and the parent compound $\text{Mn}_{1.4}\text{PtSn}$ is also found to have a ferromagnetic spin structure. Therefore, the magnetic moment of substituted Co in the unit cell aligns parallelly with the moments of Mn-atoms and thus, enhancing the magnetic moment.

6.3.2. Nickel addition

Figure 6.17(a) represents the magnetization as a function of temperature in field cooling (FC) for the series $\text{Mn}_{1.4}\text{Ni}_x\text{PtSn}$. The T_C is calculated from the derivative of the magnetization curve and its dependent as a function of x is shown in Figure 6.17(c). T_C decreases linearly in the tetragonal phase ($x \leq 0.4$) as similar to Co added compounds. For the highest Ni-concentration compound $\text{Mn}_{1.4}\text{Ni}_{0.6}\text{PtSn}$, T_C is found to be 298 K compared to the parent compound $\text{Mn}_{1.4}\text{PtSn}$ which has T_C of 395 K. This could be understood in terms of replacement of magnetic Mn atoms with non-magnetic Ni atoms. In Figure 6.17(b), isothermal magnetization at 2 K as a function of field is shown. A small amount in

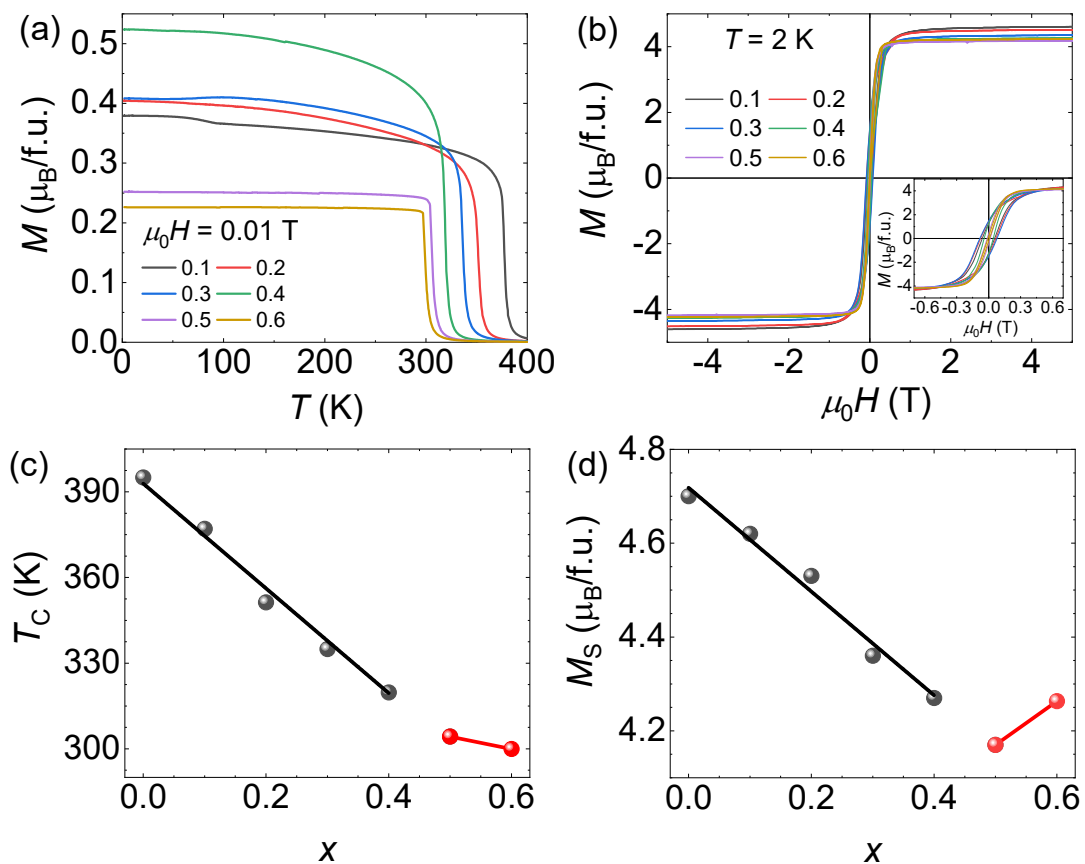


Figure 6.17. (a) M vs T (b) M vs H (c) T_C vs x and (d) M_S (2 K) vs x for compounds $\text{Mn}_{1.4}\text{Ni}_x\text{PtSn}$. The black and red color curves are representation of tetragonal and cubic crystal structure, respectively.

the coercivity present (inset 6.17(b)) might be due to either polycrystalline nature or chemical disordering present in the samples. The decreasing saturation moment with the addition of nickel in the unit cell describes the replacements of magnetic Mn with non-magnetic Ni.

6.3.3. Copper addition

The magnetization measurements of Cu substituted series $\text{Mn}_{1.4}\text{Cu}_x\text{PtSn}$ are shown in Figure 6.18. Figure 6.18(a) shows the magnetization as a function of temperature in FC condition. From these curves, it can be observed that the Cu substitution significantly changes the magnetization at low temperature (below spin-reorientation transition), indicating an effective change of a non-collinear spin structure. The extracted T_C with Cu addition is presented in Figure 6.18(c). T_C decreases marginally at the beginning while it is almost unchanged for the higher Cu in the unit cell.

The isothermal magnetization measurements as a function of the field for 2 K are given in Figure 6.18(b). The magnetization for all the compounds saturates at 1.5 T. For $x = 0$ and $x = 0.1$, the saturation magnetization shows a decreasing trend while for $x = 0.2$ – 0.4 , it is almost constant. Upon further addition of Cu, the saturation magnetization again starts to decrease.

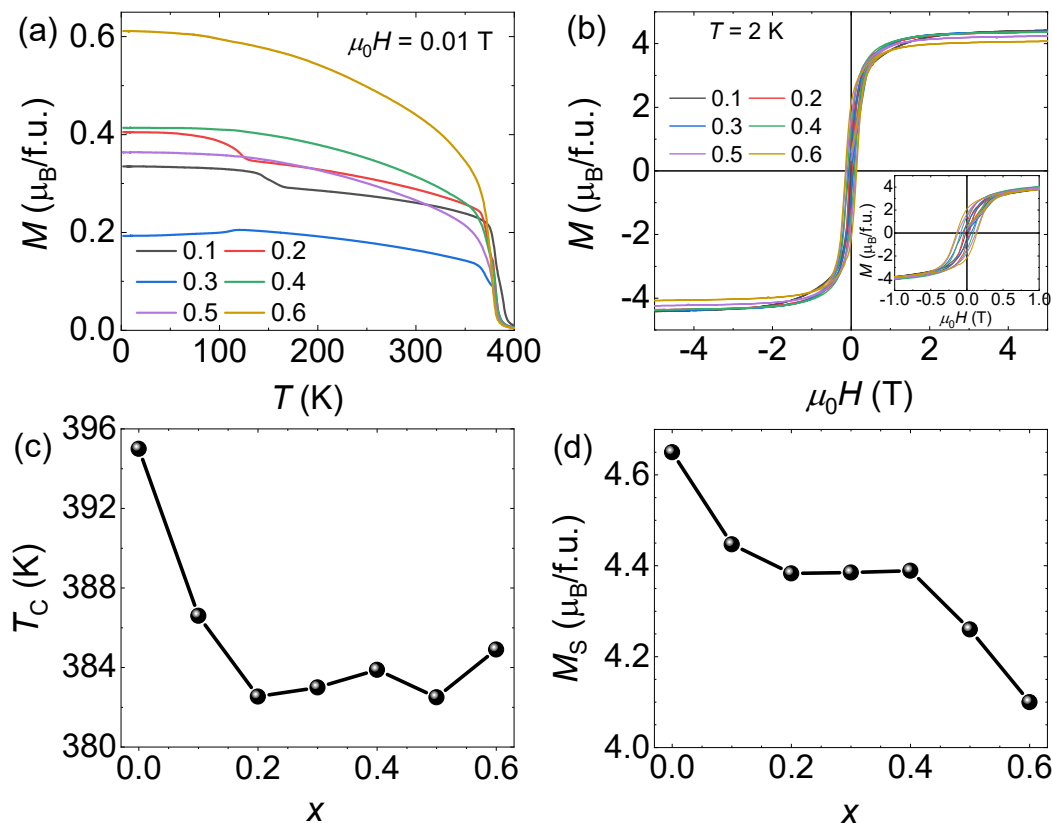


Figure 6.18. (a) M vs T (b) M vs H (c) T_C vs x and (d) M_S (2 K) vs x for compounds $\text{Mn}_{1.4}\text{Cu}_x\text{PtSn}$.

7. Mn_{1.7}Pt_{0.8}In

Mn_{1.4}PtSn is an emerging compound in the spintronics community as it hosts room-temperature antiskyrmions. However, due to the large magnetic moment in this compound, a large magnetic stray field is generated, which limits its applications in the spintronics devices. Therefore, the primary goal is to reduce the stray magnetic field. One way to do this is to reduce the moment by systematic elemental substitution in Mn_{1.4}PtSn and their related study has already been presented in chapter 5. Another way is to search for the different compounds (not related to Mn_{1.4}PtSn) that form nearly compensated ferrimagnetic structure with a negligible net magnetic moment. Mn₂PtIn is a Heusler compound with the inverse tetragonal crystal structure and low magnetic moments^{145,146}. However, similar to most of the tetragonal Heusler compounds, Mn₂PtIn also shows a martensitic transition¹⁴⁶. Therefore, the polycrystalline sample, which is prepared from melt above the martensitic transition temperature, always has microtwinned crystal grains. The size of the microtwinned structure is very small and it is not suitable for Lorentz transmission electron microscopy (LTEM) studies, a small single crystal grain (~ 1 μm) is sufficient. This also prevents any characterization related to bulk single crystals. To continue such studies, the large crystals are needed. Following a similar method as Mn_{1.4}PtSn, wherein microtwin free crystals were successfully grown below the martensitic transition temperature by flux method (see section 4.1), an attempt to grow the single crystals of Mn₂PtIn was adopted. After the reaction, some crystals of Mn-Pt-In ternary phase were obtained. However, the composition of these crystals was Mn_{1.7}Pt_{0.8}In instead of Mn₂PtIn. Upon comparing the chemical formula of Mn₂PtIn with Mn_{1.7}Pt_{0.8}In, it appears that there are some vacancies present at Mn and Pt sites. The extensive single crystal X-ray diffraction analysis reveals that these vacancies are ordered and form a 3 × 3 × 3 superstructure of the cubic Heusler compound. In this chapter, the detailed structural characterization and physical properties of Mn_{1.7}Pt_{0.8}In are presented.

7.1. Single crystal growth

The procedure of single crystal growth of Mn_{1.7}Pt_{0.8}In is similar to Mn_{1.4}PtSn with a slight modification in the growth temperature range. Single crystals of Mn_{1.7}Pt_{0.8}In were prepared by flux method using In as a flux. High purity elements Mn (Sigma-Aldrich, 99.999 %) and Pt (Sigma-Aldrich, 99.999 %) were taken into 3:1 molar ratio with a total weight of 0.75 g. They were put together with 10 g of In (Sigma-Aldrich, 99.999 %) in a dried alumina crucible and sealed in a quartz tube with 0.2 bar argon atmosphere. The tube was then put in the box furnace and heated to 1273 K with a rate of 200 K/h, and kept there for approximately 24 hours in order to homogenize the mixture. The furnace temperature was very rapidly cooled down to 973 K to avoid the growth above martensitic transition temperature. The reaction was slowly cooled from 973 K to 773 K with a rate of 2 K/h. At 773 K, it was held for an additional few hours and then the excess flux was removed with the centrifugation. The obtained crystals were a silver shiny color and stable in air and

moisture at least for few months. The In flux present on the surface of the crystals was removed by treating the crystals in dilute HCl for a few hours. Some crystals of a different composition Mn_3In were also obtained along with $\text{Mn}_{1.7}\text{Pt}_{0.8}\text{In}$ by flux method. In some of the pieces, crystals of both compositions were joined together like twins. Therefore, a very careful crystal selection procedure is needed to pick the right crystals of $\text{Mn}_{1.7}\text{Pt}_{0.8}\text{In}$.

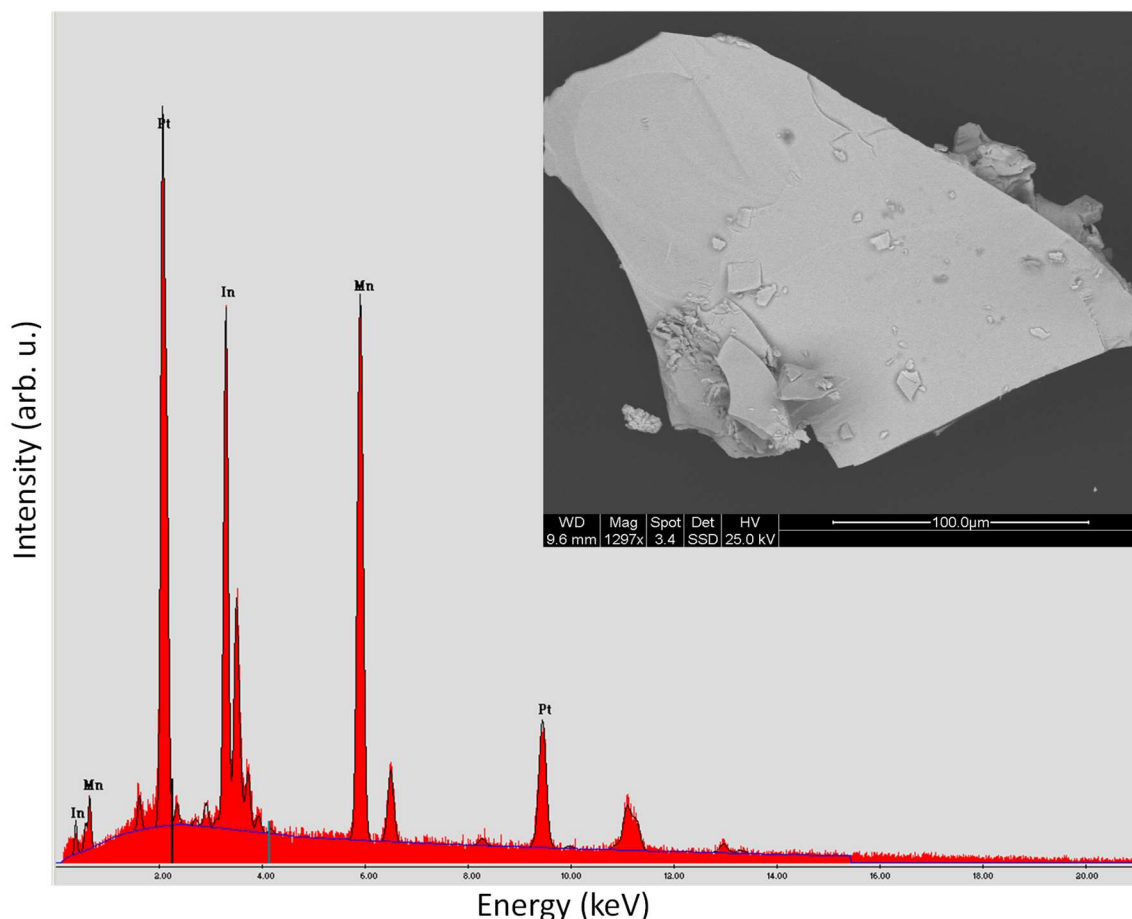
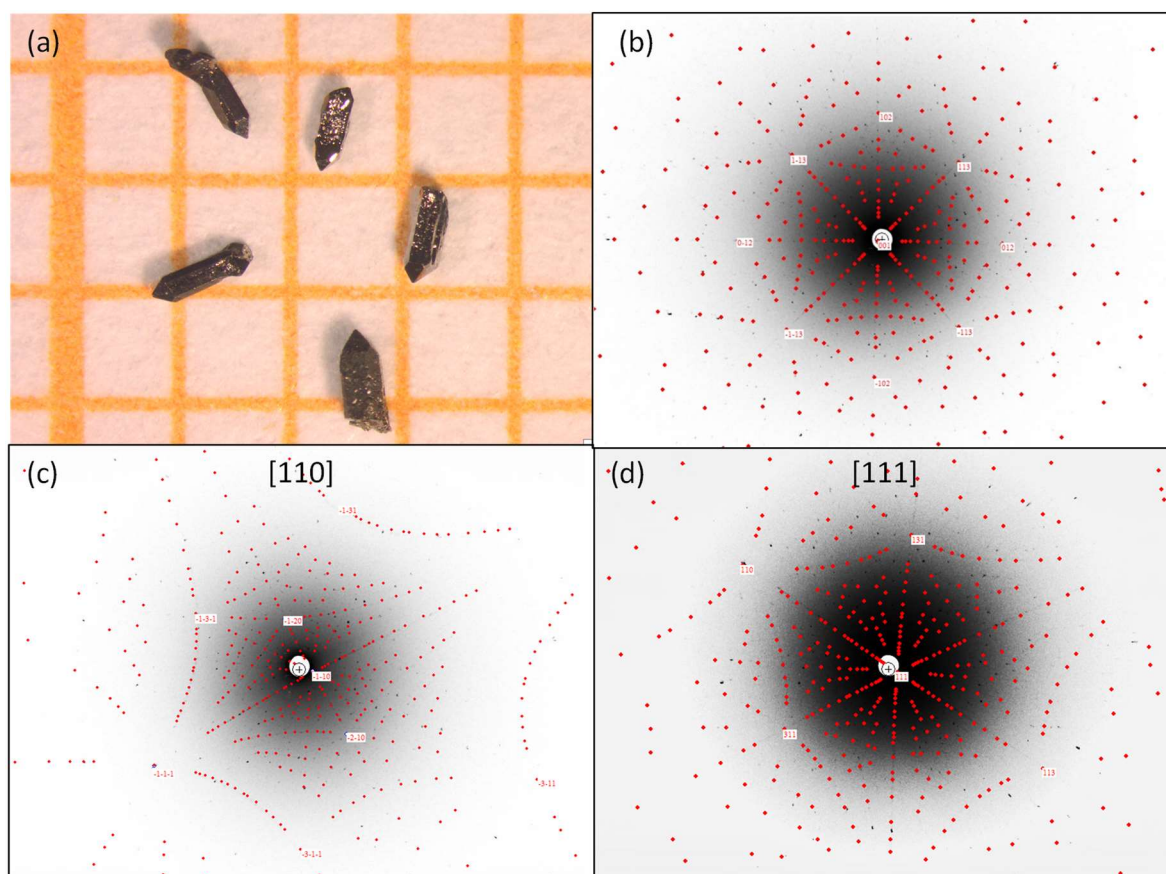


Figure 7.1. EDX spectrum along with inset SEM image of crystal platelet $\text{Mn}_{1.7}\text{Pt}_{0.8}\text{In}$.

The elemental composition of $\text{Mn}_{1.7}\text{Pt}_{0.8}\text{In}$ was measured in SEM inbuilt EDX method. To minimize the presence of In flux or Mn_3In crystal and to increase the accuracy of measurements, the large crystals were broken into small platelets, and various small pieces were used to collect the EDX spectrum at least three different points on each piece. At all the points, a similar composition was obtained and the final average composition is $\text{Mn}_{46}\text{Pt}_{23}\text{In}_{31}$ *i.e.* $\text{Mn}_{1.7}\text{Pt}_{0.8}\text{In}$. Figure 7.1 shows the typical EDX spectra collected on one of the pieces. The inset of Figure 7.1 shows the SEM image of the small crystal platelets. The contrast throughout the crystal is the same, indicating a homogeneous composition. Similar results for all the other crystal pieces were observed.

The structural analysis of the crystals was performed by Laue diffraction and single-crystal X-ray diffraction method. Almost all the crystals display a similar morphology and crystals facets. Some of the as-grown crystals are shown in Figure 7.2(a). The majority of

the crystals have three types of crystal facets, namely triangular, rectangular and hexagonal shape with crystallographic direction corresponding to $[111]$, $[110]$, and $[100]$, respectively. The Laue diffraction patterns of these facets are presented in Figure 7.2(b), (c) and (d). Figure 7.2(b) shows the diffraction pattern taken on the hexagonal-shaped facet. It shows a 4-fold pattern, which was initially quite puzzling because 3-fold or 6-fold patterns are expected from a hexagonal-shaped facet. However, after a closer look, it turned out that this is not a regular hexagon but rather a hexagon with an intermediate angle of 90° and 135° , which is really a part of the square. Figures 7.2(c) and (d) show the diffraction pattern taken on rectangular and triangular-shaped facets, respectively, displaying a 2-fold and 3-fold patterns. The angle between the rectangular and the hexagonal facet is 45° . By combining all the diffraction patterns and the angles between crystal facets, it can be estimated that the crystal symmetry of $\text{Mn}_{1.7}\text{Pt}_{0.8}\text{In}$ belongs to cubic or at least close to the cubic phase.



this, three small pieces from three different crystals of two batches were selected and mounted on 10 μm kapton tip for measurements. In the preliminary analysis, it was found that the crystal structure is cubic with a cell edge equal to 18.9 \AA . The three data sets with almost 10000 reflections from these three small pieces of single crystals were collected. The refinement was performed using SHELX software¹¹⁴. After refinement, the obtained crystal structure was analyzed and it turned out that the crystal structure of $\text{Mn}_{1.7}\text{Pt}_{0.8}\text{In}$ is related to Heusler structure. The results of crystal structure refinement are summarized in tables 7.1 and 7.2.

In table 7.1, the crystallographic data refined for a single crystal of $\text{Mn}_{1.7}\text{Pt}_{0.8}\text{In}$ is presented. The crystal structure is non-centrosymmetric cubic with space group $F\bar{4}3m$ and the unit cell parameter is 18.8985 \AA . The obtained formula from the refinement is $\text{Mn}_{1.62}\text{Pt}_{7.6}\text{In}_{9.6}$ that can be simplified to $\text{Mn}_{4.23}\text{Pt}_2\text{In}_{2.5}$ or $\text{Mn}_{1.7}\text{Pt}_{0.8}\text{In}$ which is close to the composition obtained from EDX analysis.

Table 7.1. Single-crystal XRD refinement details for $\text{Mn}_{1.7}\text{Pt}_{0.8}\text{In}$.

compound	$\text{Mn}_4\text{Pt}_2\text{In}_3$
Formula weight	954.39
temperature [K], wavelength [\AA]	295, 0.71703 (Mo $K\alpha$)
Space group	$F\bar{4}3m$
unit cell parameters [\AA]	18.8985(2)
volume [\AA^3]	6749.66(15)
reflections collected, independent	10218, 892 ($R_{\text{int}} = 0.031$)
theta range [deg], completeness	1.9–35.1, 100%
data/restraints/parameters	892/0/70
GoF	1.117
R indices (all data) ^a	$R_1 = 0.0653$, $wR_2 = 0.1717$

$${}^a R = \sum ||F_0| - |F_c|| / \sum |F_0|, wR_2 = \sum [w(|F_0|^2 - |F_c|^2)^2] / \sum [w(|F_0|^4)]^{1/2}$$

and $w = 1 / [\sigma^2(|F_0|^2) + (0.0154P)^2 + 5.5965P]$, where $P = (F_0^2 + 2F_c^2) / 3$.

Table 7.2. Fractional atomic coordinates and isotropic equivalent atomic displacement parameters for $\text{Mn}_{1.7}\text{Pt}_{0.8}\text{In}$.

atoms	Wyckoff position	x	y	z	Occupancy	U_{eq} (\AA^2)
Mn1	$24f$	1/2	0.1429	1/2	0.73	0.037
Mn2	$48h$	0.4314	0.7435	0.4314	1	0.011
Mn3	$48h$	0.3446	0.6554	0.5203	1	0.011
Pt1	$4a$	1/2	0	1/2	1	0.007
Pt2	$16e$	0.39964	0.60036	0.39964	1	0.007
Pt3	$4c$	1/4	3/4	3/4	1	0.006
In1	$24f$	1/2	1/2	0.3712	1	0.012
In2	$16e$	1/3	2/3	2/3	1	0.02
Mn4	$16e$	0.1597	0.6597	0.3403	0.9	0.004
Pt4	$16e$	0.1597	0.6597	0.3403	0.1	0.004
Mn5	$24g$	1/4	0.6072	1/4	0.81	0.008
Pt5	$24g$	1/4	0.6072	1/4	0.19	0.008
Mn6	$4d$	1/4	3/4	1/4	0.41	0.014
In3	$4d$	1/4	3/4	1/4	0.59	0.014
Mn7	$16e$	0.1671	0.6671	0.6671	0.81	0.017
In4	$16e$	0.1671	0.6671	0.6671	0.19	0.017
Pt6	$48h$	0.42317	0.7566	0.57683	0.75	0.007
In5	$48h$	0.4121	0.7802	0.5879	0.25	0.007
Pt7	$48h$	0	0.193	0.807	0.2	0.01
In6	$48h$	0.008	0.1862	0.8138	0.8	0.01

In table 7.2, the atomic coordinates of elements with isotropic displacement parameters are shown. In the unit cell, there are 14 unique Wyckoff positions and 6 of them have elemental mixing or chemical disorder. Atomic mixing between every combination of two elements is observed. For a better pictorial view, in table 7, different color shading is shown. The blue region has the atomic positions free from any elemental mixing. The Orange shaded region has atomic positions with elemental mixing of Mn and Pt. The atomic site with the mixing of Mn and In is shown in the green shaded region. The yellow region represents the atomic mixing between Pt and In atoms. Two types of elemental mixing are observed in the unit cell of $\text{Mn}_{1.7}\text{Pt}_{0.8}\text{In}$. First, where both the atoms have the same atomic coordinate in the unit cell *e.g.* between Mn and Pt (orange shaded region) as well as Mn and In (green region). In the second type of atomic mixing, two atoms have slightly different atomic coordinates (keeping the same multiplicity of Wyckoff positions) *e.g.* Pt and In (yellow region).

In Figures 7.3(a) and (b), the crystal structures of half-Heusler and full inverse Heusler compound are shown in which Mn, Pt, and Sn atoms are shown as red, blue and green color, respectively. A half-Heusler structure for the nominal compound MnPtIn, forming a NaCl-type with Mn and Sn and Pt atoms are occupying half of the tetrahedral vacancies as shown in Figure 7.3(a). Figure 7.3(b) shows the crystal structure of full inverse Heusler for the nominal compound Mn₂PtIn in which Mn and Sn are forming like NaCl-type structure and half of the tetrahedral vacancies are filled by Pt atoms while the other half is filled with Mn atoms. Both crystal structures belong to a non-centrosymmetric space group $F\bar{4}3m$. Figure 7.3(c) shows the crystal structure of Mn_{1.7}Pt_{0.8}In obtained from the refinement of single crystals that crystallizes in the cubic structure with space group $F\bar{4}3m$ and a cell edge of 18.9 Å. The presented crystal structure (called as original structure) of Mn_{1.7}Pt_{0.8}In looks very complex due to displacement from the standard atomic position and partial mixing of elements at some of the Wyckoff positions. In Figure 7.3(d), the simplified model of the unit cell of Mn_{1.7}Pt_{0.8}In is presented. The simplified model (called as Heusler invariant) can be obtained by simply shifting the atoms at the standard atomic positions. For example, in the original unit cell, the Wyckoff position of Mn₂ atoms is (0.4314, 0.7435, 0.4314) which deviates from the standard Wyckoff position (5/12, 1/4, 5/12). This simplified version is given for better clarification and understanding of the crystal structure

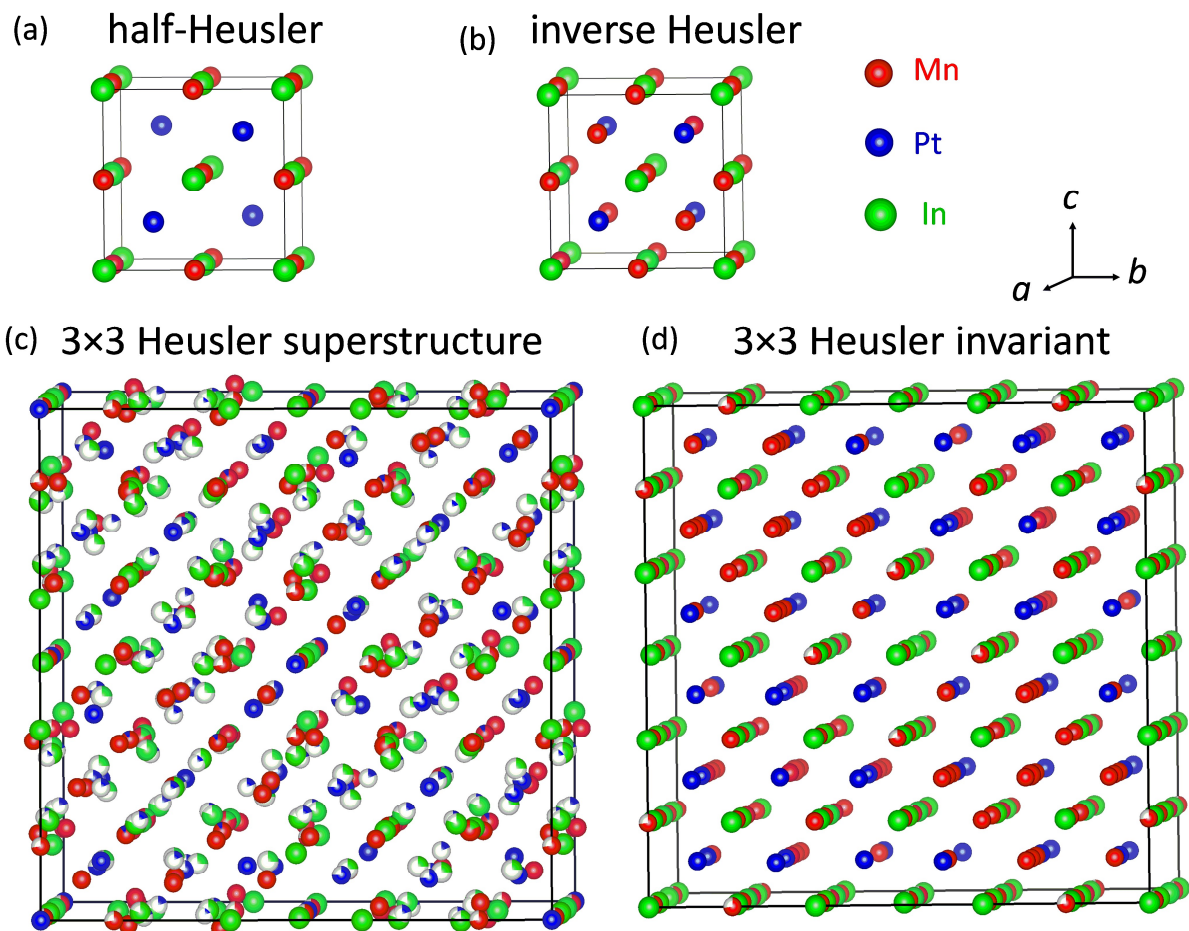


Figure 7.3. Crystal structure of (a) half-Heusler phase MnPtIn, (b) full inverse Heusler phase Mn₂PtIn, (c) 3×3 superstructure of Mn_{1.7}Pt_{0.8}In and (d) its Heusler invariant.

of $\text{Mn}_{1.7}\text{Pt}_{0.8}\text{In}$. One point to note here is that the multiplicity of the atom or Wyckoff position remains unchanged. Additionally, to make Heusler invariant model of $\text{Mn}_{1.7}\text{Pt}_{0.8}\text{In}$, elemental disordering is neglected and the atom with the higher atomic percentage at that Wyckoff position is placed. For example, 0.9 Mn (Mn4) +0.1 Pt (Pt4) is made 1.0 Mn (Mn4). One more operation to get Heusler invariant was to put the atom fitting to the description of the inverse Heusler structure. For example, Pt1 (4a) is made In (4a) because in Heusler structure Mn_2PtIn , Pt atoms sit at the tetrahedral site but not at the octahedral site.

In Figure 7.4(a), the simplified structural model (Heusler invariant) is shown again. The grey lines in the structure is put to show that the structure of $\text{Mn}_{1.7}\text{Pt}_{0.8}\text{In}$ is composed of $3 \times 3 \times 3$ Heusler unit cells. Therefore, in a unit cell of $\text{Mn}_{1.7}\text{Pt}_{0.8}\text{In}$, there are 27 Heusler subcells present. Assuming each unique Heusler subcell as an individual object, a more simplified model can be obtained, which is presented in Figure 7.4(b). Looking closely at this model, the unit cell resembles a NaCl-type structural model which consists of the objects present at body center (black color), face center (light grey), edge center (dark yellow), corner 1 (orange), and corner 2 (pink). In Figure 7.4(c), each unique Heusler subcell is shown individually. Figure 7.4(c1) shows the body center part (black) of Heusler invariant $\text{Mn}_{1.7}\text{Pt}_{0.8}\text{In}$. As can be seen in the Figure, the object resembles a half-Heusler structure with In atoms missing at the alternate corner position and Mn atom missing at the centre. The same subcell corresponding to the original structure is presented in Figure 7.4(d1). For face-centered object (light grey) (Figure 7.4(c2)), two In atoms are missing at the corner and $1/4^{\text{th}}$ of the tetrahedra vacancies are filled with Mn and $1/4^{\text{th}}$ is filled with Pt atoms. The same subcell corresponding to the original structure is shown in Figure 7.4(d2). In this structure, an elemental disordering between Pt and In atoms occurs as well as one of the In atoms are replaced with Pt atom. Figure 7.4(c3) shows the Heusler subcell for the edge center in which two In and one Mn atom are missing at octahedral sites while half of the tetrahedral site is filled with Pt atoms and $1/4^{\text{th}}$ with Mn atoms. The corresponding subcell in the original structure is presented in Figure 7.4(d3). The corner 1 object (orange color) is represented in Figure 7.4(c4), where two In atoms are missing from octahedral sites and one Mn atom is missing from the tetrahedral site. The analog of this original structure is shown in Figure 7.4(d4). In this structure, there is a chemical disordering between In and Pt atoms and also one of the In atoms is replaced with Pt atom. Finally, the corner 2 object (pink color) is shown in Figure 7.4(c5). This Heusler subcell perfectly corresponds to the half-Heusler structure. The analog of this original structure is shown in Figure 7.4(d5) in which the site mixing between Pt and In atoms as well as Mn and In are present.

In Figure 7.5, the powder XRD pattern of $\text{Mn}_{1.7}\text{Pt}_{0.8}\text{In}$ is shown, which is collected from powder obtained by grinding the single crystals. The refinements reveal that the diffraction patterns have the superimposition of two phases namely, $\text{Mn}_{1.7}\text{Pt}_{0.8}\text{In}$ and Mn_3In . As mentioned earlier, some crystals of Mn_3In were also grown with $\text{Mn}_{1.7}\text{Pt}_{0.8}\text{In}$. Therefore, some crystals of Mn_3In were possibly grinded while preparing powder for XRD measurement. The theoretical model obtained from the refinement of the single crystal of

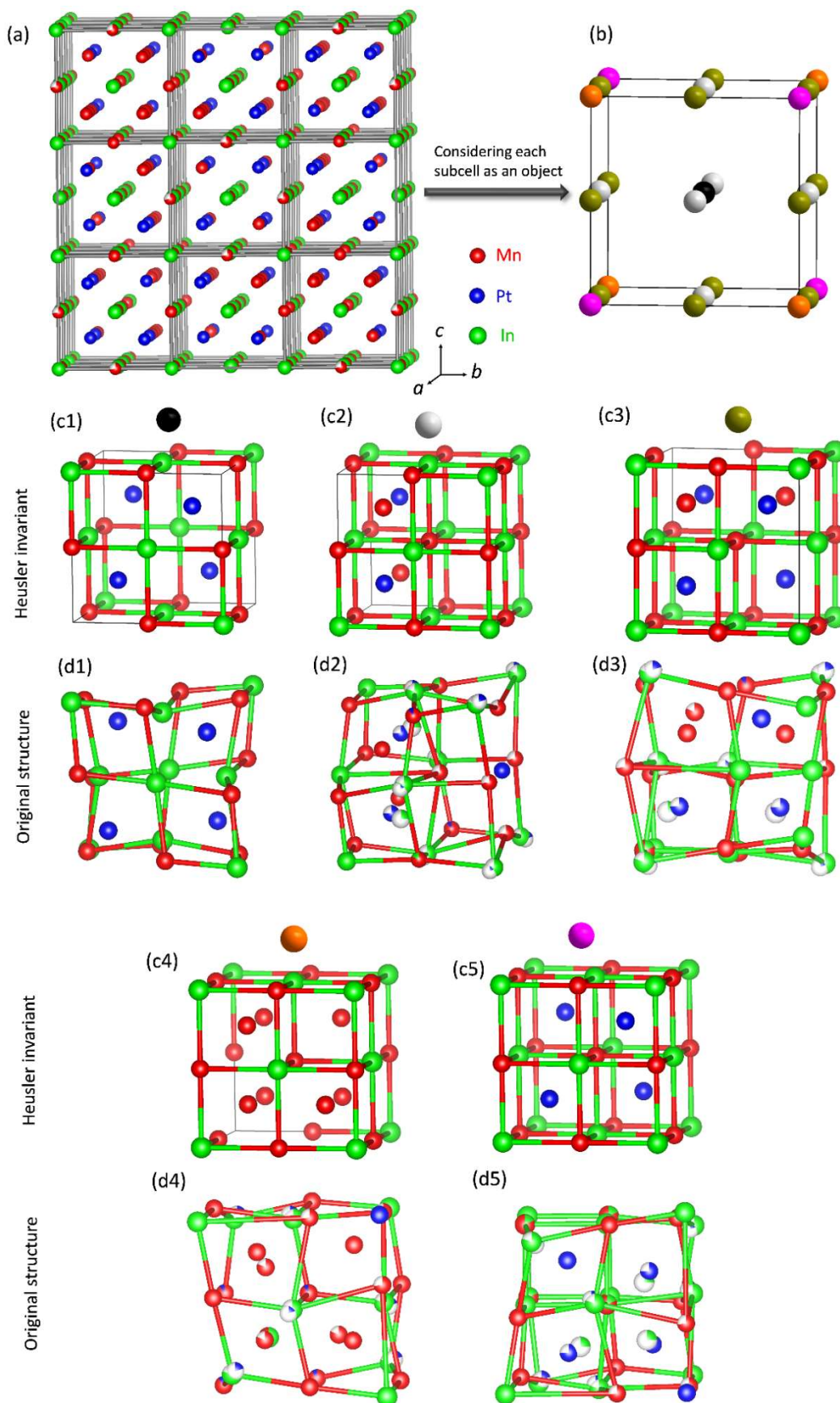


Figure 7.4. (a) Heusler invariant structure of $\text{Mn}_{1.7}\text{Pt}_{0.8}\text{In}$, (b) obtained structure after assuming each unique subcell as an object, and the structure of subcell corresponding to (c) Heusler invariant and (d) original structure.

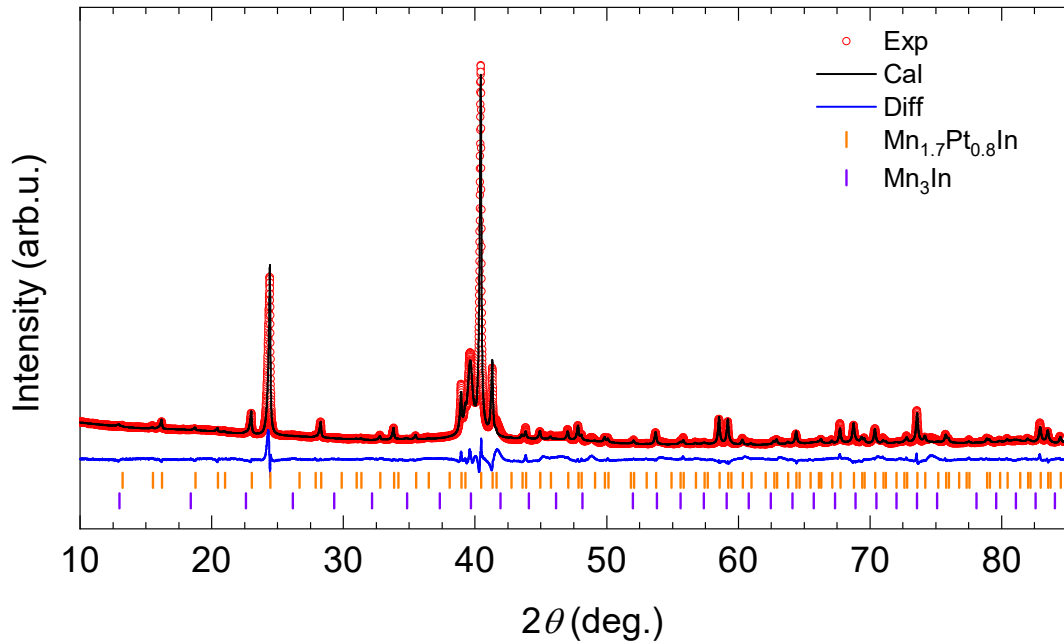


Figure 7.5. Powder XRD pattern with the experimental (red open circle), calculated (black), background (blue) and bragg positions of $\text{Mn}_{1.7}\text{Pt}_{0.8}\text{In}$ (orange) and Mn_3In (purple).

$\text{Mn}_{1.7}\text{Pt}_{0.8}\text{In}$ fits very well with the experimental pattern. In Figure 7.6, the simulated XRD patterns of $\text{Mn}_{1.7}\text{Pt}_{0.8}\text{In}$ (original model, blue color) along with the simulated XRD pattern of half Heusler (black color) and inverse Heusler structure (red color) are shown. As can be seen from the patterns that the indexation of common peaks gets tripled in the case of $\text{Mn}_{1.7}\text{Pt}_{0.8}\text{In}$ due to the $3 \times 3 \times 3$ superstructure. Moreover, there are many additional peaks

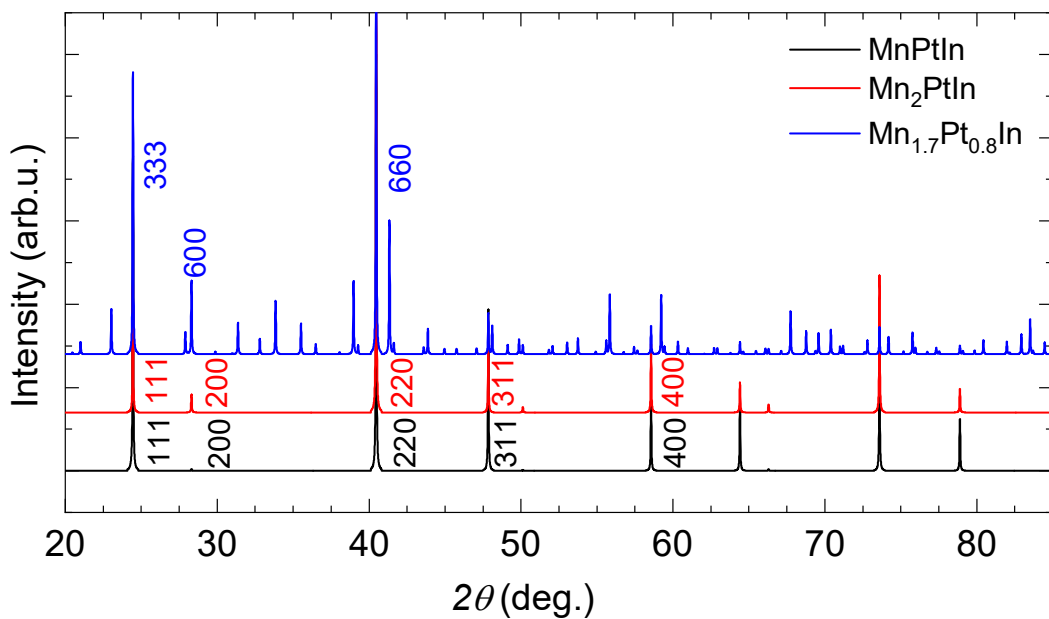


Figure 7.6. Simulated XRD patterns of superstructure $\text{Mn}_{1.7}\text{Pt}_{0.8}\text{In}$ (blue), inverse Heusler Mn_2PtIn (red), and half Heusler MnPtIn (black).

in the pattern, referring to superstructure reflections. These superstructure reflections are very clearly observed in the powder diffraction pattern.

7.3. Magnetic properties

After knowing the structural properties of $\text{Mn}_{1.7}\text{Pt}_{0.8}\text{In}$ that form a superstructure, the physical properties such as magnetization and electric transport properties are studied. In Figure 7.7, the direction-dependent magnetic properties of $\text{Mn}_{1.7}\text{Pt}_{0.8}\text{In}$ is shown. The magnetization as a function of temperature for different crystallographic directions, namely [100], [110], and [111] in the constant external field 0.01 T are presented in Figure 7.7(a). The magnetization is zero above 330 K, indicates that the magnetic ordering temperature is 330 K. Such a high magnetic ordering temperature is not seen so far in any compound with as complex crystal structure as $\text{Mn}_{1.7}\text{Pt}_{0.8}\text{In}$. Upon decreasing temperature below 330 K, the magnetization increases very sharply and saturates below 150 K. For the applied field of 0.01 T, the magnetization is the largest for [100] crystallographic direction at all the temperatures. Figure 7.7(b) represents the magnetization measured for [100] direction at various applied external fields. For 0.1 T, there is a significant change in the value for zero-field cooling (ZFC) and field cooling (FC) curves below 220 K while above 220 K, the ZFC and FC moments are approximately same. This indicates that at low-

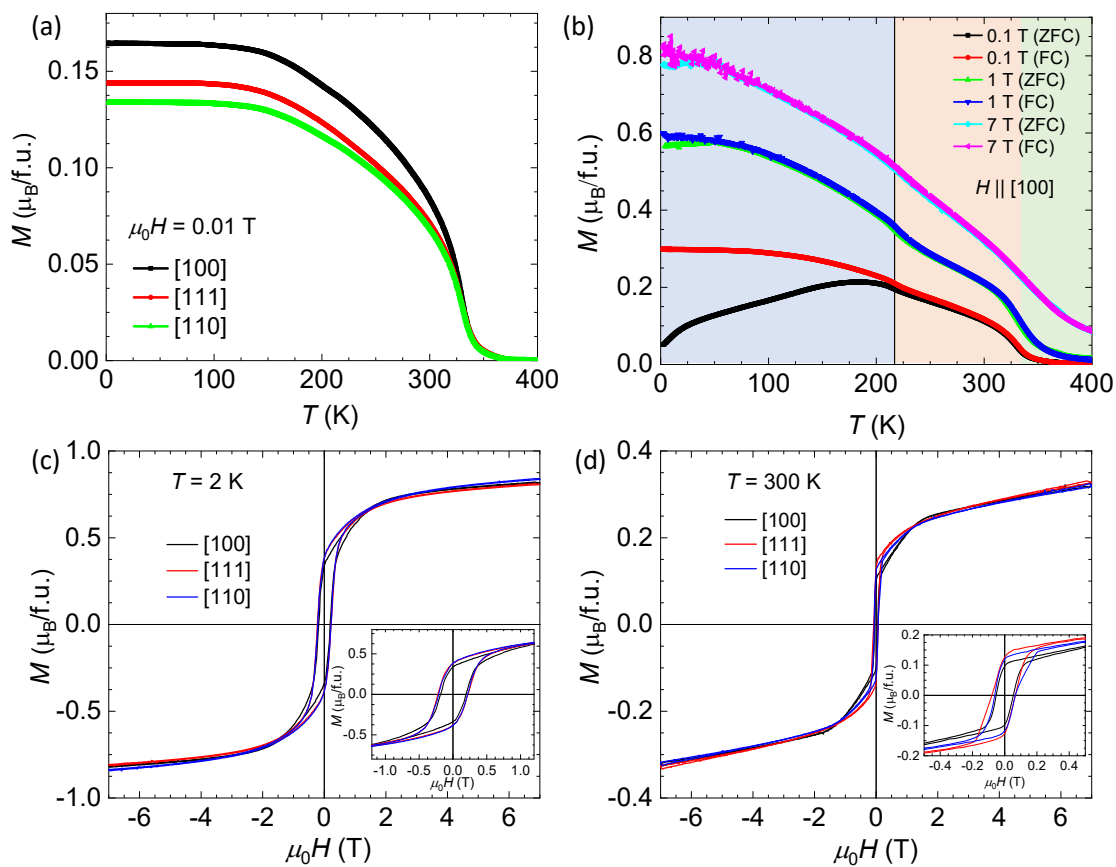


Figure 7.7. (a) M vs T for different crystallographic directions (b) M vs T for different field for direction [100], (c) isothermal magnetization at 2 K and (d) isothermal magnetization at 300 K for different directions.

temperature, there might be a different magnetic phase, possibly a non-collinear spin structure. This is further confirmed in the ZFC and FC curve for 1 T external magnetic field, where a sharp change in the magnetization is observed at 220 K. Thus, two magnetic regions have been identified for the compound $\text{Mn}_{1.7}\text{Pt}_{0.8}\text{In}$. First, a possible non-collinear spin structure exists below 220 K (blue region). Second, a possible ferrimagnetic spin structure exists between 220 K and 330 K (orange region). In Figure 7.7(c), the isothermal magnetization curves measured for 2 K temperature in different crystallographic directions are presented. For all the directions, a large value of magnetic coercivity of 0.3 T is found. Such a large coercivity is rarely observed in a cubic compound, especially in a single crystal. The magnetic moment at 2 K temperature is $0.7 \mu_{\text{B}}/\text{f.u.}$ or $0.4 \mu_{\text{B}}/\text{Mn}$ assuming Pt and In atoms share a negligible magnetic moment. In Figure 7.7(d), isothermal magnetization curves measured at 300 K for the different crystallographic directions are shown. Even at 300 K, the compound shows a significant coercivity value close to 0.1 T. For the [111], the moment saturates faster than other directions, indicating [111] as an easy axis. In the magnetization, two slope changes are observed at 0.15 T and 1.5 T before saturation. The former kink is related to the alignment of ferrimagnetic magnetic domains while the latter one belongs to slow field polarization of antiparallel ferrimagnetic moment along the applied field. At 300 K, in the ground state collinear ferrimagnetic structure, the magnetic moment observed is $0.12 \mu_{\text{B}}/\text{f.u.}$ or $0.07 \mu_{\text{B}}/\text{Mn}$. Such a low moment indicates that the moments of antiparallel aligned spins are approximately same, which means the compound is compensated ferrimagnetic. Compensated ferrimagnets (CFiM)⁴⁷ are a new class of materials that have the antiparallel aligned spins. These antiparallel aligned spins have different chemical environments or they are crystallographically inequivalent. This results in a net-zero moment while retaining finite spin-polarization. Various CFiM belonging to Heusler family have been discovered among them includes $\text{Mn}_2\text{Ru}_x\text{Ga}$ ^{49,147,148}, $\text{Mn}_{3-x}\text{Pt}_x\text{Ga}$ ⁵² and $\text{Mn}_{1.5}\text{FeV}_{0.5}\text{Al}$ ^{50,51}. Therefore, the compound $\text{Mn}_{1.7}\text{Pt}_{0.8}\text{In}$ belongs to a compensated ferrimagnetic family of materials and is possibly useful in the high-performance spintronics devices.

7.4. Electrical transport properties

In Figure 7.8, the longitudinal resistivity as a function of temperature is presented. The resistivity shows the metallic behavior of the compound as it decreases with decreasing the temperature. There is a slope change in the resistivity curve around 220 K, which is consistent with the transition observed in the magnetization. The resistivity values at 300 and 2 K are 1.73×10^{-4} and 1.06×10^{-4} Ω cm, respectively, resulting in the residual resistivity ratio of 1.63.

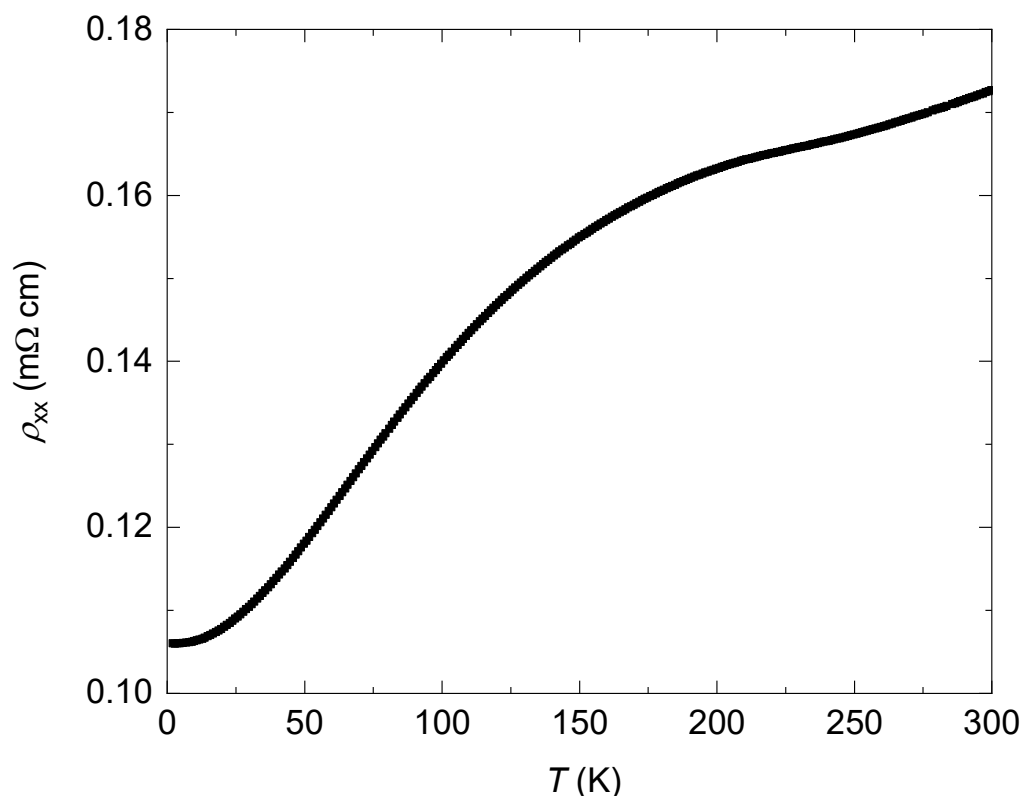


Figure 7.8. Longitudinal resistivity as a function of temperature.

The crystal size is rather small and it is hard to measure direction-dependent transport properties. Therefore, the Hall effect measurements are only performed for the field along [110]. In Figure 7.9, the electric transport properties consisting, magnetoresistance and Hall resistivity measurements of $\text{Mn}_{1.7}\text{Pt}_{0.8}\text{In}$ for the applied magnetic field along [110] and current along [001] are shown. The Hall resistivity as a function of the magnetic field at various temperatures is shown in Figure 7.9(a). The behavior of Hall resistivity follows the magnetization trend, exhibiting the significant value of anomalous Hall resistivity for all the temperatures and it is found to be $0.5 \mu\Omega$ cm at 2 K. Figure 7.9(b) shows MR (calculated using Equation 4.2) for different temperatures. At 2 K, MR first decreases up to 3 T and then starts increasing while at 300 K, it shows only decreasing behavior with the increasing magnetic field. These behaviors at different temperatures are possibly due to different magnetic structures of the compound. The value of magnetoresistance is quite small at all temperatures. The Hall conductivity and

anomalous Hall conductivity (σ^{AHE}) are calculated using Equation 4.3. Figure 7.9(c) shows the Hall conductivity as a function of the magnetic field for different temperatures.

The estimated highest value of σ^{AHE} is $45 \Omega^{-1}\text{cm}^{-1}$ for 2 K, which is a large value considering a small magnetic moment involved. The normal Hall coefficient and charge carrier concentration are extracted for this compound are presented in Figure 7.9(d). At low-temperature (below 100 K), the majority charge carrier is electrons while holes are majority charge carriers at high-temperature. The charge carrier concentration is mostly temperature independent in both electrons and holes type-regions and is approximately $4 \times 10^{21} \text{cm}^{-3}$.

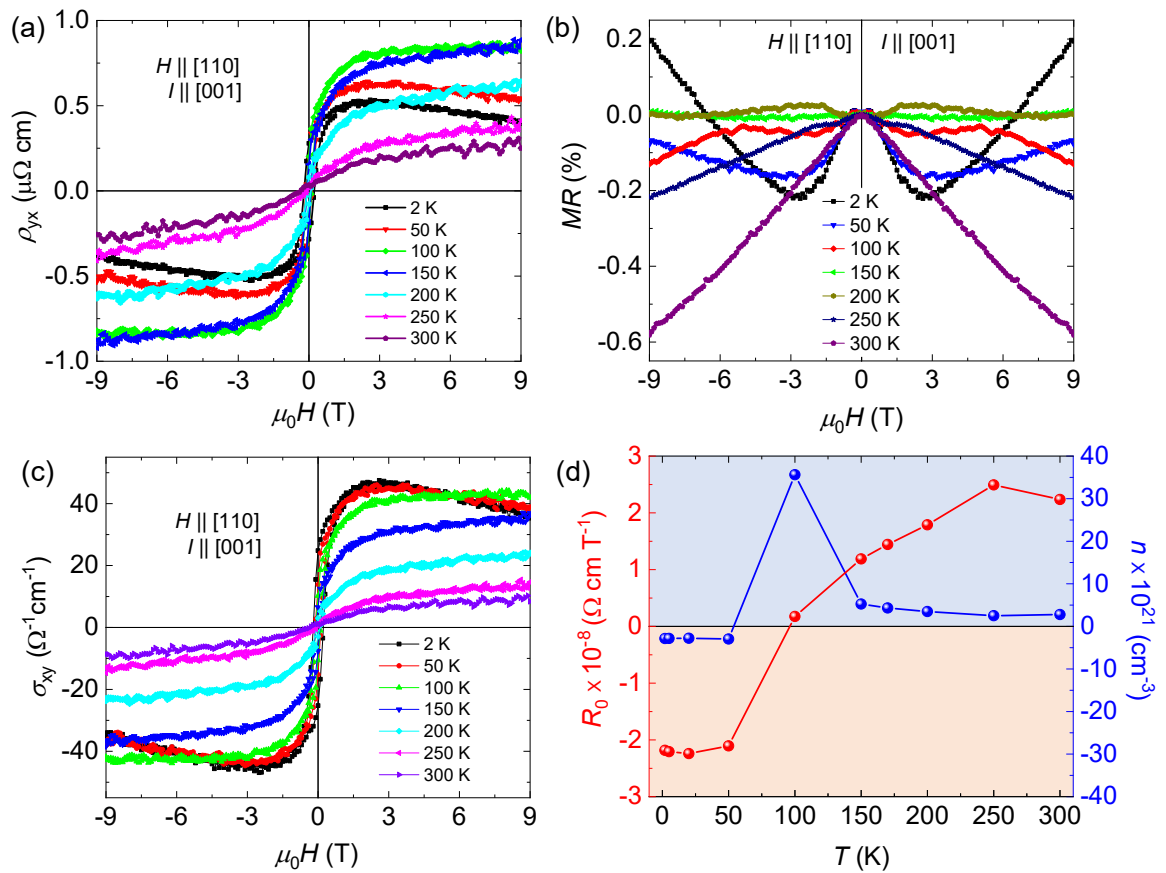


Figure 7.9. (a) Hall resistivity (ρ_{yx}) (b) magnetoresistance (MR) (c) Hall conductivity (σ_{xy}) as a function of field (H) and (d) charge carrier concentration (n , blue) and normal Hall coefficient (R_0 , red) a function of temperature (T).

Figure 7.10 represents the variation of σ^{AHE} as a function of temperature. Up to 50 K, the value of σ^{AHE} is nearly constant while it decreases linearly with increasing temperature. This almost linear variation above 50 K indicates that the contribution in the anomalous Hall effect is dominated by chemical disordering in the crystal structure.

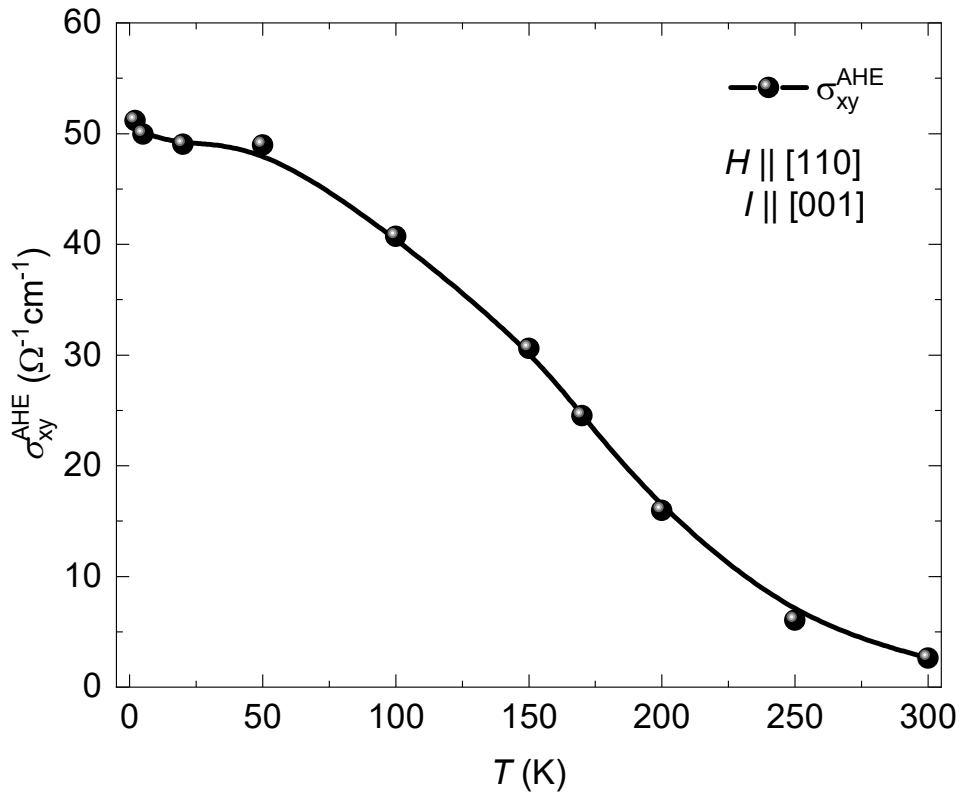


Figure 7.10. Anomalous Hall conductivity as a function of temperature.

Summary and future prospects

1. A new tetragonal Heusler compound $\text{Mn}_{1.4}\text{PtSn}$ is synthesized. Crystal growth techniques that require growth directly from melt, such as Bridgman method, always result in microtwinned crystals. To get microtwin free crystals, another technique, flux method is employed, where growth can be done far below the melting point and martensitic transition temperature. The flux method results in successful large microtwin free crystals of $\text{Mn}_{1.4}\text{PtSn}$.

The single-crystal diffraction is done on a small piece of single crystals of $\text{Mn}_{1.4}\text{PtSn}$. From structural analysis, it is found out that the crystal structure of $\text{Mn}_{1.4}\text{PtSn}$ is the first tetragonal superstructure in the family of Heusler compounds. The superstructure reflections are clearly observed in the powder X-ray diffraction patterns.

Direction-dependent magnetic properties are measured. The compound is found to undergo two magnetic transitions. First, at 392 K, which corresponds to Curie temperature and second, at 170 K, which corresponds to the spin-reorientation transition temperature. The saturation magnetic moment at 2 K is very large of 4.7 $\mu_{\text{B}}/\text{f.u.}$

The refinement of powder neutron diffraction reveals that in the temperature range of 170 to 392 K, the magnetic structure is collinear ferromagnet whereas below 170 K, it is a non-coplanar spin structure. The magnetic moment, obtained from refinement, is close to the saturation moment obtained from magnetization.

The electric transport properties are studied along the different crystallographic directions of the compound. The longitudinal resistivity measurement indicates that the compound is metallic and reveals the magnetic transitions at the same temperature as seen in the magnetization. An overall negative magnetoresistance of 3 percent is found. The Hall resistivity measurements reveal the presence of a large topological Hall resistivity (THE) of 0.9 $\mu\Omega \text{ cm}$ and -0.1 $\mu\Omega \text{ cm}$ for the magnetic field applied along [100] and [001], respectively. Two types of contributions in the THE for the field along [100] are seen. One that follows the quadratic form of longitudinal resistivity and second, that is independent of longitudinal resistivity. Anomalous Hall conductivity is found to be 250 and 165 $\Omega^{-1}\text{cm}^{-1}$ for the field along [100] and [001], respectively. This value is close to the value obtained from theoretical calculations. The topological Hall conductivity is found to be approximately the same as its anomalous analog.

The successful large microtwin free crystals will facilitate the properties related to novel antiskyrmions with Lorentz transmission electron microscopy (LTEM), small-angle neutron scattering (SANS), small-angle resonant X-ray scattering, Hall effect measurements in the micro-structured devices, and Nernst effect in future.

2. A new series of polycrystalline samples with iridium substitution at the place of platinum in $\text{Mn}_{1.4}\text{PtSn}$ are prepared. The structural characterization show the crystal structure of these compounds is the same as $\text{Mn}_{1.4}\text{PtSn}$, therefore, they also possess the tetragonal superstructure form.

Magnetic properties, along with powder neutron diffraction data, reveal that the magnetic structure changes from out-of-plane ferromagnet to in-plane ferrimagnet with Ir-substitution. All the compounds are found to have metallic character. A large anomalous Hall conductivity of $405 \text{ } \Omega^{-1}\text{cm}^{-1}$ is found for compound $\text{Mn}_{1.4}\text{Pt}_{0.7}\text{Ir}_{0.3}\text{Sn}$.

The interplay between out-of-plane and in-plane anisotropy in addition to the significant Dzyaloshinskii-Moriya interaction (DMI) in these compounds would possibly result in new types of topological spin-structures. This remains to be studied with techniques such as LTEM and SANS.

3. Three new series of compounds are prepared as an attempt to fill the vacancies present in the crystal structure of $\text{Mn}_{1.4}\text{PtSn}$ with transition-metal elements cobalt, nickel, and copper. The tetragonal superstructure survives up to 0.2 cobalt addition, 0.4 nickel addition and 0.6 copper addition. Further addition of elements leads to transformation to the inverse cubic Heusler structure. The magnetic properties show that the compounds with tetragonal structure have spin-reorientation transition, which is absent in the compounds with cubic structure.

The tetragonality nature and the magnetic properties are found to be changing with the addition of the elements. Additionally, DMI has been found to be dependent on chemical disordering. Therefore, the addition of elements would possibly change DMI and consequently lead to the tuning of the size of antiskyrmions. This remains to be studied with techniques such as LTEM and SANS.

4. A new compound $\text{Mn}_{1.7}\text{Pt}_{0.8}\text{In}$ is discovered. The single crystals are prepared by flux-method. Upon structural analysis from single-crystal refinement, it is found that the crystal structure is $3 \times 3 \times 3$ superstructure of a Heusler structure and is so far the largest discovered in the Heusler family of compounds.

Two magnetic transitions are revealed in the magnetization measurements. First, at 330 K, which corresponds to Curie temperature and second, at 220 K, which corresponds to spin-reorientation transition. The magnetic moment is $0.4 \mu_{\text{B}}/\text{Mn}$ at 2 K and $0.07 \mu_{\text{B}}/\text{Mn}$ at 300 K. Such a low moment might be due to possible compensated ferrimagnetic structure. Therefore, the compound is a potential candidate for spintronics devices.

References

- ¹ G.E. Moore, *Electronics* **38**, 114 (1965).
- ² S.A. Wolf, D.D. Awschalom, R.A. Buhrman, J.M. Daughton, S. Von Molnár, M.L. Roukes, A.Y. Chtchelkanova, and D.M. Treger, *Science* **294**, 1488 (2001).
- ³ S.A. Wolf, A.Y. Chtchelkanova, and D.M. Treger, *IBM J. Res. Dev.* **50**, 101 (2006).
- ⁴ M.N. Baibich, J.M. Broto, A. Fert, F.N. Van Dau, F. Petroff, P. Eitenne, G. Creuzet, A. Friederich, and J. Chazelas, *Phys. Rev. Lett.* **61**, 2472 (1988).
- ⁵ G. Binasch, P. Grünberg, F. Saurenbach, and W. Zinn, *Phys. Rev. B* **39**, 4828 (1989).
- ⁶ S. Ikeda, J. Hayakawa, Y. Ashizawa, Y.M. Lee, K. Miura, H. Hasegawa, M. Tsunoda, F. Matsukura, and H. Ohno, *Appl. Phys. Lett.* **93**, 082508 (2008).
- ⁷ S.S.P. Parkin, M. Hayashi, and L. Thomas, *Science* **320**, 190 (2008).
- ⁸ S. Parkin and S.H. Yang, *Nat. Nanotechnol.* **10**, 195 (2015).
- ⁹ A.N. Bogdanov and D.A. Yablonskii, *Sov. Phys. JETP* **68**, 101 (1989).
- ¹⁰ U.K. Röbber, A.N. Bogdanov, and C. Pfleiderer, *Nature* **442**, 797 (2006).
- ¹¹ D. Morikawa, X. Yu, K. Karube, Y. Tokunaga, Y. Taguchi, T. hisa Arima, and Y. Tokura, *Nano Lett.* **17**, 1637 (2017).
- ¹² T. Kurumaji, T. Nakajima, V. Ukleev, A. Feoktystov, T.H. Arima, K. Kakurai, and Y. Tokura, *Phys. Rev. Lett.* **119**, 237201 (2017).
- ¹³ S. Seki, X.Z. Yu, S. Ishiwata, and Y. Tokura, *Science* **336**, 198 (2012).
- ¹⁴ Y. Tokunaga, X.Z. Yu, J.S. White, H.M. Rønnow, D. Morikawa, Y. Taguchi, and Y. Tokura, *Nat. Commun.* **6**, 7638 (2015).
- ¹⁵ A. Bogdanov and A. Hubert, *J. Magn. Magn. Mater.* **138**, 255 (1994).
- ¹⁶ S. Mühlbauer, B. Binz, F. Jonietz, C. Pfleiderer, A. Rosch, and P.B. A. Neubauer, R. Georgii, *Science* **323**, 915 (2009).
- ¹⁷ K. Shibata, X.Z. Yu, T. Hara, D. Morikawa, N. Kanazawa, K. Kimoto, S. Ishiwata, Y. Matsui, and Y. Tokura, *Nat. Nanotechnol.* **8**, 723 (2013).
- ¹⁸ X.Z. Yu, N. Kanazawa, W.Z. Zhang, T. Nagai, T. Hara, K. Kimoto, Y. Matsui, Y. Onose, and Y. Tokura, *Nat. Commun.* **3**, 988 (2012).
- ¹⁹ T. Schulz, R. Ritz, A. Bauer, M. Halder, M. Wagner, C. Franz, C. Pfleiderer, K.

- Everschor, M. Garst, and A. Rosch, *Nat. Phys.* **8**, 301 (2012).
- ²⁰ A. Fert, V. Cros, and J. Sampaio, *Nat. Nanotechnol.* **8**, 152 (2013).
- ²¹ X.Z. Yu, N. Kanazawa, Y. Onose, K. Kimoto, W.Z. Zhang, S. Ishiwata, Y. Matsui, and Y. Tokura, *Nat. Mater.* **10**, 106 (2011).
- ²² I. Kezsmarki, S. Bordacs, P. Milde, E. Neuber, L.M. Eng, J.S. White, H.M. Rønnow, C.D. Dewhurst, M. Mochizuki, K. Yanai, H. Nakamura, D. Ehlers, V. Tsurkan, and A. Loidl, *Nat. Mater.* **14**, 1116 (2015).
- ²³ K. Karube, J.S. White, N. Reynolds, J.L. Gavilano, H. Oike, A. Kikkawa, F. Kagawa, Y. Tokunaga, H.M. Rønnow, Y. Tokura, and Y. Taguchi, *Nat. Mater.* **15**, 1237 (2016).
- ²⁴ G. Chen, *Nat. Phys.* **13**, 112 (2017).
- ²⁵ W. Koshibae and N. Nagaosa, *Nat. Commun.* **7**, 10542 (2016).
- ²⁶ A.N. Bogdanov, U.K. Röbller, M. Wolf, and K.H. Müller, *Phys. Rev. B* **66**, 214410 (2002).
- ²⁷ A.K. Nayak, V. Kumar, T. Ma, P. Werner, E. Pippel, R. Sahoo, F. Damay, U.K. Röbller, C. Felser, and S.S.P. Parkin, *Nature* **548**, 561 (2017).
- ²⁸ R. Saha, A.K. Srivastava, T. Ma, J. Jena, P. Werner, V. Kumar, C. Felser, and S.S.P. Parkin, *Nat. Commun.* **10**, 5305 (2019).
- ²⁹ J. Winterlik, S. Chadov, A. Gupta, V. Alijani, T. Gasi, K. Filsinger, B. Balke, G.H. Fecher, C.A. Jenkins, F. Casper, J. Kübler, G.D. Liu, L. Gao, S.S.P. Parkin, and C. Felser, *Adv. Mater.* **24**, 6283 (2012).
- ³⁰ L. Wollmann, A.K. Nayak, S.S.P. Parkin, and C. Felser, *Annu. Rev. Mater. Res.* **47**, 247 (2017).
- ³¹ L. Wollmann, S. Chadov, J. Kübler, and C. Felser, *Phys. Rev. B* **92**, 064417 (2015).
- ³² S. V. Faleev, Y. Ferrante, J. Jeong, M.G. Samant, B. Jones, and S.S.P. Parkin, *Phys. Rev. Appl.* **7**, 034022 (2017).
- ³³ K. Manna, Y. Sun, L. Muechler, J. Kübler, and C. Felser, *Nat. Rev. Mater.* **3**, 244 (2018).
- ³⁴ T. Graf, C. Felser, and S.S.P. Parkin, *Prog. Solid State Chem.* **39**, 1 (2011).
- ³⁵ V. Ksenofontov, G. Melnyk, M. Wojcik, S. Wurmehl, K. Kroth, S. Reiman, P. Blaha, and C. Felser, *Phys. Rev. B* **74**, 134426 (2006).
- ³⁶ D.B. Xiong, Y. Zhao, N.L. Okamoto, C. Pietzonka, T. Waki, and H. Inui, *Inorg. Chem.* **49**, 10536 (2010).

- ³⁷ D.B. Xiong, N.L. Okamoto, T. Waki, Y. Zhao, K. Kishida, and H. Inui, *Chem. - A Eur. J.* **18**, 2536 (2012).
- ³⁸ F. Heusler, *Verh. Dtsch. Phys. Ges.* **5**, 220 (1903).
- ³⁹ J.C. Suits, *Solid State Commun.* **18**, 423 (1976).
- ⁴⁰ C. Felser, L. Wollmann, S. Chadov, G.H. Fecher, and S.S.P. Parkin, *APL Mater.* **3**, 041518 (2015).
- ⁴¹ F. Casper, C. Felser, R. Seshadri, C. Peter Sebastian, and R. Pöttgen, *J. Phys. D: Appl. Phys.* **41**, 035002 (2008).
- ⁴² S.J. Murray, S.M. Allen, and T.A. Lograsso, *Appl. Phys. Lett.* **77**, 886 (2000).
- ⁴³ P.J. Webster, K.R.A. Ziebeck, S.L. Town, and M.S. Peak, *Philos. Mag. B* **49**, 295 (1984).
- ⁴⁴ Y. Xing, R. Liu, J. Liao, Q. Zhang, X. Xia, C. Wang, H. Huang, J. Chu, M. Gu, T. Zhu, C. Zhu, F. Xu, D. Yao, Y. Zeng, S. Bai, C. Uher, and L. Chen, *Energy Environ. Sci.* **12**, 3390 (2019).
- ⁴⁵ Z. Liu, S. Guo, Y. Wu, J. Mao, Q. Zhu, H. Zhu, Y. Pei, J. Sui, Y. Zhang, and Z. Ren, *Adv. Funct. Mater.* **29**, 1905044 (2019).
- ⁴⁶ L. Peng, R. Takagi, W. Koshibae, K. Shibata, K. Nakajima, T. Arima, N. Nagaosa, S. Seki, X. Yu, and Y. Tokura, *Nat. Nanotechnol.* **15**, 181 (2020).
- ⁴⁷ H. Van Leuken and R.A. De Groot, *Phys. Rev. Lett.* **74**, 1171 (1995).
- ⁴⁸ M. Jourdan, J. Minár, J. Braun, A. Kronenberg, S. Chadov, B. Balke, A. Gloskovskii, M. Kolbe, H.J. Elmers, G. Schönhense, H. Ebert, C. Felser, and M. Kläui, *Nat. Commun.* **5**, 3974 (2014).
- ⁴⁹ G. Bonfiglio, K. Rode, K. Siewerska, J. Besbas, G.Y.P. Atcheson, P. Stamenov, J.M.D. Coey, A. V. Kimel, T. Rasing, and A. Kirilyuk, *Phys. Rev. B* **100**, 104438 (2019).
- ⁵⁰ R. Stinshoff, A.K. Nayak, G.H. Fecher, B. Balke, S. Ouardi, Y. Skourski, T. Nakamura, and C. Felser, *Phys. Rev. B* **95**, 060410(R) (2017).
- ⁵¹ R. Stinshoff, G.H. Fecher, S. Chadov, A.K. Nayak, B. Balke, S. Ouardi, T. Nakamura, and C. Felser, *AIP Adv.* **7**, 105009 (2017).
- ⁵² A.K. Nayak, M. Nicklas, S. Chadov, P. Khuntia, C. Shekhar, A. Kalache, M. Baenitz, Y. Skourski, V.K. Guduru, A. Puri, U. Zeitler, J.M.D. Coey, and C. Felser, *Nat. Mater.* **14**, 679 (2015).
- ⁵³ H. Xiao, T. Hu, W. Liu, Y.L. Zhu, P.G. Li, G. Mu, J. Su, K. Li, and Z.Q. Mao, *Phys. Rev. B* **97**, 224511 (2018).

- ⁵⁴ T. Klimczuk, C.H. Wang, K. Gofryk, F. Ronning, J. Winterlik, G.H. Fecher, J.C. Griveau, E. Colineau, C. Felser, J.D. Thompson, D.J. Safarik, and R.J. Cava, *Phys. Rev. B* **85**, 174505 (2012).
- ⁵⁵ K. Manna, L. Muechler, T.H. Kao, R. Stinshoff, Y. Zhang, J. Gooth, N. Kumar, G. Kreiner, K. Koepf, R. Car, J. Kübler, G.H. Fecher, C. Shekhar, Y. Sun, and C. Felser, *Phys. Rev. X* **8**, 41045 (2018).
- ⁵⁶ I. Belopolski, K. Manna, D.S. Sanchez, G. Chang, B. Ernst, J. Yin, S.S. Zhang, T. Cochran, N. Shumiya, H. Zheng, B. Singh, G. Bian, D. Multer, M. Litskevich, X. Zhou, S.M. Huang, B. Wang, T.R. Chang, S.Y. Xu, A. Bansil, C. Felser, H. Lin, and M. Zahid Hasan, *Science* **365**, 1278 (2019).
- ⁵⁷ Z.K. Liu, L.X. Yang, S.C. Wu, C. Shekhar, J. Jiang, H.F. Yang, Y. Zhang, S.K. Mo, Z. Hussain, B. Yan, C. Felser, and Y.L. Chen, *Nat. Commun.* **7**, 12924 (2016).
- ⁵⁸ S. Chadov, X. Qi, J. Kübler, G.H. Fecher, C. Felser, and S.C. Zhang, *Nat. Mater.* **9**, 541 (2010).
- ⁵⁹ R. Sadanaga, T. Sawada, K. Ohsumi, and K. Kamiya, *J. Japan. Assoc. Min. Petr. Econ. Geol.* **2**, 23 (1980).
- ⁶⁰ M.J. Buerger, *J. Chem. Phys.* **15**, 1 (1947).
- ⁶¹ U. Müller, *Inorganic Structural Chemistry* (John Wiley & Sons Ltd, 2006).
- ⁶² W. Pfeiler, *Alloy Physics: A Comprehensive Reference* (WILEY-VCH Verlag GmbH & Co. KGaA, Weinheim, 2007).
- ⁶³ E. Gratz, A. Kottar, A. Lindbaum, M. Mantler, M. Latroche, V. Paul-Boncour, M. Acet, C. Barner, W.B. Holzapfel, V. Pacheco, and K. Yvon, *J. Phys. Condens. Matter* **8**, 8351 (1996).
- ⁶⁴ N. Frangis, C. Manolikas, and S. Amelinc, *Phys. Stat. Sol.* **126**, 99 (1991).
- ⁶⁵ Y. Ding, R. Yang, and Z.L. Wang, *Solid State Commun.* **138**, 390 (2006).
- ⁶⁶ N. Roth and B.B. Iversen, *Acta Crystallogr. Sect. A Found. Adv.* **75**, 465 (2019).
- ⁶⁷ A. Lindbaum, J. Hafner, and E. Gratz, *J. Phys. Condens. Matter* **11**, 1177 (1999).
- ⁶⁸ T.H.R. Skyrme, *Nucl. Phys.* **31**, 556 (1962).
- ⁶⁹ C. Pfleiderer, *Nat. Phys.* **7**, 673 (2011).
- ⁷⁰ U.K. Rößler, A.A. Leonov, and A.N. Bogdanov, *J. Phys. Conf. Ser.* **200**, 022029 (2010).
- ⁷¹ A. Neubauer, C. Pfleiderer, B. Binz, A. Rosch, R. Ritz, P.G. Niklowitz, P. Bo, and P.

- Böni, Phys. Rev. Lett. **102**, 186602 (2009).
- ⁷² F. Jonietz, S. Mulbauer, C. Pfleiderer, A. Neubauer, W. Munzer, A. Bauer, T. Adams, R. Georgii, P. Boni, R.A. Duine, K. Everschor, M. Garst, and A. Rosch, Science **330**, 1648 (2010).
- ⁷³ P. Milde, D. Köhler, J. Seidel, L.M. Eng, A. Bauer, A. Chacon, J. Kindervater, S. Mühlbauer, C. Pfleiderer, S. Buhrandt, C. Schütte, and A. Rosch, Science **340**, 1076 (2013).
- ⁷⁴ J. Wild, T.N.G. Meier, S. Pöllath, M. Kronseder, A. Bauer, A. Chacon, M. Halder, M. Schowalter, A. Rosenauer, J. Zweck, J. Müller, A. Rosch, C. Pfleiderer, and C.H. Back, Sci. Adv. **3**, 1701704 (2017).
- ⁷⁵ X.Z. Yu, Y. Onose, N. Kanazawa, J.H. Park, J.H. Han, Y. Matsui, N. Nagaosa, and Y. Tokura, Nature **465**, 901 (2010).
- ⁷⁶ A.K. Srivastava, P. Devi, A.K. Sharma, T. Ma, H. Deniz, H.L. Meyerheim, C. Felser, and S.S.P. Parkin, Adv. Mater. **32**, 1904327 (2020).
- ⁷⁷ A.O. Leonov, Y. Togawa, T.L. Monchesky, A.N. Bogdanov, J. Kishine, Y. Kousaka, M. Miyagawa, T. Koyama, J. Akimitsu, T. Koyama, K. Harada, S. Mori, D. McGrouther, R. Lamb, M. Krajenak, S. McVitie, R.L. Stamps, and K. Inoue, Phys. Rev. Lett. **117**, 087202 (2016).
- ⁷⁸ A.S. Sukhanov, P. Vir, A.S. Cameron, H.C. Wu, N. Martin, S. Mühlbauer, A. Heinemann, H.D. Yang, C. Felser, and D.S. Inosov, Phys. Rev. B **100**, 184408 (2019).
- ⁷⁹ A.S. Sukhanov, P. Vir, A. Heinemann, S.E. Nikitin, D. Kriegner, H. Borrmann, C. Shekhar, C. Felser, and D.S. Inosov, Phys. Rev. B **100**, 180403(R) (2019).
- ⁸⁰ S.L. Zhang, A. Bauer, H. Berger, C. Pfleiderer, G. Van Der Laan, and T. Hesjedal, Phys. Rev. B **93**, 214420 (2016).
- ⁸¹ M. Hirschberger, T. Nakajima, S. Gao, L. Peng, A. Kikkawa, T. Kurumaji, M. Kriener, Y. Yamasaki, H. Sagayama, H. Nakao, K. Ohishi, K. Kakurai, Y. Taguchi, X. Yu, T. hisa Arima, and Y. Tokura, Nat. Commun. **10**, 5831 (2019).
- ⁸² M.N. Wilson, M.T. Birch, A. Štefančič, A.C. Twitchett-Harrison, G. Balakrishnan, T.J. Hicken, R. Fan, P. Steadman, and P.D. Hatton, Phys. Rev. Res. **2**, 013096 (2020).
- ⁸³ Y. Yamasaki, D. Morikawa, T. Honda, H. Nakao, Y. Murakami, N. Kanazawa, M. Kawasaki, T. Arima, and Y. Tokura, Phys. Rev. B **92**, 220421(R) (2015).
- ⁸⁴ A. Bauer and C. Pfleiderer, Phys. Rev. B **85**, 214418 (2012).
- ⁸⁵ N. Nagaosa, J. Sinova, S. Onoda, A.H. MacDonald, and N.P. Ong, Rev. Mod. Phys. **82**, 1539 (2010).

- ⁸⁶ C. Franz, F. Freimuth, A. Bauer, R. Ritz, C. Schnarr, C. Duvinage, T. Adams, S. Blügel, A. Rosch, Y. Mokrousov, and C. Pfleiderer, *Phys. Rev. Lett.* **112**, 186601 (2014).
- ⁸⁷ C. Pfleiderer and A. Rosch, *Nature* **465**, 880 (2010).
- ⁸⁸ T. Kurumaji, T. Nakajima, M. Hirschberger, A. Kikkawa, Y. Yamasaki, H. Sagayama, H. Nakao, Y. Taguchi, T. hisa Arima, and Y. Tokura, *Science* **365**, 914 (2019).
- ⁸⁹ M. Leroux, M.J. Stolt, S. Jin, D. V. Pete, C. Reichhardt, and B. Maierov, *Sci. Rep.* **8**, 15510 (2018).
- ⁹⁰ N. Kanazawa, Y. Onose, T. Arima, D. Okuyama, K. Ohoyama, S. Wakimoto, K. Kakurai, S. Ishiwata, and Y. Tokura, *Phys. Rev. Lett.* **106**, 156603 (2011).
- ⁹¹ R. Ritz, M. Halder, C. Franz, A. Bauer, M. Wagner, R. Bamler, A. Rosch, and C. Pfleiderer, *Phys. Rev. B* **87**, 134424 (2013).
- ⁹² M. Lee, W. Kang, Y. Onose, Y. Tokura, and N.P. Ong, *Phys. Rev. Lett.* **102**, 186601 (2009).
- ⁹³ B.J. Chapman, M.G. Grossnickle, T. Wolf, and M. Lee, *Phys. Rev. B* **88**, 214406 (2013).
- ⁹⁴ S.X. Huang and C.L. Chien, *Phys. Rev. Lett.* **108**, 267201 (2012).
- ⁹⁵ J.C. Gallagher, K.Y. Meng, J.T. Brangham, H.L. Wang, B.D. Esser, D.W. McComb, and F.Y. Yang, *Phys. Rev. Lett.* **118**, 027201 (2017).
- ⁹⁶ V. Kumar, N. Kumar, M. Reehuis, J. Gayles, A.S. Sukhanov, A. Hoser, F. Damay, C. Shekhar, P. Adler, and C. Felser, *Phys. Rev. B* **101**, 014424 (2020).
- ⁹⁷ M. Hoffmann, J. Weischenberg, B. Dupè, F. Freimuth, P. Ferriani, Y. Mokrousov, and S. Heinze, *Phys. Rev. B* **92**, 020401(R) (2015).
- ⁹⁸ J. Kübler and C. Felser, *EPL* **108**, 67001 (2014).
- ⁹⁹ M. Onoda, G. Tatara, and N. Nagaosa, *J. Phys. Soc. Japan* **73**, 2624 (2004).
- ¹⁰⁰ N. Nagaosa and Y. Tokura, *Phys. Scr.* **T146**, 14020 (2012).
- ¹⁰¹ N. Nagaosa, *J. Phys. Soc. Japan* **75**, 42001 (2006).
- ¹⁰² S. Onoda and N. Nagaosa, *Phys. Rev. Lett.* **90**, 4 (2003).
- ¹⁰³ C. Sürgers, G. Fischer, P. Winkel, and H. V. Löhneysen, *Nat. Commun.* **5**, 3400 (2014).
- ¹⁰⁴ K.G. Rana, O. Meshcheriakova, J. Kübler, B. Ernst, J. Karel, R. Hillebrand, E. Pippel, P. Werner, A.K. Nayak, C. Felser, and S.S.P. Parkin, *New J. Phys.* **18**, 085007 (2016).

- ¹⁰⁵ P. Swekis, A. Markou, D. Kriegner, J. Gayles, R. Schlitz, W. Schnelle, S.T.B. Goennenwein, and C. Felser, *Phys. Rev. Mater.* **3**, 013001(R) (2019).
- ¹⁰⁶ R. Schlitz, P. Swekis, A. Markou, H. Reichlova, M. Lammel, J. Gayles, A. Thomas, K. Nielsch, C. Felser, and S.T.B. Goennenwein, *Nano Lett.* **19**, 2366 (2019).
- ¹⁰⁷ B. Ding, Y. Li, G. Xu, Y. Wang, Z. Hou, E. Liu, Z. Liu, G. Wu, and W. Wang, *Appl. Phys. Lett.* **110**, 092404 (2017).
- ¹⁰⁸ M.G. Kanatzidis, R. Pöttgen, and W. Jeitschko, *Angew. Chemie - Int. Ed.* **44**, 6996 (2005).
- ¹⁰⁹ P.C. Canfield and I.R. Fisher, *J. Cryst. Growth* **225**, 155 (2001).
- ¹¹⁰ P.C. Canfield and Z. Fisk, *Philos. Mag. B Phys. Condens. Matter; Stat. Mech. Electron. Opt. Magn. Prop.* **65**, 1117 (1992).
- ¹¹¹ C. Petrovic, P.C. Canfield, and J.Y. Mellen, *Philos. Mag.* **92**, 2448 (2012).
- ¹¹² P. W. Bridgman, *Proc. Am. Acad. Arts Sci.* **60**, 303 (1925).
- ¹¹³ W. Kraus and G. Nolze, *Fed. Inst. Mater. Res. Test.* 87, D-12205 Berlin Ger. (n.d.).
- ¹¹⁴ G.M. Sheldrick, *Acta Crystallogr. Sect. C Struct. Chem.* **C71**, 3 (2015).
- ¹¹⁵ L.J. Farrugia, *J. Appl. Crystallogr.* **45**, 849 (2012).
- ¹¹⁶ J. Rodriguez-Carvajal, *Phys. B.* **192**, 55 (1993).
- ¹¹⁷ O. Meshcheriakova, S. Chadov, A.K. Nayak, U.K. Rößler, J. Kübler, G. André, A.A. Tsirlin, J. Kiss, S. Hausdorf, A. Kalache, W. Schnelle, M. Nicklas, and C. Felser, *Phys. Rev. Lett.* **113**, 087203 (2014).
- ¹¹⁸ O. Meshcheriakova *et al.*, *Phys. Rev. Lett.* **113**, 087203 (2014) (Supplementary).
- ¹¹⁹ P. Vir, N. Kumar, H. Borrmann, B. Jamijansuren, G. Kreiner, C. Shekhar, and C. Felser, *Chem. Mater.* **31**, 5876 (2019).
- ¹²⁰ P. Vir, J. Gayles, A.S. Sukhanov, N. Kumar, F. Damay, Y. Sun, J. Kübler, C. Shekhar, and C. Felser, *Phys. Rev. B* **99**, 140406(R) (2019).
- ¹²¹ A. Sozinov, N. Lanska, A. Soroka, and W. Zou, *Appl. Phys. Lett.* **102**, 021902 (2013).
- ¹²² T. Bachaga, J. Zhang, M. Khitouni, and J.J. Sunol, *Int. J. Adv. Manuf. Technol.* **103**, 2761 (2019).
- ¹²³ Paul Drude, *Ann. Der Phys.* **306**, 566 (1900).

- ¹²⁴ H. Ishizuka and N. Nagaosa, *Sci. Adv.* **4**, 9962 (2018).
- ¹²⁵ J. Kübler, *Theory of Itinerant Electron Magnetism* (Oxford University Press, 2017).
- ¹²⁶ A.R. Williams, J. Kübler, and C.D. Gelatt, *Phys. Rev. B* **19**, 6094 (1979).
- ¹²⁷ A.A. Mostofi, J.R. Yates, Y.S. Lee, I. Souza, D. Vanderbilt, and N. Marzari, *Comput. Phys. Commun.* **178**, 685 (2008).
- ¹²⁸ G. Kresse and J. Furthmüller, *Comput. Mater. Sci.* **6**, 15 (1996).
- ¹²⁹ J.P. Perdew, K. Burke, and M. Ernzerhof, *Phys. Rev. Lett.* **77**, 3865 (1996).
- ¹³⁰ J. Barker and O.A. Tretiakov, *Phys. Rev. Lett.* **116**, 147203 (2016).
- ¹³¹ P.F. Bessarab, D. Yudin, D.R. Gulevich, P. Wadley, M. Titov, and O.A. Tretiakov, *Phys. Rev. B* **99**, 140411(R) (2019).
- ¹³² B. Göbel, A. Mook, J. Henk, and I. Mertig, *Phys. Rev. B* **96**, 060406(R) (2017).
- ¹³³ X. Zhang, Y. Zhou, and M. Ezawa, *Sci. Rep.* **6**, 24795 (2016).
- ¹³⁴ P.M. Buhl, F. Freimuth, S. Blügel, and Y. Mokrousov, *Phys. Status Solidi - Rapid Res. Lett.* **11**, 1700007 (2017).
- ¹³⁵ R. Chulist, A. Sozinov, L. Straka, N. Lanska, A. Soroka, T. Lippmann, C.G. Oertel, and W. Skrotzki, *J. Appl. Phys.* **112**, 063517 (2012).
- ¹³⁶ H.E. Karaca, I. Karaman, B. Basaran, Y.I. Chumlyakov, and H.J. Maier, *Acta Mater.* **54**, 233 (2006).
- ¹³⁷ B. Kiefer, H.E. Karaca, D.C. Lagoudas, and I. Karaman, *J. Magn. Magn. Mater.* **312**, 164 (2007).
- ¹³⁸ V.A. Chernenko, V. V. Kokorin, O.M. Babii, and I.K. Zasimchuk, *Intermetallics* **6**, 29 (1998).
- ¹³⁹ O. Söderberg, Y. Ge, A. Sozinov, S.P. Hannula, and V.K. Lindroos, *Smart Mater. Struct.* **14**, S223 (2005).
- ¹⁴⁰ L. Straka, H. Hänninen, A. Soroka, and A. Sozinov, *J. Phys. Conf. Ser.* **303**, 012079 (2011).
- ¹⁴¹ K.W. Moon, J. Yoon, C. Kim, and C. Hwang, *Phys. Rev. Appl.* **12**, 064054 (2019).
- ¹⁴² B. Göbel, A. Mook, J. Henk, I. Mertig, and O.A. Tretiakov, *Phys. Rev. B* **99**, 060407(R) (2019).

- ¹⁴³ Y. Huh, P. Kharel, A. Nelson, V.R. Shah, J. Pereiro, P. Manchanda, A. Kashyap, R. Skomski, and D.J. Sellmyer, *J. Phys. Condens. Matter* **27**, 076002 (2015).
- ¹⁴⁴ A. Nelson, H. Y, P. Kharel, V.R. Shah, R. Skomski, and D.J. Sellmyer, *J. Appl. Phys.* **115**, 17A923 (2014).
- ¹⁴⁵ A.K. Nayak, S. Chandra, W. Jürgen, G. Arunava, and C. Felser, *Appl. Phys. Lett.* **100**, 152404 (2015).
- ¹⁴⁶ H. Luo, P. Jia, G. Liu, F. Meng, H. Liu, E. Liu, W. Wang, and G. Wu, *Solid State Commun.* **170**, 44 (2013).
- ¹⁴⁷ K. Borisov, D. Betto, Y.C. Lau, C. Fowley, A. Titova, N. Thiyagarajah, G. Atcheson, J. Lindner, A.M. Deac, J.M.D. Coey, P. Stamenov, and K. Rode, *Appl. Phys. Lett.* **108**, 192407 (2016).
- ¹⁴⁸ N. Thiyagarajah, Y.C. Lau, D. Betto, K. Borisov, J.M.D. Coey, P. Stamenov, and K. Rode, *Appl. Phys. Lett.* **106**, 122402 (2015).

Versicherung

Hiermit versichere ich, dass ich die vorliegende Arbeit mit dem Titel “Superstructures in Heusler compounds and investigation of their physical properties” ohne unzulässige Hilfe Dritter und ohne Benutzung anderer als der angegebenen Hilfsmittel angefertigt habe. Die aus fremden Quellen direkt oder indirekt übernommenen Gedanken sind als solche kenntlich gemacht. Die Arbeit wurde bisher weder im Inland noch im Ausland in gleicher oder ähnlicher Form einer anderen Prüfungsbehörde vorgelegt.

Die vorliegende Dissertation wurde am Max-Planck-Institut für Chemische Physik fester Stoffe unter der wissenschaftlichen Betreuung von Frau Prof. Dr. Claudia Felser.

Praveen Vir

Dresden, 02.09.2020

Place, Date

